Development and Characterisation of Collagen-Based Scaffolds for Breast Cancer Research

John Redmond, BSc

Submitted for the degree of Doctor of Philosophy

School of Mechanical and Manufacturing Engineering
Dublin City University

Supervised by:
Professor Nicholas Dunne
Dr. Tanya Levingstone
Dr. Paul Buchanan

August 2023

I hereby certify that this material, which I now submit for assessment on the programme of study leading to the award of Doctor of Philosophy is entirely my own work, and that I have exercised reasonable care to ensure that the work is original, and does not to the best of my knowledge breach any law of copyright, and has not been taken from the work of others save and to the extent that such work has been cited and acknowledged within the text of my work.

Signed: _____John Redmond_____

ID No.: 13506183

Date: 01 August 2023

Acknowledgments

It's been a long ~~four~~ five years full of highs, lows, hardships, character development, endless stress, lab disasters, late nights, COVID, high blood pressure and endless redrafts of papers, transfers and this thesis. But, if you were to ask me would I go back to 2017 to start this journey again, I'd say yes. There has been such a sizeable support network around me over the last few years that have assisted my navigation through my studies, and a huge gratitude is owed.

The first thank you has to go to my supervisory team – Nicholas, Tanya and Paul. Nicholas as my primary supervisor went above and beyond over the last few years to ensure my passage throughout this PhD and without him, I definitely would not have got to this point. I am extremely grateful to have worked with him over these five years. Tanya and Paul alongside have provided me with endless expertise over the years, and provided a friendly, welcoming and nurturing support network. Thank you all.

It goes without saying that a huge debt of gratitude is owed to my friends here within the lab. Antzela and Nikoletta, for being the epitome of perfect students and offering inspiration to me. Hardworking, helpful and a bundle of laughs. Halima, for keeping me on the straight and narrow and delivering her brutal honesty when I needed it most. Ghayadah, the kindest soul, wouldn't dare to say no to helping me, and never ever said no to my fifth phone call of the night when I needed someone to talk to. To all four of you, thank you for making the lab and office such a great place to come to everyday.

I also owe a massive thank you to Debbie O'Reilly, the greatest cell culture mentor one could have. From my final year project and all the way through my PhD, you have been an incredible help at getting me set up in the lab and teaching me everything I know about cell culture – but also thank you for making the lab a fun place to come to. For that, I am grateful.

To my family, for the constant support and love throughout my PhD, thank you. From letting me come home and raid the presses, eat all the food, get free lifts back to Dublin…and of course the financial support – I am forever grateful.

To all my friends, of whom there are too many to go through – thank you for being there for me over the last few years. The endless social, emotional and even financial support has been incredible and paramount to me completing this PhD.

Finally, a thanks to all the staff in DCU that have assisted me along the way, both in MME, the NRF, the School of Nursing and the School of Biotechnology. Thanks to all the remaining lab mates within our MEDeng laboratory for making the lab a great place to work. I know the place is in safe hands now that I am leaving. Lastly, to Paul Barham, his expertise and assistance when it came to the freeze-drier was invaluable to completing this PhD – thank you.

Contents

Table of Figures

List of Tables

List of Equations

Abidhana and Units

Abbreviations

18S rRNA	18S ribosomal RNA
2D	Two-Dimensional
3D	Three-Dimensional
4-OHT	4-Hydroxytamoxifen
COL1A1	Collagen type I alpha 1 chain
Ct	Cycle threshold
CXCR4	CXC chemokine receptor type 4
DHT	Dehydrothermal treatment
DMEM	Dulbecco`s modified eagle media
DNA	Deoxyribonucleic acid
ECM	Extracellular matrix
EDAC	1-Ethyl-3-(3-Dimethylaminopropyl) carbodiimide
EDTA	Ethylenediaminetetraacetic acid
ER	Estrogen receptor
ER-/PR-	Estrogen receptor negative / progesterone receptor negative
ER+/PR+	Estrogen receptor positive / progesterone receptor positive
ERO1A	Endoplasmic reticulum oxidoreductase 1 alpha
FBS	Foetal bovine serum
FN1	Fibronectin 1
FTIR	Fourier-transform infrared spectroscopy
GAPDH	Glyceraldehyde 3-phosphate dehydrogenase
GLUT1	Glucose transporter 1
GTA	Glutaraldehyde
HAS1	Hyaluronan synthase 1
HAS2	Hyaluronan synthase 2
HCl	Hydrochloric acid
HMDS	Hexamethyldisilazane
HER2	Human epidermal growth factor 2

HIF1A	Hypoxia-inducible factor 1-alpha
HPRT	Hypoxanthine-guanine phosphoribosyltransferase
JAG1	Jagged 1
KCl	Potassium chloride
KH$_2$PO$_4$	Potassium phosphate monobasic
LOX	Lysyl oxidase
MMPs	Matrix metalloproteinases
MMP2	Matrix metalloproteinase -2
MMP9	Matrix metalloproteinase -9
MSCs	Mesenchymal stem cells
Na$_2$HPO$_4$	Sodium phosphate dibasic dihydrate
NaCl	Sodium chloride
NHS	N-Hydroxysuccinimide
ns	No Significance
PBS	Phosphate buffer saline
PCR/qPCR	Polymerase chain reaction/quantitative polymerase chain reaction
PenStrep	Penicillin-streptomycin
PR	Progesterone receptor
RPM	Revolutions per minute
RNA / mRNA	Ribonucleic acid / messenger ribonucleic acid
SEM	Scanning electron microscope/microscopy
SD	Standard deviation
TGFB1	Transforming growth Factor beta 1
TME	Tumour microenvironment
TRIS	Tris(hydroxymethyl)aminomethane
VEGFA	Vascular endothelial growth factor A
w/Gel	used in Figure graphs; denotes Collagen 0.5% scaffold with added gelatin

Units

°C	Degrees Celsius
cm/mm/µm/nm	Centimetre / micrometre / micrometre / nanometre
cm^2	Centimetre squared
CV% / CtCV%	Coefficient of variation / cycle threshold coefficient of variation
g/cm^3	Grams per centimetre cubed
g/µg	Gram / microgram
kPa	Kilopascals
kV	Kilovolts
mTorr	millitorr (non-SI unit of pressure used for freeze-drying)
mg/mL	Milligrams per millilitre
mL/µL	Millilitre / microlitre
µM/mM	Micromolar / millimolar
M	Molar
nM	Nanomolar
N	Newton
ng/mL	Nanograms per millilitre
Pa	Pascal
wt/v %	Weight per volume percentage
µg/mL	Micrograms per millilitre

Publications and Presentations

Papers:

J. Redmond, H.O. McCarthy, P. Buchanan, T.J. Levingstone, N.J. Dunne, Development and characterisation of 3D collagen-gelatin based scaffolds for breast cancer research, *Biomaterials Advances*. 142 (2022) 213157.

J. Redmond, H. McCarthy, P. Buchanan, T.J. Levingstone, N.J. Dunne, Advances in biofabrication techniques for collagen-based 3D *in vitro* culture models for breast cancer research, *Materials Science and Engineering C*. 122 (2021).

T.J. Levingstone, S. Herbaj, **J. Redmond**, H.O. McCarthy, N.J. Dunne, Calcium Phosphate Nanoparticles-Based Systems for RNAi Delivery: Applications in Bone Tissue Regeneration, *Nanomaterials*. 10 (2020).

Conference Presentations:

Oral podium presentation (virtual) 'Collagen-Based Scaffolds: for use in Breast Cancer Research'. 11th World Biomaterials Congress, Glasgow, Scotland (May-2020).

Oral podium presentation (virtual) 'Development and Characterisation of Collagen-Gelatin Based Scaffolds for Breast Cancer Research'. 23rd Sir Bernard Crossland Symposium, DCU, Dublin (Sept-2020).

Oral podium presentation 'Novel Collagen:Gelatin Scaffolds for Breast Cancer Research. 26th Annual BINI Conference, Mount Wolseley, Carlow (Jan-2020).

Oral podium presentation 'Collagen-Based Scaffolds for *Ex Vivo* Culture of Breast Cancer Tissue'. 25th Annual BINI Conference, Castletroy hotel, Limerick (Jan-2019).

Oral poster presentation 'Engineering Collagen-based Scaffolds for *Ex Vivo* Culture of Breast Cancer Tissue'. 29th Annual Meeting of the European Society for Biomaterials (ESB), Maastricht, Holland (Sept-2018).

Oral podium presentation 'Development of Advanced Biomimetic 3D Culture Models for Breast Cancer Research'. 21st Sir Bernard Crossland Symposium, UCD, Dublin (April-2018).

Oral podium presentation 'Developing a 3D Model for Growth of Breast Cancer Tissue'. 'Tell it Straight 2018' final (DCU, March-2018).

Oral podium presentation 'Advanced Biomimetic 3D Culture Models for Understanding Breast Cancer Research'. 24th Annual BINI Conference, Johnstown Estate, Kildare (Jan-2018).

Abstract

John Redmond

Development and Characterisation of Collagen-Based Scaffolds for Cancer Research

Collagen is the most abundant component of the extracellular matrix, and therefore represents an ideal platform for culture of a variety of cell types. Collagen has been widely used in 3D culture models for tissue engineering and musculoskeletal-related research. Recently, attempts to extend the use of collagen-based 3D culture models to cancer research have shown promise. While 2D culture presents a useful tool for cancer research, it is ultimately flawed due to poor replication of the tumour microenvironment, the lack of three-dimensional cell-cell/cell-matrix interactions and often exaggerated response to therapeutic agents. 3D models that aim to overcome the issues associated with 2D culture research offer a new frontier for cancer research with cell growth, morphology and genetic properties that more closely match *in vivo* cancer. The focus of this thesis was to develop 3D collagen-based scaffolds for use in breast cancer research. A range of collagen-based scaffolds were successfully fabricated using a freeze-drying procedure. Scaffolds were highly porous with homogenous pore sizes and an interconnected structure that was suitable for cell infiltration and nutrient/waste exchange. All scaffolds demonstrated appropriate mechanical properties for mimicking cancerous breast tissue stiffness and displayed high *in vitro* stability with low degradation. Cell line studies demonstrated scaffold biocompatibility with sustained breast cancer cell proliferation over 21 days, with cells fully infiltrating throughout the scaffolds. 3D culture led to an increase in cell malignancy compared to 2D, with MCF7 cells displaying properties of ECM modification, hypoxia and glycolysis. The fabricated scaffolds were successfully applied as an *in vitro* drug testing model, with cells cultured in the 3D scaffolds displaying increased chemoresistance compared to 2D cultured cells. Overall, this thesis successfully delivered a biologically relevant *in vitro* culture model that offers significant potential to deliver an increased understanding of breast cancer progression and augment drug discovery.

01

Chapter 1:
Introduction and
Literature Review

Sections of this Chapter have previously been presented (with some modification) in a literature review published in Materials Science and Engineering: C (2021).

J. Redmond, H. McCarthy, P. Buchanan, T.J. Levingstone, N.J. Dunne, Advances in biofabrication techniques for collagen-based 3D *in vitro* culture models for breast cancer research, Mater. Sci. Eng. C. 122 (2021) 111944.

1.1 Overview

Breast cancer is a major healthcare burden worldwide, with 2020 global estimates indicating that the disease is responsible for 11.7% (~2.3 million) of all new cancer cases and the 5th highest cause of cancer mortality with 685,000 deaths (6.9% of total deaths) across both sexes [1]. Within the female population only, breast cancer is responsible for the highest incidence and mortality rates, accounting for 24.5% of all new cases and 15.5% of cancer deaths [2]. The 2018 data represents an increase compared to previous GLOBOCAN (2018) data of 2.1 million new cases and 626,679 deaths that year [2]. With ageing populations, poorer diets and a host of other genetic and environmental factors, urgent action is needed to address breast cancer–notably in the case of metastatic breast cancer where median overall survival remains poor at only 2-3 years [3]. It is imperative to continue to invest in new and novel ways to study breast cancer across many disciplines including cancer morphology, genetics, drug testing and more.

Collagen is the most abundant human protein (approximately 30% of total body protein) and provides an essential structural role within connective tissue and the extracellular matrix (ECM). At a cellular level it is involved in cell adhesion, and cell-cell and cell-matrix communication. As the principal component of ECM, collagen plays a significant role in the tumour microenvironment [4–7]. Understanding the role of the ECM in tumour development and spread has allowed researchers to develop *in vitro* collagen-based culture models for the growth of cancer cells [8–12]. The generation of these biomimetic 3D models to culture cancer cells allows for promising investigations into understanding cancer development and progression, in addition to acting as a platform for testing the efficacy of traditional and new cancer drug compounds. Use of 3D *in vitro* culture models can reduce the reliance on

traditional 2D models and potentially pave the way to reduce the use of animals in drug testing regimes, a key goal of the research community.

1.2   Breast cancer

Cancer is a family of cellular diseases characterised by uncontrolled cellular proliferation leading to the development of tumours. Malignant tumours can spread around the body and form secondary tumours at distant sites, which is known as metastasis. Multiple factors influence the development of cancers including genetics, environment, diet/lifestyle and infection. In 2000, Hananan and Weinberg coined the six 'hallmarks' of cancers that define the capabilities and characteristics that tumours possess. These included: (1) resisting cell death, (2) evading growth suppressors, (3) an ability to induce angiogenesis, (4) sustained proliferation signals, (5) activation of invasion and metastasis, and (6) enabling replicative immortality [13]. In 2011, they expanded these hallmarks to include further emerging aspects of cancers such as tumour-promoting inflammation, evading immune destruction, genomic instability and mutation, and deregulation of cellular energetics [14].

1.2.1   Breast cancer development and progression

Breast cancers develop as cell division becomes uncontrolled, and a mass of cells known as a tumour forms. At this early stage, cells are abnormal but non-cancerous and form an atypical hyperplasia [15–17]. The hyperplasia may not progress to cancer, however in some cases these abnormal cells can begin to accrue mutations which drive these cells to becoming cancerous i.e., malignant. These cancerous cells developed the aforementioned hallmarks of cancer and the now cancerous tumour continues to grow due to the uncontrolled cell division

and avoidance of apoptosis. While the tumour remains at the original site, it is known as an *in situ* carcinoma [15–17]. As the cancer continues to progress, cells may become invasive and migrate away from the parent site to distant tissues/organise where they form secondary tumours – this process is known as metastasis [18]. It is at this late stage of breast cancer whereby the mass of cells has outgrown oxygen and nutrient supplies and promotes angiogenesis to form new vasculature which helps sustain growth and spread of the cancer [19]. The above development can be graded into various stages, labelled 0 to IV (which are discussed in more detail elsewhere [15,20]), where Stage 0 denotes an *in situ* carcinoma and Stage IV denotes a cancer where distant metastases have occurred [15,20]. The above development and spread of breast cancer has been summarised in Figure 1.1.

A **Healthy Breast tissue**

Epithelial cells {

Myoepithelial cells {

Basement membrane ▸

ECM ·

Blood vessel ▸

B **Cell division becomes uncontrolled & cell mass forms**

C **Mass of cells grows (tumour) and undergoes changes and mutations**

D **Tumour grows further and metastasis occurs (invasive carcinoma)**

Angiogenesis
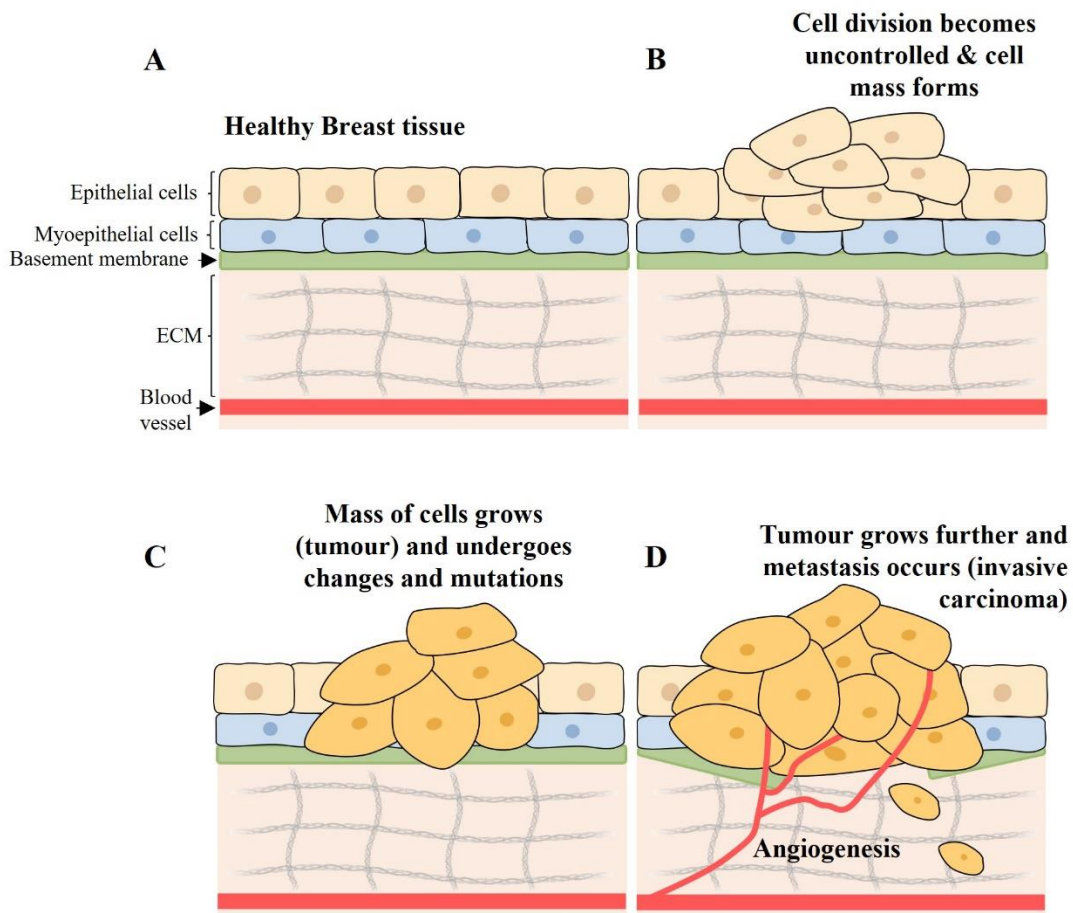
Figure 1.1: Summarised stages of cancer development. (a) Demonstrates healthy breast tissue. Breast cancer begins when cell division in the mammary tissue becomes uncontrolled and a cellular mass/tumour begins to form (B). This tumour continues to grow as cells proliferate rapidly and uncontrollably. Some of these cells undergo mutation which can drive the benign to cancerous transition (C). In (D), the tumour continues to grow with metastasis and angiogenesis occurs [13].

1.2.2   Breast cancer subtypes

The majority of breast cancers occur within the ductal or lobular tissue of the breast (Fig. 1.2). Invasive ductal carcinoma accounts for ~80% of all invasive breast cancer cases while Invasive Lobular Carcinoma accounts for the majority of the rest of invasive breast cancer cases [21]. Breast cancer can be further classified according to the tumour receptor status, the three most common of which are the Estrogen Receptor (ER), Progesterone Receptor (PR) and the Human Epidermal Growth Factor Receptor 2 (HER2) [22]. The estrogen and progesterone receptors respond to the presence or absence of the namesake hormones for each. Breast cancers may be positive or negative for these hormones. ER-positive (ER+) tumours grow in response to estrogen while PR-positive (PR+) tumours grow in response to progesterone. If a tumour is classed as negative for these receptors (ER-/PR-), then the tumour can continue to grow regardless of the presence or absence of those hormones [23]. HER2 is a protein which promotes cell proliferation and inhibits apoptosis and in certain breast cancer cases (~15%), the HER2 gene (ERBB2) become overexpressed (known as HER2 enriched). In most cases, there is a subsequent large increase in the HER2 receptor protein on the cell surface (known as HER2+ cancers) and this leads to an aggressive disease [24,25]. Patients without such amplification of HER2 on the cell surface can be classified as HER2 negative (HER2-). Patients can be classified as Triple Negative or Triple Positive in cases where they have an absence (negative) or presence (positive) of all 3 receptors. Triple-Negative tumours can be notoriously difficult to treat as they do not fall under the use of hormone therapy or HER2 specific treatments [26,27]. The above receptor statuses among other genetic or proliferation markers (such as Ki-67, a proliferation biomarker [28,29]) drive the classification of breast cancers into four primary molecular subtypes which are outlined in Table 1.1; Luminal A, Luminal B, HER2 enriched and Basal-like breast cancers.
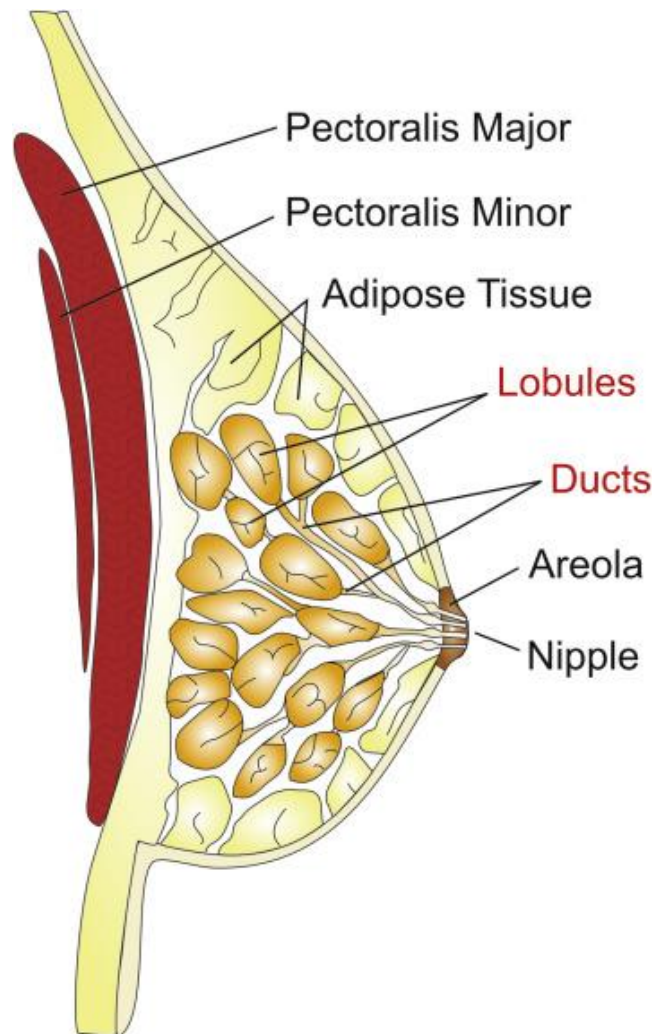
Figure 1.2: Overview of breast structure. Lobules and ducts of the breast (highlighted) are the most common sites of cancer within the breast. Figure from Feng *et al.* (2018) [15].

Table 1.1: Overview of breast cancer subtypes

Subtype	Tumour Status	Summary	Incidence
	ER+ and/or PR+, HER2- [30], Ki-67 low [31,32]	The most prevalent subtype of breast cancer. Rather slow-growing tumours relative to other subtypes and have the best overall survival of all breast cancer [30,33,34].	68.7%*
Luminal B	ER+ and/or PR+, HER2- or HER2+ [30], Ki-67 high [31,32]	Luminal B tumours are similar to Luminal A, but have a more aggressive phenotype in comparison. Tumours proliferate at a higher rate than Luminal A and have a poorer prognosis [33,35,36].	9.7%*
HER2 enriched	ER-, PR-, HER2+ [30]	Overexpression of HER2 and upregulation of HER2 receptor on cell surface. Leads to increased tumour proliferation, poor prognosis and poorer survival rates than both Luminal tumours [33,37].	4%*
Basal-like	ER-, PR-, HER2- [30]	Predominantly triple-negative breast cancer (TNBC), though not exclusively. Poor prognosis and difficult to treat and have the worst survival rates of the four subtypes [26,27,33].	10.1%*

*Incidence rates derived from the SEER registry, assessing breast cancer incidence in the United States by subtype through 2015-2019, n=588,498, unknown rate 7.6% [38]. Incidence rates can vary per region/population thus cited percentages may contrast to other subtype studies.

1.2.3 Current treatments

A variety of treatments for breast cancer are available. In many cases, surgery will be used initially for the physical removal of the tumour, and this can be followed by chemotherapy or radiation therapy. Surgery can also be used as a preventative measure for those who are deemed at high risk of developing breast cancer, such as those with BRCA1/BRCA2 mutations [39]. Treatments are often tailored based on a patient's tumour receptor status. Hormone positive tumours are tackled with compounds that interact with the hormone receptors or hormones themselves. Hormone receptor targeting compounds interact with the hormone receptor thus blocking the hormone itself from eliciting its biological effects upon binding to the receptor. Tamoxifen, an anti-estrogen agent used in ER+ cases, is a common example [40]. Other compounds work by physically lowering the amount of available estrogen. Aromatase inhibitors are an example and these compounds work by lowering estrogen production [41]. Letrozole is an example of an aromatase inhibitor indicated for either estrogen or progesterone receptor positive breast cancers [42]. HER2+ cancers are less affected by hormone therapies thus treatments include targeted therapies that selectively modulate the function of the HER2 receptor. One such therapy is Trastuzumab, a monoclonal antibody, that binds to HER2 and ultimately causes downregulation of the receptor leading to tumour regression [43]. Triple-negative presenting patients that respond poorly to hormone/HER2 therapies are often treated with chemotherapy though ultimately face a poorer prognosis [26]. Common chemotherapeutic agents used to treat multiple subtypes of breast cancer include doxorubicin [44], docetaxel [45], epirubicin [46] and fluorouracil [47].

1.3 Extracellular matrix (ECM), breast cancer and collagens

The ECM is a dynamic network of proteins that plays a role in tissue organisation, homeostasis maintenance and is also known for its preventative role in disease. Collagen is the most abundant protein present within the breast ECM, with laminins, elastin, fibronectin, proteoglycans, glycoproteins and a range of ECM remodelling enzymes also present [48]. Around the body, the ECM provides essential structural, biochemical and biomechanical support to cells [49,50]. The ECM also plays a key role in general cell activities including adhesion, proliferation, cell-cell communication and cell death [51,52]. It is through careful regulation of these processes that the ECM maintains a healthy and disease-free tissue state. However, recently the role that the ECM plays in carcinogenesis, metastatic spread and resistance to therapy has become more established, especially for breast cancer [5,48,53–56]. Various alterations in the breast ECM structure, composition and component density (Fig. 1.3) have been highlighted as key occurrences in tumour growth, spread and resistance to treatments [5,48,53–56]. Collagen is the major component of the breast ECM and thus naturally plays a key role in the development and spread of cancer [48,57,58].

A) Normal Breast ECM

B) Cancerous Breast ECM

Interstitial ECM:
- Fibrillar Collagens - I,III, V
- Fibronectin
- Elastin

Stiffening of Interstitial ECM

Basement Membrane

Migration of Cancer cells through ECM: Metastasis

Disruption of Basement Membrane

- Myoepithelial cell
- Immune cell
- Fibroblast
- Luminal Epithelial cell
- Breast Cancer cell
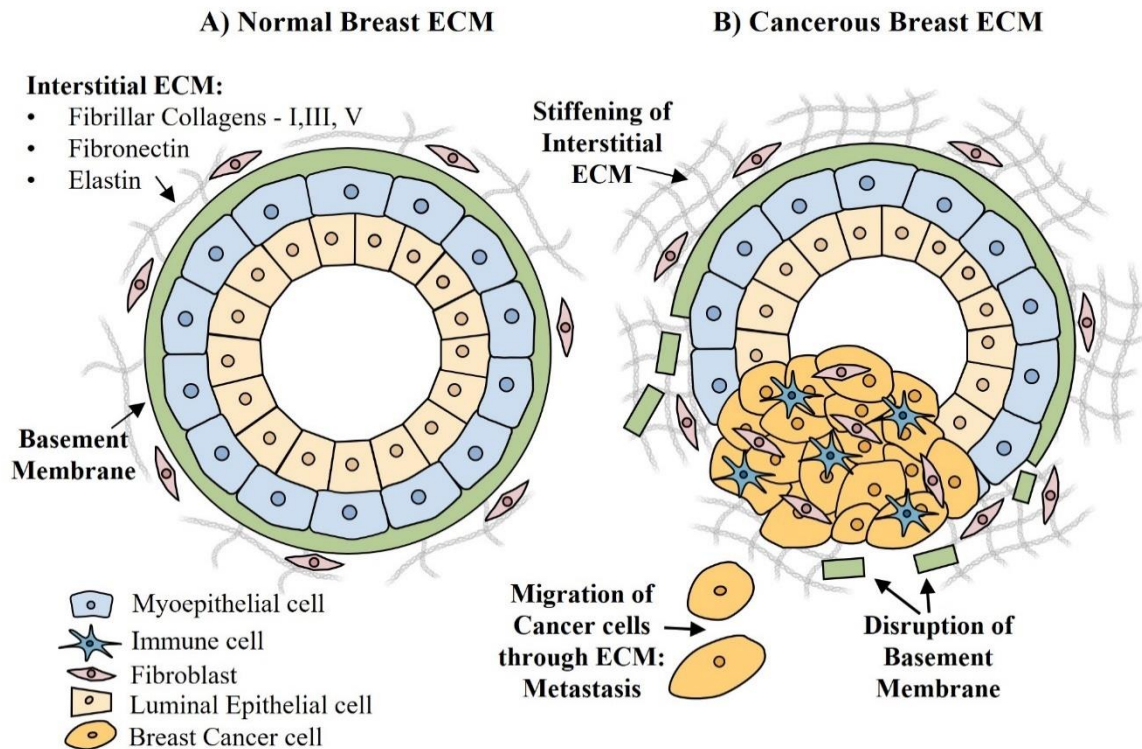
Figure 1.3: Alterations in Breast ECM during cancer progression. This figure highlights the development of invasive Ductal Carcinoma, the most common form of breast cancer. Key developments include the; uncontrolled growth of tumour cells, disruption of the basement membrane, stiffening of the interstitial ECM and migration of cancer cells through the ECM. Significant alterations take place in the collagen makeup, namely the breakdown of the basement membrane and the increased deposition of collagen in the interstitial matrix. Adapted/modified from Insua-Rodríugueza and Oskarsson, (2016) [48].

1.3.1 Collagen: general role, structure and function

There are 28 different collagen types (Type I through XXVIII) – the most common and abundant being types I, II, III, IV and V [59]. Collagens are classified according to their structure, which include; classical fibrillar and network-forming collagens, fibril-associated collagens with interrupted triple helices (FACITs), membrane-associated collagens with interrupted triple helices, and multiple triple-helix domains and interruptions (MULTIPLEXINs) [60,61]. Collagen is unique from many other proteins due to its incorporation of modified amino acids hydroxyproline and hydroxylysine, which help promote the structural arrangement of collagen [62–65]. Collagens are composed of three polypeptide strands known as alpha (α) chains/peptides, which twist together to form a triple helix structure [61] – despite the many classifications and differences among the collagen superfamily, this tightly coiled triple helix structure is a shared feature by all. The triple helix may be composed of three identical α chains, forming homotrimers or composed of different α chains, forming heterotrimers [66]. All collagens share a repeating amino acid sequence of glycine-X-Y (where X and Y are other amino acids though frequently proline and hydroxyproline), and these repeating glycines at every third residue drive the formation of the triple helix collagen structure [59–61].

Formation of the complete collagen molecule is outlined in Fig. 1.4. The process begins when three single procollagen chains interact with one another to form the tightly coiled triple helix procollagen trimer. This procollagen trimer is processed that includes the removal of N & C-propeptide tails resulting in the completed collagen molecule. Collagen molecules interact with one another to form fibrils and these fibrils then further organise with other fibrils to form collagen fibres [60,67]. Depending on tissue type, collagen fibrils

13

can organise and associate with one another in a varied manner to dictate specific tissue functions and properties [68]. Denaturation of collagen (via thermal treatment) causes the unwinding of the triple helix structure, resulting in the formation of gelatin [69].
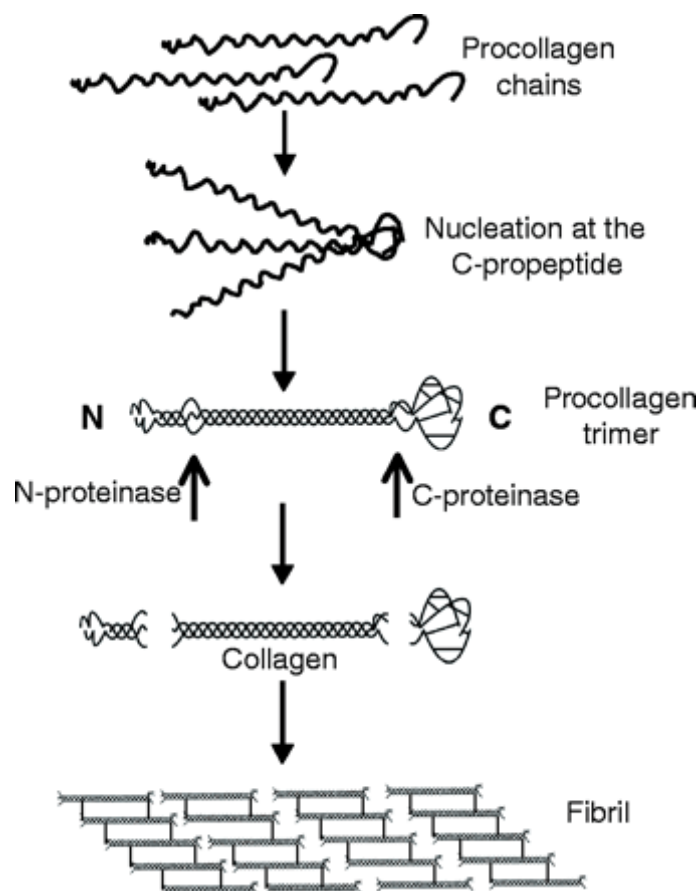
Figure 1.4: Overview of collagen molecule synthesis. Figure from Canty and Kadler (2005) [67].

As the major component of the ECM, collagen plays a significant role in not only aiding the structure and integrity of tissues but also in cell signalling, differentiation and migration through cell-matrix interactions [60,61]. Collagens have multiple binding sites for integrins,

growth factors and other ECM components which all serve in biochemical and cell signalling cascades [70]. Integrins, in particular, are of interest as they are the key mediator of cell-matrix interactions and have been shown to regulate migration, invasion, proliferation and survival of cancerous cells [71–73]. The role of integrin signalling has been observed in colorectal adenocarcinoma metastases where increased collagen deposition was observed to assist tumour growth and survival [74]. Collagen also plays a significant role in modulating matrix stiffness, which has been shown to modulate cell behaviour and stem cell differentiation [75–78]. While the role that matrix stiffness plays in cancer progression is still emerging, Engler *et al.* (2006) demonstrated the effect of matrix stiffness on cell differentiation [75]. Here, mesenchymal stem cells (MSCs) were cultured on collagen-coated hydrogels of varying stiffness which served to replicate values reported for different tissues *in vivo*. Each collagen-coated hydrogel encouraged MSC differentiation into defined lineages based on the stiffness of the matrix. Gels of a stiffness range of 0.1–1 kPa (brain mimicking) were neurogenic, gels of a stiffness range of 8–17 kPa (muscle mimicking) were myogenic and gels of a stiffness range of 25–40 kPa (bone mimicking) were osteogenic [75]. While collagen plays the aforementioned crucial roles in maintaining tissue integrity and key cellular processes – it is now known that changes in the collagen family within the ECM are important during the development and subsequent progression of breast cancer.

1.3.2 Alterations of collagen within the ECM during breast cancer

In breast cancer, increased deposition of collagen types I, III and V has been observed, which promotes tissue stiffness and is associated with increased cancer aggression and metastases risk [48,54,55,79]. Within the molecular/immunohistochemical (IHC) breast cancer subtypes (Table 1.1) there is emerging evidence of a correlation between subtype and

collagen content/arrangement. Acerbi *et al.* (2015) found increased collagen deposition and fibre linearisation in the more aggressive HER2+ and TNBC tumours in comparison to both the less aggressive Luminal A and B subtypes [58]. The breast ECM is further stiffened through the action of lysyl oxidase (LOX) enzymes. These enzymes promote crosslinking of collagen within the ECM [80] and elevated LOX levels in breast cancer patients are associated with poor overall survival [4,81,82]. *LOX* expression has been observed to be significantly increased in triple negative breast cancers (advanced and aggressive disease) in comparison to the other subtypes [83]. Increased collagen expression and deposition are not the only alterations observed – the breakdown of collagen type IV is a crucial step in breast cancer metastasis [84]. Collagen type IV is a key component of the basement membrane [85] and its degradation is key to membrane breaching, allowing cancer cells to migrate to distant sites/organs. This degradation is mediated by matrix metalloproteinases (MMPs), specifically MMP2 and MMP9 [86–89]. A further key signature of collagen alteration during breast cancer is the linearisation of collagen fibrils during carcinogenesis, which creates so-called 'highways' that facilitate the migration of cells away from the primary tumour site towards the basement membrane [56,90,91]. This feature is again seen to a greater extent in the more aggressive HER2+ and TNBC subtypes in comparison to the luminal subtypes [58].

The stiffness of the ECM is correlated to the elastic modulus of tissue–stiffer tissues demonstrate increased elastic moduli and therefore leads to altered mechanical and biomechanical responses, which often favours malignancy and cancer progression [4,78]. While stiffness and elastic modulus are technically two different measurements, they are related and typically proportional. Stiffness and elastic modulus both quantify resistance to elastic deformation but stiffness is a function of both material and geometry while elastic modulus is an inherent feature of just the material. Within this thesis, the elastic modulus

was used to give an indication of the stiffness characteristic within breast cancer tissue/ECM *in vivo*. There is limited agreement within the literature regarding the exact elastic modulus of the breast ECM. This is due to the difficulty in determining the mechanical properties of *in vivo* breast tissue and the variation in stiffness within different regions of the tumour microenvironment. Techniques used to measure tissue stiffness include standard unconfined compression, atomic force microscopy or elastography [4,92–97]. Healthy human breast tissue biopsies were found to have an elastic modulus ranging from ~1.00-1.83 kPa as determined using indentation-type atomic force microscopy (AFM). In contrast, cancerous breast tissue (patient IHC subtype not provided) demonstrates a large variance in stiffness with distinct soft regions in the tumour core of 0.3-0.75 kPa (densely populated with breast cancer cells) and significantly stiffer region with moduli ranging from 2-20 kPa towards the tumour periphery (high collagen content) [92].

AFM analysis of breast ECM surrounding induced mammary tumours in an *in vivo* murine model (MMTV-PyMT mouse model, aggressive tumour resembling HER2+ subtype) exhibited an average elastic modulus of 1.1 kPa in normal pre-cancer ECM, increasing to 1.3 kPa in the pre-malignant state and further rising to 1.7 kPa in the malignant state [93]. In two other breast cancer murine model studies (both employing unconfined compression): Paszek *et al.* (2005) found mean healthy breast tissue elastic modulus to be ~0.15-0.2 kPa, a mean tumoral tissue modulus of ~3-5 kPa and adjacent breast tumoural tissue to have a mean modulus of ~0.65-1.2 kPa (FVB-TgN (MMTV-c-myc, HER2/neu, and H-ras) – HER2+ subtype model) [94]; and Levental *et al.* (2009) found mean healthy breast tissue to have an elastic modulus of ~0.2 kPa, a mean tumoral tissue elastic modulus of ~1.25-1.75 kPa and adjacent breast tumoural tissue to have a mean elastic modulus of ~0.3-0.6 kPa (FVB-TgN MMTV-Neu mouse model, HER2+ subtype model) [4]. Tissue elasticity/stiffness values

determined using AFM or static mechanical testing (e.g., under compressive loading) can differ significantly to other techniques. Cancerous breast tissue mechanical properties measured using shear-wave elastography reported elasticity/stiffness values ≥100 kPa (all subtypes, Luminal A/B, HER2 enriched and Basal-like (TNBC), assessed in each study) [95–97]. Thus, evidence in the literature suggests that the mechanical properties of breast cancer tissue are currently not yet fully understood, with few studies exploring the relationship between mechanical properties of the different breast cancer subtypes and how they may differ. It must also be noted that the complexity of human breast tissue is difficult to replicate in simple collagen-based 3D *in vitro* scaffolds. Tumour cells among other ECM components and cell groups all contribute to the mechanical properties of breast tissue *in vivo*.

The previously discussed correlation between breast cancer subtype and collagen deposition/arrangement [58] further translated into alignment of stiffness profiles with the various subtypes. Higher elastic modulus values were reported amongst human samples for more aggressive Basal-like (triple negative tumours) and HER2+ cancers, which had increased collagen deposition while the less aggressive Luminal A and B cancers showed lower elastic modulus. In stiffness distribution profiles, determined through AFM, Basal-like and HER2+ had a large range of elastic modulus values with a greater skew towards values > 2 kPa, with many samples seeing elastic modulus values of 1-6 kPa. Both Luminal A and B tumours had a smaller distribution of elastic moduli, with the majority of samples in a range of 0.1-1.5 kPa [58]. Similarly, Min Chang *et al.* (2013), through shear wave elastography, found HER2+ (160.3 kPa) and TNBC (165.8 kPa) tumours to have a greater mean elasticity/stiffness than Luminal tumours (136.9 kPa) [96]. This potential correlation between collagen properties and breast cancer subtype may present the opportunity for

stratification of *in vitro* work whereby 3D scaffolds are tailored based on the presenting patients breast cancer subtype.

Overall, the complex alterations within the ECM that occur during breast cancer development and progression demonstrates the increasing importance of the development 3D culture models that more accurately reflect these processes.

1.4   Emergence of 3D culture models

Both 2D and 3D *in vitro* culture models are used to study many cancer types, both in terms of tumour morphology/characteristics and tumour response to therapeutic agents. The application of 3D *in vitro* culture models plays a valuable role in cancer research, however there is currently no one validated, trusted model for breast cancer. As a result, 2D *in vitro* and *in vivo* (xenografts) culture remain popular and widely used [98]. *In vitro* 2D culture models involve the growth of cancer cell lines or dissociated primary tumour cells in a monolayer [99]. The use of primary cells is preferred as they match the original tumour [100]. However, culture lifespan of primary cells is limited and they are more difficult to grow [101,102]. As a result, cancer cell lines have been developed and have proven to be a useful resource in cancer research, however their use is not without limitation. Cell lines are robust and can replicate indefinitely – but they are clonally derived and thus homogeneous populations [103,104]. They do not replicate the heterogeneity displayed within tumours, an aspect of their morphology that makes certain cancers challenging to treat [105]. Certain cancer cell lines may have subtle genetic and epigenetic differences from primary counterparts, which may further reduce their usefulness in various *in vitro* experiments [106,107]. Furthermore, existing 2D *in vitro* culture methods do not adequately replicate the

complex tumour microenvironment. The tumour-ECM interaction is fundamental in directing and controlling many aspects of cancer development and progression [5,7] and is absent in 2D culture. The lack of the 3D matrix in 2D models results in poor cell-cell interaction and a lack of cell-matrix interactions. Also, there is a lack of nutrient/oxygen gradients in 2D culture, which is not replicative of human cancer [108]. A further consequence of these 2D culture models is altered/inflated drug response by cells grown in a monolayer [9,12,109–111]. Cells in their native 3D environment, coupled with the presence of extensive ECM, frequently have a higher resistance to various drug compounds than cell line counterparts in 2D culture. This can be seen in many 2D versus 3D studies, whereby different responses to drug exposure, not just limited to increased resistance, occurs in 3D cultures compared to the same cells grown in monolayer [9,12,109–111]. Many drugs that show promise in 2D *in vitro* culture assessments are not successful in clinical trials, with only a small percentage (<5%) of compounds that demonstrate anticancer activity in preclinical development achieving licensing for use [112]. The primary advantages of 3D models over 2D culture are highlighted in Fig. 1.5.

- Lack of 3D cell-matrix interaction
- Poor cell-cell interaction
- No nutrient/waste/oxygen gradients

- Good cell-matrix interaction
- Good cell-cell interaction
- Nutrient/Waste/Oxygen gradients

Ex vivo & Co-culture possible

Cells adopt flat morphology in monolayer

Cells form aggregates

2D Culture

3D Culture - **Scaffold Based**
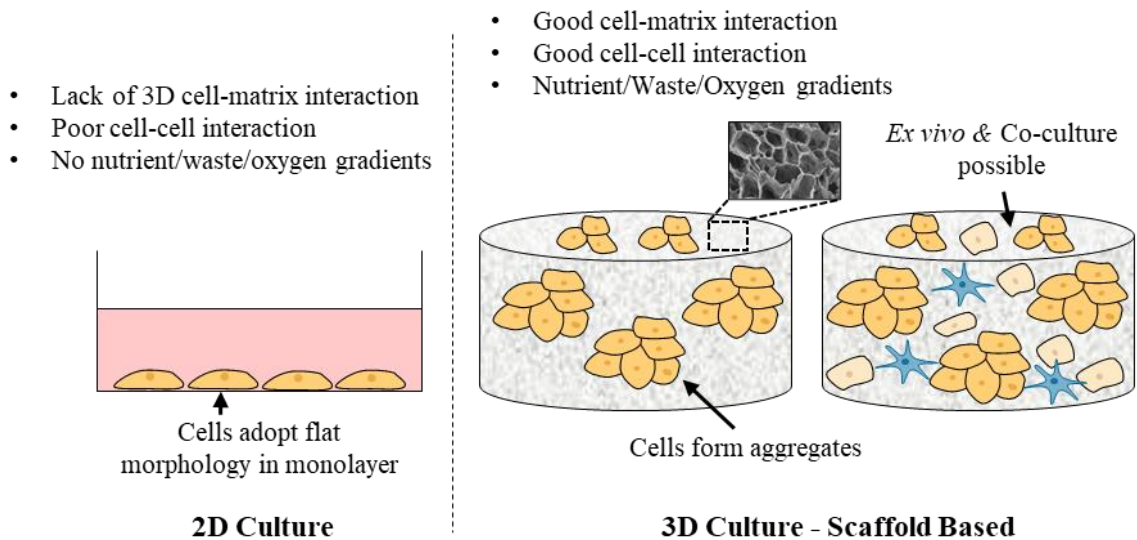
Figure 1.5: 2D Culture comparison with 3D Scaffold Based Culture. This figure highlights some of the advantages of 3D culture over 2D culture. 3D culture provides the cell-matrix interaction and vastly superior cell-cell interactions and provides nutrient/waste gradients that are not present in 2D culture. Co-culture with multiple cell types is also achievable in 3D scaffolds which in a cancer setting is crucial as multiple cell types play a role in tumour progression. *Ex vivo* of patient cells is also achievable. Cells adopt a flat morphology in 2D monolayers which allows there to be an equal distribution of nutrients and oxygen. In scaffolds, cells can form aggregates which resemble tumour masses and these masses generate internal gradients of nutrients and oxygen as is the case *in vivo* [108].

In vivo xenograft animal studies overcome many limitations of existing 2D and 3D models, however they also have associated challenges. The use of human cells in animal models has a range of potential limitations, including; size difference between humans and animals, slight genetic differences, differences in tumour microenvironment, non-orthotopic tumour development, and many xenografts are developed in immunocompromised animals meaning they lack the important interplay between tumours and the immune system [113]. These limitations contribute to the poor translation of results from preclinical animal trials to human trials [112,114]. An example of such is Endostatin, an angiogenesis inhibitor tested for anti-tumour actions. This drug saw largely positive results when tested *in vivo* in a murine animal model [115,116]. However, beyond the lack of drug-related toxicity, the tumour responses to this drug in various human cancer clinical trials were minor to non-existent [117–119]. Furthermore, increasing ethical consideration for animal welfare has led to calls to radically alter research practices, shining a light once more on the decades-old 'Three Rs' – to replace, reduce and refine our usage of animals in scientific research [120].

The various issues that arise when using 2D *in vitro* culture models and subsequently with xenografts have driven the development of a plethora of 3D *in vitro* culture models. Such 3D models provide the spatial context that replicates human (*in vivo)* cancer and the structural/biochemical cues that are more biologically relevant than the 2D culture equivalent [121,122]. Incorporating the third dimension into *in vitro* settings for cancer-based research offers many potential advantages, e.g., the provision of stroma/matrix and thus cell-matrix interactions; improved resemblance of cells to *in vivo* counterparts in terms of shape, cell-cell interactions, behaviours and genetic profiles; development of heterogenous cell populations; co-culture of multiple cell types; variable access for cells to nutrients/oxygen as is the case in *in vivo* tumours; and a more clinically representative

response to therapeutic agents as per solid tumours [99,121,122]. The inclusion of immune function to 3D models also offers significant potential due to the crucial role the immune system plays in cancer, both in terms of disease initiation and progression but also regards to therapeutic strategies [123,124]. There are limited examples of co-culture of breast cancer cells and immune cells to date [125–127], emphasising this type of co-culture is still in a nascent stage and that more research is needed to develop such complex models. Many platforms for 3D *in vitro* culture models have been developed, primarily consisting of; spheroids [128,129], organoids [130], decellularized tissue structures [131,132], 3D scaffolds [9,12] and hydrogels [10,133]

1.4.1 Spheroids

Spheroids are a form of scaffold/matrix-free 3D culture system consisting of cellular aggregates. Spheroids are an attractive platform due to low-cost of fabrication and the self-assembly of the 3D structures leads to a simple and convenient setup. Spheroids can also be an attractive cost-effective option as the lack of matrix/scaffold materials (which may be expensive such as collagen) in scaffold-free setups reduces user costs. Among the main advantages of spheroids are: (1) provision of cell-cell interactions within a 3D morphology *in vitro*, (2) they allow secretion of ECM components resulting in provision of cell-matrix interactions, (3) they can be used for co-cultures and (4) they enable the development of necrotic cores surrounded by actively proliferating periphery which drives gradient distribution of oxygen, waste and nutrients, such a feature is common of *in vivo* tumours [134,135]. Spheroids can be produced through a variety of techniques, which include the: (1) use of suspension plates/non-adherent surfaces, (2) hanging drop method, (3) use of microfluidics and (4) use of rotation [136,137]. Some limitations of spheroids include: (1)

simplified matrix recreation, (2) sensitivity to mechanical forces and (3) lack of control of spheroid size [134,135]. Some spheroid culture may make use of a matrix support (e.g., Matrigel[TM]) to assist in formation but also to improve the performance of the spheroid system through provision of improved cell to matrix interactions [138]. Applications of spheroids include general cell property investigations, drug screening/development and analysis of invasion/angiogenesis. Breast cancer spheroids developed to date have investigated the optimisation of spheroid formation, and their application for co-cultures and also drug screening [139–142].

1.4.2 Organoids

Similar to spheroids, organoids are 3D aggregates of cells, though specifically they are composed of organ-specific stem cells or progenitor cells and are of increased complexity. They self-assemble into 3D aggregates upon introduction to a scaffold support [143–145], though scaffold free organoids are also possible [146,147]. Upon stem cell differentiation and proliferation, they generate *in vivo*-like structures with good resemblance to the parent organ tissue *in vitro* [143–145]. They have been used in cancer research for disease modelling and drug screening and development. Advantages of organoid cultures include; development of complex organ-like structures that closely resemble *in vivo* tissue both histologically and genetically, development of human-derived organoids allowing for personalised strategies, provision of good cell-cell and cell-matrix interactions, and relative ease and robustness of organoid development and maintenance. Some limitations include reproducibility concerns and high levels of heterogeneity, lack of validated models and established protocols, increased costs compared to other 3D models or 2D culture, and still may lack full replication of the complex tumour microenvironment thus tumour-stroma

interactions remain limited [148–150]. Many breast cancer organoids have been developed to date and been used to investigate breast cancer morphology, cell behaviours and drug discovery and testing [148,151–156].

1.4.3   Decellularized tissue structures

Decellularized scaffolds are fabricated through the excision of tissue/ECM from an animal or human and subsequent treatment of the excised material to remove cells and other unwanted components [157,158]. Decellularization treatments may be achieved using physical, chemical or biological processes [158–161], which leaves behind the bare 3D tissue or ECM framework that serves as a scaffold for culture. As the decellularized scaffold originates directly from native tissue/ECM, they provide excellent in vitro models that are superior in composition to more simplistic ECM scaffold mimics that are fabricated in the lab that typically are composed of a limited number of materials [157,158,162]. The decellularized structures are seeded with cells and the complex ECM makeup of the scaffold allows for complex cellular processes such as growth, proliferation and gene expression to proceed in a manner similar to in vivo processes [51,158]. Advantages of decellularized scaffolds include: (1) preservation of native tissue thus an excellent scaffold for cell culture, (2) complex composition in comparison to many in vitro fabricated scaffolds, (3) wide variety of decellularization techniques with many cost friendly options and (4) retention of high bioactivity of the native tissue [157,158]. Disadvantages of the use of decellularized scaffolds include: (1) difficult to scale up production compared to lab-developed scaffolds, (2) potential risk of immunogenicity, (3) small remnants of DNA remaining in decellularised scaffold and (4) large variation in ECM source owing to the high heterogeneity of cancers [157,158]. Decellularized structures have been used in breast cancer research for the

investigation of cell behaviours/morphology, response to therapeutics and gene/protein expression patterns [132,163–165].

1.4.4 3D scaffolds and hydrogels

Scaffolds and hydrogels both provide 3D matrices to assist cell attachment and growth. Many different materials have been used to develop scaffolds and hydrogels for 3D *in vitro* culture models, generally categorised into naturally derived and synthetic polymers. Naturally derived biomaterials include collagen [8,12,166], fibroin [167,168], alginate [169–171] and hyaluronic acid [133,172,173]. Additionally, gelatin, which is denatured collagen, is an attractive natural biomaterial as it maintains the parent molecules properties but has increased solubility and reduced costs thus is a popular scaffold/hydrogel material [174–176]. Synthetic polymers used to develop these structures include polyethylene glycol [177,178], poly(lactide-co-glycolide) [179,180] or poly(ε-caprolactone) [181,182]. While the successful culture of cancer cells/tumours has occurred with synthetic models [177–179,181,183], efforts have increased in the fabrication of biocompatible systems that more closely replicate the native tumour microenvironment. Replication of the tumour microenvironment is essential to bridge the gap between *in vitro* models and the *in vivo* environment, thus, many researchers believe the scaffolds/hydrogels should contain biological components. For hydrogels, while variation in fabrication parameters exist, such as component concentration, gelation temperature or pH, the general technique is consistent. The hydrogel material is solubilised and gelated into 3D gels of high-water content [184,185]. For scaffolds, different fabrication techniques can be used, which freeze-drying, electrospinning and 3D printing [186–188]. These techniques result in 3D structures that may resemble open-cell foams or consist of dense fibrous networks. The use of scaffolds

and hydrogels are similar providing a 3D structure for cells to attach to. Scaffolds and hydrogels are widely used in multiple fields including tissue engineering, regenerative medicine and cancer research [134,189–191]. Unlike spheroids, scaffolds or hydrogels can provide a more complex ECM-like environment for cell growth. Other advantages of scaffolds and hydrogels include: (1) suitability for long-term culture, (2) good reproducibility and (3) ease of modification/fabrication [135,192,193]. Some disadvantages include: (1) mechanical weakness of natural matrices without modification, (2) biocompatibility issues of synthetic structures such as lack of attachment sites for cells to adhere to, (3) materials for scaffold/hydrogel fabrication can be expensive and (4) retrieval of viable cells from structures for analysis can be difficult due to cells remaining trapped with the 3D structures [135,192,193]. Scaffolds/hydrogels are frequently used in 3D breast cancer research with applications including general cell growth and proliferation assessments, transcriptional and translational research, disease progression and metastasis investigations and drug testing [8,186,194–197].

As this thesis involves the use of adherence-based collagen scaffolds, the remainder of this chapter will focus on matrix/adherent based systems including 3D scaffolds and hydrogels. The use of collagen in the fabrication of 3D culture models will be the primary focus due to collagen being the primary scaffold component used within this thesis.

1.5 Collagen-based breast cancer models

Biologically, collagen-based *in vitro* scaffolds are excellent examples of biocompatible platforms suitable for use in cell culture. In recognition of this fact, there has been a growing interest in the use of collagen-based scaffolds to study a range of cancer types, including

breast cancer [8,10,186,188,197,198]. Initial research using collagen-based 3D *in vitro* culture models carried out by Yang *et al.* (1979), focused on the use of simplistic collagen hydrogels composed of rat tail collagen fibres solubilised in acetic acid [199]. This study demonstrated that dissociated primary mouse breast cancer cells could be successfully maintained over an 8-week period on a 3D *in vitro* collagen hydrogel. The culture model was further validated by transplanting outgrowths from the 3D gels into a murine model where the development of mammary adenocarcinomas, displaying histological similarity to the original tumour from which the primary cells were dissociated from, was observed [199]. Similar success in the growth of mammary tumour cells on collagen hydrogels was reported during a similar time frame (1980-1995) [200–202]. While the success of these early collagen-based 3D *in vitro* models represented an important step forward in breast cancer research, these collagen hydrogels have limited ability to adequately replicate the breast cancer ECM. Recent advances in biofabrication techniques have allowed greater control over scaffold microarchitecture providing new opportunities for the development of biomimetic 3D breast cancer scaffolds.

Several techniques (summarised in Table 1.2) are available for fabrication of 3D collagen structures. The most widely used include freeze-drying (lyophilisation), hydrogel synthesis, electrospinning and 3D printing – all of which produce 3D adherence-based scaffolds or hydrogels. The collagen-based scaffolds fabricated in this research thesis were produced using a freeze-drying procedure.

1.5.1 Hydrogels

Hydrogels are a versatile biomaterial system with a large range of applications spanning drug delivery, wound repair, tissue engineering and, to a lesser extent, cancer culture. Hydrogels are 3D water-swollen gels consisting of hydrophilic polymers that interact with one another through random interactions (i.e., hydrogen bonding) or enforced crosslinks [184,185]. The physical characteristics of gelated hydrogels typically differ from that of scaffolds fabricated using other techniques such as freeze-drying, appearing as a 3D mesh-like network of collagen fibres demonstrating no consistent pore shape or porosity (Fig. 1.6A).

Collagen is the most predominant natural material used for hydrogel synthesis due to its excellent biocompatibility and its abundance within the ECM. Differences in the hydrogel preparation techniques and parameters result in the fabrication of hydrogels exhibiting different properties, which vary in degree of polymerisation, mechanical properties, architecture and biodegradability [184,185,189,203]. The architecture of collagen-based hydrogels can be controlled through manipulation of the ionic strength, pH and temperature during gel polymerisation [204,205], although it is more difficult to control these parameters during hydrogel synthesis in comparison to other scaffold fabrication techniques. Increasing collagen concentration (i.e., the gels ionic strength) results in increased fibre density, reduced pore size but has no effect on fibre diameter [205]. Increasing temperature and the pH value accelerates polymerisation (i.e., the chemical joining of monomers to form chain-like polymers) due to promoting fibre nucleation and electrostatic interactions and results in reduced fibre diameter and smaller pore sizes. Increasing the pH value also increases the mechanical properties of the hydrogel [204,205]. Besides control of the architecture, the mechanical properties of collagen-based hydrogels are also of key interest.

Lee *et al.* (2019) demonstrated collagen hydrogel compressive moduli values of 1.5–8 kPa [206], demonstrating a wide range of mechanical properties achievable through hydrogel fabrication (through variation of the gels ionic strength in this case). Crosslinking techniques have been used to further increase the mechanical properties of the scaffold. Collagen hydrogel crosslinking can be achieved by using crosslinking reagents/methods including common chemical methods such as 1-ethyl-3-3-dimethyl aminopropyl carbodiimide (EDAC) and glutaraldehyde (GTA) crosslinking [207–209]. Chemical methods can offer a significant increase in scaffold mechanical properties, though such methods may cause cytotoxicity. EDAC is generally well tolerated [210–212] as it is not incorporated into the final scaffold structure thus thorough construct washing prior to use can eliminate cytotoxicity concerns. Nonetheless, at high EDAC concentrations, cytotoxicity and poor cell proliferation has been observed [211,213]. GTA is incorporated into the final scaffold as a result of its crosslinking mechanism and poses a greater cytotoxicity concern as there is the potential for the GTA to leach out of the scaffold and contaminate the culture media [174,210,214]–though again this may be heavily influenced by GTA concentration and can be avoided.

Matrigel^{TM} is a commercially available hydrogel that comprises different ECM components including collagen type IV [215]. It has been widely used in cancer research as a versatile platform for the 3D *in vitro* culture of cells [216–218]. While easy to use, batch-to-batch variation can negatively impact research due to differences in hydrogel components and concentrations. As a result, many researchers may prefer to fabricate their hydrogel systems using defined concentrations. Use of collagen-based hydrogels for breast cancer cell growth is common, including growth of MDA-MB-231 (basal-like, triple negative) breast cancer cells on type 1 collagen gels [10,188,197] and culture of MCF7 (luminal A type) breast

cancer cells also on a type 1 collagen gel [219]. Good cell proliferation and viability have been reported for the above examples, demonstrating the use of hydrogels as a viable platform for applications in cancer research.

1.5.2   Freeze-drying

Freeze-drying, or lyophilisation, is a dehydration technique, whereby a solution is frozen before undergoing a drying process under vacuum leading to sublimation of formed ice crystals, resulting in the formation of a dry, interconnected, well-defined porous microstructure that can be tailored for specific applications (Fig. 1.6B). This contrasts with electrospun or hydrogel-based scaffolds that have a less defined pore shape. One advantage of fabricating collagen-based scaffolds using the freeze-drying technique is the relative ease that the architecture and mechanical properties can be controlled to more closely replicate the native *in vivo* tumour environment. Controlling the temperature profile of the freeze-drying process can affect the pore structure and size within the scaffold. It has been demonstrated that a lower final freezing temperature results in reduced ice crystal size, and therefore a scaffold exhibiting a smaller pore size [220]. The rate of temperature reduction to the final freezing point has also been shown to influence the architecture of the final scaffold [221]. Rapid freezing reportedly results in a scaffold exhibiting a heterogeneous architecture, whereas adopting a slower and controlled freezing rate results in a scaffold demonstrating a homogeneous structure in terms of pore shape and size [221]. The porosity (i.e., the empty space or void fraction of the internal scaffold) of collagen scaffolds is generally observed to be ~99.5%, which is ideal for tumour cell infiltration and culture [172,222,223]. Varying the collagen concentration has also been shown to influence scaffold

pore size and porosity–increasing collagen concentration from 0.5% to 1% (wt/v) increased pore size and reduced scaffold porosity [223].

Mould design also plays a key role in determining the final properties of the resultant freeze-dried scaffold. O'Brien *et al.* (2004) report that the use of large rectangular moulds (16.9×25.3 cm) results in scaffolds demonstrating poor homogeneity in terms of pore size, shape and alignment when compared to smaller rectangular moulds (12.4×12.4 cm) [221]. Further alterations in mould design in terms of material-type and use of secondary mould features, have enabled control of pore alignment, resulting in the development of multidirectional porous collagen-based scaffolds. Isotropic or anisotropic structures have been fabricated by tailoring mould design [8,224]. Isotropic scaffolds have pores of a random arrangement (independent of direction) while anisotropic scaffolds are direction dependant and pores are aligned along one axis. Campbell *et al.* (2017) used a polycarbonate mould with cylindrical wells with pointed copper inserts (PTFE coated). The inserts were thermally insulated from the freeze dryer shelf by a thin 1 mm rubber mat. The features generated a single thermal gradient throughout the collagen slurries resulting in pores aligned in one direction. This ability to tailor the architecture is promising as it could facilitate the fabrication of scaffolds that more closely represent the complexity of component alignment observed in native ECM during breast cancer development, where collagen fibrils frequently linearise [56,90,91].

Freeze-dried collagen-based scaffolds typically have weak mechanical properties (e.g., elastic modulus), i.e., ~0.3-0.5 kPa [172,222,223]. Therefore, like with hydrogels, a critical step in the fabrication of freeze-dried collagen-based scaffolds is the inclusion of a

crosslinking technique. These include not only chemical methods such EDAC or GTA [213,225,226], but also the use of physical methods such as dehydrothermal treatment (DHT) [213,227] and ultra-violet (UV) [225,228]. Physical methods are well tolerated and elicit no cytotoxic effects. However, chemical methods are considered more robust and offer a larger improvement in scaffold mechanical properties compared to physical methods [213]. Apart from crosslinking techniques, varying the collagen concentration [223] and co-polymerisation of collagen with other materials [172] can also influence the scaffold mechanical properties. Scaffolds produced via freeze-drying have been used more frequently in the culture of breast cancer cells compared to the other techniques discussed in this review [8,186,194,195,198,229]. Viable and proliferating cells were observed across all aforementioned scaffolds, with a variety of aspects of breast cancer explored from general proliferation to hypoxia, angiogenesis, invasiveness and response to therapeutic agents. The high porosities, wide range of pore sizes achievable, control over pore alignment and ease of modification of mechanical properties make freeze-dried scaffolds an attractive option for a breast cancer model.

Table 1.2: Summary of scaffold fabrication methods

Fabrication Method	Advantages	Disadvantages
Hydrogel Synthesis [10,173,294–296]	- Ease of fabrication. - Good proliferation and viability achieved. - Matrigel^{TM} is widely studied and frequently used in cancer research thus many guides for use available.	- Reduced porosity compared to other models. Can result in poorer cell and nutrient distribution. - More difficult to control architecture thus less reproducibility of exact desired architectures. - Weak mechanically prior to crosslinking
Freeze Drying [90,172,186,198,213, 223,297]	- Good control over scaffold architecture through variation in process parameters. Can produce large range of pore size and orientation. - High porosity levels. - Inexpensive. - Good proliferation and viability achieved.	- Can be batch to batch variation in final scaffold architecture due to challenges in controlling the freezing process - Weak mechanically prior to crosslinking
Electrospinning [11,262–267]	- Production of fibrous network that closely resemble native collagen fibres. - Large range of fibre size/diameter/pattern achievable - Good proliferation and viability achieved.	- Use of harmful solvents required for the fabrication of collagen scaffolds - Solvents expensive -Weak mechanically prior to crosslinking
3D printing [187,282–284]	- Control over architecture through use of computer design software. - High porosities achievable - Use of bioinks for inclusion of live cells into scaffold - Good proliferation and viability achieved.	-Difficult to print collagen due to viscosity issues and difficultly working at room temperature. - Expensive to scale up. - Often must be combined with a lyophilisation step. - Weak mechanically prior to crosslinking
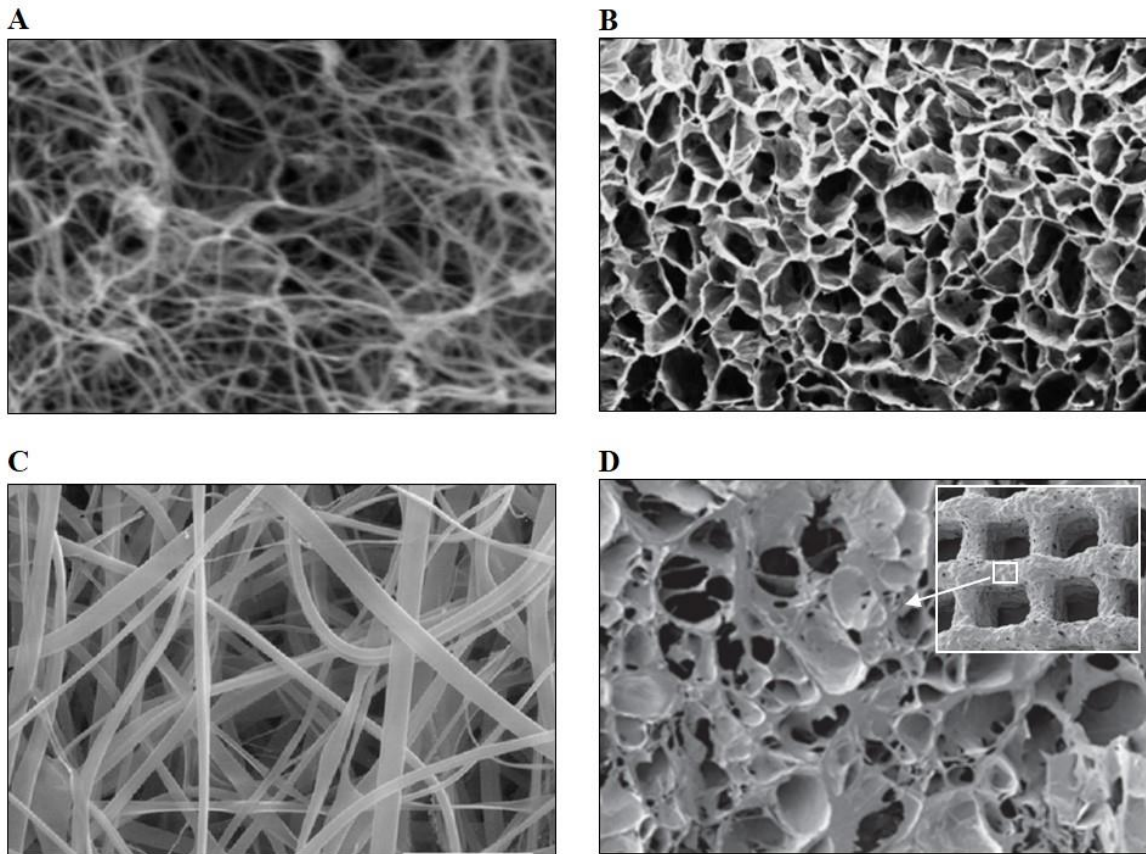
Figure 1.6: Comparison of microarchitecture achieved by the four fabrication methods discussed. (A) Collagen hydrogel (adapted from Achilli *et al.* (2010)) [205] (B) Freeze-dried collagen scaffold (adapted from Offeddu *et al.* (2015)) [230] (C) Collagen electrospun scaffold (adapted from Simpson *et al.* (2011)) [231] (D) 3D printed collagen scaffold (adapted from Lode *et al.* (2016)) [187].

1.5.3 Electrospinning

The electrospinning process makes use of electrical forces (positively or negatively charged) to form fibres from polymer solutions or melts. The resultant electrospun scaffold consists of a network of fibres that offer a large surface area (Fig. 1.6C), which makes them an attractive platform for cancer cell growth and adhesion [232–235]. The electrospinning technique is fast, efficient, relatively inexpensive and versatile, producing fibres ranging from micrometres [236] to sub-100 nanometres [237] in diameter. Significant advancements in electrospinning technology and knowledge have allowed for controlled fibre architecture in terms of fibre diameter and alignment. Increasing polymer concentration/viscosity [238–241] can increase the fibre diameter, which also benefits fibre uniformity and reduces the incidence of fibre defects such as beading (low concentration or surface tension issues causing formation of sphere-like defects along fibres) [239,242,243]. Solution conductivity also promotes the production of uniform fibres, with increased conductivity equating to smoother fibres and lower rates of beading [239,242,244]. Reducing the polymer flow rate can also decrease the fibre diameter [239] and increasing the flow rate beyond an optimal value can affect solvent evaporation resulting in highly beaded wet fibres on the collection plate [239,245,246]. The pore size (space between adjacent fibres) within the structure of the electrospun scaffold can be indirectly altered through varying the fibre diameter. Thicker fibres generally increase the pore size and fibres of reduced diameter exhibit the opposite effect due to the higher density of the fibre network within the electrospun scaffold [247]. The inclusion of water-soluble fibres that are sacrificial can increase pore size–these fibres are dispersed homogenously within the main electrospun material and their controlled 'sacrifice' results in the formation of larger pores and a higher porosity [248,249]. High porosity is essential as dense fibrous networks may prevent cell infiltration into the scaffold [248,250,251], thus when generating collagen scaffolds via electrospinning, fabrication

parameters should be tailored to avoid overly dense tightly packed fibrous networks. Porous fibres have also been developed which further increase surface area due to the presence of pores within the fibres themselves [252,253]. Zhang *et al.* (2006) achieved their porous fibres through leaching of the water soluble constituent of gelatin from poly(ε-caprolactone)/gelatin composite fibres [252]. Kalra and Tran (2013) created porous fibres through high temperature degradation of a sulfonated tetrafluoroethylene based fluoropolymer-copolymer (known commercially as Nafion during carbonization of a polyacrylonitrile/Nafion composite scaffold [253]. During conventional electrospinning techniques, collection plates are typically flat surfaces, and due to the 'whipping' action of the charged polymer, the solution collects in a random non-woven pattern. Rotating drum collecting plates have also been used to generate aligned fibres [254–256]. Other parameters used during the electrospinning process such as surface tension, field voltage, needle tip design and collection plate design can also alter the architecture of the resultant scaffold [257]. Electrospinning techniques have been developed to produce more complex electrospun networks, such as multilayer scaffolds or scaffolds with loaded/conjugated compounds (e.g., chemotherapeutic conjugation or genetic cargo) [258–261].

Collagen-based scaffolds fabricated using electrospinning have been well documented [11,262–268]. Typical solvents used during electrospinning of collagen-based scaffolds include 1,1,1,3,3,3-hexafluoroisopropanol (HFIP) [264,267] and trifluoroethanol (TFE) [262,263]–though nanofibrous collagen-based scaffolds have been spun using a more benign water/salt/alcohol solvent system [266]. Fibre diameter in these collagen-based scaffolds ranged from 100-900 nm, with differences achieved through changing the specific electrospinning parameters. Similar to scaffolds fabricated using the freeze-drying technique and hydrogel synthesis, crosslinking agents (e.g., EDAC and GTA) can be used to increase

the mechanical properties of electrospun scaffolds [11,263–267]. Excellent cell proliferation and viability have been observed in many collagen-based scaffolds fabricated using electrospinning [11,264,265,269], highlighting their potential as for use as 3D models *in vitro*. However, their use in breast cancer research remains scarce compared to other tissue engineering applications. In one study, MDA-MB-231 breast cancer cells were cultured on an electrospun scaffold composed of a 1:1 ratio of collagen type 1 and PCL with varied weight/volumes of 5–15%. Fibre diameters ranged from ~400 nm to 2.25 µm, concentration dependent. Breast cancer cells showed sustained viability and successful proliferation on the electrospun scaffolds. However, the dense fibre network of the structure significantly impacted cell infiltration, resulting in few cells infiltrating to the centre of the scaffold [250].

To date, the use of electrospun collagen for breast cancer is rare, collagen has been more frequently used as a coating to non-collagenous electrospun fibres, in attempts to improve the biological relevance of the fibres while bypassing the difficulties of using collagen in electrospinning [175,270]. MCF7 and MDA-MB-231 breast cancer cells were successfully cultured on collagen coated polycaprolactone fibres, fabricated through collection on a rotating drum collector using two different speeds to alter fibre diameter and alignment. Both cell lines adopted a more *in vivo* like morphology within the fibre scaffold with an increase in expression of cancer stem cell markers and in addition markers of epithelial-mesenchymal transition markers [270]. Gelatin (type B) fibres similarly were coated with collagen (type 1) to improve biomimicry, resulting in uniform fibres of 440 ± 86 nm in diameter. MCF7 cells displayed successful attachment and proliferation on the fibre network [175]. Electrospun scaffolds composed of synthetic biomaterials have been used at a greater frequency for breast cancer culture [271–274]. Nevertheless, electrospun collagen remains an attractive option due to the high level of user control over fibre architecture, rapid production process and the

fibrous collagen network achieved has greater resemblance to the fibrous collagenous network of the ECM than the open-cell foam like structures produced by freeze-drying.

1.5.4   3D printing

Since its development in the 1980s, significant advancements in 3D printing technology have resulted in its application in the fields of tissue engineering, regenerative medicine and cancer research [275–277]. 3D printing of biological-based materials has now become a reality and allows for the creation of complex biocompatible 3D structures. Many different techniques are available for the 3D printing of scaffolds, including; droplet-based, extrusion-based, inkjet, micro-valve, laser-induced and stereolithography bioprinting [277,278]. Careful control of the design and architecture of the scaffold using available tissue imaging techniques and computer-aided design (CAD) software facilitates the precise and detailed generation of both simple and complex 3D structures. Furthermore, user control over the spatial positioning can facilitate control of the physical, mechanical and signal transduction properties of the resultant 3D printed scaffolds [50,279]. This high level of control may offer a significant advancement in accurately modelling the breast cancer ECM/tumour microenvironment *in vitro*.

Collagen has proven to be a versatile material for bioprinting and has been used in many different 3D printing techniques [187,280–283]. Such collagen-based scaffolds have the classic printed layered lattice appearance, structure and alignment. The struts/fibres of the 3D printed scaffolds normally contain a distribution of micropores on their surface, which facilitates cellular attachment and infiltration, while macropores are located between the

layered fibres (Fig. 1.6D). 3D printing using collagen poses challenges due to the low viscosity of collagen solutions and their inability to solubilise. Therefore, higher viscosity collagen-based solutions have been developed to overcome these issues. Nocera *et al.* (2018) used a highly viscous collagen solution (60 mg/mL collagen in phosphate buffered saline (PBS)) to fabricate fibrillar collagen scaffolds with an interconnected porous structure using 3D printing [284]. The 3D printed scaffold exhibited a porous (≥90% porosity) structure with pores ranging in size from 50-500 µm, and cell viability ≥70% using both the fibroblastic NIH3T3 and epithelial Vero cell lines [284].

Collagen scaffolds exhibiting highly porous (≥95%) structures with pore sizes ranging from ~10-300 µm have been fabricated using a combination of 3D printing and freeze-drying. The addition of freeze-drying to the printing process offered scaffold stabilisation and allowed for the development of more complex structures [187,283]. A literature search revealed a low number of collagen-based printed scaffolds with applications in breast cancer research, with preference for non-collagenous inks. Nerger *et al.* (2019) successfully printed collagen (acid-solubilized bovine type I collagen) – Matrigel^{TM} composite inks into 3D scaffolds using a microextrusion 3D printing technique. The fabricated scaffolds demonstrated spatially controlled aligned collagen fibres. MDA-MB-231 breast cancer cells were successfully cultured by seeding them on top of the scaffolds [285]. Another advantage of bioprinting is the potential to incorporate cells within collagen solutions to create "bioinks" that allow cells to be seeded within the scaffold during the printing process [278]. This presents a distinct advantage as cells can be dispersed throughout a 3D scaffold during fabrication negating potential risks of poor and slow cell infiltration when manually seeded onto the scaffold surface. MDA-MB-231 breast cancer cells were successfully cultured by incorporating them within a bioink prior to printing [285]. Both MCF7 and MDA-MB-231

breast cancer cells were printed within a collagen type 1/DMEM media ink. Constructs were printed in a variety of shapes from simple spheroid structures to crosses, cubes and dumbbells. Cells were of high viability and evenly distributed throughout the printed shapes [286]. MCF7 and MDA-MB-468 (basal-like, triple negative) were printed within 3D collagen gels (rat tail collagen), resulting in the formation of tumouroids with high ki67 positivity through a 3-week duration. In addition, either of the cell lines were co-cultured with the MCF12A cell line (non-tumourigenic breast cells) resulting in successful printing of mammary organoids [287]. Elsewhere, collagen-based bioinks containing cells such as fibroblasts [288,289], MSC cells [290], osteoblasts [280,291] and hepatocytes [289] have been well documented and have demonstrated good/excellent cell viability and proliferation – highlighting the overall promise of bioinks, and the application across multiple cell types opens up potential for multicellular printed constructs which more accurately represents the tumour microenvironment. As with other collagen-based *in vitro* scaffolds, different crosslinking options are available to increase the mechanical properties of 3D printed collagen-based scaffolds including EDAC [187,283], genipin [280] and tannic acid [292,293]. Notwithstanding the fact that 3D printing has been minimally used in the development of collagen-based 3D models for breast cancer [285], it nonetheless holds significant potential to produce models that more accurately model the breast cancer tumour microenvironment.

1.6   Current applications: collagen-based models in breast cancer research

Collagen-based platforms have been utilised in a range of *in vitro* breast cancer models aimed at advancing the current understanding of breast cancer development and progression. A selection of these studies are discussed. Initial validation and confirmation of platform biocompatibility is common throughout these studies, but recently studies have focused on complex investigations into various breast cancer phenomena. Some areas of study include alterations in cell morphology and growth kinetics, assessment of therapeutic response, genetic and metabolic analysis, metastasis and the interplay between matrix stiffness and a variety of cell properties.

Several studies have focused on the validation of collagen-based 3D *in vitro* culture scaffolds with general confirmation of breast cancer cell growth and assessment of cell behaviour within the 3D platforms. The MCF7 breast cancer cell line was successfully grown in a 3D collagen scaffold fabricated using a freeze-drying technique [194]. Cells in this 3D *in vitro* scaffold displayed similar proliferation rates to 2D cultures during the initial days, though culture life was longer in the 3D models as 2D cultures reached confluency more quickly and began undergoing apoptosis. Cells in 3D also displayed a more rounded morphology than those in monolayer. Furthermore, the MCF7 cells demonstrated increased malignancy and an invasive phenotype compared to when grown in 2D [194]. There was also an increased expression of proangiogenic growth factors and MMPs within the 3D scaffolds [194]–expression signatures such as these are common in clinical malignant cases [86,88]. The increased malignant-like behaviour of the cells grown in 3D was confirmed through xenograft development–tumours derived from 3D cultured cells were significantly larger and displayed increased tumorigenicity compared to 2D culture-derived xenografts. A

further interesting observation was the display of stem cell-like properties and markers within the MCF7 population in 3D cultures compared to their 2D counterparts [194]. Electrospun collagen scaffolds have rarely been used for breast cancer research, despite frequent use elsewhere in tissue engineering. MDA-MB-231 breast cancer cells were culture on electrospun collagen-based scaffolds, with viable breast cancer cell growth and proliferation demonstrated–though poor cellular infiltration was observed as a limiting factor of their application [250]. To overcome this, techniques to improve infiltration and increase pore size of the scaffold would be required, such as altering solution concentration [240] or use of sacrificial fibres [248]. While this study demonstrated the potential of electrospun scaffolds to support breast cancer cell growth, to date electrospun scaffold-based 3D scaffolds have not been used in to explore breast cancer cell behaviour or in drug screening studies.

1.6.1 Breast cancer and bone metastases

Bone is the most common site of metastasis in breast cancer for all subtypes–though progression to bone metastasis from initial breast cancer diagnosis is faster in the more aggressive HER2+ and TNBC subtypes [298,299]. Once breast cancer has spread to the bone, it is considered incurable [300]–thus greater attention is urgently needed to develop new approaches to increase survival and eventually to discover potential cures. 3D *in vitro* scaffolds provide a useful tool for the investigation of metastasis. James-Bhasin *et al.* (2018) developed a 3D *in vitro* co-culture consisting of osteolytic breast cancer MDA-MB-231 cells and pre-osteoblast MC3T3-E1 cells within a dense collagen hydrogel (rat tail collagen type 1 solubilised in acetic acid) to investigate the interaction between triple negative breast cancer cells and osteoblasts, [188]. They reported that the co-culture of the MDA-MB-231 and

MC3T3-E1 cells resulted in an impairment of the differentiation of MC3T3-E1 cells to osteoblasts and subsequently a reduction of osteoblast-mediated mineralisation [188]. A similar effect was observed on exposure of MC3T3-E1 cells to MDA-MB-231 conditioned media. The suppression of osteoblast activity by breast cancer cells in this study is of interest as it may be a potential target for the therapeutic reduction of bone density loss in metastatic breast cancer. Murine mammary adenocarcinoma 4T1 cells have also been successfully grown on a 3D collagen-glycosaminoglycan freeze-dried scaffold in an investigation to assess the adaptability of breast cancer cells to the bone microenvironment, which may explain why bone is a preferential site of metastasis for breast cancers [195]. The cells were capable of osteomimicry and showed enhanced mineralisation properties, further highlighting the potential of 3D *in vitro* collagen-based scaffolds in the study of breast cancer cells and their high rate of bone metastases [195]. A further study focusing on the interplay between breast cancer cells and bone cells used a 3D collagen scaffold to increase understanding in breast cancer cell dormancy and eventual metastasis [196]. A range of breast cancer cell lines (8 cell lines total – SUM159, SUM149, MDA-MB-231, MDA-MB-435, BT474, MCF7, T47D and ZR75-1 cells) and bone marrow cells were successfully grown in co-culture on the scaffolds. Significant findings from this study were the development of supportive and inhibitory niches to breast cancer cell proliferation by varying the co-cultures on the scaffolds. Primary bone marrow stromal cells supported breast cancer cell proliferation while bone marrow cell lines (including osteoblast, mesenchymal, and endothelial cell lines) suppressed proliferation of breast cancer cells and induced dormancy. The ability to model dormancy *in vitro* may lead to eventual biomarker discovery concerning dormant disseminated cells that may cause metastasis upon proliferation at distant sites [196]–discovering these biomarkers and assessing patients for them may offer a new frontier in predicting metastasis risk.

1.6.2 Collagen alignment and cell invasion

A signature of breast cancer development and increased invasiveness is the linearisation of collagen fibres, creating 'highways' for cells to migrate along away from the primary tumour [57,90]. This linearisation is seen increasingly in aggressive cancer subtypes including HER2+ and TNBC tumours [58] thus is an important point of investigation. In an attempt to investigate the development of a new migration/invasive potential assay, Campbell *et al.* (2017) [8] developed 3D collagen-based scaffolds demonstrating both direction aligned (anisotropic) and non-directional random (isotropic) pore architectures [8]. In this study a freeze-dried collagen scaffold (bovine Achilles tendon derived collagen type 1 solubilised in acetic acid) was fabricated with axially aligned pores as it was hypothesised that such scaffolds could better mimic the *in vivo* linearised collagen fibres. Pores within this scaffold were ~100 μm in size. Data from this study showed that the anisotropic scaffold significantly increased the migration and invasion capacity of invasive breast cell line MDA-MB-231 when compared to the isotropic scaffold equivalent. High numbers of MDA-MB-231 cells migrated through the full depth of the collagen-based scaffold, whereas non-invasive MCF7 cells travelled a significantly lower migration distance through the scaffold [8]. The anisotropic scaffold developed by Campbell *et al*. (2017) [8] was further applied for migratory analysis in a study investigating xenograft tumour invasiveness and response to chemotherapeutics. The study increased replication of the breast ECM through culture of adipocytes within the collagen scaffolds prior to seeding of tumour fragments [229].

Adipocytes are a prevalent cell group within mammary tissues and are reported to play a role in breast cancer invasion [301,302]. Following 10 days of tumour fragment culture, adipocytes were found to increase migration of tumour cells within the scaffolds. Treatment

of cultures with chemotherapeutic canertinib (tyrosine kinase inhibitor) resulted in significant reduction of tumour cell migration into the scaffold, both in terms of distance and number [229]. Such results further emphasise the potential of collagen *in vitro* models for drug development and discovery within cancer research. Furthermore, the successful culture of xenograft tumour fragments showed the potential in application of these models for *ex vivo* culture of patient tumour fragments. This could facilitate advancements of personalised treatment strategies through investigation of tumour properties and response to therapies on a patient-by-patient basis. A further 3D collagen model highlighted the key role aligned collagen fibres play in cancer cell migration. Aligned collagen hydrogels resulted in an increased net migration distance through the constructs by MDA-MB-231 cells when compared to randomly organised collagen gels. The study also reported that collagen fibre alignment was the dominant factor affecting the migration distance, leading to a greater increase in migration distance than hydrogel elastic modulus [197].

1.6.3 Scaffold mechanical properties and breast cancer interplay

Stiffness of the ECM is a key prognostic feature of breast cancers and collagen plays a key role in this matrix stiffening [48,54,55,79]. While it is generally accepted that stiffness plays a role in progression and spread of breast cancer, the exact mechanisms of the influence of stiffness remain poorly understood. Barcus *et al.* (2014) sought to understand the role of matrix stiffness on prolactin signalling in breast cancer cells [219]. Prolactin levels are associated with breast cancer progression [303–305] and as a result prolactin has attracted much interest in breast cancer research, though its exact actions and role in the disease are not fully understood. In this study, two collagen gels (rat tail type 1 collagen) of different stiffness profiles, one a low stiffness 1.2 mg/mL gel and the other a high stiffness 2.8 mg/mL

gel, were fabricated. Both T47D and MCF7 breast cancer cell lines were cultured. The stiffer collagen gels led to prolactin induced stimulation of ERK1/2 signalling pathways in both cell lines (potential protumourigenic role), increased expression of *MMP2* in both cell lines (key factor in ECM degradation and spread of breast cancer [86–89]), linearisation of collagen fibres within the gels cultured with T47D cells (assists metastasis and is a signature of poor breast cancer prognosis [56,90]) and a general increase in invasive and disorganised behaviour by T47D cells. Similar effects of prolactin were not observed in the lower stiffness collagen gel, demonstrating the key role of stiffness in directing cell signalling/activity and its association with favourable conditions for cancer spread and progression [219]. Liverani *et al.* (2017) further investigated the mechanobiology of breast cancers through culture of two breast cancer cell lines, MCF7 (non-invasive) and MDA-MB-231 (invasive), on collagen scaffolds. Scaffolds consisted of a 1% (wt/v) bovine collagen (type I) suspension, prepared with an acetate buffer. The scaffolds were crosslinked with an 1,4-butanediol diglycidyl ether solution before undergoing a freeze-drying procedure, producing an interconnected porous structure (porosity of 87.8% and pores within a range of 150-300 µm). Upon culture, both cell lines formed tissue-like 3D features and maintained expected morphology. The more aggressive MDA-MB-231 cells caused a significant increase in scaffold elastic modulus with increased *LOX* expression–such properties resemble *in vivo* tumours generated from MDA-MB-231 cells. Upon treatment of MDA-MB-231 cells with LOX inhibitor β-aminopropionitrile, the cells ability to increase scaffolds elastic modulus was impaired [198]. Due to the correlation between increased ECM stiffness and poor patient prognosis [4,78], *in vitro* models such as the above can serve as a useful investigational tool for cell-ECM interactions and their influence on patient tumour behaviour.

1.6.4 Hypoxic environment generation and investigation

Hypoxia is a key factor in breast cancer progression and metastasis risk [306,307], thus it is important to investigate the development of hypoxia in a relevant 3D microenvironment *in vitro* and its influence on key genetic and cellular behaviours. A collagen hydrogel (type 1 extracted from rat tail) demonstrated generation of hypoxic conditions *in vitro* that showed similarity to *in vivo* breast tumours. MDA-MB-231 cells were cultured on 3 mm thick collagen gels and generated spheroid like clusters within the gels with oxygen/nutrient gradients present and the development of necrotic regions was observed. Compared to 2D culture, there was a significant upregulation in hypoxia-inducible factor, *HIF1A* (hypoxia marker) and vascular endothelial growth factor A (*VEGFA*, angiogenesis marker) [10]. Liverani *et al.* (2019) also demonstrated the development of a hypoxia model with high mimicry to *in vivo* tumours using a freeze dried collagen scaffold (type 1 collagen solubilised in acetic acid, crosslinked with 1,4-butanediol diglycidyl eter, average porosity of 84.8%) [186].

Through modelling the low oxygen environment typical of primary tumours, they were able to successfully investigate a range of hypoxia-driven cell behaviours including proliferation, aggressiveness, senescence and metabolic activity. Culture of MCF7 and MDA-MB-231 breast cancer cells within the scaffolds resulted in generation of a tissue-like environment and ECM secretions by the cancer cells resulting in a scaffold microenvironment that closely corresponded with an *in vivo* mouse comparator. Both cell lines showed development of a hypoxic niche with high *HIF1A* expression, upregulation of glyceraldehyde 3-phosphate dehydrogenase (*GAPDH*) and successful pimonidazole staining (stains for poorly oxygenated cells). Furthermore, *LOX* expression and VEGF secretion was significantly

higher in the 3D scaffolds when compared to monolayer 2D culture [186]. Models such as the above hydrogel [10] and scaffold [186] platforms that can accurately replicate *in vivo* tumour hypoxic environments provide a powerful *in vitro* tool for investigation into breast cancer progression and for therapeutic targeting of hypoxia associated cell invasiveness.

1.6.5 Scaffold use in drug screening

A key application of 3D scaffolds is in drug screening and discovery. 2D cultures are known for altered or inflated response to therapeutics, with poor translation of drug efficacies seen in 2D cultures when they progress to animal models [9,12,109–111]. The use of collagen scaffolds for drug screening or discovery for breast cancer is at a low level at present, though the area offers huge potential and is a key factor in 3D *in vitro* platforms bridging the gap between 2D culture and animal testing. In one study, patient tumour fragments were cultured on a collagen gels (type 1, rat tail, 0.3 mg/mL) for *ex vivo* culture validation and tamoxifen (Estrogen Receptor (ER)+ treatment) assessment [308]. Patient tumours maintained high levels of cell viability in culture and ER+ tumours showed a measured response to tamoxifen treatment versus untreated counterparts (ER+ tumour fragment with no tamoxifen exposure). Low ER or ER- tumours showed no significant reduction in tumour volumes with tamoxifen treatment compared to untreated counterparts (ER low/- tumour fragment with no tamoxifen exposure). These responses/lack of responses correspond with expected tamoxifen action in human patients, demonstrating the useful application of collagen platforms for drug screening and also as an *ex vivo* platform [308]. MCF7 spheroids embedded and unembedded in collagen gels treated with anticancer compound doxorubicin displayed increased resistance to drug-mediated cytotoxicity in comparison to a 2D monolayer of MCF7 cells [141]. Reduced susceptibly to drug compounds in 3D platforms is a key

advantage of their use compared to 2D monolayer and allows for increased *in vitro* correlation to typical animal model/human response profiles.

1.7 Summary

The emerging use of 3D *in vitro* models over the last two decades for different applications has seen a promising shift away from the heavy reliance on 2D *in vitro* culture models. While collagen is a current mainstay as a culture scaffold in tissue engineering and regenerative medicine research, its potential in the field of oncology research is still in the nascent stage. A range of fabrication techniques (e.g., freeze-drying, hydrogel synthesis, electrospinning and 3D printing) are currently used to produce collagen-based scaffolds. Each technique confers their advantages and disadvantages (Table 1.2) and depending on the end application and the desired architecture/final properties the most suitable method can vary. Collagen-based scaffolds fabricated using the freeze-drying technique or through hydrogel fabrication appear as the most popular methods of production, though if cancer research follows the same trajectory as tissue engineering and regenerative medicine, then 3D printing offers enormous potential and opportunity. Collagen-based scaffolds fabricated using freeze-drying, 3D printing and electrospinning techniques offer many advantages when considering replicating breast cancer tissue, e.g., demonstration of a highly interconnected porous structure, ease of fabrication and ability to tailor the physical, mechanical and biological properties. Similar scaffolds produced by hydrogel synthesis demonstrate structures of lower interconnectivity, porosity and poorer reproducibility, making them a less attractive option.

Successful culture of breast cancer cells has been achieved using different collagen-based scaffolds [8,188,194–196]. High cell viability, stable proliferation over days in culture and formation of spheroids within these 3D *in vitro* culture models highlight the promise of

collagen-based scaffolds in understanding cancer development and progression. Building and expanding on research in the field to date, 3D collagen-based *in vitro* models may also facilitate the use of patient-derived tumour samples for research and drug screening purposes–known as *ex vivo* culture models. By developing such a culture model for the rapid *ex vivo* culture of patient tumour samples, it will revolutionise personalised medicine strategies, thereby devising treatments of best fit on a patient-by-patient basis.

It must be noted that research to date on the use of collagen-based 3D culture models for breast cancer research has limitations. Exhaustive characterisation of scaffold-based 3D breast cancer models discussed has not taken place with respect to their suitability for breast cancer culture. Many of the aforementioned studies have not focused on the fabrication of scaffolds with tailored pore size, porosity, mechanical properties and scaffold composition that increase their biomimicry for the breast cancer microenvironment. Going forward, a greater focus needs to be directed towards the tailoring of scaffold properties to more accurately model the breast cancer microenvironment and assess how this affects their use as a culture model.

1.8 Project aims and objectives

The overall goal of this research is to develop and validate a novel 3D biologically relevant collagen-based scaffold as a culture model for breast cancer research. The model aims to provide a controlled and reproducible 3D collagen environment that mimics the breast cancer ECM, thus overcoming many of the limitations associated with traditional 2D research. The scaffolds fabricated were used in the for the exploration of breast cancer phenomena, including: cell proliferation, morphology and invasive/angiogenic potential. Furthermore, the breast cancer model developed will be employed to explore the efficacy of therapeutic agents.

The specific objectives of this project are:

Objective 1: Fabrication and characterisation of collagen-based scaffolds for application as a breast cancer culture model. (Chapter 2)

Objective 2: Validation of collagen-based scaffolds as suitable breast cancer culture models (Chapter 3).

Objective 3: Profile the gene expression patterns of breast cancer cells cultured in collagen-based scaffolds (Chapter 4).

Objective 4: Assessment and validation of the collagen-based scaffolds for use as *in vitro* drug testing models (Chapter 5).

02

Chapter 2: Fabrication and Characterisation of Collagen-Based Scaffolds

Sections of this Chapter have previously been presented (with some modification) in *Biomaterials Advances* (2022).

Table of Contents

2.1 Introduction

The ideal scaffold-based breast cancer culture model should closely match the chemical, structural and mechanical properties of breast cancer ECM. Thus, extensive characterisation of the scaffold properties is a key aspect of the biofabrication process. Current scaffold-based breast cancer culture models reported in the literature have not undergone extensive characterisation and instead, a 'seed and see' approach was commonplace. The lack of tailoring of the scaffold properties can result in inadequate replication of the breast cancer microenvironment/ECM, which may limit their ability to model key breast cancer characteristics. Detailed characterisation provides information on the ideal scaffolds for cell culture applications in breast cancer research, opening the door for future works that can increase our knowledge on a variety of breast cancer phenomena.

In the design of collagen-based scaffolds several criteria must be considered. These include characteristics such as the chemical, architectural, mechanical, degradative, and biological properties. An ideal collagen-based scaffold for use as an *in vitro* breast cancer model should demonstrate a high porosity with an interconnected structure and a suitable pore size to enable the infiltration of cells throughout the scaffold and the diffusion of nutrients into the scaffold and removal of waste. The pore size must not be too small, as this can impact cellular migration, and equally the pore size should not be too large as this can reduce cellular attachment due to less scaffold surface area being available [297,309]. Considering common breast cancer cell lines, MCF7 cells have a reported size (diameter) of ~16-25 μm [310] and MDA-MB-231 cells with a mean cell diameter of 15.81 μm [311] - thus the lower limit of pore sizes for scaffolds culturing these cells must be larger than these values to allow for cell infiltration and migration throughout the scaffold. An optimal pore size or an upper pore size

limit has not yet been determined for breast cancer cells. Reported pore sizes with successful culture of breast cancer cells have ranged from 50-300 μm [8,186]. Large pores in excess of 500 μm would likely have detrimental effects on the initial adhesion of breast cancer cells due to a significant reduction in scaffold surface area and therefore a significant reduction in ligand binding sites which would impact initial cell attachment and thus all future cell growth dynamics [297,309].

Scaffolds for use in scaffold-based breast cancer models must demonstrate mechanical properties similar to the properties of native breast tissue during cancer development [92]. Scaffolds that do not replicate the mechanical properties of native tissue may poorly reflect the *in vivo* mechanotransduction [78]. Scaffold mechanical properties (not limited to breast cancer) have been observed to be crucial in driving various cellular pathways and behaviours including proliferation, invasion and differentiation [198,312–314] – thus it is of paramount concern to design scaffolds with the required mechanical properties during the fabrication process. Based on the reported data of human cancerous breast tissue the ideal scaffolds should have an elastic modulus of ~0.5-3 kPa [92,315]. There is little need to have excessively high moduli (e.g., greater than ~5 kPa) as values greater than this represents values not frequently seen in breast cancer ECM/tissue. Values at the lower end of the range better represent the tumour environment nearer the core where cells cause regions of low stiffness, while the higher stiffness values better capture the tumour peripheries where there is a dense fibrotic stroma [92,93]. There may be no 'one shoe fits all' in terms of scaffold mechanical properties, but the ease at which collagen scaffolds can be crosslinked, thus altering elastic modulus, allows for the fabrication of culture models with a range of moduli values if required.

Mechanical properties of 3D scaffolds could also be tailored to replicate the ECM of specific subtypes of cancers, such as increased scaffold modulus for culture of aggressive HER2+ and TNBC tumours/cell lines and lower stiffnesses in Luminal tumours/cell lines [58]. Compressive strength (resistance to compression or crushing forces) of 3D scaffolds is of greater interest during cell culture applications for cancer research in comparison to tensile strength (resistance to elongating of pulling apart forces). Culturing cells within 3D scaffolds is known to result in compressive forces between the cells and the surrounding matrix and may potentially result in pore buckling as cells traverse through the scaffold [316,317]. Furthermore, cell/aggregate expansion (representative of tumour expansion *in vivo*) and the resistance provided by the surrounding scaffold generates compressive forces [318,319]. Li *et al.* (2020) recently observed that volumetric compression of 3D organoid cultures induced intracellular crowding which led to increased Wnt/β-Catenin signalling in their intestinal organoid based research [320]. Wnt/β-Catenin signalling plays a crucial role in many cell functions including proliferation, migration and cell fate determination but also has documented roles in cancer [321]. Thus, the Li *et al.* (2020) study emphasises the importance of investigating the interplay between mechanical forces and cell processes, and how 3D models can advance our understanding of the relationship. Freeze-dried collagen-based 3D scaffolds of a 0.5% (weight/volume (wt/v)) composition have well profiled compressive moduli, exhibiting values of ~0.3-0.5 kPa (standard uniaxial compression, hydrated sample) [172,222,223]. Crosslinking can increase the compressive moduli values to a range of ~1-2 kPa, crosslinking method and crosslinker concentration dependent [213]. Collagen-based scaffolds should exhibit long-term stability during culture to ensure the maintenance of scaffold integrity over many weeks of *in vitro* investigations (high scaffold mass retention for a minimum of two weeks). Collagen-based scaffolds contain the necessary binding motifs (e.g., RGD motifs) to allow for cell adhesion [322], demonstrating

biocompatibility and suitability as a primary scaffold material. Within this study, collagen served of the primary component of the scaffolds investigated. Gelatin was incorporated into the collagen-based scaffolds in varying concentrations to enable the mechanical properties and micro-architecture of the scaffold to be altered. Further to this, in order to more closely mimic the composition of the breast ECM, hyaluronic acid (Hya) was also incorporated into an additional composition.

Gelatin is a denatured form of collagen [69] and retains the biocompatibility and low toxicity of native collagen and has been widely used across a range of cell culture and tissue engineering applications [176,323–325]. Upon denaturation of collagen by hydrolysis, the collagen triple helix unwinds resulting in the formation of gelatin [69]. Not only is gelatin highly biocompatible like the parent collagen molecule, it is also significantly cheaper which is an attractive feature of gelatin use in tissue engineering. Hyaluronic acid, or hyaluronan, is a glycosaminoglycan widely used in tissue engineering and wound healing. It is a polysaccharide composed of repeating disaccharide chains of N-acetyl-glucosamine and glucuronic acid. Hyaluronic acid is known for its extremely high hydrophilic nature and water retention [326,327]. Hyaluronic acid is a key component of the ECM and plays a key role in a wide range of cellular and tissue functions including; cell proliferation and migration, tissue homeostasis and repair, inflammation and biomechanical integrity [326,327]. While it is involved in these key processes, it has also been shown to play an important role in the spread and progression of breast cancer. Hyaluronic acid is highly upregulated in breast cancer tissue in comparison to the healthy tissue state, and this overexpression correlates with poor prognosis and patient survival [328,329]. A variety of mechanisms in promoting cancer progression are attributed to glycosaminoglycans, a notable one being hyaluronic acid mediated activation of the PI3K-AKT signalling pathway

which promotes cell survival [327]. Thus, hyaluronic acid is an attractive third material to incorporate into the scaffold makeup.

2.1.1 Chapter aims

The overall aim of this chapter was to develop and characterise collagen-based scaffolds for application as a 3D breast cancer culture model. The initial focus was developing and optimising our selected fabrication technique of freeze drying in order to produce a range of collagen-based scaffolds of suitable properties for application in future biological studies within this thesis. Once fabricated, all scaffolds were characterised against a range of chemical, architectural, mechanical and degradative properties. Six scaffold compositions were under investigation: a collagen-only scaffold, four gelatin containing collagen-gelatin composite scaffolds and a final composition containing collagen, gelatin and hyaluronic acid.

The specific objectives of this chapter were to:

- Fabricate a range of the collagen-based scaffolds for use as breast cancer culture models using a freeze-drying technique
- Characterise the architectural and mechanical properties of fabricated scaffolds
- Assess the *in vitro* stability of the scaffolds and their swelling ability
- Determine the effect of the incorporation of gelatin or hyaluronic acid on the scaffold properties

2.2 Materials and methods

2.2.1 Solutions/reagents

Phosphate Buffered Saline Solution 10X: 80 g sodium chloride (NaCl), 2 g potassium chloride (KCl), 14.4 g sodium phosphate dibasic dihydrate (Na_2HPO_4), 2.4 g potassium phosphate monobasic (KH_2PO_4) into 800 mL distilled water and adjusted to 1 L. Diluted to 1x when needed. All mentions of PBS in the following studies were a 1x/0.01 M concentration. All materials from Sigma-Aldrich Chemical Co, Wicklow, Ireland.

2.2.2 Collagen and collagen-gelatin slurry fabrication

Collagen (Col) and collagen/gelatin (Gel) scaffolds were produced using a freeze-drying process. 0.5 g of fibrillar sheet type 1 bovine tendon collagen (Southern Lights Biomaterials, New Zealand) was added to 100 mL 0.05 M acetic acid (Sigma-Aldrich Chemical Co, Wicklow, Ireland) resulting in a final collagen concentration of 0.5% weight/volume (wt/v). For collagen/gelatin composite scaffolds, varying amounts of porcine gelatin (Sigma-Aldrich Chemical Co, Wicklow, Ireland) were added to create collagen 0.5% (wt/v) & Gelatin 0.05/0.1/0.15/0.25% (wt/v) slurries, listed below.

- Col 0.5% (referred to as 'Col 0.5%)
- Col 0.5% + Gel 0.05% (referred to as w/Gel 0.05%)
- Col 0.5% + Gel 0.1% (referred to as w/Gel 0.1%)
- Col 0.5% + Gel 0.15% (referred to as w/Gel 0.15%)
- Col 0.5% + Gel 0.25% (referred to as w/Gel 0.25%)

All slurries were stored at 4 °C for 48 h to aid in solubilisation of the collagen. The slurries were blended in a cooled reaction vessel set to 4 °C (to avoid denaturation of collagen fibres)

for 90 min at 10,000-15,000 revolutions per minute (RPM) using an overhead blender (IKA ULTRA-TURRAX™ T25 Basic, IKA Werke GmbH & Co. KG, Staufen, Germany). Slurries were degassed under vacuum for ~30 min. Prior to freeze-drying slurries were brought to room temperature (~20 °C) and then poured into custom-designed moulds (Fig. 2.1) composed of a stainless-steel base and polytetrafluoroethylene polymer body. The moulds allowed for the production of homogenous cylindrical specimens (9 x 9 mm, diameter x height). Conditioning to 20 °C ensured that all slurries start at a homogenous temperature and the cooling rate is consistent during freeze drying cycle.
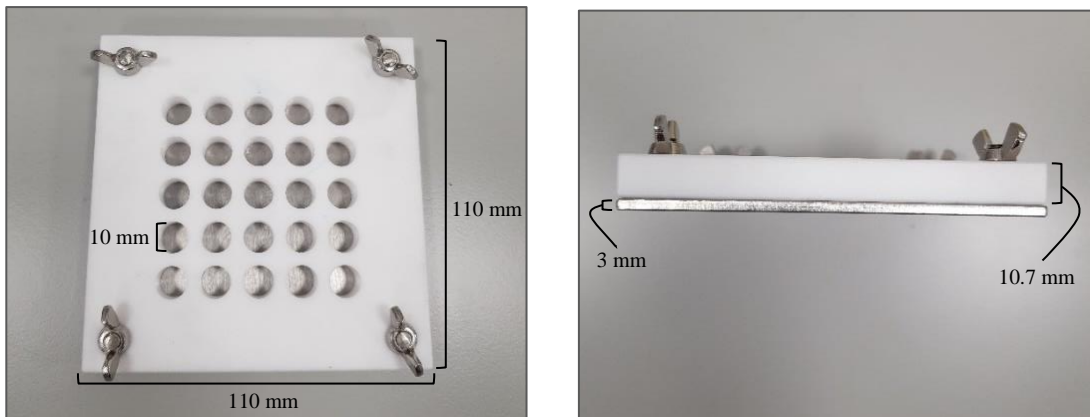
Figure 2.1: Custom Designed moulds for the freeze-drying procedure. Custom designed trays were designed using SolidWorks. The trays had removable bases and cylindrical wells (10 mm diameter and 10.7 mm depth) enabling efficient retrieval of homogenous (size and shape) scaffolds with minimal handling of scaffolds.

2.2.3   Collagen-gelatin-hyaluronic acid slurry fabrication

After completion of initial assessment of the collagen-gelatin scaffolds, an additional scaffold group containing collagen, gelatin and hyaluronic acid was included. The new scaffold was a modification of the w/Gel 0.15% composition (0.5% (wt/v) type 1 bovine

tendon collagen, 0.15% (wt/v) porcine gelatin) with an addition of 0.05% (wt/v) hyaluronic acid sodium salt (Contipro, Czech Republic). This new composition is referred to as the 'Col-Gel-Hya' composition. For this composition, 0.5 g of collagen and 0.15 g of gelatin were added to 90 mL 0.05 M acetic acid and 0.05 g of hyaluronic acid sodium salt was separately added to 10 mL of 0.05 M acetic acid. Both solutions were left at 4 °C for 48 h prior to blending. The hyaluronic acid sodium salt was fully solubilised within this period. The collagen/gelatin slurry was blended for 30 min at 10,000-15,000 revolutions per minute (RPM) using the overhead blender as per §2.2.2. The hyaluronic acid solution was added dropwise to the 90 mL collagen/gelatin slurry after the initial 30 min of blending. The slow addition was necessary to avoid clumping/gelation of the hyaluronic acid which occurs when added in more rapidly. The Col-Gel-Hya slurry was blended for a further 60 min, for a total blend time of 90 min. The slurry was then degassed prior to freeze drying as previously described.

2.2.4   Freeze-drying procedure

Scaffolds were fabricated using a freeze-drying procedure. Filled moulds were placed into a freeze-dryer (VirTis 35XL Ultra Super XL, Biopharma, Winchester, UK) with shelves pre-cooled to 20 °C. Preliminary studies had identified -40 °C as the optimal freezing for desired pore size. The freeze-drying cycle consisted of a series of ramps and holds through initial freezing stages and then the drying phase (Table 2.1). Slurries were cooled from room temperature (~20 °C) to a final freezing temperature of -40 °C at a cooling rate of 0.25 °C/min^{-1}. Scaffolds were then held at -40 °C for 30 min to ensure even and complete freezing. The scaffolds were ramped to 0 °C and then held at this temperature for 20 h under a vacuum of 27 Pa (machine unit of 200 mTorr), during which sublimation occurred. Post sublimation, scaffolds were return to room temperature to complete the cycle. This freeze-

drying cycle produced scaffolds of isotropic (non-directional) architecture. Repeatability of scaffold production was confirmed by using K-type thermocouples (sample of thermocouple probe report in Appendix 1.1) to monitor the temperature profile during the freeze drying cycles, and also by routine checks of fabricated scaffolds properties (e.g., porosity, pore size and mechanical properties).

Table 2.1: Overview of freeze drying process

Temperature (°C)	Time (min)	Ramp/Hold (R/H)	Pressure - mTorr (Pascal (Pa))
20	Shelf start	N/A	Atm
20	10	H	Atm
-40	240	R	Atm
-40	30	H	Atm
0	200	R	200 (27)
0	1200	H	200 (27)
20	60	R	200 (27)
20	20	H	200 (27)

2.2.5   Dehydrothermal treatment (DHT)

Following freeze drying, scaffolds were carefully removed from moulds and placed in tin foil packages to protect the scaffolds from moisture and bacteria. Scaffolds then underwent dehydrothermal (DHT) treatment using a vacuum oven (Memmert VO200, MEMMERT, Schwabach, Germany) at 105 ºC for 24 h under a vacuum of 5,000 Pa. DHT treatment was used to provide initial physical crosslinking of the scaffolds, as well as sterilise them. The foil packages were open during treatment to allow the removal of residual moisture and acetic acid from the scaffolds. Subsequently the foil packages were sealed post-DHT to maintain sterility. Scaffolds were stored in a desiccator at room temperature. For use in experiments, the top and bottom surfaces of each cylinder scaffold was carefully removed using a scalpel blade as these surfaces had a skin-like covering from the freeze drying procedure that consisted of smaller pores compared to the remainder of the scaffold depth. The scaffolds were then bisected to produce structures with dimensions of 9 x 4.5 mm (diameter x height) for use in all experiments in this thesis. Initial mechanical and degradation studies were conducted to assess if the DHT alone was sufficient to provide suitable scaffold mechanical properties and *in vitro* stability. These preliminary studies highlighted the relatively low mechanical properties and rapid *in vitro* degradation of the DHT treated scaffolds. Although the results correlated well with similar collagen scaffolds in literature, EDAC/NHS crosslinking was used in addition to DHT in order to improve scaffold stability and mechanical properties. Throughout this thesis, scaffolds treated only with DHT treatment were referred to as 'non-crosslinked'.

2.2.6 EDAC/NHS crosslinking

Each scaffold composition underwent a secondary chemical crosslinking using 1-Ethyl-3-(3-Dimethlamniopropyl)-carbodiimide (EDAC) (Sigma-Aldrich Chemical Co, Wicklow, Ireland) coupled with catalyst, N-Hydroxysuccinimide (NHS) (Sigma-Aldrich Chemical Co, Wicklow, Ireland) at a molar (M) ratio of 5 M EDAC:2 M NHS. EDAC is a zero-length crosslinking agent that crosslinks collagen/gelatin molecules directly adjacent to one another, specifically forming links between carboxylic and free amine groups, with the EDAC itself not being incorporated into the final structure [213]. The concentration of EDAC used was 6 mM per gram of scaffold, calculated using Equation 1, as this amount has previously achieved significant increases in scaffold elastic moduli which differ minimally to much greater amounts of EDAC [213]. The amount (g) of NHS for a 5:2 molar ratio of EDAC:NHS was the calculated using Equation 2.

Equation 1 – Amount (g) of EDAC required:

$$EDAC\,(g) =$$
$$mass\ of\ collagen\ (g) x\ 0.006\ mol\ EDAC/g\ collagen\ x\ 191.7\ g\ EDAC/mol\ EDAC$$

Equation 2 – Amount (g) of NHS required:

$$NHS\ (g) =$$
$$mass\ of\ collagen\ (g)\ x\ 0.006\ mol\ EDAC/g\ collagen\ x\ 2\ mol\ NHS/5\ mol\ EDAC$$
$$x\ 116\ g\ NHS/mol\ EDAC$$

The above values were per one scaffold, so each figure was multiplied by 'X' number of scaffolds depending on the quantity to be crosslinked. EDAC was removed from the freezer prior to its usage and defrosted for 1 h at room temperature in a desiccator. The required amounts of EDAC and NHS were weighed using an analytical balance (METTLER AT261,

Mettler Toledo, Belgium) and added to a 50 mL tube. The required amount of distilled water was calculated through the simple equation: 2 mL dH_2O x no. of scaffolds. The dH_2O was added to the 50 mL tube and vortexed for 30 sec to ensure full solubilisation of EDAC/NHS. The EDAC/NHS solution was then sterile filtered (0.2 µm filter size, cellulose acetate). Scaffolds were initially hydrated in ethanol and then transferred to a fresh 24-well plate. Each scaffold was incubated with 2 mL of EDAC/NHS solution and then left at room temperature for a total of 2 h. Crosslinked scaffolds were then removed from EDAC/NHS wells and soaked in 70% ethanol for sterilisation for ~5-10 min. The scaffolds were then transferred to sterile PBS for a preliminary wash and removal of excess ethanol and EDAC/NHS. Following this, scaffolds were transferred to 50 mL centrifuge tubes (labelled according to composition) to which ~30 mL sterile PBS was added. The tubes were then placed on an orbital shaker at 30 RPM for 30 min for washing. This step was repeated for a second time with fresh sterile PBS for an additional 30 min. Scaffolds were generally prepared on an as-needed basis and were used immediately for testing. In instances where scaffolds required short term storage (i.e., ~2 days), scaffolds were stored in sterile 1x PBS at 4 ºC.

2.2.7   SEM analysis

Scaffold architecture was analysed using scanning electron microscopy (SEM) (Mono Cl Evo L515). Crosslinked scaffolds were prepared for SEM by freeze-drying using the standard freeze-drying cycle. Before imaging, both the crosslinked and non-crosslinked scaffolds were sectioned in the longitudinal and transverse planes at various depths throughout each scaffold. Scaffolds were then mounted on stainless steel stubs coated with a carbon adhesive. Prior to SEM, scaffolds were sputter-coated with gold (Scancoat Six Sputter Coater, BOC Edwards, United Kingdom). SEM imaging was conducted at an

accelerating voltage of 15 kV. The microarchitecture was assessed at various depths throughout the scaffold in both the longitudinal and transverse planes to ensure pore structure was largely homogenous. Scaffolds were viewed before and after the crosslinking procedure.

2.2.8   Porosity

Porosity was calculated using a gravimetric method [172], which measured the relative density of the scaffold (ρScaffold) in relation to the theoretical dry solid density (ρSolid). The volume of each scaffold was measured using a Vernier caliper and the mass was recorded using an analytical balance (METTLER AT261, Mettler Toledo, Belgium). Density was calculated by dividing the mass by the volume for each sample. Theoretical densities of collagen and gelatin were taken as 1.3 and 1.369 g cm^{-3} [330,331], and for sodium hyaluronate, 1.1 g cm^{-3} [332]. For composite scaffolds, the ratio of collagen:gelatin:hyaluronic acid was first determined to calculate the theoretical dry solid densities of composite scaffolds. Porosity (%) was then determined (Equation 3). Equation 3 shows how to calculate the ratio for the composite scaffolds.

Equation 3 – Porosity of scaffolds:

$$\text{Theoretical solid density } (\rho Solid) =$$

$$\left(\frac{\% \; Collagen}{100}\right)(\rho Collagen \; Solid) + \left(\frac{\% \; Gelatin}{100}\right)(\rho Gelatin \; Solid)$$

$$+ \left(\frac{\% \; Hyaluronic \; acid}{100}\right)(\rho Hyaluronic \; acid \; Solid)$$

$$Density \; (\rho) \; of \; scaffold \; (\rho Scaffold) = \left(\frac{Scaffold \; mass}{Scaffold \; volume}\right)$$

Porosity was then calculated as per the below:

$$Porosity \; (\%) = 100 - \left[\left(\frac{\rho Scaffold}{\rho Solid}\right) x \; 100\% \right]$$

2.2.9   Pore size

Pore size analysis (n=3) was completed using ImageJ2 software (v1.53n, NIH, Bethesda, Maryland, USA) [333] using images captured via SEM. For pore measurements, SEM images of non-crosslinked scaffolds for each scaffold type in both the longitudinal and transverse planes at various depths was taken. Each SEM image was uploaded to ImageJ2 and a relevant scale was set for each image. Images were converted to binary to increase the contrast between pore walls and empty space. Grids were applied to images and pores were measured in each of the four corner sections and the centremost section in order to get a representative pore size for each scaffold image. A linear measuring tool was used to measure the major axis of ~50 pores per image. Pores were measured in microns (µm). Mean pore sizes were calculated for each composition, alongside histograms of raw pore size distribution data.

2.2.10 Fourier transform infra-red (FTIR) spectroscopy

Attenuated total reflectance (ATR) FTIR spectroscopy was carried out to examine the composition of each scaffold type confirm the presence of signature collagen, gelatin and hyaluronic acid peaks with no contaminants. Discs of each scaffold (n=3) composition of equal size (~5 x 2 mm, diameter x height) were used for analysis on the Spectrum Two FTIR spectrophotometer (PerkinElmer, Beaconsfield, UK). Each spectrum for each repeat was combined into a single spectrum for graphing purposes. Spectra were generated for wavelengths of 400-4,000 cm^{-1} at a resolution of 4 cm^{-1}, with four scans recorded per sample. The Spectrum Two FTIR spectrophotometer was fitted with a diamond universal ATR accessory, lithium tantalate detector and mid-infrared (MIR) source. Prior to the

sample scan, a background scan was carried out to account for any potential signal from the environmental conditions.

2.2.11 Mechanical testing

Unconfined compression testing was completed to determine the elastic modulus of each scaffold (n=6 for non-crosslinked and n=4 for crosslinked) composition using a mechanical testing machine (Z2.5 Zwick/Roell, Zwick Roell Ltd., Leominster, UK). Cylindrical-shaped specimens of ~9 x 4.5 mm (diameter x height) were hydrated overnight at 37 °C in PBS prior to testing. Scaffolds were placed in a water bath, maintained to at 37 °C, containing PBS during testing to maintain the scaffolds in a hydrated state. Testing was performed using a 5 N load cell at a rate of 10% strain/min to a maximum strain of 20%. The elastic modulus was calculated by determining the slope of the linear 2-5% region of the stress/strain curves for each scaffold. The elastic modulus was used as a representative measure of tumour tissue/ECM stiffness *in vivo*.

2.2.12 *In vitro* degradation

In vitro degradation rates were determined gravimetrically by monitoring the extent of weight loss of the scaffolds at scheduled times (1, 3, 5, 7 and 14 days). Each scaffold (n=6 or non-crosslinked scaffolds and n=3 for crosslinked) for each composition was incubated at 37 °C and 5% CO_2 in 1.5 mL of Dulbecco's Modified Eagle's Medium (DMEM) high glucose, supplemented with 1% PenStrep (Sigma-Aldrich Chemical Co, Wicklow, Ireland). At each timepoint, each scaffold was removed from media and thoroughly washed with distilled water to remove media components from the scaffold. The scaffold was briefly dried on filter paper to remove excess liquid. Scaffolds then underwent an overnight freeze-

drying procedure (VirTis 35XL Ultra Super XL, Biopharma, Winchester, UK) to remove the remaining liquid. Dried samples were weighed using an analytical balance and the weight loss (%) was determined (Equation 4).

Equation 4 - Weight loss (%):

$$\left(\frac{W_0 - W_1}{W_0}\right) x \; 100\%$$

W_0 = Initial dry weight.

W_1 = Dry weight post-incubation and freeze drying.

2.2.13 Swelling ratio

Scaffold swelling ratio was determined gravimetrically. As the non-crosslinked scaffolds were found from initial testing to have low elastic moduli and rapid *in vitro* degradation, the swelling ratio assessment was only carried out on EDAC crosslinked scaffolds. Scaffolds (n=6) were weighed using an analytical balance to determine the starting dry mass (W_0). Scaffolds were then placed in a 24-well plate and 2 mL PBS was added to each scaffold. Plates were then incubated at 37 °C. At selected timepoints (1 5, 24, 48, 72 & 120 h), plates were removed from the incubator and scaffolds were briefly blotted with filter paper to remove excess liquid. Scaffolds were then re-weighed to determine their swollen/wet weight (W_1). The swelling ratio (%) was calculated using Equation 5:

Equation 5 – Swelling ratio %:

$$\left(\frac{W_1 - W_0}{W_0}\right) x \; 100$$

W_0 = Initial dry weight of scaffolds.

W_1 = Wet weight of scaffolds.

2.2.14 Statistical analysis

Statistical analysis was completed using the GraphPad Prism software, version 8.0.2 (GraphPad Software, Inc., San Diego, CA). The minimum number of samples tested per study for each composition was n=3. One-way ANOVA or Two-way ANOVA was used to compare means of multiple groups, alongside Tukey or Bonferroni post-hoc tests. Results calculated and shown in graphs were the mean ± the standard deviation (SD). p-value ≤0.05 = *, p-value ≤0.01 = **, p-value ≤0.001 = ***, ns = no significance.

2.3 Results

2.3.1 Analysis of scaffold architecture

Collagen and composite scaffolds of homogenous shape and size (~9 x 9 mm, diameter x height) were successfully and reliably fabricated using the defined freeze-drying procedure (Fig. 2.2). Scaffolds were bisected to a size of 9 x 4.5 mm, and the 'skin' like layer of smaller pores on the top and bottom of each scaffold cylinder was removed. The scaffold microarchitecture was assessed using SEM imaging alongside quantitative measurements of porosity and pore size. SEM imaging demonstrated the scaffolds were highly porous with an interconnected isotropic pore structure (Fig. 2.3 & 2.4).
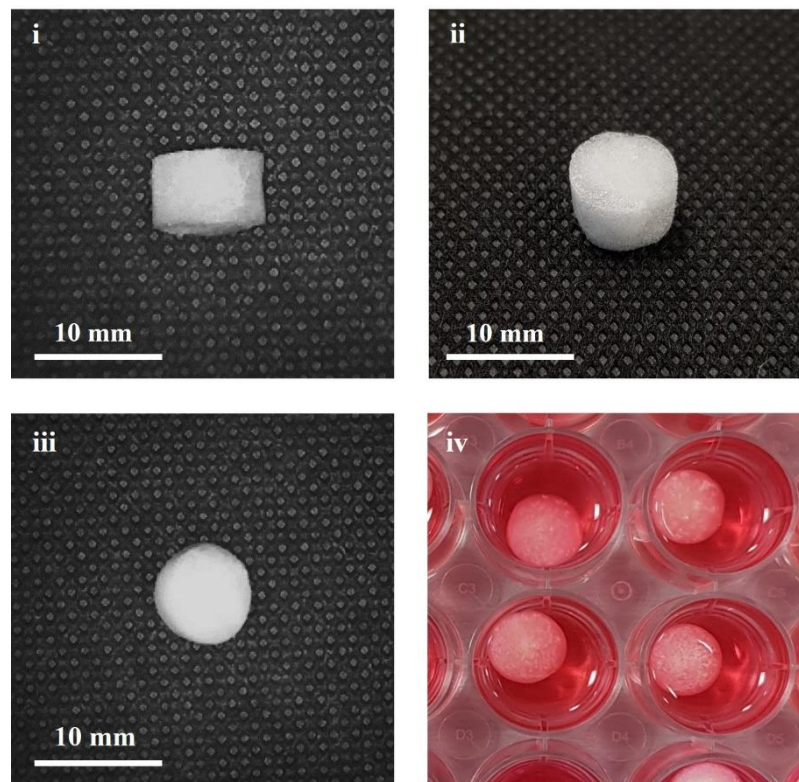
Figure 2.2: Visualisation of collagen-based scaffolds. Cylindrical porous scaffolds (~9 mm in diameter and 4.5 mm in height) fabricated via a freeze-drying procedure with the i) side view, ii) front view and iii) top view shown with scale bar for size indication. Hydrated scaffolds during cell culture are shown in iv).
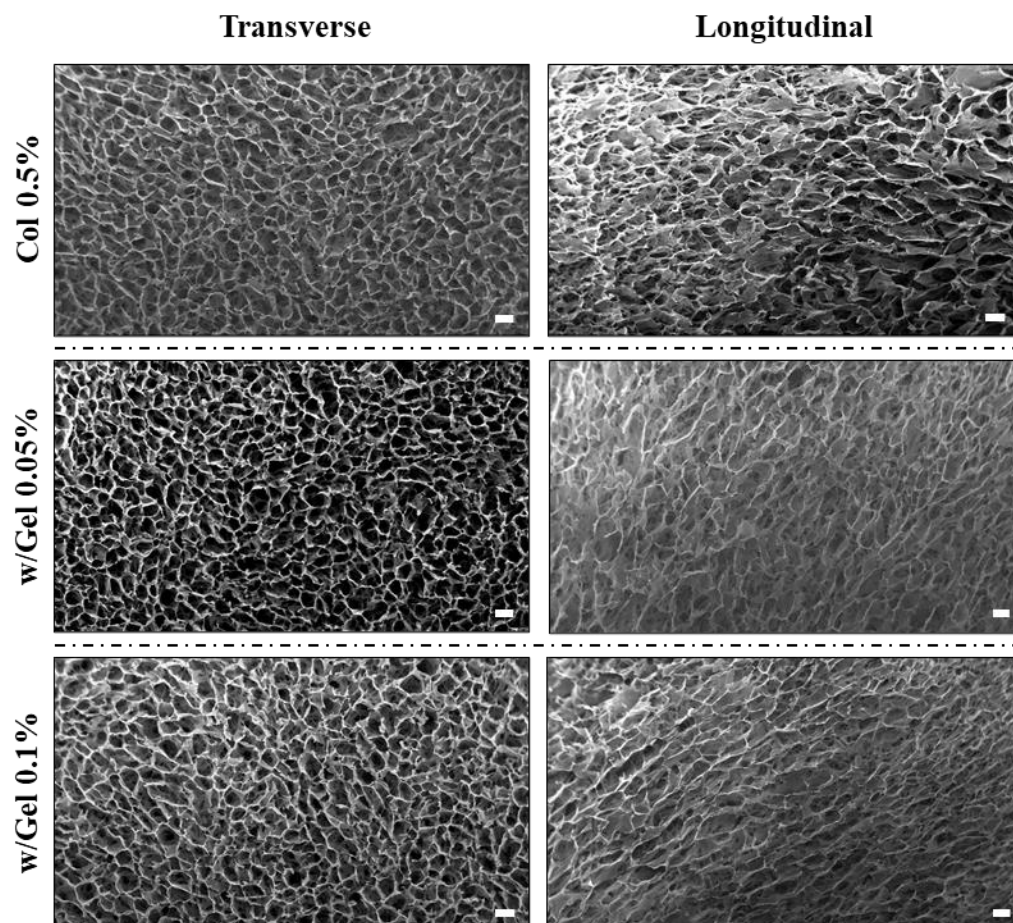
Figure 2.3: Transverse/longitudinal cross-sections of Col 0.5%, w/Gel 0.05% and w/Gel 0.1% scaffolds. Scaffolds were sectioned at various depths in both the transverse and longitudinal axis. SEM imaging confirmed the highly porous and interconnected structure across all compositions (non-crosslinked scaffolds). All scale bars represent 200 μm.
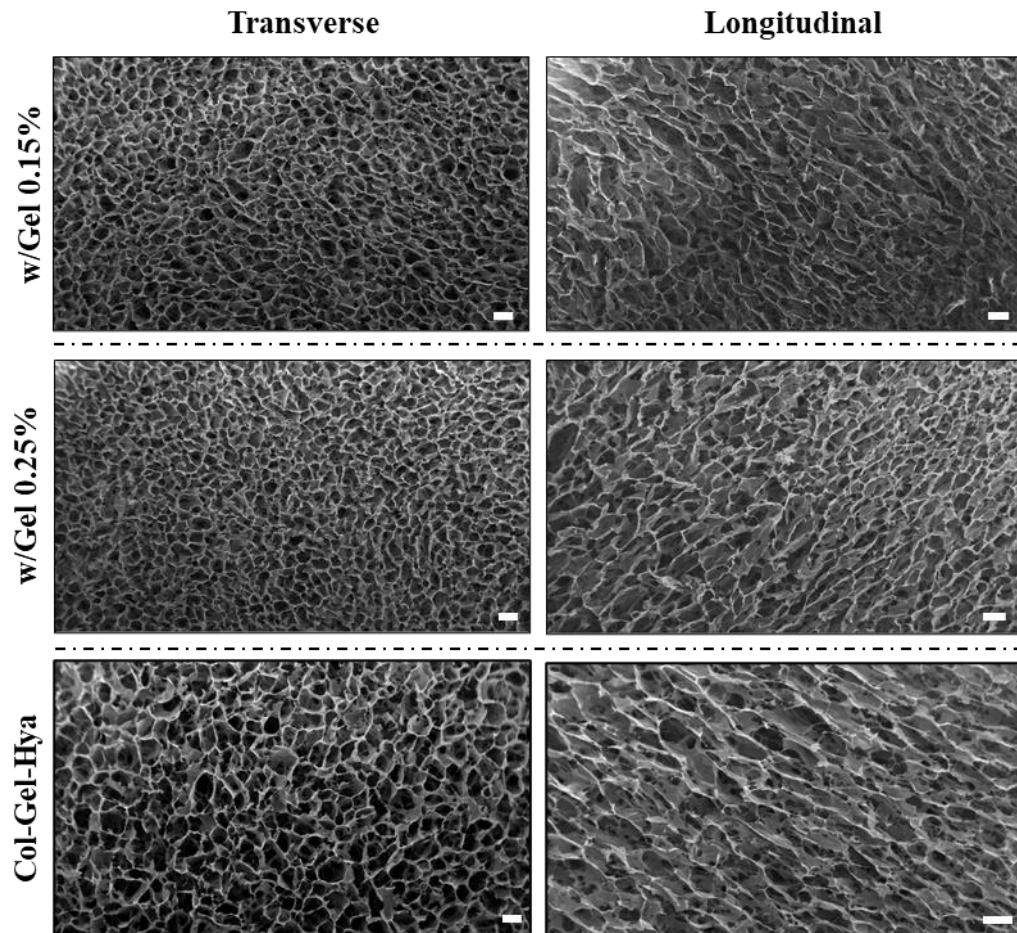
Figure 2.4: Transverse/longitudinal cross-sections of w/Gel 0.15%, w/Gel 0.25% and Col-Gel-Hya scaffolds. Scaffolds were sectioned at various depths in both the transverse and longitudinal axis. SEM imaging confirmed the highly porous and interconnected structure across all compositions (non-crosslinked scaffolds). All scale bars represent 200 μm.

Porosity analysis confirmed that each composition demonstrated a high porosity (>99.30%) across all groups. Analysis revealed statistically significant differences between the means of almost all groupings to one another (Fig. 2.5). Porosity decreased as a function of increasing gelatin concentration. However, all six compositions retained high porosity values. The Col 0.5% group had the largest porosity of $99.53 \pm 0.029\%$, while the w/Gel 0.25% group had the lowest recorded porosity of $99.32 \pm 0.038\%$.
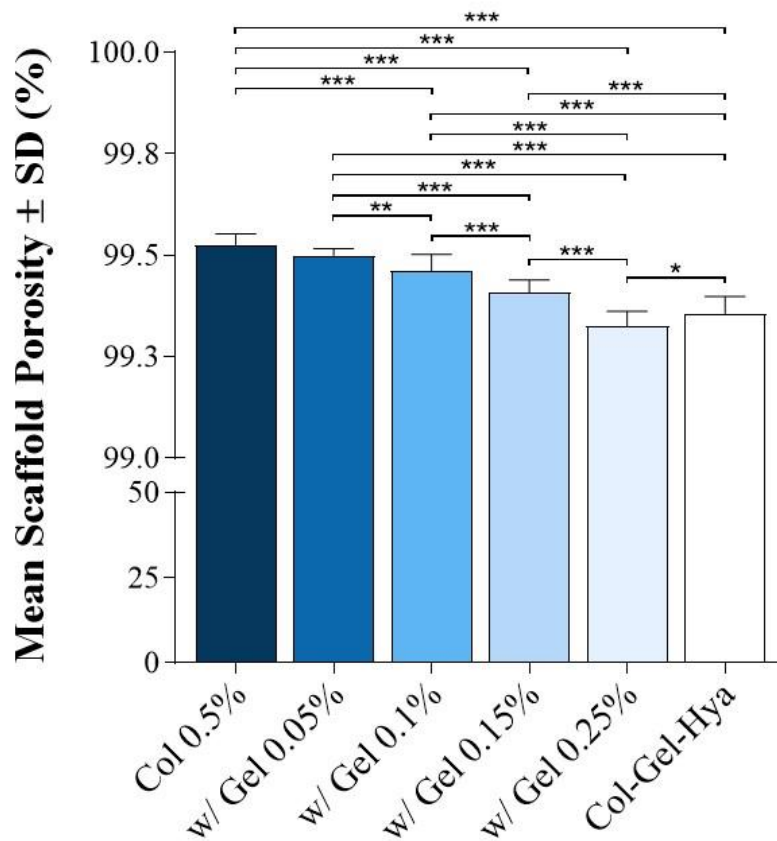
Figure 2.5: Scaffold porosity. Porosity was determined through a gravimetric technique, comparing relative densities to the theoretical solid density and thus determining the empty space (i.e., the porosity) of the scaffold. Variance was tested using one-way ANOVA with Tukey post-hoc test. Results shown are mean $\pm$ SD (n=20). p-value $\leq 0.05 = *$, p-value $\leq 0.01 = **$, p-value $\leq 0.001 = ***$.

Regarding pore size, the Col-Gel-Hya scaffold had the largest mean pore size in the transverse (T) axis at 216.2 ± 20.02 µm, while the Col 0.5% composition had the largest mean pore size in the longitudinal (L) cross-section at 290.42 ± 29.09 µm – although there was negligible true difference in pore size across the six compositions investigated (Fig. 2.6). The majority of pores for all compositions were within a range of 150-250 µm in the transverse axis and 200-350 µm in the longitudinal axis. Full details on mean pore sizes in the transverse and longitudinal axis can be seen in the summary table (Table 2.2). Pore sizes were larger in the longitudinal axis compared to the transverse axis (p-value ≤0.05), and this difference in size resulted in pores that were oval in shape. The raw distribution of pore sizes for each scaffold group is displayed in Fig. 2.7 and Fig. 2.8.
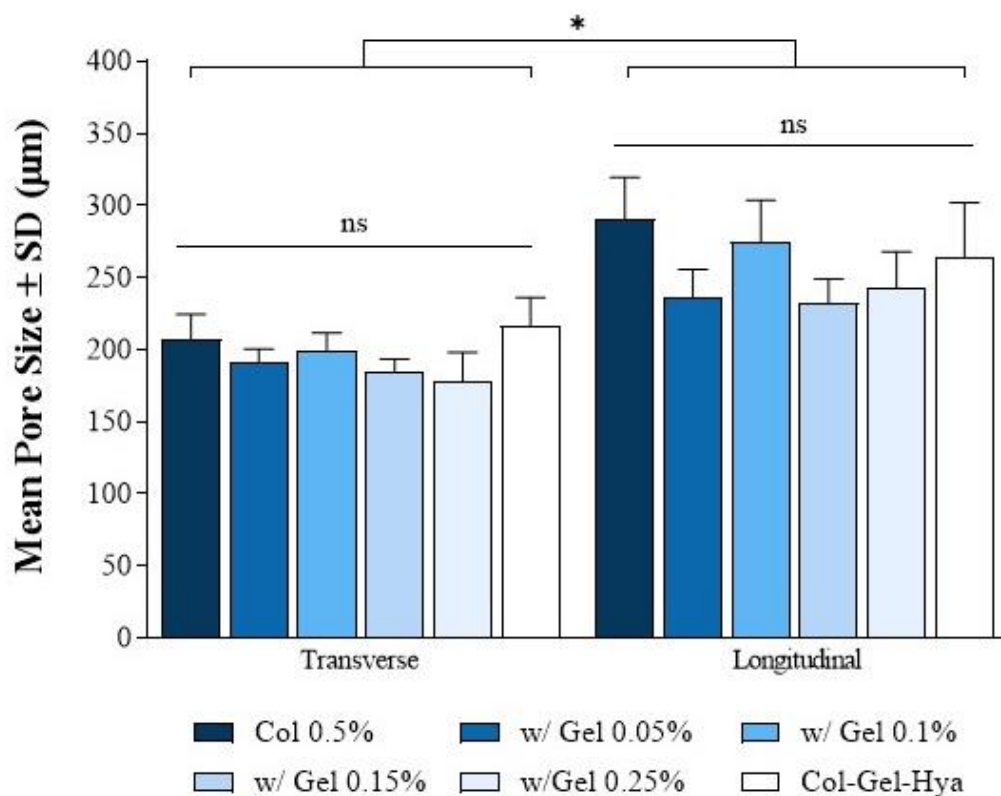
Figure 2.6: Pore size analysis. Pore size was measured using ImageJ software, by measuring the major axis of pores on SEM acquired images. Raw measurements for pores were averaged for each repeat, resulting in an average pore size for n = 3. Variance was tested using two-way ANOVA with Bonferroni post-hoc test. Results shown are mean ± SD (n=3). p-value ≤0.05 = *, p-value ≤0.01 = **, p-value ≤0.001 = ***, ns = no significance.
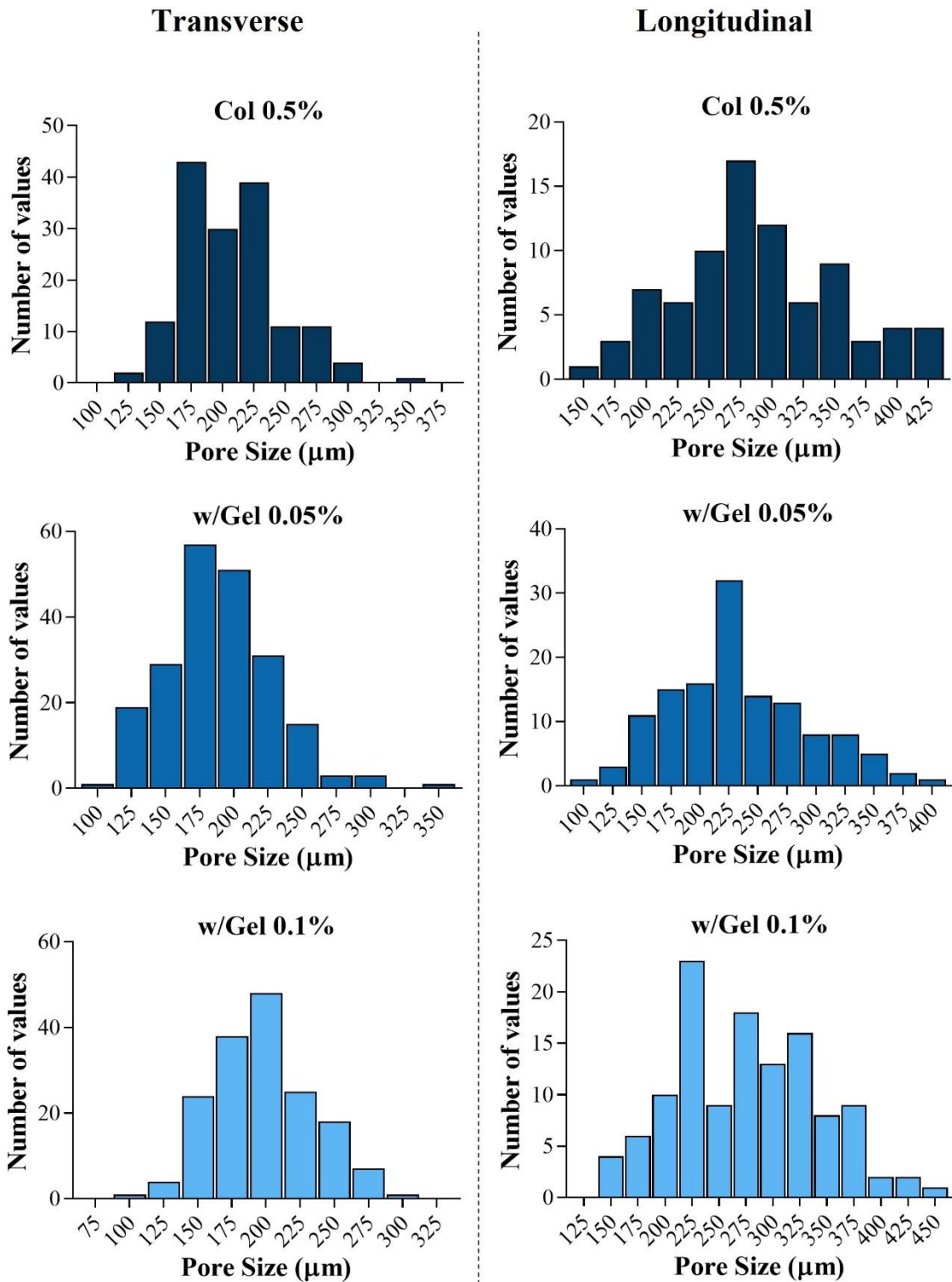
Figure 2.7: Pore size distribution data. Raw data of all measured pores are displayed above in histogram format, for the Col 0.5%, w/Gel 0.05% and w/Gel 0.1% compositions. Pores were measured at various scaffold depths in both the transverse and longitudinal axis.
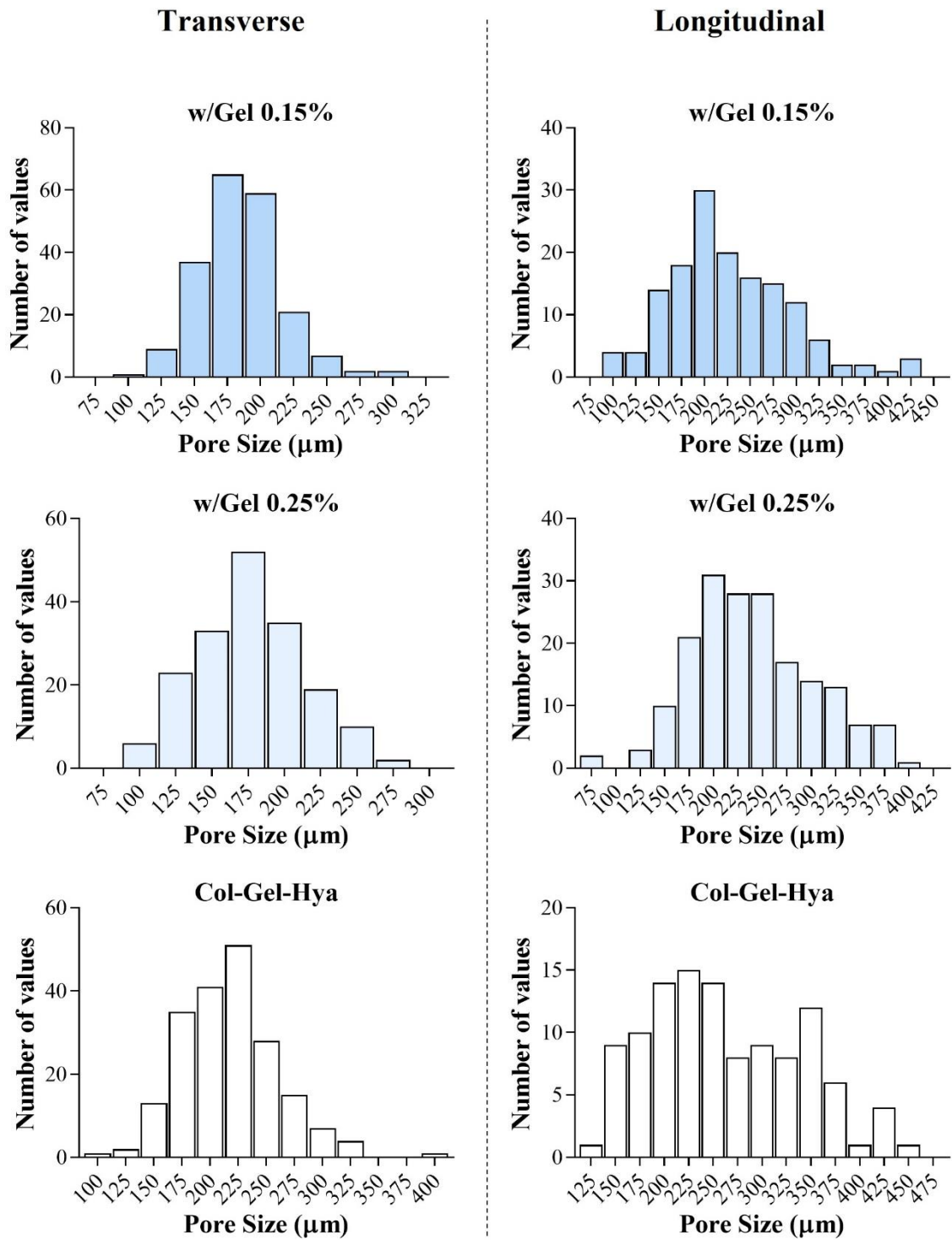
Figure 2.8: Pore size distribution data. Raw data of all measured pores are displayed above in histogram format, for the w/Gel 0.15%, w/Gel 0.25% and Col-Gel-Hya compositions. Pores were measured at various scaffold depths in both the transverse and longitudinal axis.

Table 2.2: Summary table of scaffold architectural properties.

Note (T) Transverse, (L) Longitudinal.

Property	Porosity (%)	Pore Size (µm)
Col 0.5%	99.53 ± 0.03	207.2 ± 17.5 (T) 290.4 ± 29.1 (L)
w/Gel 0.05%	99.50 ± 0.02	191.0 ± 9.3 (T) 236.4 ± 19.3 (L)
w/Gel 0.1%	99.46 ± 0.03	199.3 ± 12.4 (T) 274.9 ± 28.9 (L)
w/Gel 0.15%	99.41 ± 0.03	184.9 ± 8.53 (T) 232.1 ± 16.80 (L)
w/Gel 0.25%	99.33 ± 0.04	178.2 ± 20.0 (T) 242.3 ± 25.6 (L)
Col-Gel-Hya	99.36 ± 0.04	216.2 ± 19.86 (T) 264.3 ± 37.80 (L)

FTIR spectroscopy confirmed the expected collagen and gelatin composition of each scaffold (Fig. 2.9) for the initial five compositions. The five primary amide peaks associated with collagen/gelatin were observed across all compositions at the expected locations with no contaminant materials. The amide A (3,300 cm^{-1}) peak assignment represents N-H stretching vibrations, amide B (2,940 cm^{-1}) represents asymmetrical stretching of CH$_2$, amide I (1635 cm^{-1}) represents stretching of the carbonyl group (C=O) coupled with N-H bending and C-N stretching vibrations, amide II (1,550 cm^{-1}) represents N-H bending and C-N stretching vibrations, and amide III (1,240 cm^{-1}) represents N-H bending and C-N stretching vibrations [334–336]. Some selected hyaluronic acid peaks are labelled 1-3. Peak 1 at 1,607 cm^{-1} represents C=O (carbonyl group) stretching, peak 2 at 1,405 cm^{-1} highlights COO$^-$ (carboxylic salt group) stretching while peak 3 at 1,036 cm^{-1} indicates C-O-C stretching vibration related to ester bonds [337,338]. The incorporation of hyaluronic acid into the collagen/gelatin scaffolds is largely undetectable with no clear shifts or changes to the peaks already seen in the other compositions – likely owing to the low concentration of hyaluronic acid added to this composition relative to both collagen and gelatin. There is some indication of successful hyaluronic acid incorporation within the 1,036 cm^{-1} region of the Col-Gel-Hya spectra. Here a slight increase in the peak depth and broadening of the peak was observed. This can result from the increase in ester linkages between carboxylic and hydroxyl groups of collagen and hyaluronic acid in the composite scaffold mediated by the crosslinking procedure [339].
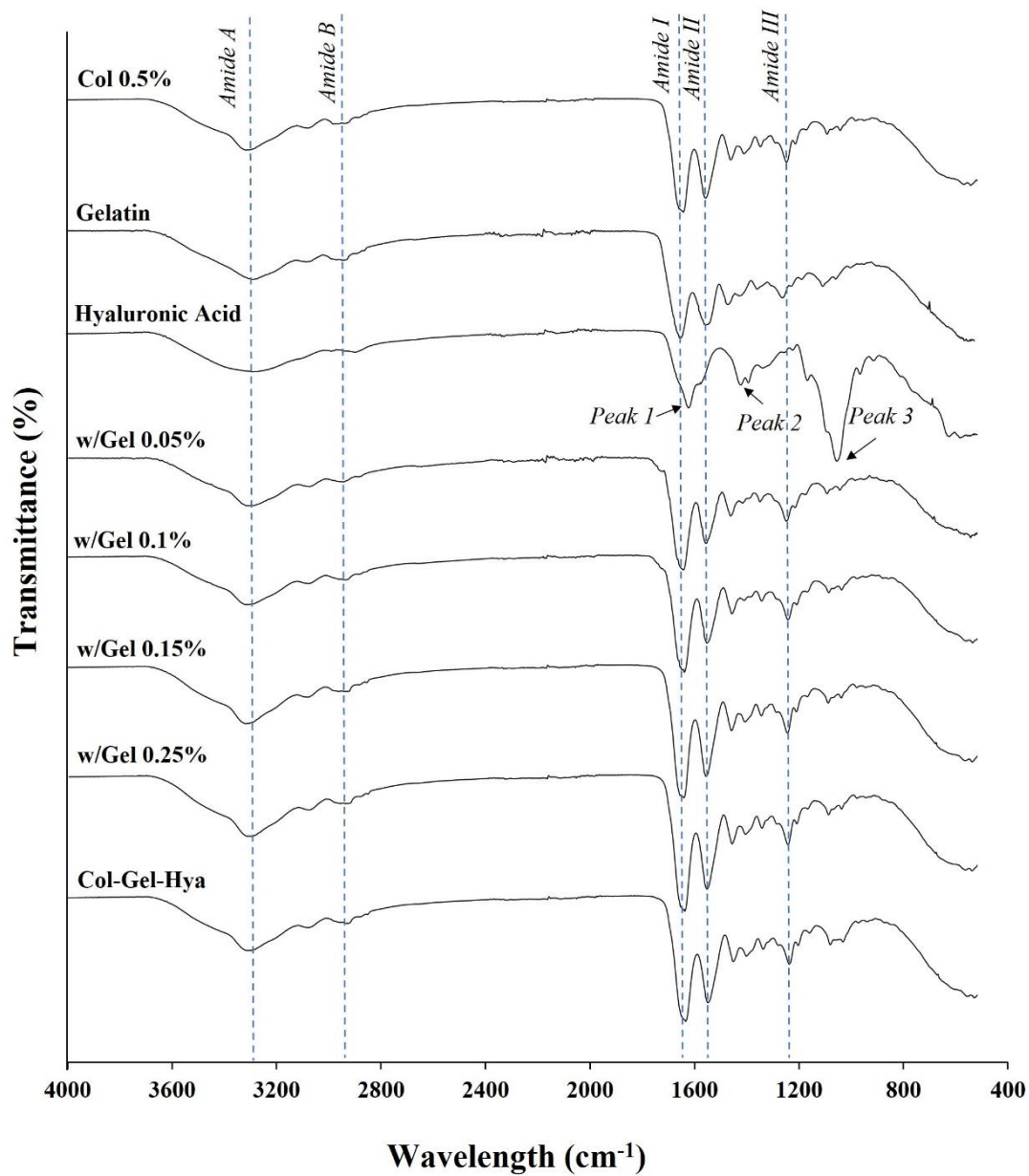
Figure 2.9: FTIR analysis. FTIR spectra of collagen (0.5%), gelatin, hyaluronic acid and the composite scaffolds are shown above. All primary amide peaks were identified and labelled for one composition for example. Each individual spectra for each repeat were combined into a single spectrum for visualisation purposes. Dashed lines represent each amide peak. Separate peaks (1-3) have been labelled with black arrows for hyaluronic acid.

2.3.2 Assessment of scaffold mechanical properties

The scaffolds were assessed under compressive loading to determine the elastic modulus (Fig. 2.10). In the non-crosslinked group, the Col 0.5% scaffold demonstrated the lowest modulus with a mean elastic modulus of 0.30 ± 0.04 kPa. The w/Gel 0.15% had the highest value of the six compositions with a mean modulus of 0.46 ± 0.08 kPa. The addition of gelatin resulted in an increase in elastic modulus (p-value ≤ 0.01). Crosslinking resulted in an increase in the elastic modulus for all six scaffold compositions when compared to their non-crosslinked equivalent counterpart (p-value ≤ 0.001). The w/Gel 0.1% scaffold had the highest elastic modulus amongst the crosslinked scaffolds with a mean modulus of 1.85 ± 0.37 kPa (p-value ≤ 0.01 vs. Col 0.5%), followed by the w/Gel 0.15% scaffold with a mean elastic modulus of 1.56 ± 0.25 kPa. The Col 0.5% scaffold again had the lowest mean elastic modulus of 1.03 ± 0.04 kPa. The addition of hyaluronic acid to the w/Gel 0.15% composition did not have any significant effect on the elastic modulus. Complete modulus data can be seen in Table 2.3 (crosslinked data only shown).
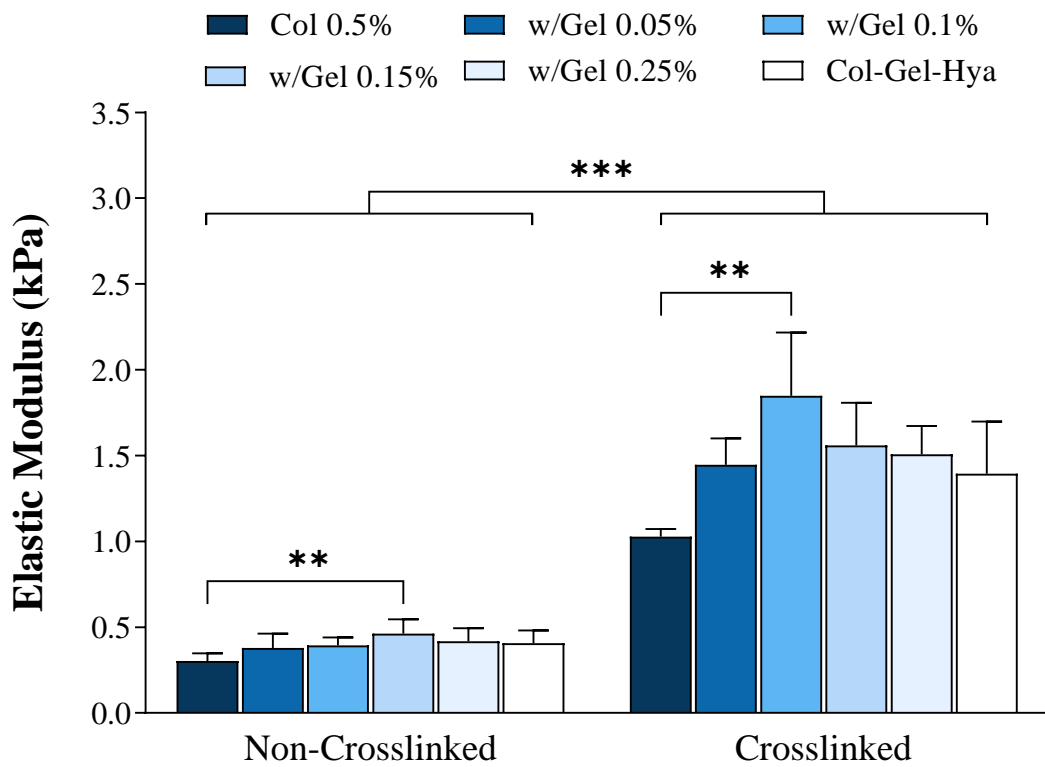
Figure 2.10 Comparison of elastic modulus between non-crosslinked and EDAC/NHS crosslinked scaffolds. The elastic modulus for each scaffold, non-crosslinked and crosslinked was determined using unconfined compression testing in a hydrated environment. The modulus was determined through the slope of the line of the 2-5% linear region of the stress-strain curves. Variance within either group (non-crosslinked or crosslinked) was tested using one-way ANOVA with Tukey post-hoc test and variance between both groups was tested using two-way ANOVA with Tukey post-hoc test. Results shown are mean ± SD (n=6 for non-crosslinked and n=4 for EDAC/NHS crosslinked). p-value ≤0.05 = *, p-value ≤0.01 = **, p-value ≤0.001 = ***.

2.3.3 Degradation and swelling properties of scaffolds

For non-crosslinked scaffolds, five scaffold group displayed rapid degradation in a short period, with over 50% degradation seen after 24 h in all compositions and many scaffolds had completely degraded within 3-5 days (Fig. 2.11A). What mass remained presented as weak fragmented structures that were not measurable or readily removed from well plates. In contrast, the Col-Gel-Hya scaffolds displayed significantly lower mass loss compared to the other compositions (p-value ≤0.001). The EDAC/NHS crosslinking procedure reduced the extent of degradation for all scaffold compositions investigated (Fig. 2.11B). By Day 14, degradation of <15% had occurred in all scaffold groups (Table 2.3). The Col-Gel-Hya scaffolds underwent an initial mass loss in the first three days before a selection of these scaffolds displayed an increase in mass at Day 5, seen through the large increase in standard deviation. This continued until Day 14 where all of the Col-Gel-Hya scaffolds increased in mass. Of the other five scaffold compositions, at Day 14 there was no difference amongst the compositions in terms of their mass loss. The high retention of scaffold mass demonstrates the crosslinked scaffolds applicability in long-term cultures. Qualitatively, non-crosslinked scaffolds were difficult to handle upon hydration and lost their shape readily–which would lend to difficulties in scaffold preparation and processing in culture applications. Crosslinking greatly improved the shape retention of the scaffolds and made handling of specimens easier.
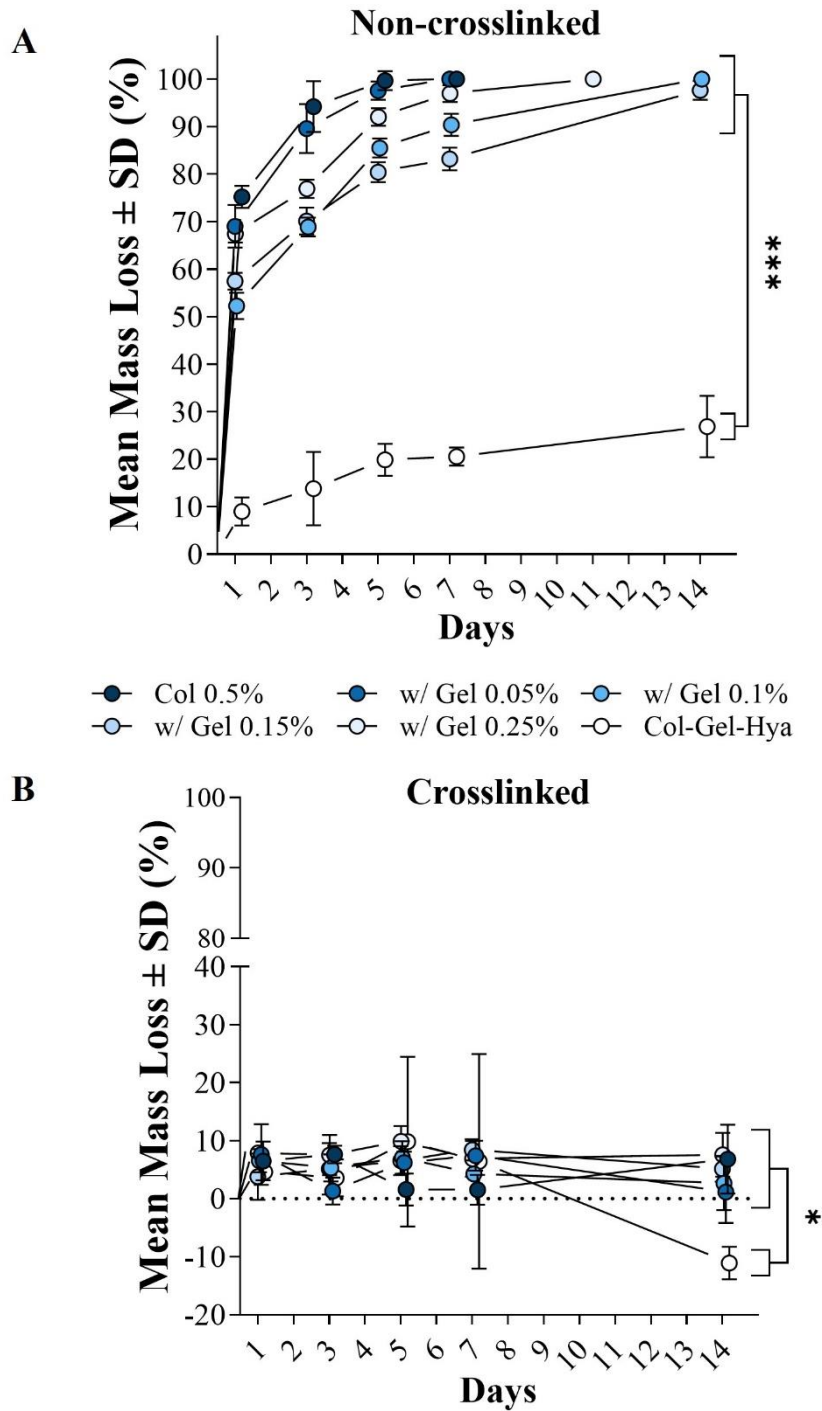
Figure 2.11: Degradation of non-crosslinked and EDAC/NHS crosslinked scaffolds *in vitro*. Degradation of both (A) non-crosslinked and (B) crosslinked scaffolds was determined gravimetrically after incubation at 37 °C and 5% CO_2 in 1.5 mL of DMEM over a 2-week period. Variance was tested using -way ANOVA with post-hoc test. Results shown are mean ± SD (n=3). p-value ≤0.05 = *, p-value ≤0.01 = **, p-value ≤0.001 = ***.

In swelling tests, all six compositions rapidly swelled and quickly attained equilibrium (Fig. 2.12). From the initial analysis point at 1 h all the way until 120 h, there was no change in the swelling ratio within each group. At 120 h, the Col 0.5% scaffolds had the highest degree of swelling at 9531.53%, significantly higher than the w/Gel 0.15%, w/Gel 0.25% and Col-Gel-Hya scaffolds (p-value ≤0.001). Overall, the w/Gel 0.25% group had the lowest swelling at 5642.48%.

A

B
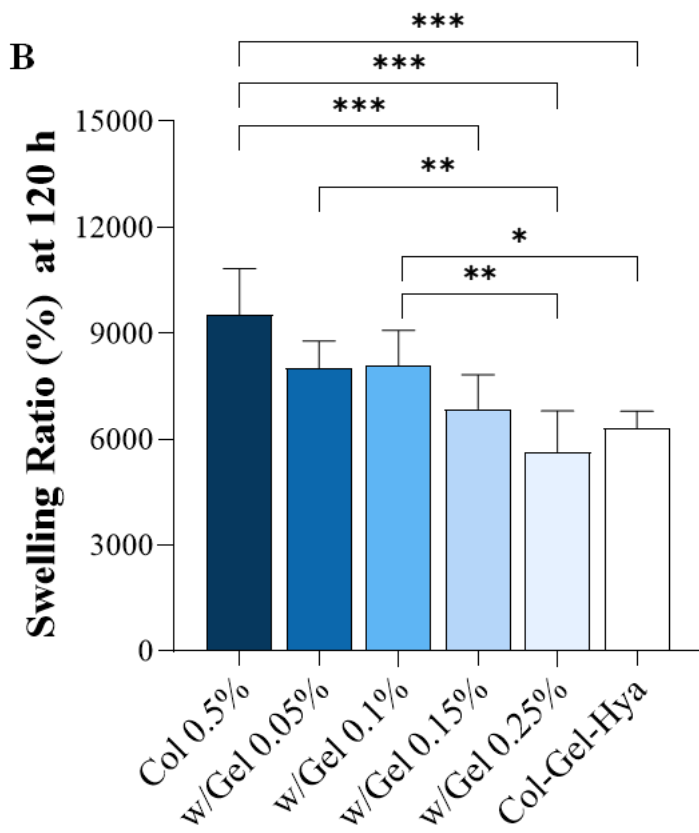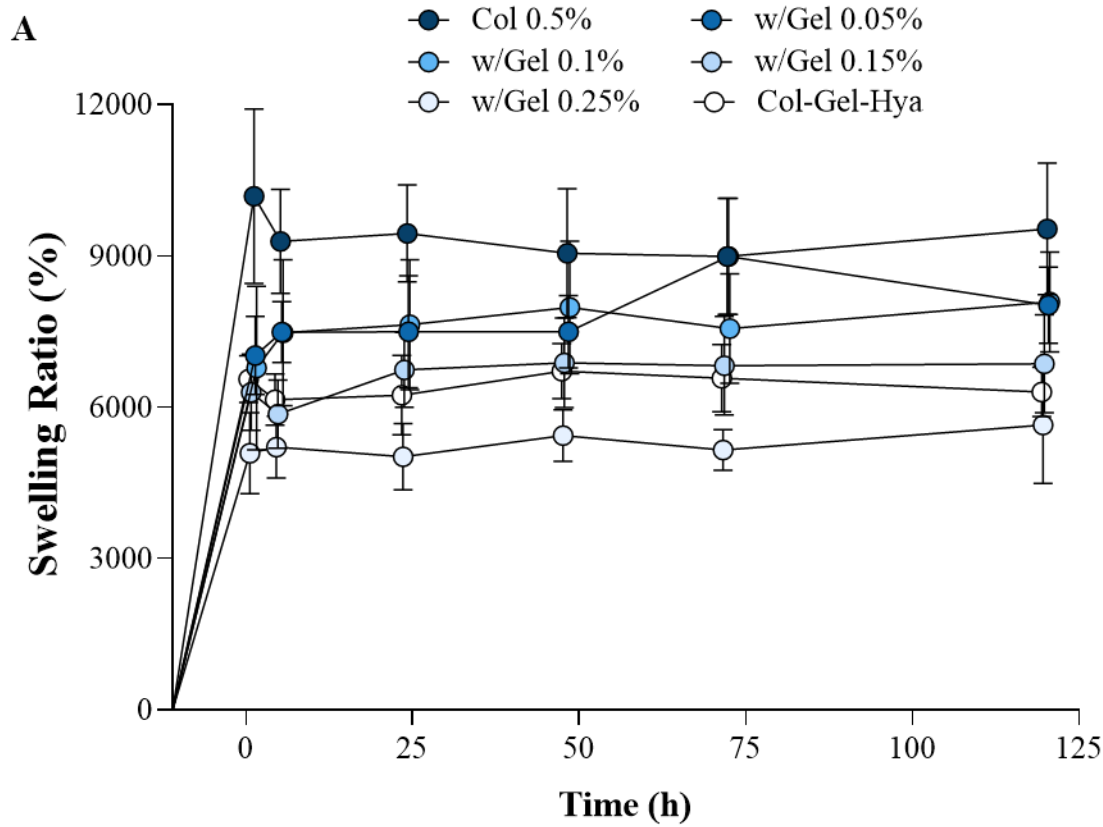
Figure 2.12: Swelling ratio (%) analysis. **A)** Swelling ratios for scaffold compositions across five days was determined gravimetrically post-hydration in PBS. **B)** Scaffold swelling ratios observed at Day 5. Results shown are mean ± SD (n=6). Variance was tested using one-way ANOVA with Tukey post-hoc test. p-value ≤0.05 = *, p-value ≤0.01 = **, p-value ≤0.001 = ***.

Table 2.3: Summary table of scaffold physical properties (crosslinked only)

*Negative value indicates a mass gain.

Property	Elastic Modulus (kPa)	Mass Loss at Day 14 (%)	Swelling Ratio (%) at 120 h
Col 0.5%	1.03 ± 0.04	6.84 ± 5.93	9531.53 ± 1302.47
w/Gel 0.05%	1.45 ± 0.15	1.18 ± 5.36	8018.12 ± 760.16
w/Gel 0.1%	1.85 ± 0.37	2.67 ± 4.62	8084.37 ± 993.34
w/Gel 0.15%	1.56 ± 0.25	5.16± 2.24	6856.85 ± 969.67
w/Gel 0.25%	1.51 ± 0.16	7.56 ± 3.79	5642.48 ± 1159.23
Col-Gel-Hya	1.39 ± 0.30	-11.06 ± 2.79*	6300.56 ± 490.36

2.4   Discussion

This chapter aimed to fabricate and characterise a range of collagen-based scaffolds for application as a 3D breast cancer culture model. For use as a cell culture model, scaffolds must be fabricated with suitable pore architecture and mechanical/degradative properties that provide an optimal environment for cell proliferation, while mimicking the properties of breast cancer ECM. Furthermore, this chapter sought to evaluate the impact of the addition of gelatin and/or hyaluronic acid to the Collagen 0.5% scaffold (i.e., the collagen-only comparator) in terms of these structural and physical properties.

Collagen is an extremely versatile material and its biological relevance in breast cancer [48,54,55,79] makes it a standout choice in culture model fabrication. Gelatin, which is denatured collagen, retains the biocompatibility of collagen and as such is a similarly versatile and beneficial scaffold component. Across the various physical characterisations, the addition of gelatin to the Col 0.5% base scaffold had a measurable impact. Furthermore, the addition of hyaluronic acid to the equivalent w/Gel 0.15% composition led to a decrease in porosity. The decrease in scaffold porosity was expected as the addition of various wt/v % of gelatin or hyaluronic acid to the Col 0.5% scaffold increased the relative density of the scaffolds. Increases in relative scaffold density results in less empty space per unit volume thus a reduction in porosity [176,223,340]. While this decrease was found to be statistically significant, the actual decrease was negligible, and all scaffolds maintained a highly porous architecture. The scaffold porosities match closely with collagen-based scaffolds previously reported in terms of composition, though these scaffolds were fabricated for applications in bone tissue engineering [172,222,223]. Values achieved are desirable for 3D culture as they

provide a large surface area for cellular attachment and efficient exchange and diffusion of waste and nutrients [341].

In addition to porosity, pore size is of crucial importance to cellular behaviour in scaffolds in other applications such as bone repair/regeneration [190,309]. In these instances, tailoring the pore size has wide ranging impacts from directing cell attachment and proliferation, stimulating bone formation and even in cell differentiation [309,342,343]. In terms of optimising collagen-based scaffolds for use as 3D breast cancer culture models, the ideal pore size will facilitate attachment and proliferation of breast cancer cells, allow for sufficient diffusion of nutrients and waste, enable provision of structural support while contributing to the required scaffold mechanical properties, provide sufficient pore space for 3D cell-cell interactions, and promote cell migration and infiltration throughout the full scaffold depth. However, the precise relationship between the cancer cell and pore size of collagen scaffolds has not yet been fully elucidated.

Studies elsewhere have successfully cultured viable and proliferating breast cancer [8,186,194,195], prostate cancer [9] and glioma cancer cells [166] on collagen scaffolds with pore sizes ranging from 50-300 μm – scaffolds fabricated achieved this target pore size range (Fig. 2.6). Due to the nature of using the same freeze-drying cycle across all six compositions, no significant changes in scaffold architecture were observed resulting from scaffold materials alone. Nor did the gelatin or hyaluronic acid addition have any observable effect on ice crystal formation during the freezing procedure, thus little to no downstream implications on pore architecture occurred. Changing the freezing temperature of the freeze drying procedure [344] or a more sizeable change in scaffold relative density/material

concentration [223] would likely have far more meaningful architectural changes. This would allow a more detailed study of the impact of pore size on breast cancer cell behaviour to be completed.

A crucial property of a culture model is the elastic modulus of the scaffold, which was used as an indicator/representative of breast cancer ECM/tissue stiffness. A scaffolds mechanical properties provide physical benefits in terms of scaffold stability through links between mechanical properties/crosslinking density and degradation rates, but also the degree of scaffold modulus plays a crucial role in cell activity. The elastic modulus values reported for the Col 0.5% scaffold, both non-crosslinked and crosslinked (~0.4 kPa for non-crosslinked and ~1 kPa for crosslinked), are consistent with those of collagen scaffolds reported in other studies [172,213,222,223]. The increase in scaffold modulus observed as a function of gelatin addition was largely attributed to the increase in relative density [317,345]. The higher relative densities and previously discussed reduction in porosities attributes greater resistance to force induced pore buckling, thus higher elastic moduli were achieved. Qualitatively, the addition of hyaluronic acid seemed to create a more gel-like consistency, which made the resultant scaffolds difficult to handle and they did not hold its cylindrical shape as well as the other compositions. Though ultimately, there was no statistically significant decrease in scaffold modulus compared to other scaffold compositions.

Elastic moduli values achieved in this study of 1-2 kPa (Fig. 2.10) correlate well with mechanical mapping of cancerous mammary ECM within a murine model, where a moduli range of 1.3–1.7 kPa was observed [93]. Stiffness of breast tissue is seen as a key driver of cancer progression and metastasis [4,48,54,78,346]. Therefore, the mimicking of similar

stiffness/modulus values within an *in vitro* breast cancer model is crucial. As the stiffness of breast cancer ECM increases with disease progression, there is a large variation in breast cancer tissue stiffness in humans [92] and lack of complete understanding of these breast cancer stiffness properties make the replication of human breast tissue more difficult *in vitro*. As mentioned previously in §2.1, scaffolds exhibiting an elastic modulus ranging from 0.5-3 kPa are suitable to replicate human breast cancer tissue [92,93]. The replication of elastic modulus values seen in the aforementioned murine model of breast cancer [93] in the collagen-based scaffolds fabricated is promising as it demonstrates how 3D scaffolds can bridge the model complexity gap between 2D culture and animal models.

Scaffold degradation rate is a crucial factor to take into consideration for *in vitro* culture models. Suitable culture models for cancer research require stable degradation kinetics with minimal mass loss over multiple weeks to allow long term observations *in vitro*. In this study, the non-crosslinked scaffolds demonstrated rapid *in vitro* degradation with significant loss of mass within 24 h, with degradation patterns similar to previously reported values for collagen/gelatin scaffolds [347]. EDAC/NHS crosslinking resulted in a significant reduction in degradation rates amongst all six compositions (Fig. 2.11). At Day 14 all scaffolds had ~90% of their mass remaining, highlighting that the addition of crosslinking resulted in scaffolds that are highly stable *in vitro* and could be used in long term experiments (2 weeks or more). By Day 14, a mass gain was evident within the Col-Gel-Hya scaffold composition. This was not an unexpected outcome due to the water-binding and highly hydrophilic behaviour of hyaluronic acid [348,349]. While the hyaluronic acid addition did not impact scaffold elastic modulus to any measurable degree, it enhanced the stabilisation of the scaffold under culture conditions and reduced dissolution of the construct. Combining the degradative properties with the initial mechanical results of the non-crosslinked scaffolds

resulted in the decision to move forward only with EDAC/NHS crosslinked scaffolds. This crosslinking resulted in a significant increase in scaffold elastic modulus and stability without negative impacts on scaffold architecture.
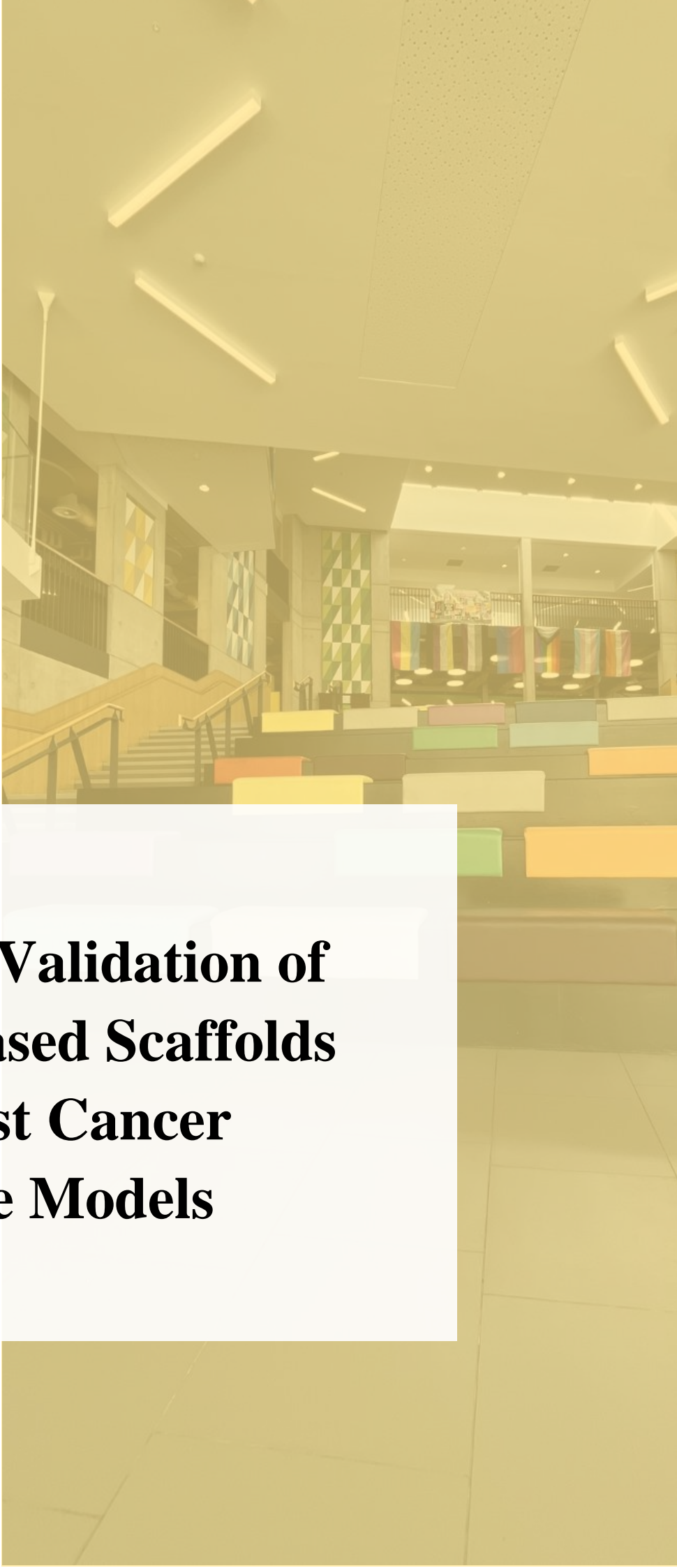
Crosslinked scaffolds retained their shape during experiments and handling whereas non-crosslinked scaffolds were deformed easily upon handling and lost their cylindrical shape. The poor handling properties subsequently lead to difficulties during preliminary cell seeding procedures. All six compositions had large degrees of swelling, with groups holding 50-100 times their original dry weight (Fig. 2.12). While gelatin and hyaluronic acid are both hydrophilic and therefore their addition to original collagen only scaffold was expected to increase scaffold swelling, the results showed that the Col 0.5% scaffold had the greatest swelling and the max gelatin containing scaffold (w/Gel 0.25%) and the Col-Gel-Hya scaffold had the lowest. This was likely due to EDAC/NHS mediated crosslinking and formation of ester linkages between hydroxyl/amino collagen groups and carboxylic groups of hyaluronic acid [350]–and it is known that greater crosslink density reduces swelling capacity [351]. Similar results, in relation to addition of hyaluronic acid, have been reported elsewhere whereby Davidenko *et al.* (2010) observed that the addition of hyaluronic acid to collagen reduced swelling/water uptake. Nonetheless, all swelling ratios achieved were relatively high and of a nature that would support cell infiltration and exchange and absorption of nutrients within the culture medium during cell culture.

2.4.1 Concluding remarks

In conclusion, a protocol to enable the successful fabrication of collagen and collagen/gelatin/hyaluronic acid composite scaffolds using a controlled rate freeze-drying procedure has been developed. All six scaffold compositions investigated underwent a detailed characterisation in terms of their chemical, architectural, mechanical and degradative properties. Each of these characterisations served to assess whether the scaffold is a suitable platform for use in tissue culture applications. The scaffolds fabricated were highly porous with homogenous pore sizes and porosity across all compositions. Addition of gelatin did significantly alter the porosity of the scaffolds, with a reduction of porosity observed as a function of increasing gelatin concentration–though the magnitude of the change was small. The mechanical and degradation studies highlighted low inherent structural integrity and poor workability for the non-crosslinked scaffolds. Upon hydration, these scaffolds lost their structure and degraded rapidly *in vitro.* Following crosslinking, scaffolds displayed improved mechanical stability in terms of elastic modulus and were now in a suitable range to mimic the mechanical properties of the ECM of breast cancer tissue. The addition of gelatin led to significant increases in scaffold modulus compared to the collagen-only scaffolds–generating scaffolds with the preferred elastic moduli profiles in terms of the above breast cancer ECM recreation. Crosslinking also greatly improved scaffold shape retention and handling, with significantly reduced mass loss *in vitro* confirming all scaffold compositions were suitable for long term *in vitro* culture applications. All six scaffold groups again displayed high degrees of swelling, an important attribute for cell culture as it allows for optimal nutrient absorption and exchange. As a result of the promising improvements owing to the crosslinking procedure, the decision was made to only carry forward using EDAC/NHS crosslinked scaffolds for remaining chapters within this

thesis. The crosslinked scaffolds displayed the properties required, as discussed throughout

this chapter, for their use as a scaffold-based breast cancer culture model.

03

Chapter 3: Validation of Collagen-Based Scaffolds as Breast Cancer Culture Models

Sections of this Chapter have previously been presented (with some modification) in *Biomaterials Advances* (2022).

Table of Contents

3.1 Introduction

Interest in 3D culture has rapidly increased in recent times. While 2D culture has provided significant advancements in cancer research, limitations of 2D culture and the desire to improve the replication of *in vivo* conditions in lab-based research has led to a growing shift from 2D to 3D. Within this chapter, the biocompatibility of the collagen and composite scaffolds and their ability to support the growth and proliferation of the MCF7 breast cancer cell line (Objective 2) was investigated. The structural characterisations in Chapter 2 enabled the identification of scaffolds that closely replicate the breast cancer ECM and thus suggested their suitability for cell culture applications. However, the determination of the ability of the scaffolds to support the proliferation of breast cancer cells requires *in vitro* investigation. Further to validating the biocompatibility of the scaffolds, this chapter investigated if the addition of gelatin or hyaluronic acid to collagen scaffolds improved cell attachment and proliferation.

Collagen-based scaffolds have become a mainstay in the world of tissue engineering and bone repair [352]. In recent years there has been a surge in their use as a culture model for cancer research [193,353,354]. Culture of breast cancer cells using 3D collagen models dates back to the late 1970s, where pioneering studies demonstrated the successful transplant and long-term culture of dissociated mouse breast cancer cells on simplistic collagen gels [199]. Over the following decades research continued in the field with continuing advancements in the biofabrication techniques used for producing collagen-based models, offering higher degrees of biomimicry and replication of the breast cancer tumour microenvironment - thus increasing the significance of research outputs. As discussed in the literature review (§1.6), collagen-based scaffolds have been used in breast cancer research across a variety of

applications including: (1) disease modelling from initiation to progression to metastasis, (2) scaffold biocompatibility and cell growth dynamics, (3) therapeutic agent assessment, (4) interactions between the 3D scaffold environment and cells, and (5) modelling development of hypoxia and related processes [8,10,186,188,194,195,197,198,229,355]. These studies demonstrate the potential that collagen-based scaffolds offer in becoming a mainstay in *in vitro* breast cancer research and the ultimate health benefits that may arise from their prominent use.

Studies have shown the addition of gelatin to scaffolds (non-collagenous) improved proliferation and cell biocompatibility [356–359]. Denaturation of collagen is proposed to expose cryptic RGD-motifs that are not accessible to cells in collagens native triple-helix state [360,361]. Thus, it is hypothesised that the addition of gelatin will provide increased cellular attachment sites and improved proliferation. In addition to gelatin, an additional scaffold composition containing hyaluronic acid was under investigation. Hyaluronic acid is highly upregulated in breast cancer tissue, and this overexpression correlates with a poor disease prognosis [328,329], thus its addition served to increase the biomimicry of the scaffold in terms of recreating the breast cancer microenvironment. In terms of functionality as part of a 3D culture model, it has been observed that the addition of hyaluronic acid to collagen-based scaffolds resulted in an increase in cell infiltration [362], and as such the potential effects of its incorporation on cellular infiltration and other aspects of cell behaviour within the scaffold was of interest.

3.1.1 Chapter aims

Within this chapter, the overall objective was to investigate the biocompatibility of the collagen and composite scaffolds. To demonstrate the suitability of the scaffolds as a breast cancer culture model, a range of cell studies were then carried out to profile cell behaviour within the six scaffold compositions. Aspects of cell behaviour under investigation included: cell attachment efficiency, cell viability within the scaffolds, cell proliferation rates, cellular infiltration throughout the scaffolds and finally cell morphology and growth patterns within the scaffolds. All six scaffold compositions (Col 0.5%, w/Gel 0.05%, w/Gel 0.1%, w/Gel 0.15%, w/Gel 0.25% and Col-Gel-Hya) were carried forward from Chapter 2 for initial assessments, before reduction of the working compositions to four took place.

Primary aims of this chapter were to:

- Assess biocompatibility of scaffolds to ensure scaffold materials themselves or degradation by-products do not cause cytotoxicity towards the MCF7 cells.

- Demonstrate the successful attachment and proliferation of breast cancer cells in the scaffolds.

- Assess cellular infiltration and general morphology of cells cultured within the scaffolds.

- Investigate the potential impacts of gelatin and hyaluronic acid incorporation on the various cell properties and their behaviour.

3.2   Materials and methods

3.2.1   Solutions/reagents

Phosphate Buffer Saline Solution 10x: 80 g NaCl, 2 g KCl, 14.4 g Na$_2$HPO$_4$, 2.4 g KH$_2$PO$_4$ into 800 mL distilled water and adjusted to 1 L. Diluted to 1x when needed. All mentions of PBS in the following studies were a 1x/0.01 M concentration.

Papain digestion buffer pH 6: 0.1 M Sodium phosphate buffer, 1.1 mM (millimolar) ethylenediaminetetraacetic acid (EDTA), 5.5 mM L-cysteine-hydrochloric acid (HCl); 125 μg papain enzyme per 1 mL of buffer (all materials from Sigma-Aldrich Chemical Co, Wicklow, Ireland).

10x TNE buffer pH 7.4: 100 mM Tris(hydroxymethyl)aminomethane-HCI (TRIS-HCI), 10 mM EDTA, 2 M NaCl (all Sigma-Aldrich Chemical Co, Wicklow, Ireland).

1x TNE buffer pH 7.4: 1 mL 10x TNE into 9 mL molecular grade Water (Sigma-Aldrich Chemical Co, Wicklow, Ireland).

2 μg/mL Hoechst working dye solution (per 12 mL); 24 μL Hoechst 1 mg/mL stock solution, was diluted into 11.976 mL 1x TNE buffer.

3.2.2   Cell culture

Cells

MCF7 cells (ATCC #HTB-22) were kindly received from the National Institute for Cellular Biotechnology at DCU. MCF7 cells are a human breast adenocarcinoma ER+ cell line derived from a metastatic site.

Cell line maintenance

MCF7 cells were maintained in DMEM-high glucose media (Sigma-Aldrich Chemical Co, Wicklow, Ireland) supplemented with 10% foetal bovine serum (FBS) (Thermo Fisher Scientific, Hemel Hempstead, United Kingdom), 1% PenStrep (Sigma-Aldrich Chemical Co, Wicklow, Ireland) and 2 mM L-glutamine (Thermo Fisher Scientific, Hemel Hempstead, United Kingdom) in 75 cm^2 flasks. Going forward the fully supplemented DMEM media will be referred to as 'DMEM media'. Cells were cultured in a humidified 5% CO$_2$ incubator at 37 °C. Cells were passaged when 70-85% confluency was reached. The split ratio used during passaging was typically 1:3-1:6. The cell culture medium was replaced every 48 h. For *in vitro* procedures, cells were trypsinised with 0.25% Trypsin (Thermo Fisher Scientific, Hemel Hempstead, United Kingdom), collected via centrifugation (800 RPM for 5 min) and resuspended in fresh media to be used in below studies. A cell bank was generated by occasionally freezing down 75 cm^2 flasks. Cell suspensions post-trypsinisation were spun down and the pellet was resuspended in DMEM media with 10% DMSO at ~1 x 10^6 cells/mL. Cell suspensions were stored at -80 °C and each vial was labelled with key information (e.g., storage date and passage number).

3.2.3   Scaffold preparation for cell culture assessments

All scaffolds (Col 0.5%, w/Gel 0.05%, w/Gel 0.1%, w/Gel 0.15%, w/Gel 0.25% and Col-Gel-Hya) were EDAC/NHS crosslinked as per §2.2.6 prior to cell culture applications. Crosslinked scaffolds, ~9 x 4.5 mm (diameter x height), were sterilised prior to cell culture experiments through immersion in 70% ethanol for 10 min. Following sterilisation, scaffolds were then thoroughly washed with sterile 1x PBS. Scaffolds were then incubated overnight in DMEM supplemented with 50% FBS at 5% CO_2 and 37°C and then placed into 24-well plates for the seeding procedure.

3.2.4   Cytotoxicity analysis

Potential cytotoxicity of the scaffolds and degradation by-products from the scaffolds towards MCF7 breast cancer cells was investigated in 2D. Cytotoxicity was analysed in accordance with the extraction method outlined in ISO 10993-5 (Part 5: Tests for in vitro cytotoxicity) [363], with cytotoxicity itself measured via the thiazolyl blue tetrazolium bromide (MTT) assay (Sigma-Aldrich Chemical Co, Wicklow, Ireland). The extract based method is routinely used to evaluate if biomaterial composition or degradation product is cytotoxic to cells [344,364–366]. Cytotoxicity testing was only performed on crosslinked scaffolds as non-crosslinked scaffolds were not used in cell culture studies. $1x10^5$ MCF7 cells per well were seeded in a 24-well plate with 1 mL of regular supplemented DMEM media (as per §3.2.2) and placed in an incubator (5% CO_2, 37 °C) for 24 h (n=4). Concurrently, scaffold-derived extracts for analysis were developed following immersion of each of the six crosslinked scaffold compositions in supplemented DMEM media. The extraction ratio used was one scaffold (9 x 4.5 mm (diameter x height)) per one mL of media– this ratio simulates the experimental use of the scaffolds during 3D culture, which conforms

to the ISO 10993-5 extraction ratio guidelines. The extraction process took place at 37 ℃ for 24 h. The negative control (NC) was unaltered, supplemented DMEM media with no scaffold immersion and the positive control (PC) was a 70% methanol/DMEM solution. After 24 h, the culture media was removed from the MCF7 cells and replaced with 1 mL of the scaffold-derived extract media of each scaffold composition. Plates were returned to the incubator at 37 ℃ for either 24 h or 72 h. After 24/72 h incubation, 100 μL of the extract media/controls was removed and replaced with 100 μL of a 5 mg/mL MTT stock (final well concentration of 0.5 mg/mL). Well plates were incubated for 4 h, after which the media was carefully removed and 500 μL of dimethyl sulfoxide (DMSO) was added to each well to solubilise the formazon crystals. Plates were incubated at 37 ℃ for 15-20 min to aid solubilisation. 100 μL of the solubilised formazan was transferred to a labelled 96-well plate for reading. Absorbance (Abs) was read at 540 nm (Infinite 200 PRO plate reader, TECAN, Switzerland). A DMSO-only background blank was subtracted from all readings. Negative control readings were averaged and set as 100% viable. Cell viability (%) was then determined (Equation 6).

Equation 6 – Calculation of cell viability %:

$$\left(\frac{Experimental\ Abs\ 540\ nm}{Mean\ Negative\ Control\ Abs\ 540\ nm} \right) x\ 100\%$$

3.2.5   3D scaffold seeding

Prior to seeding, each scaffold was prepared as outlined in §3.2.3. MCF7 cells were collected from 75 cm^2 culture flasks via trypsin treatment and pelleted via centrifugation at 800 RPM for 5 min. Cell pellets were resuspended in 1-2 mL DMEM media and then cells were

counted using the trypan blue exclusion method and the volume of cell suspension needed for seeding was calculated.
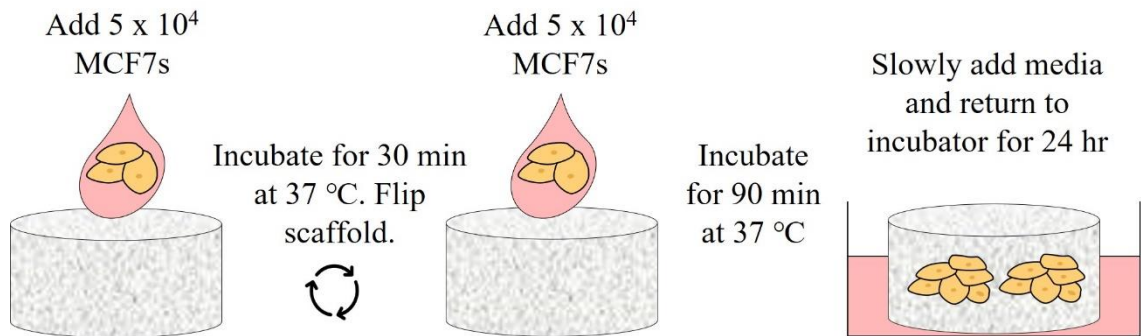
Figure 3.1: Two-sided scaffold seeding procedure. MCF7 cells were seeded onto both the top and bottom surfaces of each scaffold, with half the total amount of cells seeded to each surface.

The seeding approached used in all the following studies was a two-sided method (Fig. 3.1). This involved seeding cells onto both the top and bottom surface of each scaffold. Unless otherwise stated, each scaffold was seeded with 1×10^5 cells, derived from a study elsewhere using a similar size collagen scaffold, albeit with prostate cancer cells (which were a similar size to the MCF7 cells used) [9]. Each scaffold was placed in a well of a 6-well plate and was manually seeded (via pipette) with an aliquot of 5×10^4 MCF7 cells on both the top and bottom surfaces (1×10^5 cells total) under static conditions in a dropwise manner. Seeding of the initial 5×10^4 MCF7 cells on the top surface was followed by 30 min incubation at 37 °C to allow for initial attachment. Then, each scaffold was turned over carefully and the bottom surface was seeded with the additional 5×10^4 MCF7 cells. Each scaffold was returned to the incubator for a further 1.5 h (total 2 h attachment incubation). After the 2 h incubation, each scaffold was carefully transferred to a 24-well plate and 1.5 mL of DMEM media was

slowly added to the wells, and plates were returned to the incubator. For mid to long-term culture, the media was replaced every 48-72 h.

3.2.6   3D cell viability

Scaffolds were assessed for cell viability during 3D culture using the trypan blue exclusion method. Scaffolds were prepared for culture and seeded as per §3.2.3 and §3.2.5 (n=3). Post-seeding, each scaffold was placed in 1.5 mL of supplemented DMEM media and returned to the incubator at 37 °C / 5% CO_2 for 48 h, 7 and 14 days. At each respective timepoint, plates were removed from the incubator and scaffold/cell constructs were washed with sterile PBS to remove media traces (as serum in the media can inhibit the action of trypsin). Each scaffold was physically disrupted with a blunted needle before being treated with 0.5 mL of 0.25% trypsin at 37 °C for 10 min to detach cells from the scaffolds. After 10 min, 0.5 mL of DMEM media was added to each scaffold to inhibit trypsin action. This procedure did not remove the entire cell population from the scaffold, however excessive trypsin treatment can cause cell lysis which would negatively influence the results. The 1 mL of scaffold/cell supernatant was collected and placed in a 1.5 mL microcentrifuge tube and centrifuged at 800 RPM for 5 min to pellet the cells. The supernatant was removed, and the cell pellet was resuspended in just 20 μL of DMEM media. Trypan blue viability was then performed. 10 μL of cells/trypan blue suspension was added to a haemocytometer and cells in the four corner quadrants were counted. Cell viability was determined by Equation 7.

Equation 7 – Calculation of 3D cell viability (%):

$$3D\ Cell\ viability\ (\%) = \left(\frac{Number\ of\ live\ cells}{Number\ of\ total\ cells}\right) x\ 100\%$$

3.2.7   alamarBlue assay: cell proliferation/biocompatibility

The alamarBlue assay was used to initially assess cell proliferation/viability of MCF7 cells growing within the collagen scaffolds. The alamarBlue assay is based on the measurable reduction of resazurin to resorufin by metabolically active cells [367]. Scaffolds of ~9 x 4.5 mm (diameter x height) were used. An initial alamarBlue cell proliferation study was used to assess general biocompatibility on all six scaffold compositions over a 7-day period. This study along with the previous cytotoxicity/viability studies were combined with the characterisation data from Chapter 2 to refine the number of working scaffold compositions from six to four for the remainder of the biological characterisations in this chapter.

The initial alamarBlue on all six scaffold compositions spanned a 7-day period with timepoints at Day 1, 4 and 7. A further alamarBlue study on the selected four compositions (Col 0.5%, w/Gel 0.15%, w/Gel 0.25% and Col-Gel-Hya), alongside a 2D growth comparator (consisting of $1x10^5$ MCF7 cells seeded in 2D in a 6-well plate), spanned a 14-day period with timepoints at Day 1, Day 4, Day 7 and Day 14. Each crosslinked scaffold was seeded with a total of $1x10^5$ MCF7 cells under static conditions as per §3.2.5. 1.5 mL of supplemented DMEM media was added to each well and the 24-well plates were returned to the incubator until the various timepoints. At each timepoint, culture media was aspirated, and each scaffold was washed with sterile PBS to remove excess media and loosely attached cells. Following washing, each scaffold was transferred to a new 24-well plate that contained supplemented DMEM media with 10% alamarBlue solution (Thermo Fisher Scientific, Hemel Hempstead, United Kingdom). The negative control for background normalisation consisted of supplemented media with 10% alamarBlue and an unseeded scaffold (no cells). For 2D cells, the media was aspirated and cells were washed with sterile PBS before the

10% alamarBlue solution was added. The negative control for 2D cultures was 10% alamarBlue solution with no cells. The plates were returned to the incubator for 4 h to allow the reduction of resazurin to occur. Following incubation, scaffolds were discarded and 100 µL of now reduced media from each well was transferred to a 96-well plate for measurement. Reduction of alamarBlue was determined through the colourimetric method with the absorbance read at wavelengths of 570 nm and 600 nm (Infinite 200 PRO plate reader, TECAN, Männedorf, Switzerland). The reduction percentage for each scaffold was calculated as per Equation 8 below. The manufacturer guidelines provided the relevant values for the molar extinction coefficients (E) for oxidised (Eoxi) and reduced (Ered) alamarBlue.

Equation 8 – Percentage (%) reduction of alamarBlue reagent:

$$\left(\frac{(Eoxi600 \times A570) - (Eoxi570 \times A600)}{(Ered570 \times C600) - (Ered600 \times C570)} \right) x \ 100 \ \%$$

A570/600 – Absorbance (sample) at 570/600 nm

C570/600 – Absorbance (control) at 570/600 nm

Eoxi 570 – molar extinction coefficient of oxidised alamarBlue at 570 nm = 80,586

Eoxi 600 - molar extinction coefficient of oxidised alamarBlue at 600 nm = 11,7216

Ered 570 - molar extinction coefficient of reduced alamarBlue at 570 nm = 15,5677

Ered 600 - molar extinction coefficient of reduced alamarBlue at 600 nm = 14,652

3.2.8 DNA quantification

DNA quantifications were completed using a Hoechst 33258 (Sigma-Aldrich Chemical Co, Wicklow, Ireland) DNA quantification microplate assay. Hoechst 33258 is a cell permeable

dye that selectively binds to double stranded DNA and emits a bright fluorescence at 440/460 nm. Each crosslinked scaffold (Col 0.5%, w/Gel 0.15%, w/Gel 0.25% and Col-Gel-Hya) was seeded with $1x10^5$ MCF7 cells (two-sided as per §3.2.5). Four timepoints were subject to analysis; Day 1, Day 4, Day 7 and Day 14. At each timepoint, scaffolds were removed from the culture media, washed with sterile 1x PBS to remove loosely adhered cells and excess media and then transferred to an individual sterile 1.5 mL microcentrifuge tube. Each scaffold was digested using the cysteine protease Papain (Sigma-Aldrich Chemical Co, Wicklow, Ireland). Papain solubilised the scaffold and assisted with cellular lysis to release cellular DNA into solution. 500 μL of 125 μg/mL papain digestion buffer (§3.2.1) was added to each scaffold. Each microcentrifuge tube was then placed in a preheated water bath set to 60 °C for 24 h under constant agitation. Post-digestion, the scaffold DNA lysates were stored on ice if being used immediately or at -20 °C for short-term storage (1-2 weeks) or -80 °C for long-term storage (+2 weeks).

DNA quantities were to be determined using a calf thymus DNA (Sigma-Aldrich Chemical Co, Wicklow, Ireland) standard curve ranging from 0-10 μg/mL of DNA. 100 μL of digested scaffold DNA lysate was added to 100 μL of 2 μg/mL Hoechst 33258 working dye (§3.2.1). Samples and dye were mixed thoroughly and read immediately at an excitation of 340 nm and an emission of 460 nm using a plate reader (Wallac Victor2, PerkinElmer Life Sciences). Samples were diluted with 1x TNE (§3.2.1) if required to ensure they fit onto the standard curve. The concentration of DNA per scaffold was calculated using the standard curve equation of the line on Microsoft Excel. For assessing proliferation rates, the relative change of DNA amounts relative to Day 1 (initial value) for each respective timepoint (final value) was also calculated as per Equation 9.

Equation 9 – DNA relative change (vs. Day 1):

$$\frac{(final\ value - initial\ value\ [Day\ 1]\ )}{(initial\ value\ [Day\ 1])}$$

3.2.9 Cell attachment efficiency

The efficiency of cell attachment to the scaffolds was assessed by comparing the number of cells within the scaffolds after 24 h compared to the number of cells originally seeded. A total of $1x10^5$ MCF7 cells were seeded on each crosslinked scaffold. Cells were seeded using a two-sided seeding which was used in all experiments in this thesis (as per §3.2.4). After an initial attachment period of 24 h, each scaffold was carefully removed from the well plate and washed in sterile 1x PBS to remove any excess media. DNA quantification of cells adhered to each scaffold was completed using the papain digest/Hoechst 33258 assay (as per §3.2.8). Values were converted to a cell number using a MCF7 cell standard curve (cell number vs. fluorescence intensity) of 0-100,000 cells, cultured in 2D in a 24 well plate overnight prior to undergoing DNA quantification as above. Seeding efficiency (%) was then determined (Equation 10).

Equation 10 - Seeding efficiency %:

$$\frac{number\ of\ cells\ attached}{number\ of\ cells\ seeded}\ x\ 100\ \%$$

3.2.10 Cellular morphology assessment via SEM

For qualitative cell morphology analysis, scaffolds were seeded $1x10^5$ MCF7 cells as per §3.2.5. Scaffolds were removed from culture at Day 1 and Day 14 for SEM analysis and each scaffold was washed three times in 1x PBS to remove loosely attached/unattached cells

and culture media remnants. Each scaffold was then fixed in 2.5% glutaraldehyde in 1x PBS (pH 7.4) for 24 h at 4 °C. After fixing, each scaffold was washed three times in 1x PBS (10 min per wash) and then washed twice in distilled H_2O (10 min per wash) before undergoing a graded ethanol (EtOH) dehydration composed of the following steps each consisting of 15 min: 30% EtOH, 50% EtOH, 70% EtOH, 90% EtOH, 95% EtOH and 100% EtOH (x2). Each scaffold was then submerged in 1-2 mL of hexamethyldisilazane (HMDS, Sigma-Aldrich Chemical Co, Wicklow, Ireland) solution for 10 min (x2) to improve drying. After HMDS treatment, each scaffold was then moved to a dry 24-well plate and placed in a desiccator for overnight drying. When dry, each scaffold was then sectioned in both transverse and longitudinal axes, mounted on a carbon adhesive/aluminium stub before being sputter-coated with gold particles. SEM imaging was conducted at an accelerating voltage of 5 kV, as per §2.2.7.

3.2.11 Cellular infiltration assessment via fluorescence imaging

For qualitative cell infiltration/migration analysis, scaffolds were seeded $1x10^5$ MCF7 cells as per previously described in §3.2.5. At each timepoint (Day 1 and Day 14), each scaffold was removed from culture and washed three times in 1x PBS to remove loosely attached/unattached cells and culture media remnants. Each scaffold was then fixed overnight in 4% formaldehyde at 4 °C. Following fixation, each scaffold was bisected on the longitudinal axis (Fig. 3.2). Each scaffold half was then washed in 1x PBS (x3) before being submerged in a 0.5 µg/mL solution of DAPI for 15 min at room temperature in the dark. Each scaffold was then washed a further two times in fresh 1x PBS to remove excess DAPI solution to avoid high background fluorescence. Each scaffold was placed faced down in a glass 8-well ibidi µ-slide for imaging (ibidi GmbH, Lochhamer Schlag 11 | 82166 Gräfelfing,

Germany). Scaffolds were imaged on a Nikon TiE Widefield Fluorescence Microscope (Nikon, Amsterdam, Netherlands) fitted with a 20 X objective lens and a DAPI filter cube. Due to the relatively large scaffold size in comparison to the lens field of view, images were captured of both top and bottom surfaces of each scaffold and the central regions (Fig. 3.2).
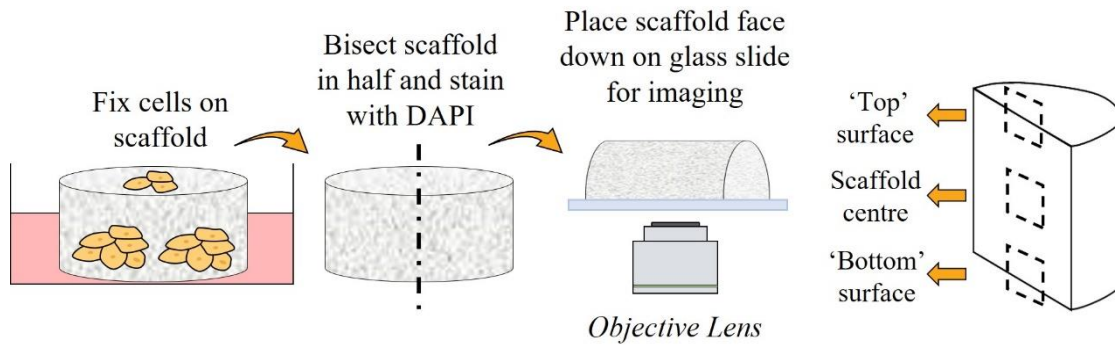
Figure 3.2: Preparation of Scaffolds for DAPI staining and fluorescent imaging. MCF7 cells were seeded onto scaffolds before fixation in 4% formaldehyde. Scaffolds were then bisected, stained with DAPI dye and placed face down on a glass slide for imaging. Images were taken at three locations: top surface, the centre of the scaffold and the bottom surface.

3.2.12 Statistical analysis

Statistical analysis was completed using the GraphPad Prism software, version 8.0.2 (GraphPad Software, Inc., San Diego, CA, www.graphpad.com). The minimum number of biological replicates tested per study for each composition was n=3. One-way ANOVA or Two-way ANOVA was used to compare means of multiple groups, alongside Tukey post-hoc tests. Results calculated and shown in graphs were the mean ± the standard deviation (SD). p-value ≤0.05 = *, p-value ≤0.01 = **, p-value ≤0.001 = ***, ns = no significance.

3.3   Results

3.3.1   Scaffold cytotoxicity and 3D cell viability assessment

To ensure each scaffold material composition was not cytotoxic towards the cell line in use, the extract method described in ISO 10993-5 [363] was used to investigate potential toxic effects of scaffold components or degradation by-products in 2D culture. At 24 h, MCF7 cells exposed to extracts derived from all scaffold groups demonstrated mean viabilities in the range of 90 - 100%, which is higher than the 70% viability requirement defined by the ISO standard (Fig. 3.3A). Furthermore, there was no difference (p-value >0.05) in viability compared to the negative control of unaltered media (normalised to 100% viability) for any scaffold composition extract. Qualitative evaluation via microscopic analysis revealed no/negligible cell lysis, changes in morphology or presence of intracytoplasmic granules in either the negative control or the scaffold-based extracts (Fig. 3.4 A-E). This was in contrast with the positive control (cells exposed to DMEM with 70% methanol), whereby a large reduction in attached cells was observed, along with increased cell lysis and cellular debris in the media (Fig. 3.4 F). At 72 h, viability across all extracts remained above 70%, though there was a drop in viability compared to the 24 h samples, with mean viabilities across the six compositions now in the range of 80 – 90% (Fig. 3.3B). Though importantly, there was again no statistical difference between the negative control and the six scaffold compositions (p-value >0.05). At 72 h, microscopic evaluation observed visible over-confluency in multiple samples leading to cell death, which likely contributed to the decrease in cell viability measurements. Nonetheless, results demonstrated that the scaffold components, both the collagen type 1 base and the addition of gelatin and hyaluronic acid, and also any potential scaffold degradation by-products are non-toxic for in vitro culture applications.

115
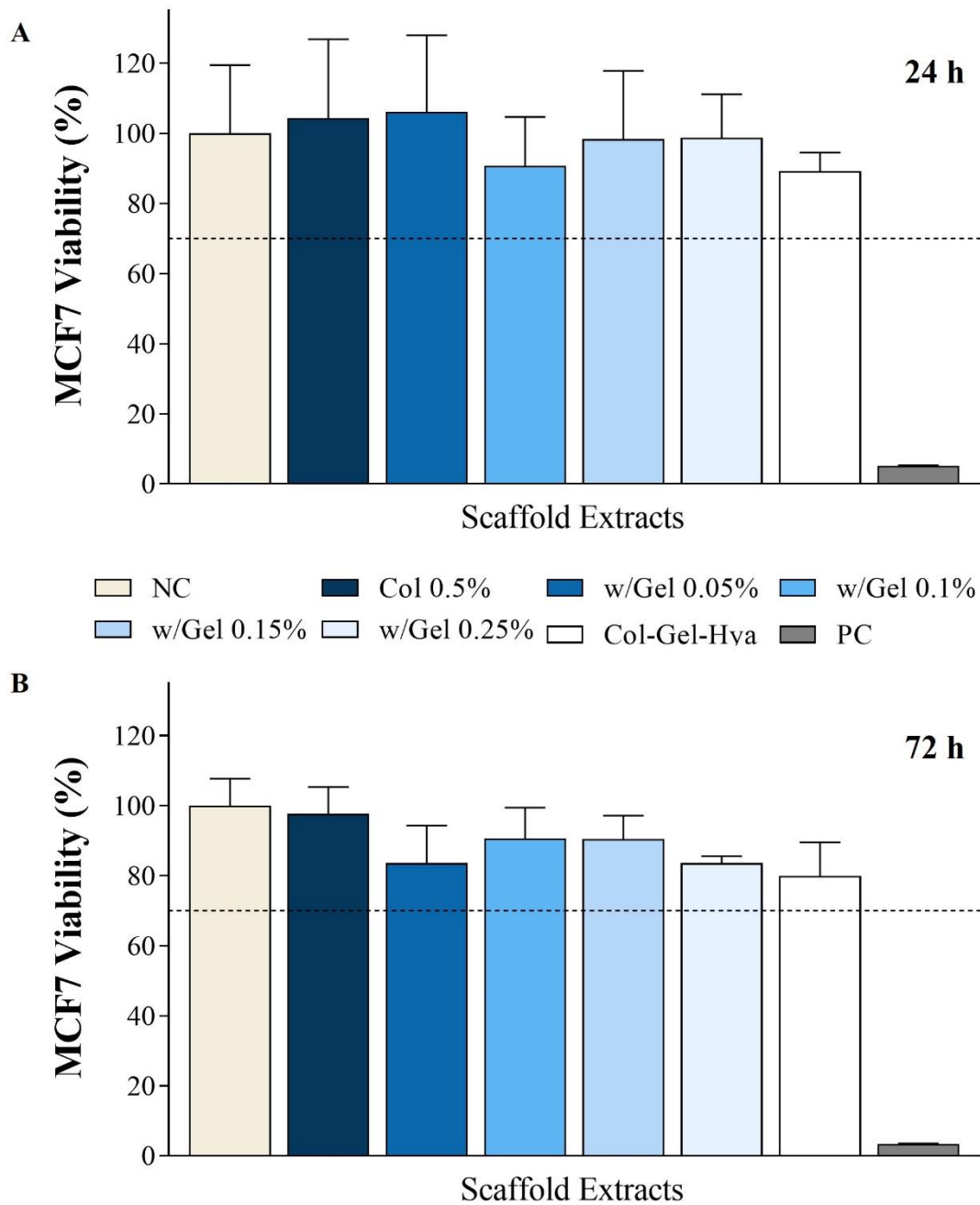
Figure 3.3: Cytotoxicity analysis of collagen-based scaffolds. Cytotoxicity analysis of scaffolds was carried out through the extraction based method in ISO 10993-5. MCF7 cells grown in 2D monolayer were exposed to scaffold-derived extract media for **(A)** 24 h or **(B)** 72 h. Dashed line at 70% represents the threshold whereby materials are considered cytotoxic if cell viability decreases below this value (as per ISO 10993-5). Cell viability was determined through MTT assay. NC = negative control and PC = positive control. Variance was tested using one-way ANOVA with Tukey post-hoc test. Results shown are mean ± SD (n=4).
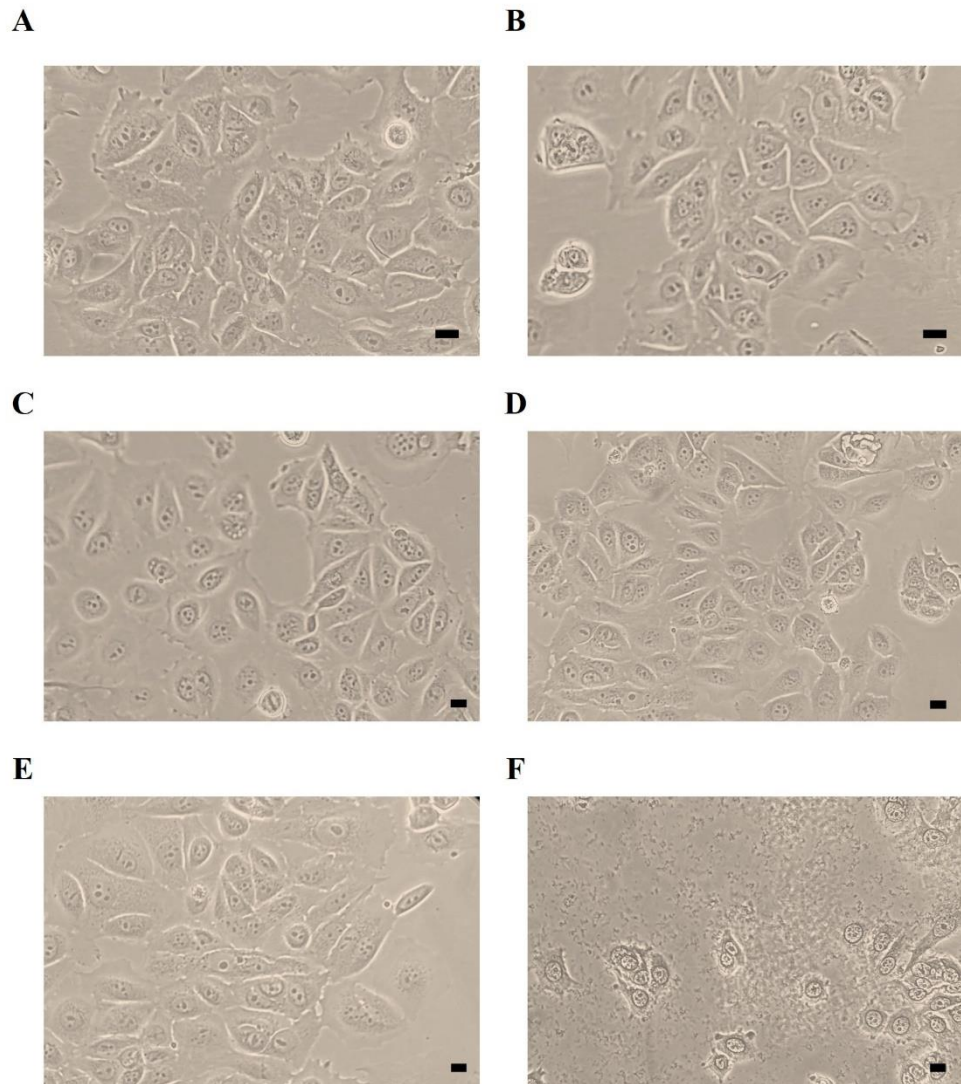
Figure 3.4: Cytotoxicity analysis of scaffolds. Qualitative assessment of the extract samples and controls revealed viable attached cells with no observable signs of cell lysis or cytotoxic effects in all groups **(A)** negative control, **(B)** Col 0.5%, **(C)** w/Gel 0.15%, **(D)** w/Gel 0.25% and **(E)** Col-Gel-Hya) compared to the positive control **(F)**, where large scale cell lysis was observed. Scale bars illustrate a size of 10 µm.

In addition to the 2D assessment of scaffold materials/by-products potential cytotoxicity, the trypan blue exclusion method was used to directly check for cell viability of cells growing on the scaffolds in 3D. Viabilities for all groups were >85% after 48 h of culture (Fig. 3.5), demonstrating the growth of healthy and viable cell populations within the scaffolds. At Day 7, viability had decreased to ~70% for the four scaffold compositions and by Day 14 there was a further decrease (p-value ≤0.001 comparing Day 1 and Day 14) to ~50% viability across the six scaffold compositions.
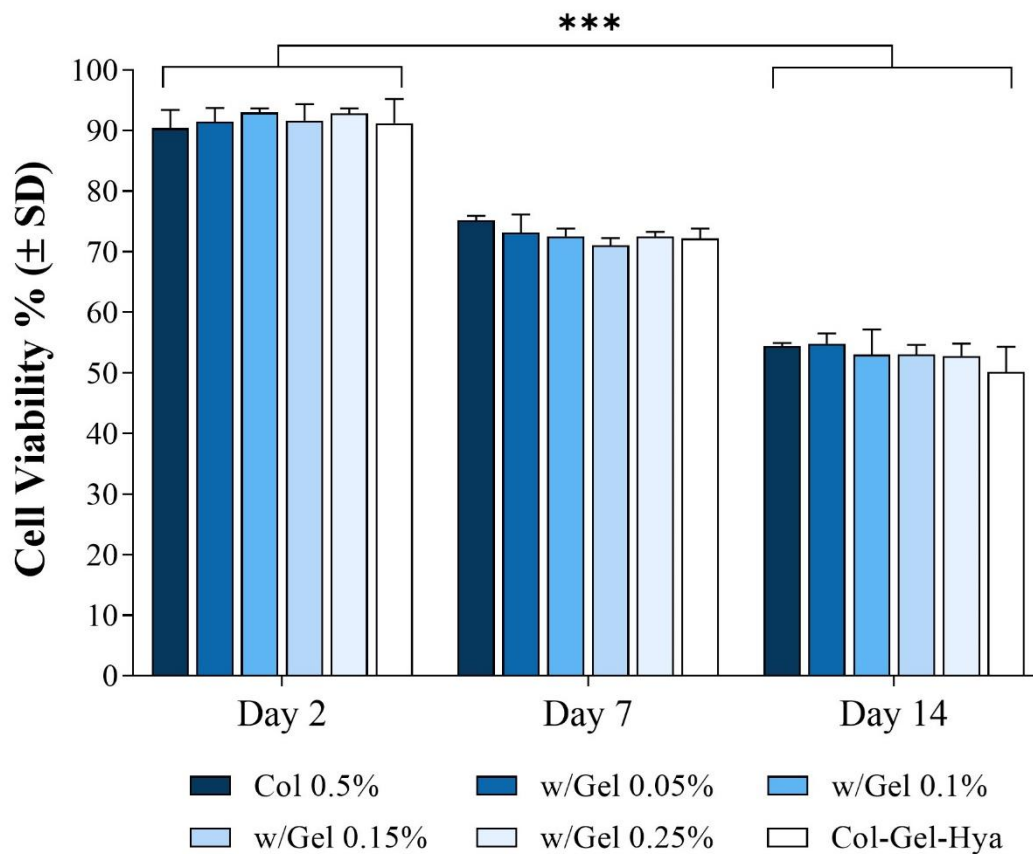
Figure 3.5: 3D Cell viability assessment. Trypan blue exclusion was used to assess cell viability in 3D (n=3). MCF7 cells were seeded on each scaffold group and incubated for 2, 7 or 14 days. Then, scaffolds underwent a trypsin treatment to remove cells from the scaffolds for counting. Variance was tested using two-way ANOVA with Tukey post-hoc test. Results shown are mean ± SD (n=3). p-value ≤0.05 = *, p-value ≤0.01 = **, p-value ≤0.001 = ***.

3.3.2 alamarBlue results

An initial 7-day alamarBlue study (Fig 3.6A) showed that all six scaffold compositions had a significant increase in the reduction of alamarBlue when compared to their Day 1 counterparts (p-value ≤0.001). At Day 1, there was no significant difference in the reduction of alamarBlue among the six scaffold compositions. At Day 4 (Fig. 3.6B), the w/Gel 0.05% had a larger reduction of the alamarBlue dye than both the w/Gel 0.25% and Col-Gel-Hya scaffolds (p-value ≤0.05). In addition, the w/Gel 0.1% had a higher dye reduction than the w/Gel 0.25% scaffold group (p-value ≤0.05). However, by Day 7, there were no differences in dye reduction amongst the six groups, with mean reduction values across all six groups in the range of 30-40%.
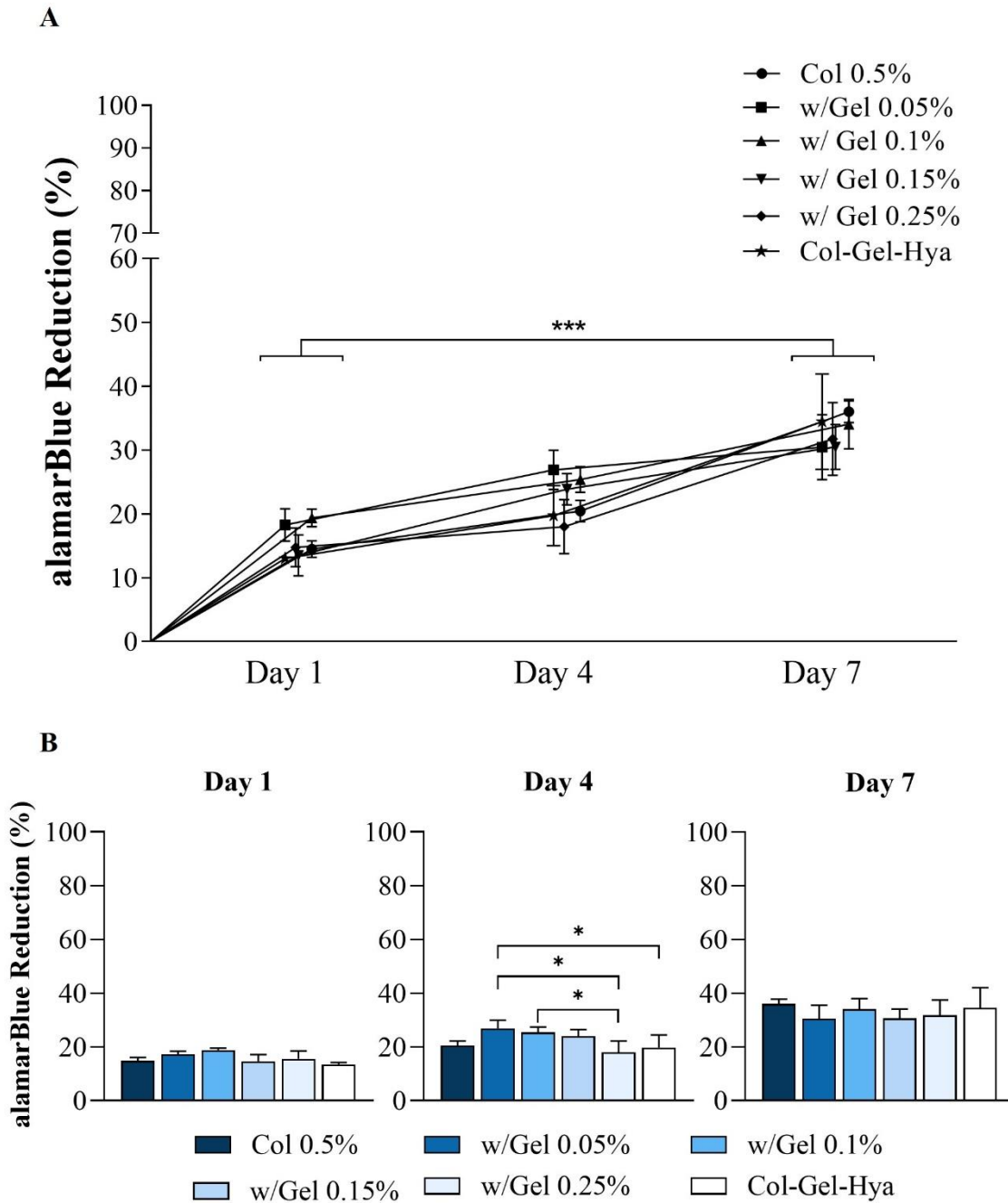
Figure 3.6: Reduction of alamarBlue by MCF7 cells on collagen-based scaffolds. (A) All six scaffold compositions had a significant increase in the reduction of alamarBlue at Day 7 when compared to their Day 1 counterparts. **(B)** Shows timepoints separated into individual graphs. Variance was tested using two-way ANOVA with Tukey post-hoc test (A) or using one-way ANOVA with Tukey post-hoc test (B). Results shown are mean ± SD (n=5). p-value ≤0.05 = *, p-value ≤0.01 = **, p-value ≤0.001 = ***.

All data collected from Chapter 2 and 3 was assessed to select four scaffold compositions out of the six groups to carry forward into subsequent biological studies within this chapter. There was limited to no significant differences across the physical characterisations and the initial cell viability studies in this chapter. Chapter 2 showed that all six scaffold groups demonstrated high porosity, suitable pore size and mechanical properties and stable *in vitro* degradation kinetics, with similar value ranges observed between groups. Thus, the w/Gel 0.05% and w/Gel 0.1% compositions were excluded from further analysis and just the w/Gel 0.15% and w/Gel 0.25% collagen-gelatin compositions were included in further studies. It was no envisaged the lower concentrations of gelatin added to the scaffolds would have any impact in future studies. The Col 0.5% composition was included as a non-gelatin comparator, to ensure all future cell work would allow for the assessment of any potential benefit of adding the gelatin or hyaluronic acid to the collagen only scaffold. The Col-Gel-Hya composition was included as the fourth group, to further assess the influence of hyaluronic acid on cell behaviour, as hyaluronic acid is a key component of the breast cancer ECM and plays an important role in the progression of the disease [328]. The four selected scaffolds were the following compositions:

- Col 0.5%
- w/Gel 0.15%
- w/Gel 0.25%
- Col-Gel-Hya

The expanded 14-day alamarBlue study, including the selected four scaffold compositions (Col 0.5%, w/Gel 0.05%, w/Gel 0.1%, w/Gel 0.15%, w/Gel 0.25% and Col-Gel-Hya) alongside a 2D comparator, again showed an increase in reduction of alamarBlue as a function of time (Fig. 3.7). All Day 14 values showed a significant increase in reduction of

alamarBlue compared to Day 1 (p-value ≤0.001). Amongst the four scaffold compositions only, at each timepoint, there were no statistical difference in reduction levels. At Day 1, the 2D comparator had a higher dye reduction than the Col 0.5% (p-value ≤0.001), w/Gel 0.15% (p-value ≤0.01) and the w/Gel 0.25% (p-value ≤0.05) scaffolds–though not the Col-Gel-Hya scaffold. By Day 4, the 2D cultured cells displayed higher reduction compared to all 3D cultures (p-value ≤0.001). However, by Day 6, cells in the 2D study were 100% confluent, with large levels of floating dead cells observed, and there was a yellowing of the culture media due to large amounts of cellular waste/metabolites causing a drop in the media pH. As such, the 2D comparator was not continued beyond this point.
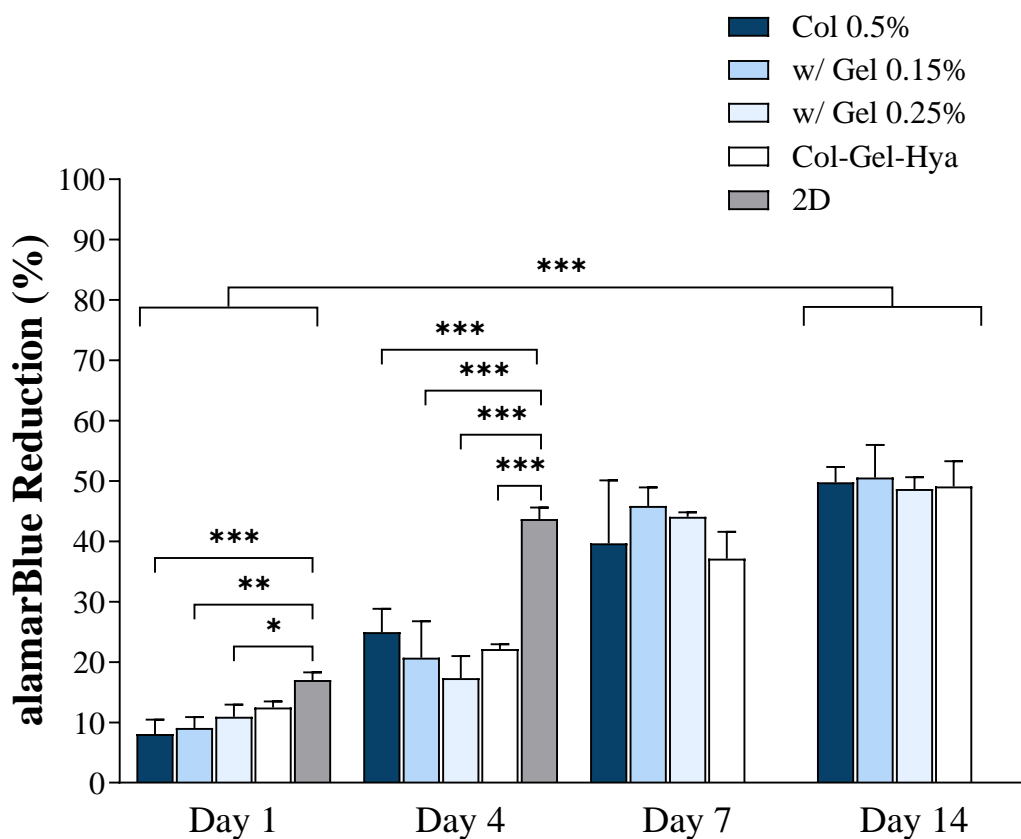
Figure 3.7: Reduction of alamarBlue by MCF7 cells with selected collagen-based scaffolds. The alamarBlue study was repeated to an extended 14-day period, and additionally a 2D comparator was included. Variance was tested using two-way ANOVA with Tukey post-hoc test. Results shown are mean ± SD (n=3). p-value ≤0.05 = *, p-value ≤0.01 = **, p-value ≤0.001 = ***.

3.3.3 Cell attachment efficiency

The efficiency of initial cell attachment to the scaffolds was assessed by quantifying the attached cells present within the scaffolds after an initial 24 h period. All scaffold compositions showed mean attachment efficiencies of >50% (Fig. 3.8). The w/Gel 0.25% scaffolds had a mean attachment percentage 65.34 ± 10.17%, followed by the Col 0.5% scaffold at 59.32 ± 16.14%, the w/Gel 0.15% with a mean attachment of 52.84 ± 9.14% and finally the Col-Gel-Hya scaffold with a mean attachment of 50.69 ± 8.63%. There were no statistical differences amongst the four compositions.
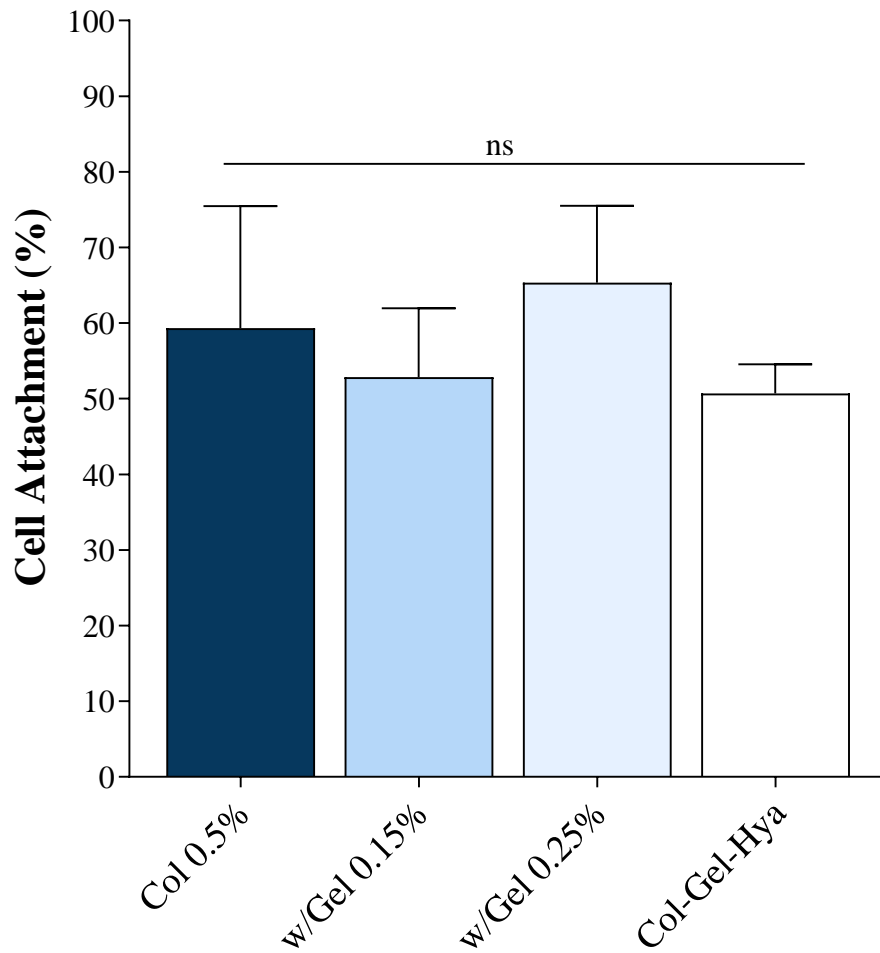
Figure 3.8: Cell attachment efficiency (%). Cellular attachment was assessed 24 h post-seeding. 1×10^5 MCF7s were seeded using a two-sided technique and using a cell number standard curve, percentage of cells adhered to the scaffold after 24 h was calculated. Variance was tested using one-way ANOVA with Tukey post-hoc test. Results shown are mean ± SD (n=5). p-value ≤0.05 = *, p-value ≤0.01 = **, p-value ≤0.001 = ***, ns = no significance.

3.3.4 DNA quantification

The Hoechst-based DNA quantification showed increasing DNA amounts as a function of time for all scaffold compositions (Fig. 3.9). This indicates that cells are actively proliferating within the scaffolds. Unlike the alamarBlue assay (Fig. 3.6 and 3.7), DNA quantifications can directly indicate proliferating cells as DNA content can only increase if the number of cells increases. Discrepancies between results of metabolic based assays and DNA quantifications can occur, with overestimations of cell proliferation in metabolic assays possible [368]–thus DNA quantifications are a more accurate barometer of cell proliferation within this thesis.

All four scaffold compositions demonstrated a significant increase in DNA amount for the 3-week study (p-value ≤0.001 for Day 1 vs. Day 7, Day 14 and Day 21 for all four groups, (Fig. 3.9). In terms of raw totals, there were no differences (p-value >0.05) amongst the four compositions at any of the five timepoints (Fig. 3.10). By Day 21, all four compositions had mean DNA amounts per scaffold of 20 µg or greater. When looking at DNA quantities through relative changes (i.e., proliferation rates), calculated by comparing the relative change of DNA amounts at each timepoint relative to Day 1), there were no differences in the rate of change of DNA amount per scaffold amongst the four groups at any timepoint (Fig. 3.11). At Day 21, the relative change in quantity compared to Day 1 across all groups were in the range of ~55-75 fold-increases. Overall, all four compositions had similar rates of DNA increase across the full 4-week period.
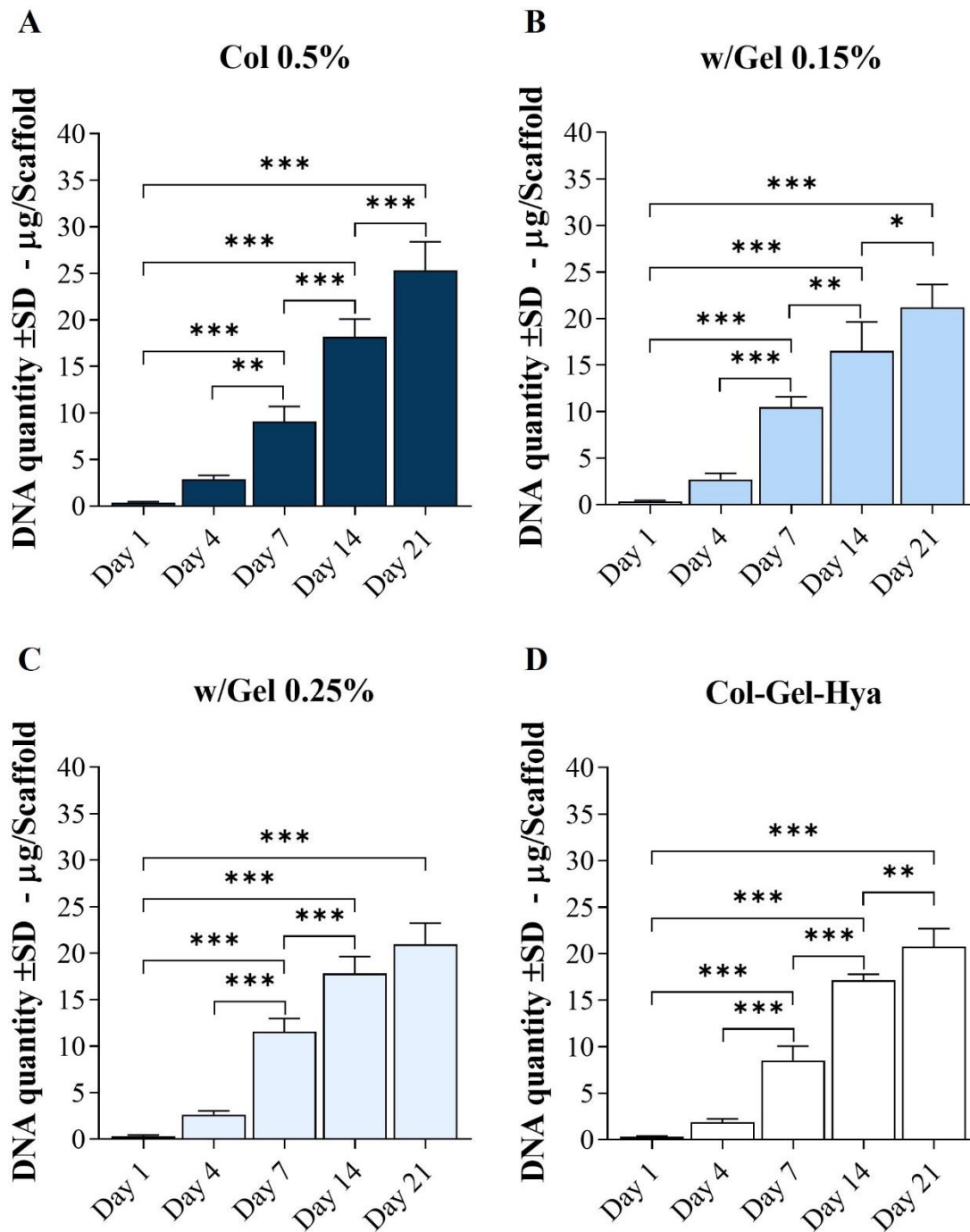
Figure 3.9: Raw quantification of DNA from 3D scaffolds. Cells were seeded onto scaffolds for a three-week timeframe. Scaffold/Cell constructs were then digested via papain enzyme, with DNA quantified using the HOECHST-based fluorometric assay. **(A)** Col 0.5% **(B)** w/Gel 0.15% **(C)** w/Gel 0.25% and **(D)** Col-Gel-Hya. Variance was tested using one-way ANOVA with Tukey post-hoc test. Results shown are mean ± SD (n=4). p-value ≤0.05 = *, p-value ≤0.01 = **, p-value ≤0.001 = ***.
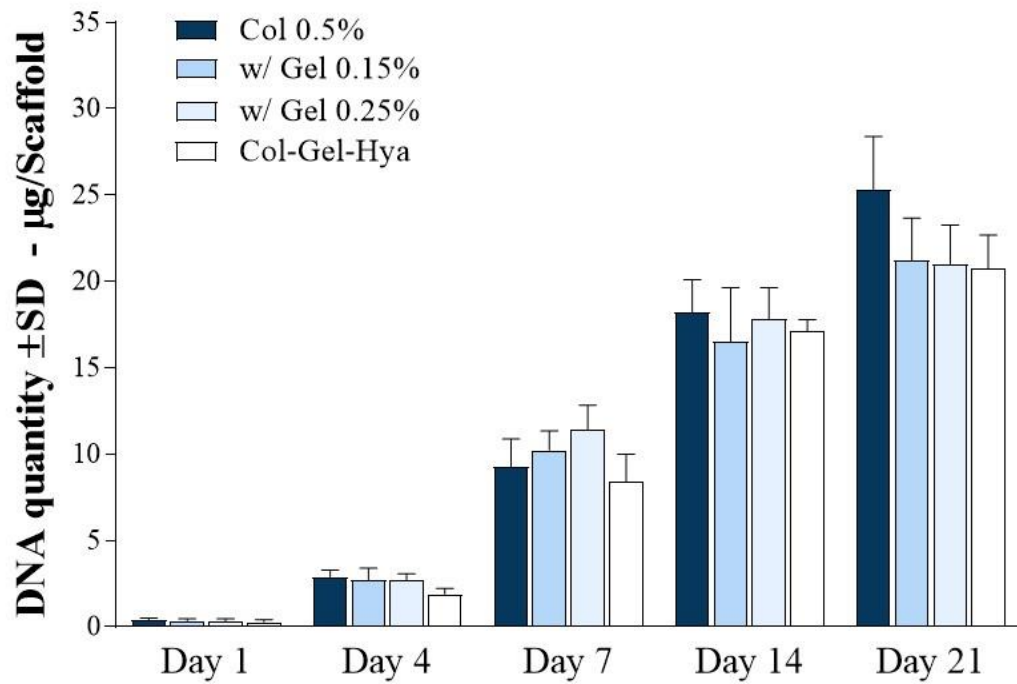
Figure 3.10: Raw quantification of DNA from 3D scaffolds (grouped). Cells were seeded onto scaffolds for a two-week timeframe. Scaffold/Cell constructs were then digested via papain enzyme, with DNA quantified using the HOECHST-based fluorometric assay. At all timepoints (Day 1, Day 4, Day 7, Day 14 and Day 21) there were no differences across the four compositions in terms of raw DNA amounts per scaffold. Variance was tested using two-way ANOVA with Tukey post-hoc test. Results shown are mean $\pm$ SD (n=4).
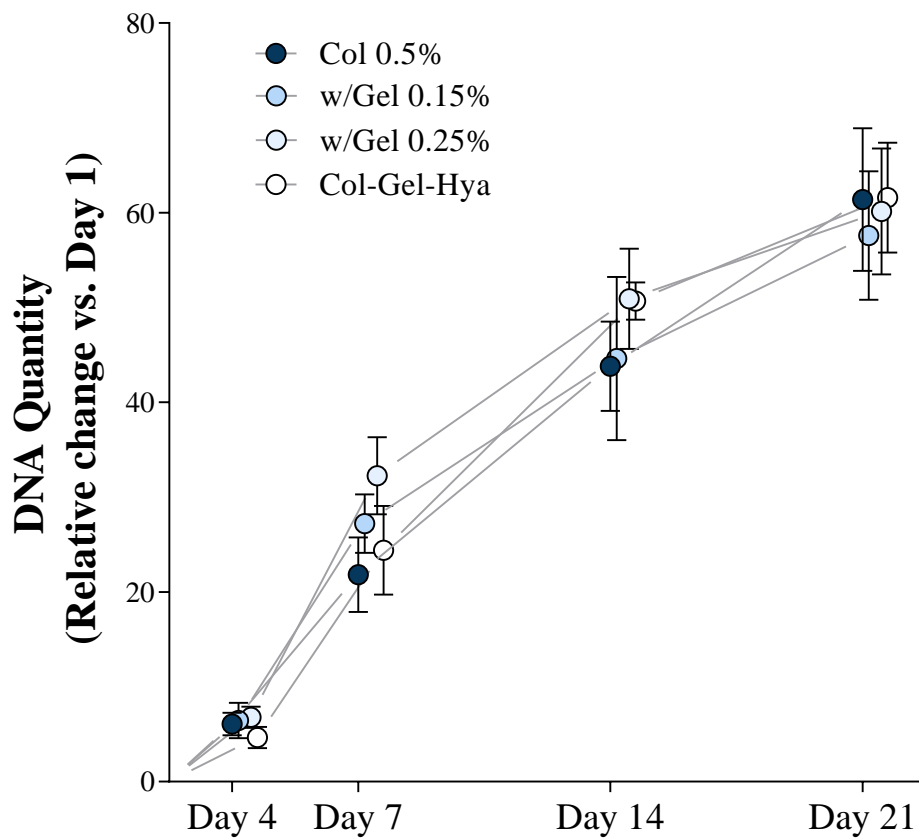
Figure 3.11: DNA quantity (relative change vs. Day 1). Cells were seeded onto scaffolds for a two-week timeframe. Scaffold/Cell constructs were then digested via papain enzyme, with DNA quantified using the HOECHST-based fluorometric assay. For assessing proliferation rates, the relative change of DNA amounts versus Day 1 (initial value) for each respective timepoint (final value) was calculated. Variance was tested using two-way ANOVA with Tukey post-hoc test. Results shown are mean $\pm$ SD (n=3).

3.3.5 Cell morphology analysis

SEM analysis of dehydrated scaffold demonstrated MCF7 cells attached and proliferating for all scaffold compositions (examples in Fig. 3.12 A-D). Both rounded globular cells and also flat elongated cells were clearly visible throughout the porous architecture. At Day 1, cells grew in an isolated fashion, though clusters of cells in spheroid-like formations were already visible at this timepoint (Fig. 3.12 E-F). The majority of cells were observed at the periphery surfaces–where cell clusters were also observed. At locations further into the scaffolds, cells were more isolated. At Day 14, there was an increase in cells observed across the four compositions throughout the scaffold structure. Many more clusters of cells were seen, with some very densely populated cell structures observed (Appendix 3.1). There was an apparent increase in cells in the central regions of the scaffolds compared to the Day 1 counterparts. Alongside cell proliferation and cell-cell interactions, cell-matrix interactions were observed through lamellipodia interaction with the collagen surfaces (Fig. 3.12 G-H). No morphological or growth pattern differences were observed between the four scaffold compositions at either Day 1 or Day 14.
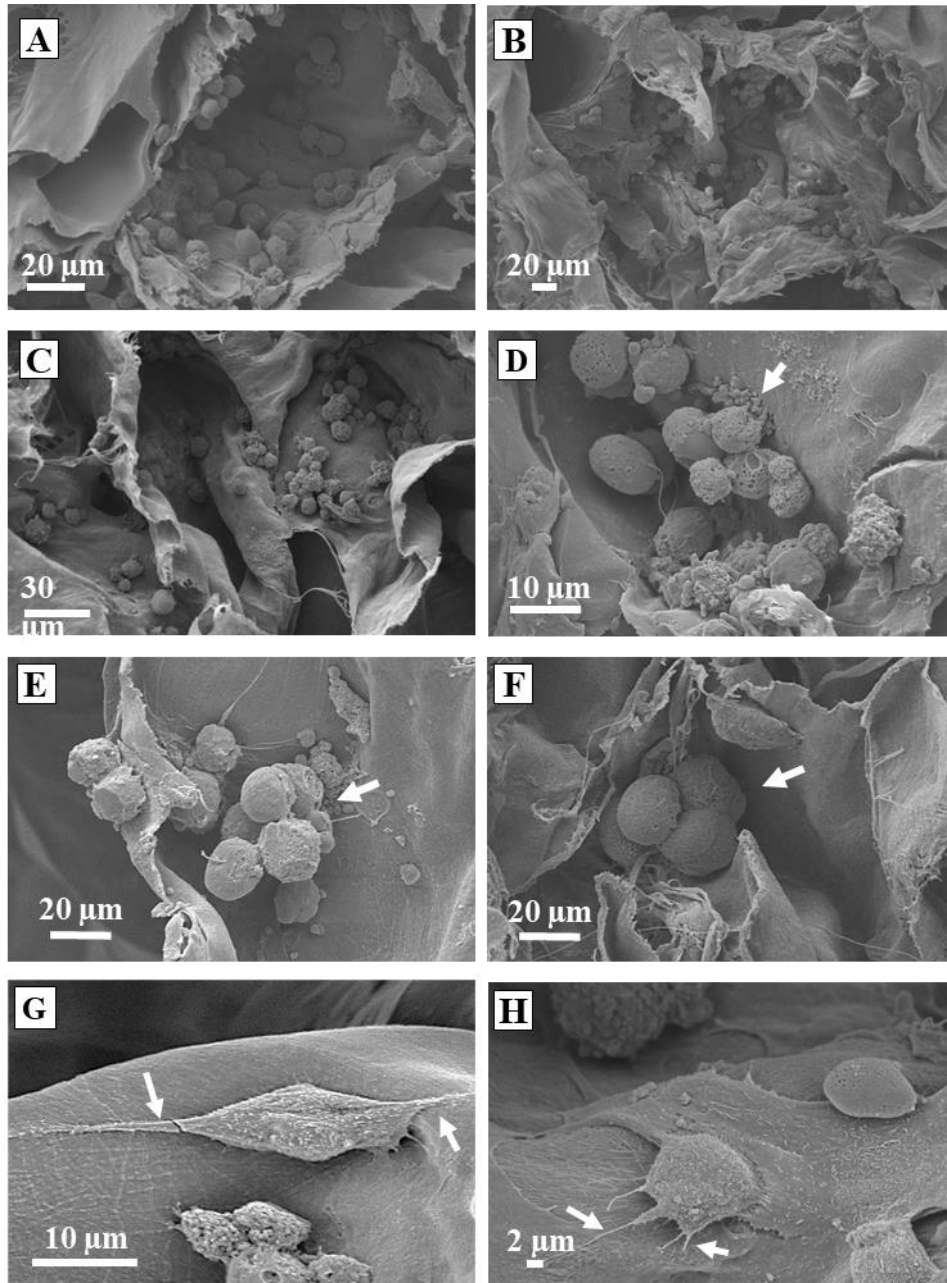
Figure 3.12: SEM imaging of dehydrated cell/scaffold constructs. (**A-CD**) General attachment of MCF7 cells on pore walls was observed (image shows A) w/Gel 0.15% at Day 14, B) w/Gel 0.25% at Day 14, C) Col-Gel-Hya at Day 14). (**D**) Cell cluster observed at Day 14 (white arrow, Col 0.5% scaffold). (**E-F**) The formation of spheroid-like cell aggregates (white arrow) was observed within the Col 0.5% (E) and Col-Gel-Hya (F) scaffolds, both at Day 1, indicating 3D cell-cell interactions in a short timeframe. (**G-H**) Cell-matrix interactions were observed with cell lamellipodia seen interacting with the collagen pore surface (white arrows) (image shows (**G**) w/Gel 0.15% scaffold at Day 14 and (**H**) Col-Gel-Hya at Day 14.

3.3.6 Cell infiltration and migration analysis

Infiltration/migration analysis via DAPI staining of cell nuclei provides qualitative confirmation of successful cell attachment and proliferation within the scaffolds (Fig. 3.13 – Fig. 3.17). At Day 1, across all four compositions, many cells were located near the top and bottom surfaces of the scaffold – the points at which cells were originally seeded. The Col 0.5% scaffold had less cells populating the central regions of the scaffold at Day 1 compared to the w/Gel 0.15%, w/Gel 0.25% and Col-Gel-Hya compositions. These groups had superior infiltration of cells towards the centre of the scaffolds. The Col-Gel-Hya scaffolds had the best observed distribution of cells, with an even spread of cells throughout the entire depth of the scaffold already at Day 1. By Day 14, an increase in cells was observed across all compositions, including an increase in infiltration to the centre of the scaffold in the Col 0.5% group, bringing it more in line with the other four compositions. The greatest cell numbers remained on the peripheral surfaces of the scaffolds across all four groups. Unseeded scaffolds (one example shown in Fig. 3.17) confirmed the fluorescence observed in seeded constructs were cells, as the unseeded controls produced no visible DAPI fluorescence.
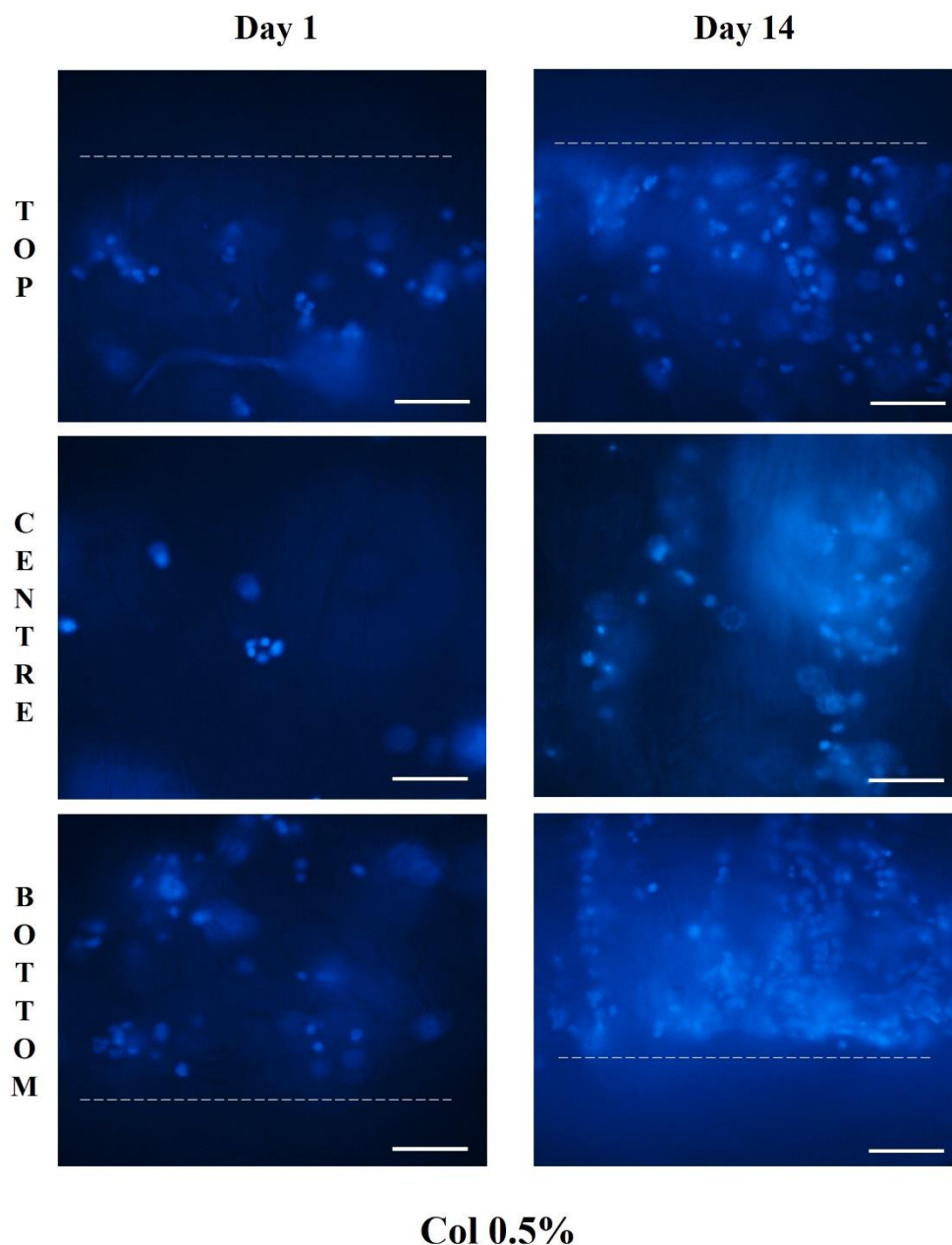
Figure 3.13: DAPI staining of Col 0.5% scaffold. At Day 1, imaging demonstrated many cells at the peripheral regions, both top and bottom surfaces, of the Col 0.5% composition. Cell numbers were more sparse towards the centre region of the scaffolds. At Day 14 the Col 0.5% scaffolds had higher levels of cells present throughout the scaffolds, including a notable increase in cells within the central region of the scaffolds. Scale bar represents 100 μm. White dotted lines indicate the scaffold edge/periphery.
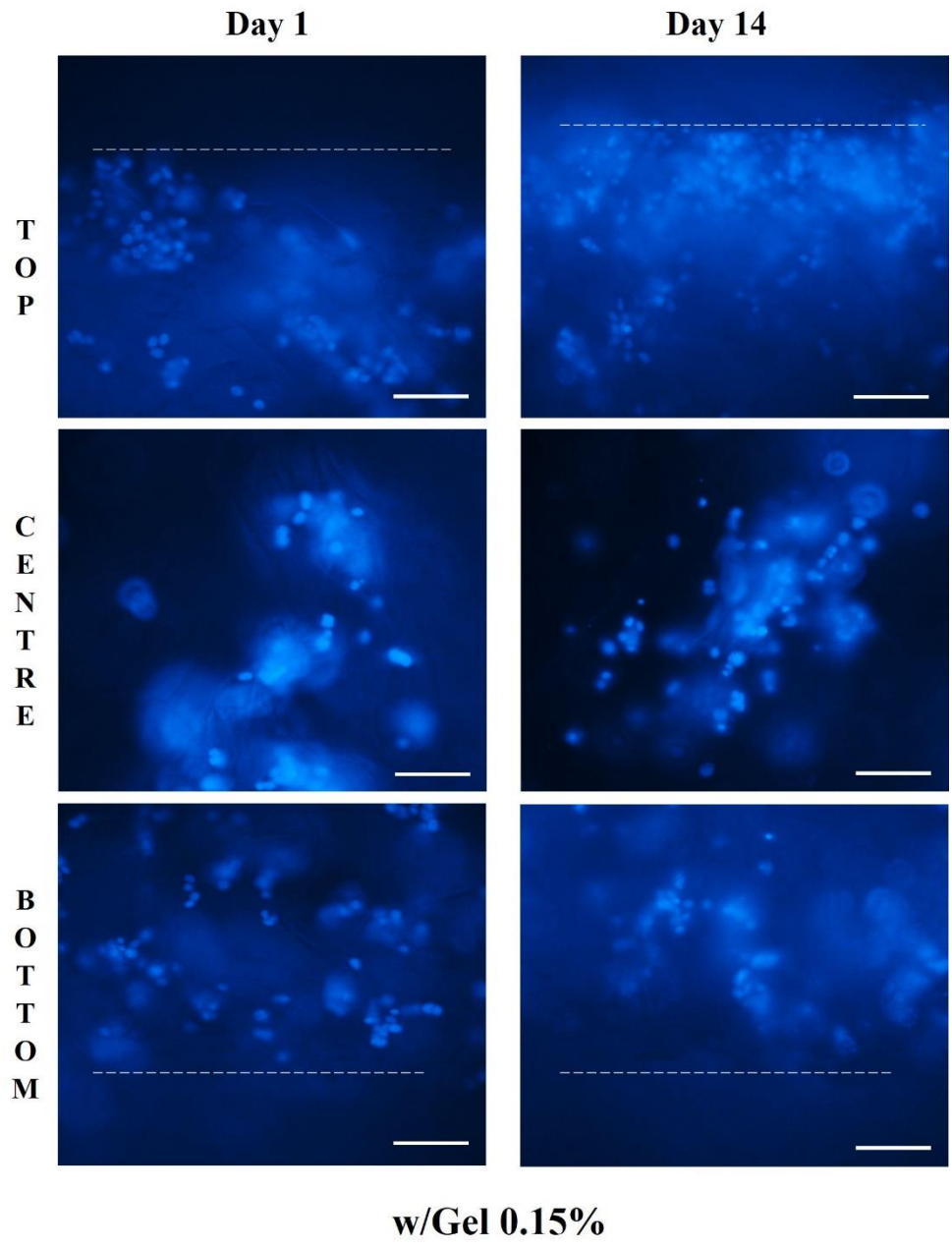
Figure 3.14: DAPI staining of w/Gel 0.15% scaffold. At Day 1, imaging demonstrated many cells at the peripheral regions, both top and bottom surfaces, of the w/Gel 0.15% composition. More cells were visible in the central region of the scaffolds compared to the collagen only (Col 0.5%) scaffold already at Day 1. At Day 14 the w/Gel 0.15% scaffolds had a higher level of cells present throughout the scaffolds. Scale bar represents 100 µm. White dotted lines indicate the scaffold edge/periphery.
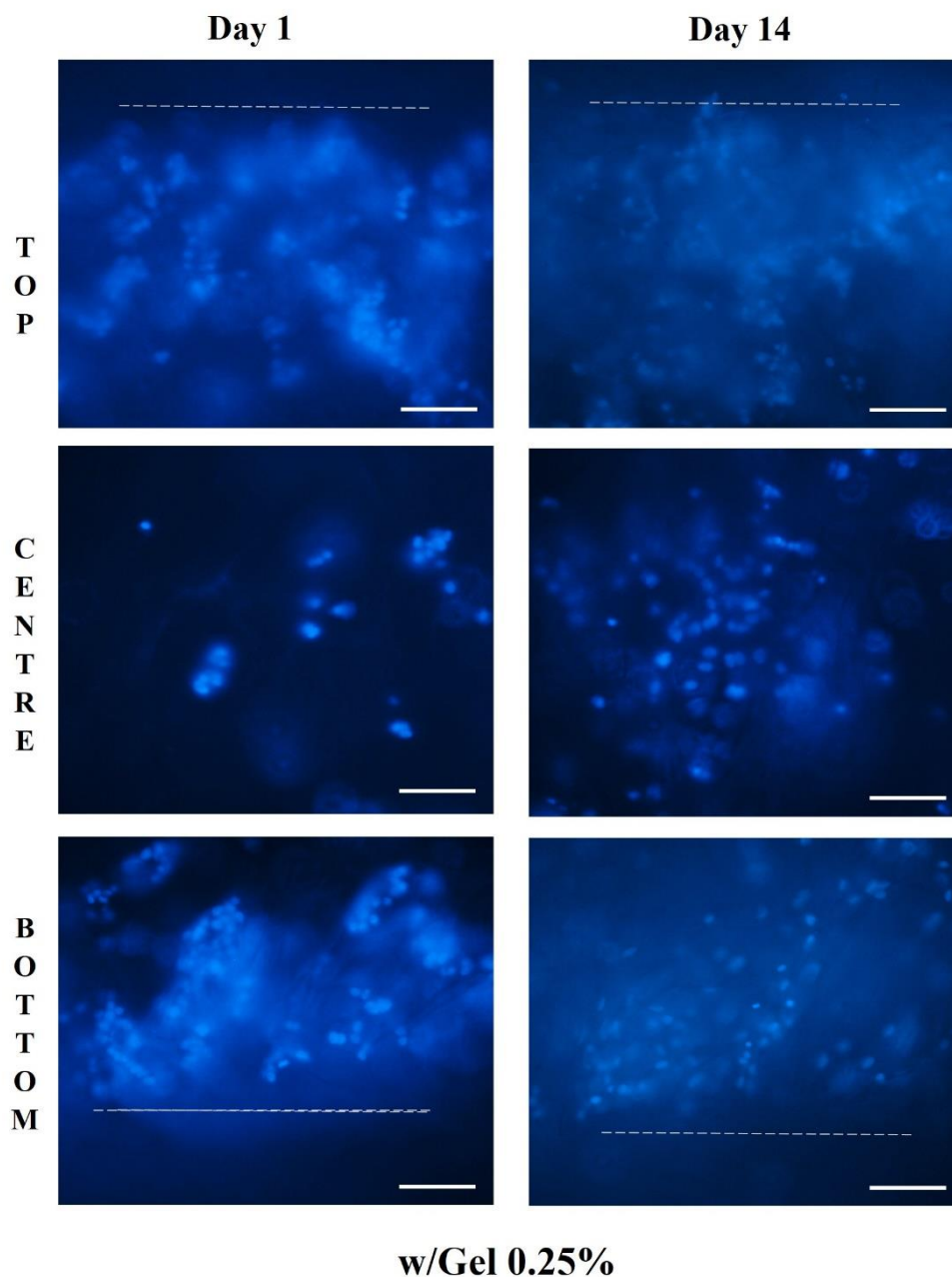
Figure 3.15: DAPI staining of w/Gel 0.25% scaffold after seeding. At Day 1, imaging demonstrated many cells at the peripheral regions, both top and bottom surfaces, of the w/Gel 0.25% composition. At Day 14 the w/Gel 0.15% scaffolds had a higher level of cells present throughout the scaffolds. Scale bar represents 100 µm. White dotted lines indicate the scaffold edge/periphery.

Day 1   **Day 14**

T O P

C E N T R E

B O T T O M
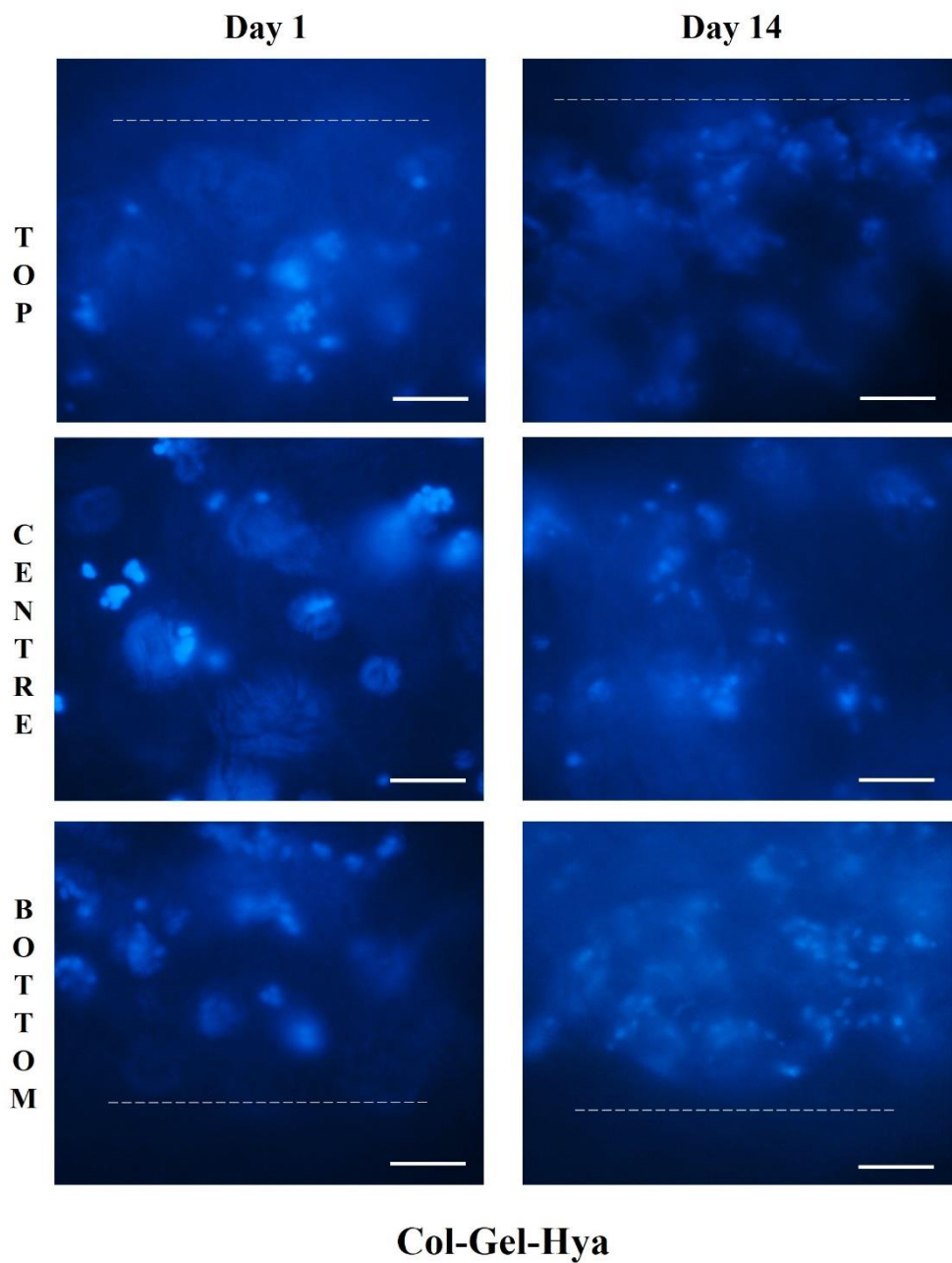
Col-Gel-Hya

Figure 3.16: DAPI staining of Col-Gel-Hya scaffold. At Day 1, imaging revealed an even distribution of cells throughout the scaffold. At Day 14, the scaffolds had a higher level of cells present throughout the scaffolds. Scale bar represents 100 µm. White dotted lines indicate the scaffold edge/periphery.

Day 1   **Day 14**

T O P

C E N T R E

B O T T O M
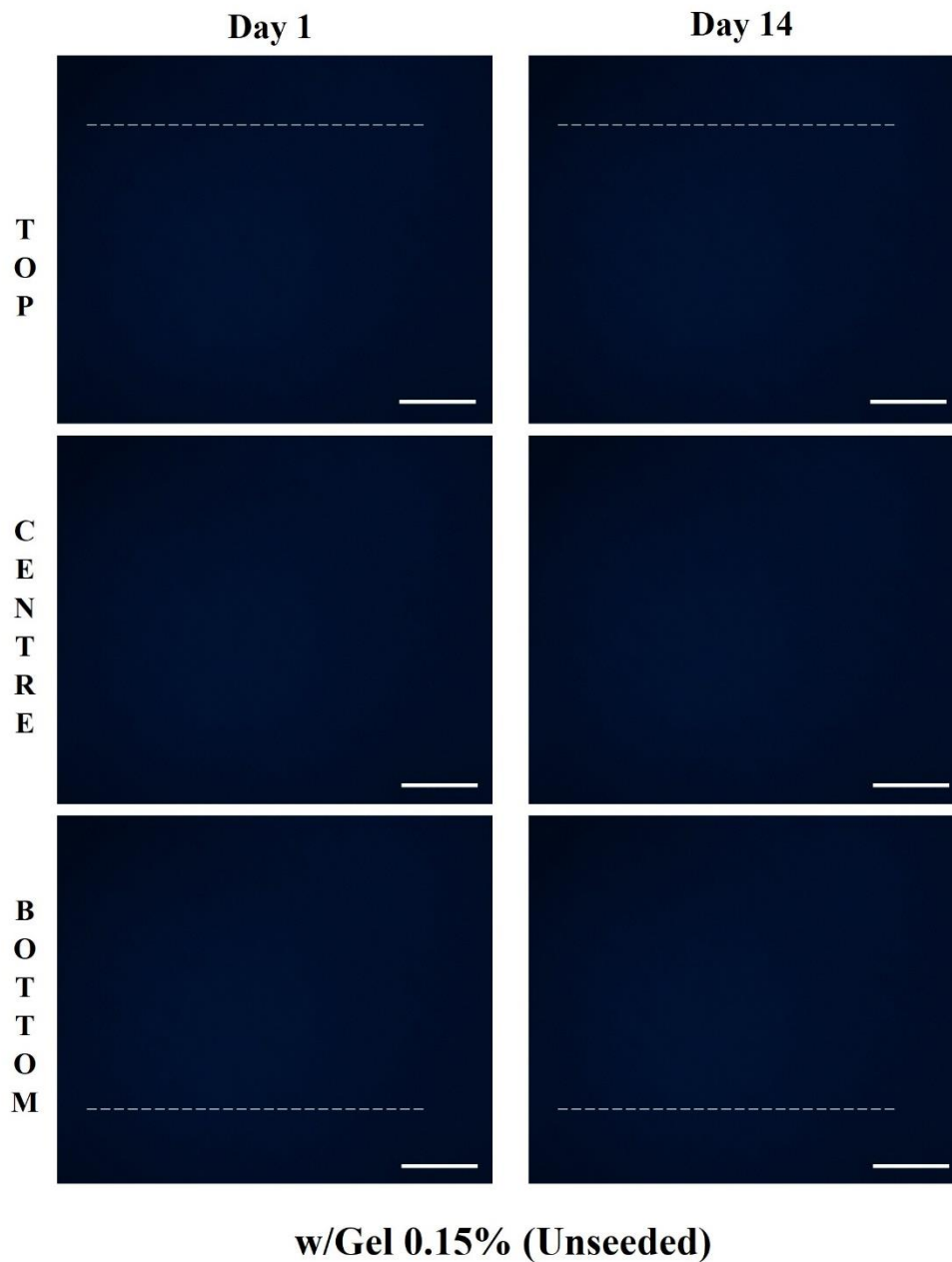
w/Gel 0.15% (Unseeded)

Figure 3.17: Example of DAPI stained unseeded w/Gel 0.15% scaffold. Unseeded control revealed low background autofluorescence of the scaffold. Unseeded scaffolds were used as comparators to make identification of fluorescence generated by cells on the scaffolds easier. Scale bar represents 100 µm. White dotted lines indicate the scaffold edge/periphery.

3.4 Discussion

This chapter aimed to assess the biocompatibility of the various collagen-based scaffolds and their ability to support breast cancer cell attachment and proliferation. The ideal culture model for cancer cells would allow for initial cell attachment and subsequent sustained cell growth and proliferation over multiple weeks to allow for long-term analysis of cell behaviour within the scaffolds. Studies began using all six previously fabricated scaffolds, though after initial cell studies (cytotoxicity, viability and alamarBlue) and the data from the previous physical and structural characterisations, four compositions were selected for further assessment. This chapter also aimed to assess the effect of the addition of gelatin or hyaluronic acid to the scaffold in terms of cell biocompatibility and ultimate performance.

Biocompatibility assessments firstly confirmed that the scaffold materials themselves did not constitute any cytotoxic effect towards breast cancer cells (Fig. 3.3). Cytotoxicity testing via ISO 10993-5 revealed no adverse effects of the crosslinked scaffold extracts on MCF7 cells grown in 2D. The use of EDAC may be cytotoxic to cells if traces of the chemical remain in the 3D scaffolds [211]. Results indicate that the proposed washing procedures were effective, and no crosslinking agent remnants were present in the final scaffold. Furthermore, there were no adverse issues relating to the acetic acid, collagen, gelatin or hyaluronic acid used for fabricating the scaffolds, as expected. Supplementing this cytotoxicity data, the growth and proliferation of cells when cultured directly within all four scaffold compositions at the Day 2 timepoint was confirmed. Viability was observed to decrease as a function of time, to ~70% at Day 7 and ~50% on Day 14 (Fig. 3.5). This decrease over time was largely expected due to increasing confluency within the scaffold and also features like necrotic regions/hypoxia developing within cellular aggregates which

contribute to cellular death [186,369,370]. The lack of a scaffold vascular network results in an eventual strain on cells due to the development of low oxygen niches, and without this vascular network to replenish oxygen levels, apoptosis will occur [371]–though in the context of replicating the tumour environment, the provision of hypoxic/necrotic niches within the *in vitro* scaffolds mimics the generation of hypoxic/necrotic regions within breast cancer tumours thus improving the biological relevance of the model. A previous study by Liverani *et al.* (2019) reported that MCF7 cells grown on a similar collagen 3D scaffold (type 1 collagen, 1% (wt/v), freeze dried scaffold, 85% porosity) saw a reduction in viability to ~20-30% after 10 days of culture, with a parallel increase in apoptotic cells and expression of hypoxia markers [186]. This decrease in viability is larger than observed herein. Of interest, Liverani *et al.* (2019) noted that the more aggressive breast cancer cell line, MDA-MB-231, showed preferential migration towards the peripheral regions of the scaffold, away from the regions of low oxygen that were observed in the central region of the scaffold. The lowly-invasive MCF7 cells did not show the same behaviour, and as such saw apoptosis rise instead of the possible escape mechanism of migrating towards the oxygen source [186]–such a phenomenon likely contributed to a similar decrease in viability within our 3D system also using the lowly-invasive MCF7 cell line. The initial cell proliferation studies used the alamarBlue assay to assess the metabolic activity of MCF7 cells within all six scaffold compositions over a 7-day period (Fig. 3.6). A sustained and continually increasing reduction of the alamarBlue dye was observed. A slight increase in alamarBlue reduction upon addition of gelatin to the scaffolds was observed at Day 4, however no such differences in reduction were observed at either Day 1 or Day 7, thus the impact of gelatin or hyaluronic acid on cell metabolic activity was considered negligible. The above biological studies, alongside results from Chapter 2, led to the selection of four scaffold compositions to

continue to more detailed biological assessments with – the Col 0.5%, w/Gel 0.15%, w/Gel 0.25% and Col-Gel-Hya scaffold compositions.

MCF7 cells adhered readily to the scaffolds, with cell attachment efficiencies for the four selected scaffold compositions ranging from 40-70% (Fig. 3.8). These values compare favourably to reported cell attachment rates for similar collagen scaffolds, albeit not with cancer cells [213,309]. In these studies, a mean attachment of ~30% was achieved in a 0.5% (wt/v) collagen scaffold (with an additional 0.05% (wt/v) chondroitin-6-sulfate) of a mean pore size of 190 µm (MC3T3-E1 cells, pre-osteoblastic cell line) [309] and a mean attachment of ~40% was achieved in a 0.5% (wt/v) collagen scaffold (with an additional 0.044% (wt/v) chondroitin-6-sulfate) of a mean pore size of 120 µm (MC3T3-E1 cell line) [213]. A high level of cell attachment is crucial as a low successful seeding density can impact cell growth and behaviour [372,373]. Furthermore, low attachment can impact experimental procedures, such as PCR analysis, due to low DNA/protein yields in the early days of culture. It was hypothesised that the addition of gelatin to the collagen scaffolds would enhance cellular attachment by increasing cell attachment sites [360,361]. While the attachment levels were highest in the w/Gel 0.25% scaffold (max gelatin concentration), no significant difference in cellular attachment was observed between the four scaffolds groups in the two-sided seeding approach. Therefore, there was no benefit of gelatin addition to the collagen-only scaffold base in terms of increasing cell attachment. In addition, in aforementioned instances of gelatin addition improving cell attachment and proliferation in §3.1, it must be acknowledged that the primary scaffold materials included materials such as chitosan [359] and alginate [356]. While both materials are considered biocompatible, alginate and chitosan are known for a lack of or low level of cell adhesion when used as a single scaffold material, thus they are normally functionalised or improved through

incorporation of secondary scaffold materials with superior biological properties [374,375]. In our case, the use of collagen as the primary scaffold material, which is noted for its excellent biocompatibility and cell adhesion properties [322,352], may negate potential benefits of gelatin addition because collagen alone is sufficient to reach the maximum achievable level of initial cell adhesion within the collagen-based scaffolds fabricated.

A significant and continuously increasing reduction of the alamarBlue dye was observed when the proliferation period was extended to 14 days, thus suggesting constant proliferation of the MCF7 cells within the scaffolds (Fig. 3.7). The physical properties of the scaffold, or the incorporation of gelatin/hyaluronic acid did not affect cell activity. In the 2D culture comparator group, cells rapidly reached over-confluency within six days with substantial levels of floating dead cells observed. It has been previously reported that cells growing in 3D proliferate at a slower rate in comparison to the same cells in 2D. Liverani *et al.* (2019) observed similar whereby MCF7 cells cultured in 2D demonstrated a rapid increase in cell number from Day 1 to Day 7), significantly greater than 3D cultured MCF7 cells, before reaching confluency and undergoing growth arrest and ultimately apoptosis [186]. Similarly, MCF7 cell proliferation was significantly higher in 2D culture compared to 3D culture within collagen type 1 hydrogels. Cell doubling time was found to be ~96 h in 3D and 30-36 h in 2D–a three-fold increase [376]. While the 2D cultured cells showed increased alamarBlue reduction in the first two timepoints compared to 3D cultures, the culture span of cells growing in 2D is limited based on the surface area of the culture dish/flask in use. Once cells are confluent, they must be subcultured. This is an advantage of the 3D scaffolds that developed herein, with the provision of a more prolonged period of continuous expansion of cells within the scaffolds allowing for long-term investigations without the need for subculture. Longer culture periods may be beneficial when looking at long-term

gene or protein expression patterns within 3D cell cultures or culturing cells for longer durations in 3D prior to drug exposure. DNA quantification assessments offer a more accurate method to confirm increasing cell numbers with the scaffolds compared to cell metabolic activity assays (due to the ability of non-dividing but metabolically active cells to reduce dyes involved in metabolic assays such as the alamarBlue) [368]. Overall, the study once again confirmed the successful attachment and proliferation of breast cancer cells on the scaffolds over 21 days (Fig. 3.9). As with the previous alamarBlue data, proliferation rates were greatest during the initial period of culture and reduced thereafter, with no apparent effect of the addition of gelatin or hyaluronic acid observed. Previously, it was observed that cell viability in 3D dropped during the 14-day culture period. However, the reported DNA quantifications revealed continuous expansion of cell numbers within the scaffolds despite the increase of apoptosis/cell death. Taking into account the above results, the hypothesis that the addition of gelatin or hyaluronic acid could improve the attachment and proliferation of MCF7 cells was disproven. Perhaps it is a case that the gelatin or hyaluronic acid concentrations need to be increased to higher levels. Also, it may be a point of future work to alter physical properties of the scaffold (e.g., pore architecture and elastic modulus) in a more significant manner. Fabricating scaffolds with vastly different physical properties would conclusively determine if these altered physical properties, with a greater magnitude of difference than in this research, have more complex cellular effects in terms of cell proliferation.

A major advantage of 3D culture systems is their greater resemblance to *in vivo* cancer cell morphology and behaviour. Formation of spheroid-like aggregates within the scaffolds is a positive result as it highlights the superior cell-cell interactions seen in 3D in comparison to 2D cultures (Fig. 3.12). Elsewhere, Liverani *et al.* (2022) observed MCF7 forming round

clusters upon culture within a freeze-dried collagen scaffold [355]. Spheroids have been documented to develop hypoxic cores [377,378], a feature of solid tumours in humans that plays a significant role in disease progression and spread [379] – thus their replication in a 3D scaffold is an attractive feature as it paves the way for research into hypoxia in a 3D *in vitro* setting. In addition, cell-matrix interactions were also observed within the scaffolds, which again demonstrates an advantage over 2D culture. DAPI staining showed successful infiltration of cells throughout the full depth of all four scaffolds after 14 days (Fig. 3.13 – 3.17). Both the addition of gelatin and hyaluronic acid appeared to have a beneficial impact on infiltration, as the Col 0.5% scaffold had the lowest observed levels of cells in the central regions of the scaffold at Day 1 – though the passing of time seemed to negate this feature as by Day 14 there were no issues with infiltration in this scaffold. The Col-Gel-Hya scaffolds in particular had many clusters of cells observed at the centre of the scaffold after just 24 h of culture, suggesting the addition of hyaluronic acid does indeed improve cell infiltration, as seen elsewhere [362]. Successful infiltration is a positive feature here as other 3D scaffolds have reported challenges in achieving cell migration throughout scaffolds, with dense layers of cells forming in the peripheral regions of scaffolds [380,381]. Providing a scaffold that cells can freely migrate through opens up potential for research into the various genetic processes involved in cancer cell migration, and the interplay between the scaffold mechanical and architectural properties.

3.4.1   Concluding remarks

The developed scaffolds demonstrated excellent biocompatibility. The attachment studies exhibited promising levels of cell attachment for all four scaffold groups evaluated, with MCF7 cells readily adhering throughout the scaffold. DNA quantifications alongside alamarBlue assays highlighted the continuous proliferation of cells over a 21-day period. Provision of a 3D scaffold, demonstrating a porous and interconnected network, allowed for the MCF7 cells to adopt a rounded morphology that is more representative of their *in vivo* cell morphology. Additionally, the cells were observed to grow as spheroid-like clusters, demonstrating enhanced cell-cell interactions than seen in the 2D culture studies. Cells were observed to migrate throughout the scaffold irrespective of composition. In summary, irrespective of composition, the developed scaffolds represent excellent biomimetic, biocompatible and functional templates for the investigation of more complex breast cancer processes, gene expression patterns and applications in therapeutic assessment.

04

Chapter 4: Assessment of Gene Expression of Breast Cancer Cells in Collagen-Based Scaffolds
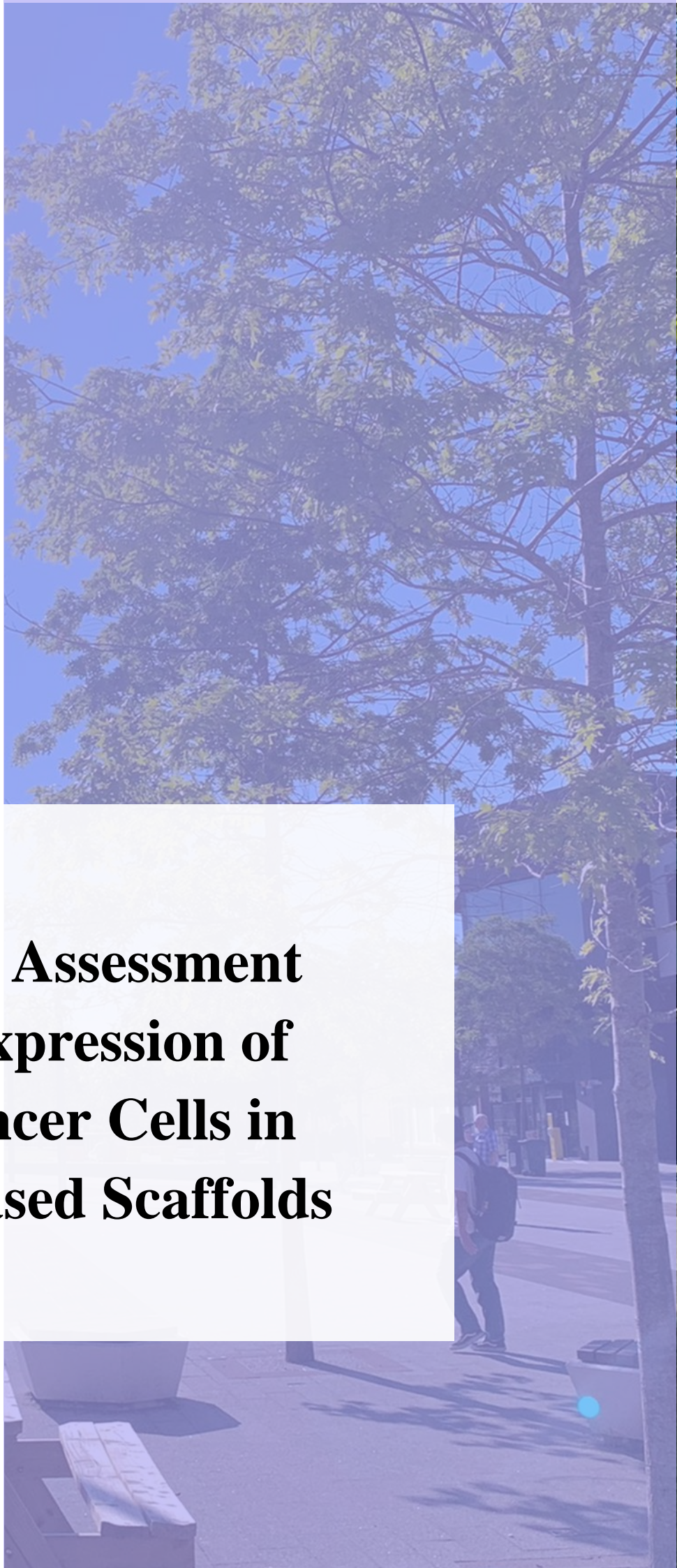
Table of Contents

4.1 Introduction

3D culture of cells has been shown to result in cell behaviours and expression patterns that differ significantly from 2D culture and more closely resemble *in vivo* tumours [382,383]. Within the literature, it has been observed that expression patterns differ between 3D and 2D cultures across a range of targets [186,194,384], and these differences often demonstrate a more phenotypically relevant model with the 3D cultures. Within this chapter the gene expression of the breast cancer MCF7 cells grown in 2D compared to the 3D collagen-based scaffolds, as developed in Chapter 2 and 3, was investigated. As no sizeable or significant differences in physical or biological performance were found between the different scaffold compositions in Chapters 2 and 3, it was not anticipated that scaffold composition would drive significant differences in cell behaviour in terms of gene expression that would warrant the use of multiple scaffold compositions. Therefore, for the study described within this chapter, a single scaffold composition was selected from the previously used four groups in the cellular studies in Chapter 3. The composition group selected was w/Gel 0.15% as it demonstrated good architectural and physical properties (Chapter 2) and strong cell attachment, infiltration and continuous proliferation for a 3-week period (Chapter 3). It is not without possibility that gene expression may differ amongst the different scaffolds, the primary objective of the chapter was to assess any expression differences between 3D scaffold culture and 2D culture.

Extracellular matrix (ECM) modification [4,80–82,86–89], ECM component synthesis [48,57,392,58,385–391], angiogenesis [393–397], glycolysis [398–406] and hypoxia [407–414] are crucial processes involved in breast cancer development, progression and ultimate spread (metastasis). These hallmarks of cancers are of high importance to replicate within

an *in vitro* 3D culture model to demonstrate these models can acquire the same increased expression of genes associated with these hallmarks that is seen *in vivo*–and notably is not seen in 2D cultures. A panel of 15 targets consisting of genes involved in the aforementioned processes were selected. The selected targets and their relevance to breast cancer are summarized in Table 4.1.

Table 4.1: Selected gene targets and role in breast cancer.

Target	General function and link to breast cancer
Matrix metalloproteinase -2 (*MMP2*) [86–89]	*MMP2* encodes an enzyme that is involved in the breakdown of the ECM, notably collagen type I and IV (basement membrane). As such, MMP2 may play a role in metastatic spread in breast cancer.
Matrix metalloproteinase -2 (*MMP9*) [86–89]	*MMP9* encodes an enzyme that is involved in the breakdown of the ECM, notably collagen type IV. Similar to MMP2, *MMP9* may play a role in metastatic spread in breast cancer due to the ability to degrade the basement membrane, an essential barrier to cancer cell migration.
Lysyl oxidase (*LOX*) [4,80–82]	*LOX* encodes an enzyme which crosslinks ECM components such as collagen and elastin. This increases ECM stiffness which is associated with breast cancer progression.
Collagen type I alpha 1 chain (*COL1A1*) [48,57,58,385,386]	*COL1A1* encodes for a major portion of the full collagen type I molecule. Collagen is the major component of the breast ECM and dysregulation of collagen within the breast ECM plays a key role in breast cancer.
Fibronectin 1 (*FN1*) [48,385,387,388]	*FN1* encodes for fibronectin, a major glycoprotein of the ECM. Fibronectin interacts with collagen but also modulates key signalling pathways that mediate adhesion, migration and proliferation. FN1 is overexpressed in breast cancer.

Hyaluronan synthase 1/2 (*HAS1/HAS2*) [389–392]	*HAS1/2* code for two of three enzymes responsible for hyaluronan/hyaluronic acid synthesis. Hyaluronic acid is a glycosaminoglycan which has size dependent interactions with other proteins and receptors. Hyaluronic acid is highly upregulated in breast cancer tissue compared to healthy tissue.
Vascular endothelial growth factor A (*VEGFA*) [393–395]	*VEGFA* encodes for a glycoprotein which plays a role in cell migration, proliferation and angiogenesis. *VEGFA* is highly expressed in breast cancer cells and plays a crucial role in angiogenesis, which is key for continued survival and progression of breast cancer tumours.
Transforming growth Factor beta 1 (*TGFB1*) [396,397]	*TGFB1* encodes for a multi-function cytokine with roles in general cell activity such as proliferation, differentiation and apoptosis but also in wound healing, cancer and angiogenesis and epithelial-to-mesenchymal transition (EMT). *TGFB1* has been found at elevated levels in breast cancer patients.
Jagged 1 (*JAG1*) [415–417]	*JAG1* codes for a key cell surface ligand, which interacts with the notch receptor family. Notch signalling is crucial in many aspects of cell differentiation across multiple cell/tissue types. Overexpression of *JAG1* in breast cancer (and resulting dysregulated Notch signalling) has been observed and is associated with a poor prognosis.
CXC chemokine receptor type 4 (*CXCR4*) [418–420]	*CXCR4* encodes a chemokine receptor, which upon ligand binding plays a role in cell migration and movement. High *CXCR4* expression has been linked to metastasis in breast cancer and a poorer patient outcome.

Glyceraldehyde 3-phosphate dehydrogenase (*GAPDH*) [398–401]	*GAPDH* encodes for an enzyme, which plays a key role in glycolysis but also other non-metabolic activities. Elevated *GAPDH* expression has been recorded in breast cancer and is linked to a poor prognosis and disease progression.
Glucose transporter 1 (*GLUT1*) [402–406]	*GLUT1* codes for a uniporter protein which assists in the transport of glucose across the plasma membrane. As such it has links to glycolytic pathways and is involved in many cancers. *GLUT1* is upregulated in breast cancer and again is associated with a poor disease prognosis.
Endoplasmic reticulum oxidoreductase 1 alpha (*ERO1A*) [407–409]	*ERO1A* encodes an endoplasmic reticulum-based protein involved in protein refolding. *ERO1A* expression is induced by hypoxia thus serves as a novel biomarker for this feature. Its high expression in breast cancer is linked with a poor prognosis.
Hypoxia-inducible factor 1-alpha (*HIF1A*) [410–414]	*HIF1A* encodes for a subunit of the HIF1 transcription factor protein. HIF1 plays a key role in cell responses to oxygen levels (thus linked with tumour adaption to hypoxia). High levels of *HIF1A* expression in breast cancer patients is associated with increased metastasis thus a poorer outcome.

Note: Gene and protein nomenclature and formatting in the above table and elsewhere derived from HUGO Gene Nomenclature Committee (HGNC). Gene names use italics, to differentiate from the protein form (non-italic) [421].

Initial targets were selected for their involvement in modification or alteration of the ECM, which plays a key role in the development, progression and spread of breast cancer [5,48]. These targets were *MMP2*, *MMP9* and *LOX*. It was investigated if the 3D scaffolds would induce increased expression of these enzymes compared to 2D cultured cells, improving the biological relevance of the collagen-based scaffolds through demonstrating the high expression of ECM modifying genes which is also seen in *in vivo* tumours. These targets have previously been shown to have altered expression in 3D compared to 2D using MCF7 cells [186,194]. *MMP2* and *MMP9* code for enzymes belonging to the matrix metalloproteinase family and are involved in the breakdown of collagen type IV, the key component of the ECM basement membrane [48,86–89]. As such, they may play a key role in facilitating cancer cell migration away from the parent tumour and allow for metastasis to occur. Both *MMP2* and *MMP9* have been observed to be overexpressed in breast cancer tissue compared to non-cancerous breast tissue [86–89]. LOX enzymes promote the crosslinking of collagen within the ECM [80] and elevated *LOX* levels in patients are associated with poor overall survival in breast cancer [4,81,82]. Increases in collagen crosslinking result in stiffening of the ECM, and these stiffness increases are associated with increased tumour aggressiveness and metastasis [48,54,55,79].

Alongside genes involved in modifying the breast cancer ECM, a group of ECM component synthesising genes were investigated–including *COL1A1*, *FN1*, *HAS1* and *HAS2*. These genes are involved in the synthesis of collagen, fibronectin and hyaluronic acid, and each of these plays a significant role in breast cancer disease progression and spread. Of particular interest here is determining whether the 3D scaffold induces the production of ECM materials to a greater extent than in 2D culture, in a manner that is more analogous to *in vivo* tumours. As these materials are of high importance, it would be beneficial to have an *in vitro*

model that can promote their production. Collagen, as discussed in detail in Chapter 1, undergoes significant alterations within the tumour microenvironment [48,57,58]. Of key interest within this chapter is to assess if expression of *COL1A1* is increased under 3D culture, aligning with the *in vivo* increase of collagen deposition during cancer development and progression [385,386]. Fibronectin plays a key role in breast cancer due to its involvement in a multitude of signalling pathways that control adhesion, migration and proliferation [48,387]. *FN1* (codes for fibronectin) is overexpressed in breast cancer [385,388]. *HAS1* and *HAS2* are two of three isoforms that are involved in the synthesis of hyaluronic acid [389]. Hyaluronic acid is an ECM glycosaminoglycan that is overexpressed in many breast cancers and promotes a more aggressive phenotype and disease progression [390–392].

VEGFA, *TGFB1*, *JAG1* and *CXCR4* were next to be assessed. These genes have links to many general cell functions, such as proliferation, differentiation, migration and apoptosis, but also in more complex processes, like angiogenesis, metastasis and epithelial-to-mesenchymal transition (EMT). Vascular endothelial growth factor A (VEGFA) is known for its angiogenic properties and typically promotes more aggressive tumour growth and metastasis [393]. It is highly upregulated in breast cancer tissues and is a poor prognostic factor for patients [394,395]. *TGFB1* encodes a protein with a vast array of functions, governing cell proliferation, differentiation and apoptosis [396] but it is also known for its role (albeit paradoxical at times) in cancer, angiogenesis [397] and notably epithelial-to-mesenchymal transition (EMT) [422]. *JAG1* codes for a cell surface ligand which is closely involved with the notch receptor family [415]. Overexpression of *JAG1* has been observed in breast cancer and is associated with a poor prognosis [416,417], and also with metastasis to the bone [423], which is progression to an incurable form of breast cancer [300]. *CXCR4*

is overexpressed in many breast cancers and is associated with a poor prognosis [418,419]. It plays a key role in cell migration and movement and thus is linked to metastasis [420].

HIF1A, *GLUT1*, *GAPDH* and *ERO1A* were assessed due to their association with the development of hypoxia and related processes (such as anaerobic respiration) within the scaffolds. Hypoxia is a crucial feature in cancer progression and spread thus is of high interest to create an *in vitro* culture model that can replicate these conditions. Currently, hypoxia is manually induced in 2D cultures using low oxygen environments [424]. However, in a 3D collagen scaffold, it has recently been demonstrated that the scaffold itself was capable of inducing hypoxia and related cell processes [186]. HIF1A is a transcription factor heavily associated with hypoxia and angiogenesis, along with other general cell processes including proliferation and survival. Upon development of hypoxic environments in solid tumours, *HIF1A* activates and regulates the expression of target genes involved in adaption to the hypoxic environment [410,411]. *HIF1A* also plays a role in a shift to anaerobic metabolism–a feature that is commonly associated with improved tumour cell survival and continued growth and spread [425]. *HIF1A* is highly upregulated in breast cancers and is a poor prognostic factor [412–414]. Endoplasmic reticulum oxidoreductase 1 alpha (*ERO1A*) is induced by hypoxia [407,408]. Recently it has been designated a novel poor prognostic factor for breast cancer [409] and serves as a useful biomarker for detecting hypoxia *in vitro*. While its role in breast cancer remains poorly defined, it is purported to have an impact in disease progression through influencing tumour cell proliferation and migration and also immune escape [426–428]. The glucose transporter 1 (GLUT1) protein allows for glucose transportation across plasma membranes [402]. Increased glycolysis (breakdown of glucose for energy)/anaerobic respiration is a hallmark of several cancer types thus *GLUT1* plays a key role in continued tumour growth and spread [403,404]. In breast cancer, elevated *GLUT1*

expression is associated with a poor prognosis and outcome, thus it was selected as another relevant biomarker for assessment [405,406]. *GAPDH* is primarily involved in glycolysis, metabolic activity and transcription. It has also been associated with carcinogenesis and tumour progression [398,399]. In breast cancer, high expression of *GAPDH* is linked to poorer overall patient survival [400,401]. *GAPDH* was initially used during the housekeeping gene assessments, but due to its above roles in glycolysis it was also considered a gene of interest as it was believed that increases in hypoxia within the scaffold would lead to abnormal *GAPDH* expression in 3D cultures compared to 2D. Thus, it would not be suitable as a housekeeping gene as it would not be constitutively expressed under all experimental conditions. Such an occurrence was evident within the literature, where in the culture of MCF7 and MDA-MB-231 breast cancer cells, Liverani *et al.* (2019) found *GAPDH* to be significantly upregulated in 3D cultures when compared to 2D monolayers [186].

4.1.1 Chapter aims

Within this chapter, the primary objective was to assess the expression of several gene targets that are required to support a biologically relevant 3D *in vitro* breast cancer model. These targets are involved in a variety of key processes in breast cancer development and progression including the modification of the ECM, synthesis of new ECM materials, development of hypoxia, shifts in cell metabolism and the occurrence of glycolysis, and the development of a more aggressive/malignant phenotype.

Primary aims of this chapter were to:

- Assess a panel of four housekeeping genes to determine the two most stable expressed genes for use in the calculation of relative expression levels of all selected targets.
- Determine the expression of selected gene targets in 3D cultured MCF7 cells.
- Investigate if there is a differential expression of the selected targets in 3D compared to 2D culture.

4.2 Materials and methods

4.2.1 Solutions/reagents

Phosphate buffer saline solution 10X: 80 g NaCl, 2 g KCl, 14.4 g Na_2HPO_4, 2.4 g KH_2PO_4 into 800 mL distilled water and adjusted to 1 L. Diluted to 1x when needed. All mentions of PBS in the following studies were a 1x/0.01 M concentration.

0.2 M EDTA stock (300 mL batches): 17.534 g EDTA (Sigma-Aldrich Chemical Co, Wicklow, Ireland) into 200 mL distilled water. NaOH pellets slowly added until pH reached ~8. Volume adjusted to 300 mL. 0.2 M stock diluted to required concentration with distilled water when needed.

4.2.2 Scaffold fabrication and seeding

w/Gel 0.15% scaffolds were prepared as described in Chapter 2. In brief, scaffolds were EDAC/NHS crosslinked as per §2.2.5 prior to cell culture applications. Each scaffold was thoroughly washed, and scaffolds were then prepared for cell seeding via overnight incubation of unseeded scaffolds in DMEM supplemented with 50% FBS in a humidified 5% CO_2 incubator at 37 °C. Scaffolds used in all the following experiments were of the dimensions ~9 x 4.5 mm (diameter x height). Scaffolds were seeded with $3x10^5$ MCF7 cells as per the two-sided seeding method described in Chapter 3 (§3.2.4). After seeding, each scaffold was submerged in 1.5 mL of DMEM media and incubated at 37 °C/5% CO_2. Timepoints for qPCR analysis consisted of culture periods of 1, 7 and 14 days. 2D cell monolayers were cultured alongside scaffolds for each timepoint as controls. 2D cultures were in 6-well plates and were passaged at confluency as per standard 2D culture protocol.

4.2.3　RNA isolation

Total RNA was isolated from each scaffold/cell construct using TRIzol reagent (Invitrogen, Waltham, Massachusetts, USA). At each timepoint (Day 1, 7 or 14), each scaffold or 2D monolayer was removed from culture and washed three times in 1x PBS to remove loosely attached/unattached cells and culture media remnants. Each scaffold was then transferred to a new 24-well plate, at which point 1 mL of TRIzol reagent was added to each well. Each scaffold was homogenised with an IKA ULTRA-TURRAX™ T25 Basic blender for 30 sec to breakdown the scaffold. This was to facilitate future steps as larger remnants of the scaffold could impact solution separations during the density-based centrifugation steps. After homogenisation, the scaffold/TRIzol or 2D monolayer/TRIzol mix was left to incubate for 5 min to allow for cell disruption and nucleoprotein dissociation. After 5 min, each scaffold or 2D lysate was transferred to an RNAse free 1.5 mL tube. 0.2 mL of chloroform was added to each tube and the tube was gently shaken for 10 sec before being left to incubate at room temperature for 3 min. Each sample was then centrifuged at 12,000 RPM for 15 min at 4 °C. This centrifugation separates the solution into three layers–the clear upper aqueous layer contains the RNA. The upper layer was then transferred to a new RNAse free tube, avoiding disturbing the lower layers which would reduce the purity and quality of the RNA containing upper phase. 0.5 mL of isopropanol was added to each tube and the solution was incubated for 10 min. Samples were then centrifuged at 12,000 RPM for 10 min at 4 °C. The RNA was pelleted at the bottom of the tube and the supernatant was discarded. 1 mL of 75% EtOH was added to each tube to resuspend the pellet, washing the RNA. Each tube was briefly vortexed and then centrifuged at 7500 RPM for 5 min at 4 °C to re-pellet the RNA. The supernatant was again discarded and the RNA pellet in each tube was let air dry for 5-10 min. The RNA was then solubilised in RNAse free water (with 0.1 mM EDTA), with brief heating of each sample to 55-60 °C to aid solubilisation. RNA quantity was assessed

via the NanoDrop 1000™ (Thermo Fisher, Scientific, Hemel Hempstead, United Kingdom). RNA purity was assessed by measuring the absorbance at 260 nm and 280 nm (A260/280 ratio). An A260/280 ratio of ~2 was considered pure, with an acceptable limit set at 1.8-2.2.

4.2.4   cDNA synthesis

Complementary DNA (cDNA) synthesis of isolated total RNA was completed using the Transcriptor First Strand cDNA Synthesis Kit (Roche, Penzberg, Germany). 1 µg of RNA was first added to a PCR tube containing a mix of random hexamer (2 µL) and anchored-oligo(dT) primers (1 µL) at concentrations of 60 µM and 2.5 µM respectively. PCR grade H_2O was added to each tube to a total reaction volume of 13 µL. The RNA template-primer mix was then denatured at 65 ºC for 10 min in a PTC-100 thermocycler (MJ Research Inc, Quebec, Canada) before each tube was cooled on ice immediately. The remaining components of the cDNA synthesis reaction were then added to each tube, including; 4 µL of transcriptor reverse transcriptase reaction Buffer (5 X), 0.5 µL of protector RNase inhibitor 40 U/µL, 2 µL of deoxynucleotide mix (10 mM each) and 0.5 µL transcriptor reverse transcriptase (20 U/µL)–bringing the final reaction volume including the RNA-primer mix to 20 µL. Each tube was then mixed gently (no vortexing) and briefly centrifuged if necessary to ensure the liquid was gathered at the bottom of the tube. Each tube was then returned to the thermal cycler and incubated at 25 ºC for 10 min, followed by 30 min at 55 ºC. The Transcriptor Reverse Transcriptase enzyme was then inactivated at 85 ºC for 5 min. Each tube was then removed from the thermal cycler and the reaction was terminated by placing the tube on ice. The newly synthesized cDNA was either left on ice if being used immediately in PCR reactions, stored at -20 ºC for short-term storage (1-2 weeks) or at -80 ºC for longer-term storage.

4.2.5   Primer design

Primers were designed using Primer Blast software [429], which implements Primer 3 and BLAST technologies. Each primer was assessed firstly on Primer Blast but also on Oligo Calc [430] to ensure minimal risk of self-annealing or hairpin formation. Primers were designed to have between 18-22 base pairs in length, exon spanning where possible, targeting amplicons between 70-170 base pairs, GC content (%) between 40-60% and with melt temperatures for forward/reverse primers within ± 2 °C of each other. Following design, primer sequences (Table 4.2) were synthesized by Sigma Aldrich (Sigma-Aldrich Chemical Co, Wicklow, Ireland) and delivered as lyophilised powder. Each primer was reconstituted in PCR grade H_2O to a stock concentration of 100 µM. Stock primers were aliquoted into 20 µL units to reduce number of freeze-thaw cycles needed, labelled and stored at -20 °C. When needed, stock aliquots were defrosted and diluted to a working concentration of 5 µM by adding 5 µL of stock primers to 95 µL of PCR grade H_2O. 1 µL of each primer (forward and reverse) was added to each 10 µL PCR reaction, resulting in a final primer concentration of 0.5 µM for both forward and reverse primer.

Table 4.2: Primer sequences for target genes.

Target	Forward (5'-3')	Reverse (5'-3')
MMP2	CTCATCGCAGATGCCTGGAA	TTCAGGTAATAGGCACCCTTGAAGA
MMP9	CGCGCTGGGCTTAGATCATT	TCAGGGCGAGGACCATAGAG
LOX	GGATACGGCACTGGCTACTT	GCCCTGTATGCTGTACTGGC
COL1A1	CCCCGAGGCTCTGAAGGT	GCAATACCAGGAGCACCATTG
FN1	GGGACTCAATCCAAATGCCTC	TCCAGGAACCCTGAACTGTAA
HAS1	TGGGTTATGCTACCAAGTACACC	GTTGTACAGCCACTCACGGA
HAS2	GTTGGGGGAGATGTCCAGATTT	TGCACTGAACACACCCAAAA
VEGFA	AACAAATGTGAATGCAGACCAAAG	CACCAACGTACACGCTCCA
TGFB1	CGACTCGCCAGAGTGGTTAT	CCGGTAGTGAACCCGTTGAT
JAG1	GACCCCCTGTGAAGTGATTGA	ATTTGCCTCCCGACTGACTC
CXCR4	TCAGCGTCTCAGTGCCCTTT	AATCCTACAACTCTCCTCCCCA
GLUT1	GAACTCTTCAGCCAGGGTCC	ACCACACAGTTGCTCCACAT
ERO1A	TGGATGAATCTCTGAGTGAGGAAA	AGATGACCACCAGCAGATCC
HIF1A	TTGGCAGCAACGACACAGAA	GAAGTGGCTTTGGCGTTTCA
GAPDH	GACAGTCAGCCGCATCTTCT	GCCCAATACGACCAAATCCGT
β-Actin	GCCGCCAGCTCACCA	CACGATGGAGGGGAAGACG
18S rRNA	GGAGTATGGTTGCAAAGCTGA	ATCTGTCAATCCTGTCCGTGT
HPRT	CCCTGGCGTCGTGATTAGTG	TCGAGCAAGACGTTCAGTCC

4.2.6 Real time polymerase chain reaction (qPCR)

qPCR was completed using the FastStart Essential DNA Green Master kit (Roche, Penzberg, Germany) and performed on a Lightcycler Nano™ Instrument (Roche, Penzberg, Germany). This kit makes use of the SybrGreen dye which selectively binds to double stranded DNA to allow for detection of target genes. Each qPCR final reaction was of volume 10 µL consisting of; 1 µL cDNA (equated to 50 ng cDNA per reaction), 1 µL of both forward and reverse primer (0.5 µM final concentration), 5 µL FastStart Essential DNA Green Master (Contains FastStart Taq DNA polymerase, reaction buffer, dNTPs, Sybr Green I dye, and MgCl$_2$) and 2 µL PCR grade H$_2$O. The qPCR controls consisted of a no-DNA control where PCR grade H$_2$O was used in place of cDNA. The qPCR program consisted of a 600 sec hold at 95 ºC for activation of FastStart Taq DNA polymerase and denaturation of DNA, followed by 45 cycles of a 3-step amplification involving; denaturation at 95 ºC for 20 sec, an annealing step at ~58 ºC for 20 s (primer dependent) and extension at 72 ºC for 20 sec. Following the qPCR program, a melt curve analysis (from 65 ºC to 95 ºC) was conducted to ensure no non-specific binding or primer-dimer interactions occurred. The relative gene expression was calculated using the method outlined by Vandesompele *et al.* (2002) [431] and Hellemans *et al.* (2007) [432].

Briefly, this method utilises the geometric mean of multiple housekeeping genes (x2) for more accurate normalisation of qPCR data in order to calculate relative expression levels of desired target genes [431,432]. Cycle threshold (CT) values from 2D cultured samples were selected as the control group (i.e., calibrator group), and the n=3 for control samples was averaged, thus all gene of interest results were relative to average control CT values. Delta CT (ΔCT) values were then calculated by subtracting the 3D culture sample values, both for

housekeeping genes (reference (REF) genes) and gene of interests (GOI), from the average control CT value. Relative quantities (RQ) for each ΔCT value using '$2^{\Delta CT}$' (a value of 2 assumes a primer efficiency of 100%, as per the traditional delta-delta CT method [433]). Next, the geometric mean of the selected two housekeeping/reference genes is calculated by applying the '=GEOMEAN' function in Microsoft Excel to the two housekeeping gene relative quantity (RQ$_{REF}$) values previously calculated. Upon completion of above calculations, relative expression values for each gene of interest is calculated (Equation 11).

Equation 11 – Relative gene expression:

$$\frac{RQ_{GOI}}{GEOMEAN\ [RQ_{REF}]}$$

4.2.7 qPCR housekeeping panel selection process

To calculate relative expression values from the qPCR method in §4.2.6, four potential housekeeping genes were subject to analysis: *β-Actin*, hypoxanthine-guanine phosphoribosyltransferase (*HPRT*), Glyceraldehyde-3-phosphate dehydrogenase (*GAPDH*) and 18S ribosomal RNA (*18S rRNA*). The housekeeping genes were assessed for stability of expression across the different experimental conditions (the three timepoints and both 2D/3D culture) using the cycle threshold (Ct) mean/range, standard deviation (SD), standard (Std.) error mean and decisively the coefficient of variation (CV%) of the Ct values (i.e., the CtCV%).

4.2.8 Statistical analysis

Statistical analysis was completed using the GraphPad Prism software, version 8.0.2 (GraphPad Software, Inc., San Diego, CA). The minimum number of samples tested was n=3. Unpaired t-tests were performed to assess difference amongst samples. Statistical

significance was determined without correction for multiple comparisons. Each row (each timepoint) was analysed individually, without assuming a consistent SD. Results calculated and shown in graphs were the mean ± the standard deviation (SD). For all result figures in this chapter: p-value ≤0.05 = *, p-value ≤0.01 = **, p-value ≤0.001 = ***.

4.3   Results

4.3.1   Selection of stably expressed housekeeping genes

Assessment of candidate housekeeping genes showed that *HPRT* and *β-Actin* were the two most stable expressed housekeeping genes of the four under investigation (Fig. 4.1 and Table 4.3). These two genes had the lowest CtCV% of the four, with *HPRT* having the lowest variation overall at 2.28% followed by *β-Actin* with a CtCV% of 2.9%. These two genes also had the lowest Ct range, the lowest standard deviations and the lowest standard error mean (Std. error mean). *18s rRNA* was the poorest performing gene in relation to the CtCV% with a value of 8.25%. *GAPDH* had the highest standard deviation, highest Std. error mean and the largest Ct range. Notably, *GAPDH* had large variation between 2D and 3D at Day 7 and 14 which drove its poor performance after displaying stable expression at Day 1. *HPRT* and *β-Actin* progressed as the housekeeping panel in the investigation of the selected gene of interests used in the remaining studies within this chapter.
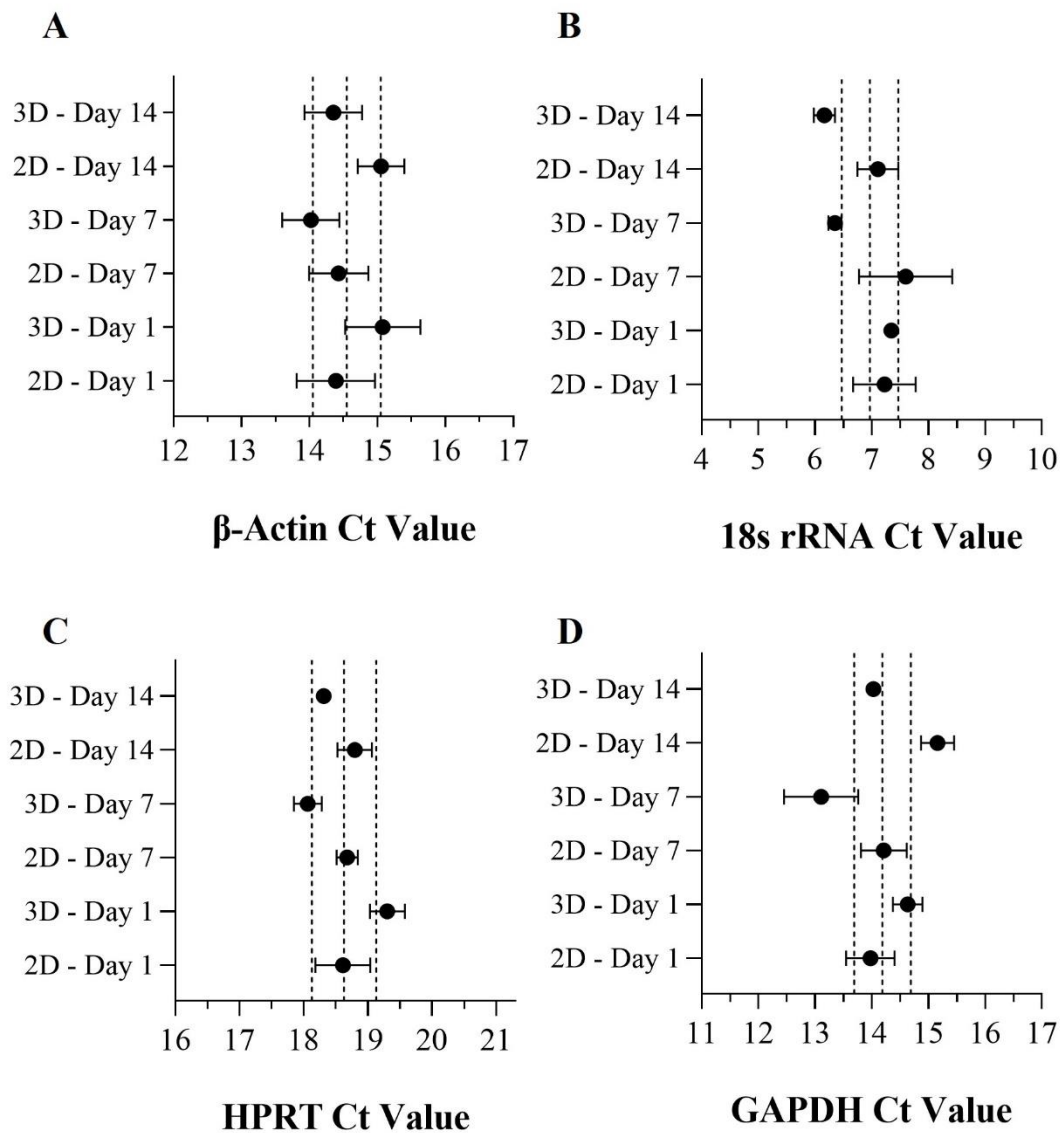
Figure 4.1: Expression analysis of housekeeping genes. Analysis of Ct values in A-D of the four investigated housekeeping genes are highlighted. The four genes were assessed for their stability across both variables, the culture method (2D or 3D) or the timepoint (Day 1, 7 or 14). The central dashed line represents the mean Ct value while the outer dashed lines indicate $\pm$ 0.5 from the mean, which overall illustrates a range of 1 Ct value around the mean. Results shown are mean $\pm$ SD (n=3).

Table 4.3: Selection of stably expressed housekeeping gene panel.

	Mean Ct	Std. Dev	Std. Error Mean	Ct Range	CtCV (%)
β-Actin	14.55	0.42	0.17	1.06	2.90
18s rRNA	6.97	0.58	0.23	1.43	8.25
HPRT	18.63	0.43	0.17	1.24	2.28
GAPDH	14.19	0.69	0.28	2.05	4.86

4.3.2   Relative mRNA expression of gene of interests in 3D vs. 2D.

The first cohort of target genes that expression patterns were assessed for consisted of genes with links to the ECM in terms of either modification of the matrix or synthesis of common matrix components. ECM modifying targets were *MMP2*, *MMP9* and *LOX* while ECM synthesis related targets were *COL1A1*, *FN1*, *HAS1* and *HAS2*.

MMP2 displayed no expression differences between 2D and 3D at both Day 1 and 7 (Fig. 4.2). By Day 14, there was an ~3.5-fold upregulation in *MMP2* expression in 3D cultured MCF7 cells in comparison to 2D (p-value ≤0.001). For *MMP9,* Day 7 and Day 14 saw increases in expression (Fig. 4.3), both ~two-fold, in 3D versus 2D (both p-value ≤0.01). *LOX* represented the most sizeable alteration in expression pattern between 3D and 2D amongst the various targets assessed (Fig. 4.4). Large differences in expression arose by Day 7 and continued at Day 14–though to a lesser extent. At Day 7, there was a 25-40-fold increase in expression in 3D cultured MCF7 cells compared to 2D (p-value ≤0.01). By Day

14, this had reduced to a 10-20 fold increase in expression in 3D–which remained significantly higher than 2D cultured cells (p-value ≤0.01).
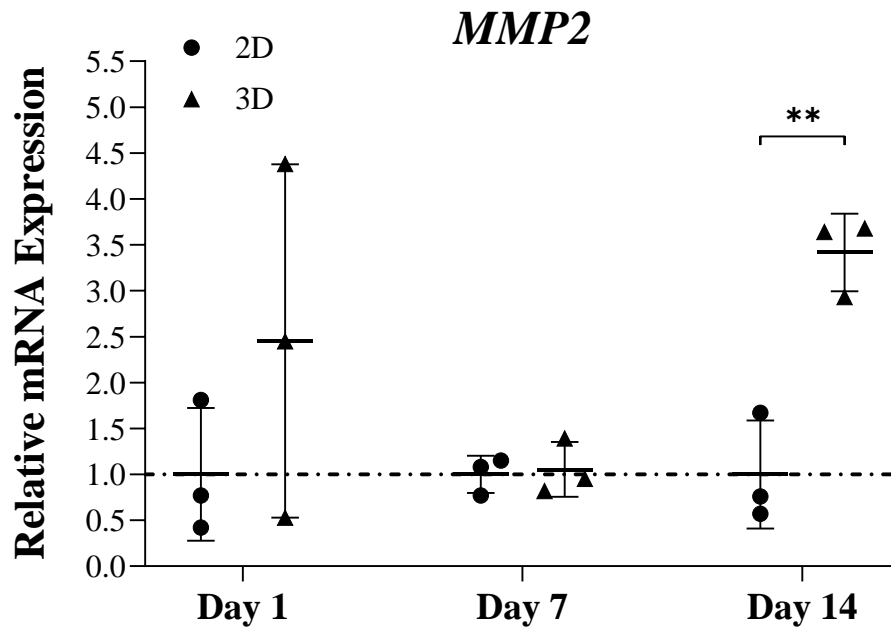
Figure 4.2: Relative mRNA expression of *MMP2* in 2D vs. 3D. Relative expression of the target gene of interest was determined in comparison to the expression of the housekeeping reference genes. Variance was tested using unpaired t-test. Results shown are individual data points and the mean ± SD (n=3). p-value ≤0.05 = *, p-value ≤0.01 = **, p-value ≤0.001 = ***.
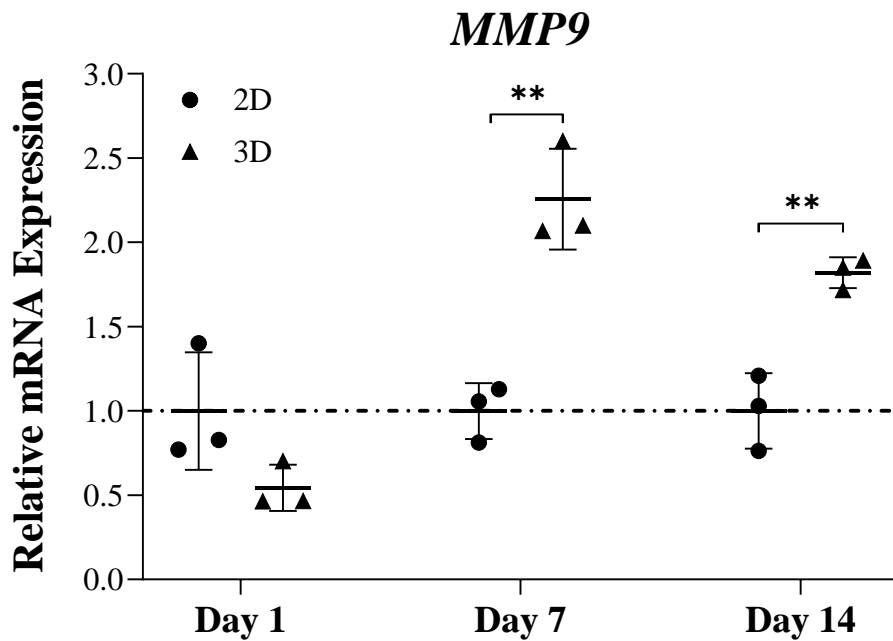
Figure 4.3: Relative mRNA expression of *MMP9* in 2D vs. 3D. Relative expression of the target gene of interest was determined in comparison to the expression of the housekeeping reference genes. Variance was tested using unpaired t-test. Results shown are individual data points and the mean ± SD (n=3). p-value ≤0.05 = *, p-value ≤0.01 = **, p-value ≤0.001 = ***.
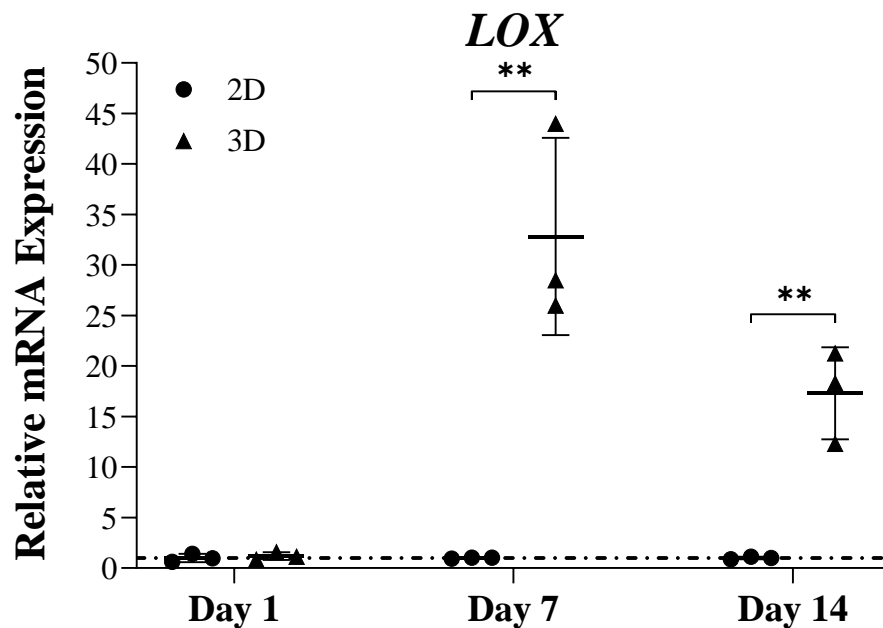
Figure 4.4: Relative mRNA expression of *LOX* in 2D vs. 3D. Relative expression of the target gene of interest was determined in comparison to the expression of the housekeeping reference genes. Variance was tested using unpaired t-test. Results shown are individual data points and the mean ± SD (n=3). p-value ≤0.05 = *, p-value ≤0.01 = **, p-value ≤0.001 = ***.

Moving to targets that are involved in synthesis of key ECM components, *COL1A1* did not display any increase in expression in 3D in comparison to 2D cultured cells (Fig. 4.5). In fact, there was a measurable decrease in *COL1A1* expression in 3D compared to 2D at Day 14 (p-value ≤0.01)–translating to a 0.5-fold decrease in expression. *FN1* on the other hand, did display increased expression in 3D cultured cells (Fig. 4.6). While at Day 1 there were no expression differences, by Day 7 a slight but significant increase in expression in 3D was observed (p-value ≤0.05). By Day 14, the expressional difference between 3D and 2D increased further, with a two-fold increase in 3D observed (p-value ≤0.001). *HAS1* did not display any measurable change in expression across the three timepoints investigated (Fig. 4.7). There was however a large deviation in the expression of *HAS1* at each timepoint in 3D – most notably at Day 14. Here, a decrease in 3D expression compared to 2D in one sample and a nine-fold increase in expression in 3D in another was observed. *HAS2* displayed no expressional differences between 2D and 3D at both Day 1 and Day 14. However at Day 7, there was a significant upregulation of *HAS2* (3-fold, p-value ≤0.01) in 3D cultured cells compared to 2D (Fig. 4.8).

Figure 4.5: Relative mRNA expression of *COL1A1* in 2D vs. 3D. Relative expression of the target gene of interest was determined in comparison to the expression of the housekeeping reference genes. Variance was tested using unpaired t-test. Results shown are individual data points and the mean ± SD (n=3). p-value ≤0.05 = *, p-value ≤0.01 = **, p-value ≤0.001 = ***.

Figure 4.6: Relative mRNA expression of *FN1* in 2D vs. 3D. Relative expression of the target gene of interest was determined in comparison to the expression of the housekeeping reference genes. Variance was tested using unpaired t-test. Results shown are individual data points and the mean ± SD (n=3). p-value ≤0.05 = *, p-value ≤0.01 = **, p-value ≤0.001 = ***.

Figure 4.7: Relative mRNA expression of *HAS1* in 2D vs. 3D. Relative expression of the target gene of interest was determined in comparison to the expression of the housekeeping reference genes. Variance was tested using unpaired t-test. Results shown are individual data points and the mean ± SD (n=3). p-value ≤0.05 = *, p-value ≤0.01 = **, p-value ≤0.001 = ***.

Figure 4.8: Relative mRNA expression of *HAS2* in 2D vs. 3D. Relative expression of the target gene of interest was determined in comparison to the expression of the housekeeping reference genes. Variance was tested using unpaired t-test. Results shown are individual data points and the mean ± SD (n=3). p-value ≤0.05 = *, p-value ≤0.01 = **, p-value ≤0.001 = ***.

The next cohort of target genes that expression patterns assessed were of genes with links to general cell functions such as proliferation, differentiation, migration and apoptosis but also in more complex processes like angiogenesis and metastasis.

VEGFA, primarily associated with angiogenesis and thus progression of breast cancer, did not show any alterations in expression between 2D and 3D at both Day 1 and Day 14 (Fig. 4.9). In contrast, there was a significant upregulation in expression, a two-fold change, at Day 7 in 3D cultured MCF7 cells when compared to 2D cultures (p-value ≤0.05). *TGFB1*, which has roles in cell proliferation, differentiation, apoptosis and angiogenesis, showed stable expression between 2D and 3D at each of the respective timepoints (Fig. 4.10). Similarly, *JAG1* which is also involved in differentiation, did not see any differences in expression levels across the two culture conditions at the three timepoints (Fig. 4.11). *CXCR4*, with links to metastasis and cell migration, was significantly upregulated at both Day 1 and 7 (Fig. 4.12). At Day 1, 3D expression levels were three-fold higher than 2D levels (p-value ≤0.01). At Day 7, expression levels were four-fold higher in 3D cultures than in 2D (p-value ≤0.05). No expression differences were detected at Day 14.

Figure 4.9: Relative mRNA expression of *VEGFA* in 2D vs. 3D. Relative expression of the target gene of interest was determined in comparison to the expression of the housekeeping reference genes. Variance was tested using unpaired t-test. Results shown are individual data points and the mean ± SD (n=3). p-value ≤0.05 = *, p-value ≤0.01 = **, p-value ≤0.001 = ***.
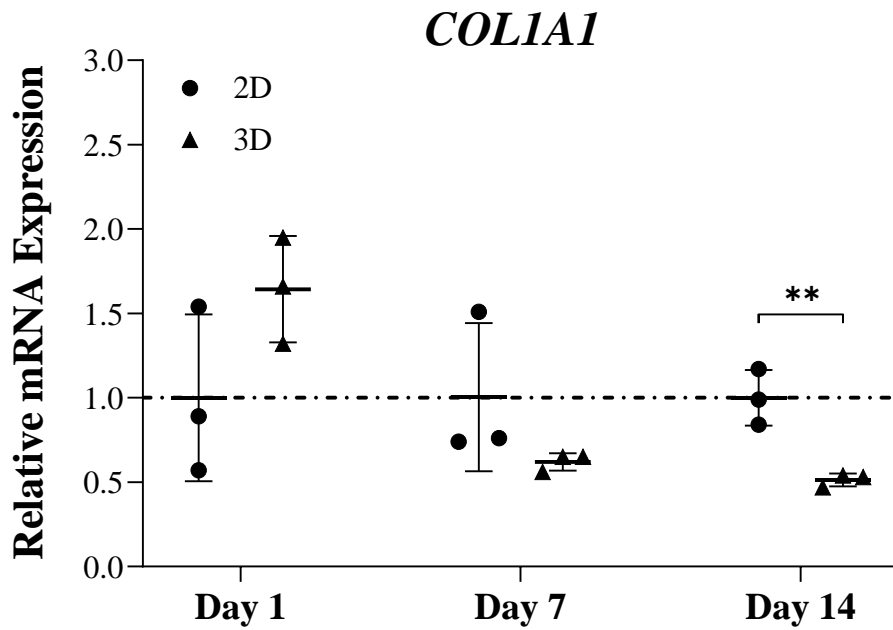

Figure 4.10: Relative mRNA expression of *TGFB1* in 2D vs. 3D. Relative expression of the target gene of interest was determined in comparison to the expression of the housekeeping reference genes. Variance was tested using unpaired t-test. Results shown are individual data points and the mean ± SD (n=3). p-value ≤0.05 = *, p-value ≤0.01 = **, p-value ≤0.001 = ***.
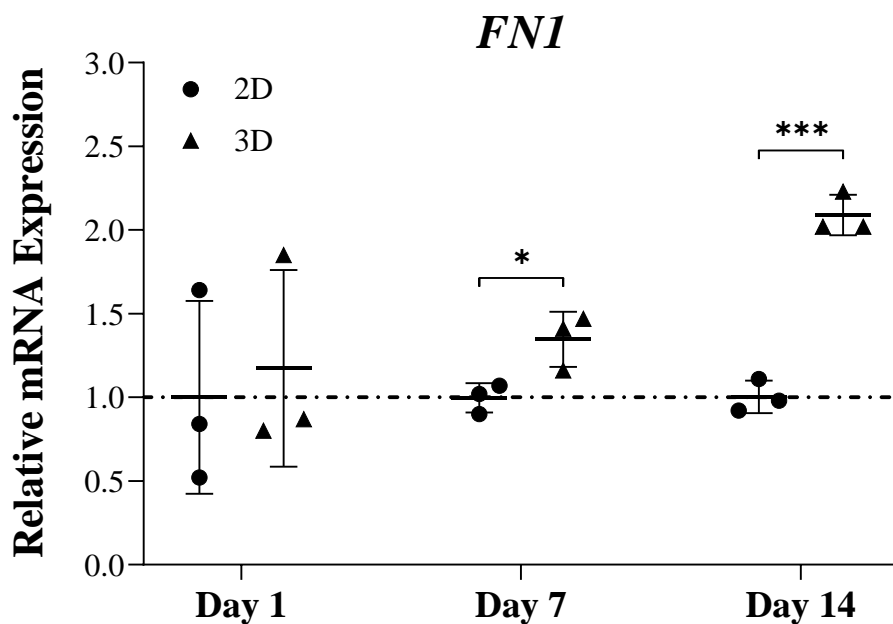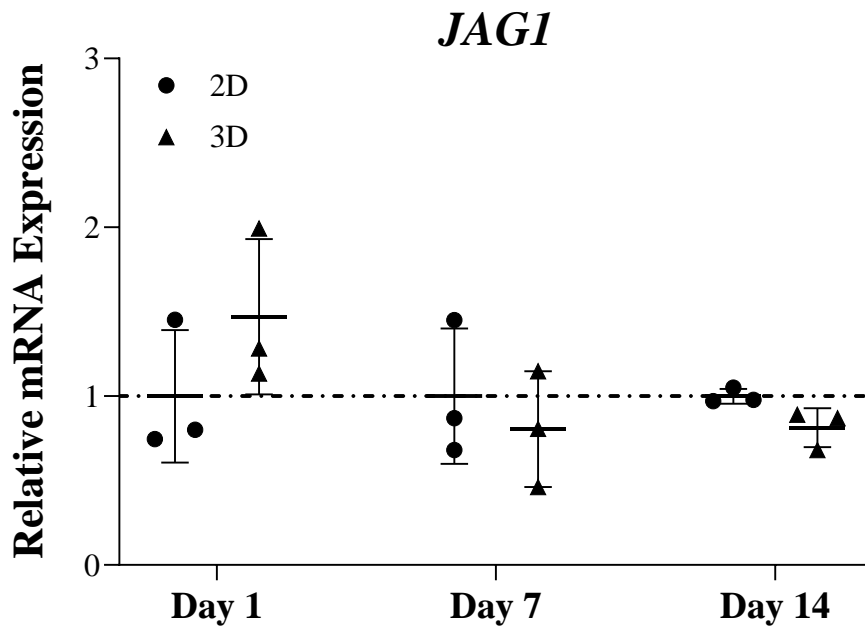
Figure 4.11: Relative mRNA expression of *JAG1* in 2D vs. 3D. Relative expression of the target gene of interest was determined in comparison to the expression of the housekeeping reference genes. Variance was tested using unpaired t-test. Results shown are individual data points and the mean ± SD (n=3). p-value ≤0.05 = *, p-value ≤0.01 = **, p-value ≤0.001 = ***.
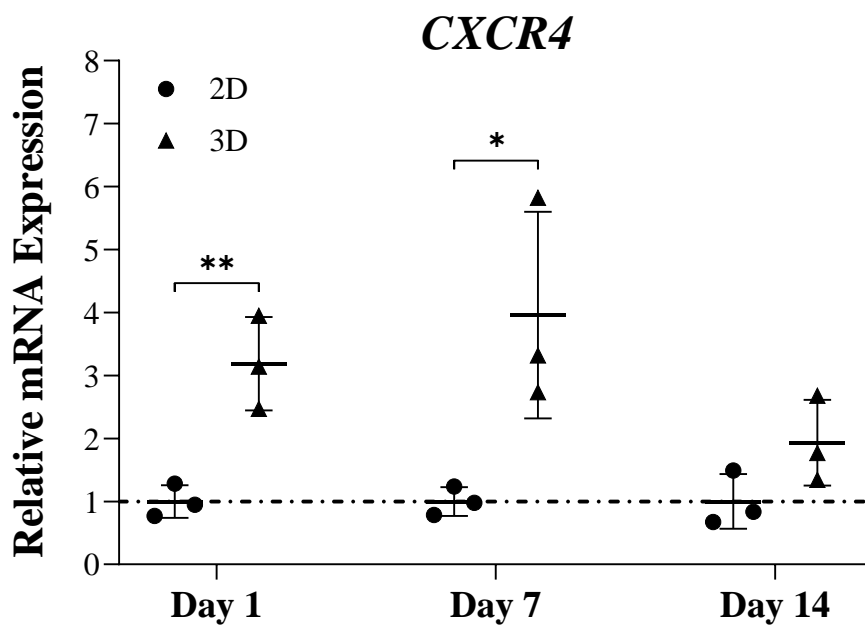
Figure 4.12: Relative mRNA expression of *CXCR4* in 2D vs. 3D. Relative expression of the target gene of interest was determined in comparison to the expression of the housekeeping reference genes. Variance was tested using unpaired t-test. Results shown are individual data points and the mean ± SD (n=3). p-value ≤0.05 = *, p-value ≤0.01 = **, p-value ≤0.001 = ***.

The third cohort of target genes that expression patterns were assessed for consisted of genes involved largely in cell metabolism/glycolysis (*GAPDH* and *GLUT1*), and also those associated with hypoxia (*ERO1A* and *HIF1A*).

GAPDH displayed no differences in expressions between 2D and 3D cultures at Day 1. By Day 7, there was an upward trend in expression in 3D samples, however it was just below the significant threshold (Fig. 4.13, p-value = 0.07). At Day 14, a clear 1.5 fold-change in expression was recorded, with *GAPDH* expression higher in 3D cultured MCF7 cells than in 2D (p-value ≤0.01). For *GLUT1*, there were no differences in expression levels in either culture conditions at Day 1 or Day 7 (Fig. 4.14). By Day 14, a large increase in expression occurred in 3D cultured cells in comparison to 2D (p-value ≤0.01), representing a 1.8-fold increase. Interestingly, for both the metabolism/glycolysis relating targets, expression profiles were closely matched in terms of overall pattern and fold increases in 3D compared to 2D cultured cells. *ERO1A* displayed no alterations in expression between 2D and 3D at Day 1. Both Day 7 and Day 14 provided increased expression in 3D cultured cells in comparison to 2D cultured cells (Fig. 4.15). This was a 2.8-fold difference at Day 7 (p-value ≤0.05) and a 2.2-fold difference on Day 14 (p-value ≤0.001). Finally, *HIF1A* displayed increased expression (2.6-fold) in 3D relative to 2D at Day 1 (Fig. 4.16, p-value ≤0.05). At Day 7, expression between 2D and 3D was stable with no differences in expression levels. At Day 14, there was a slight (0.6-fold) but significant decrease in expression in 3D cells relative to their 2D counterparts (p-value ≤0.05).

All resulting cell expression analysis has been summarised in Fig. 4.17, presented through a colourised heat map displaying the expression of the various targets in 3D cultured cells relative to 2D cultured cells at each respective timepoint.
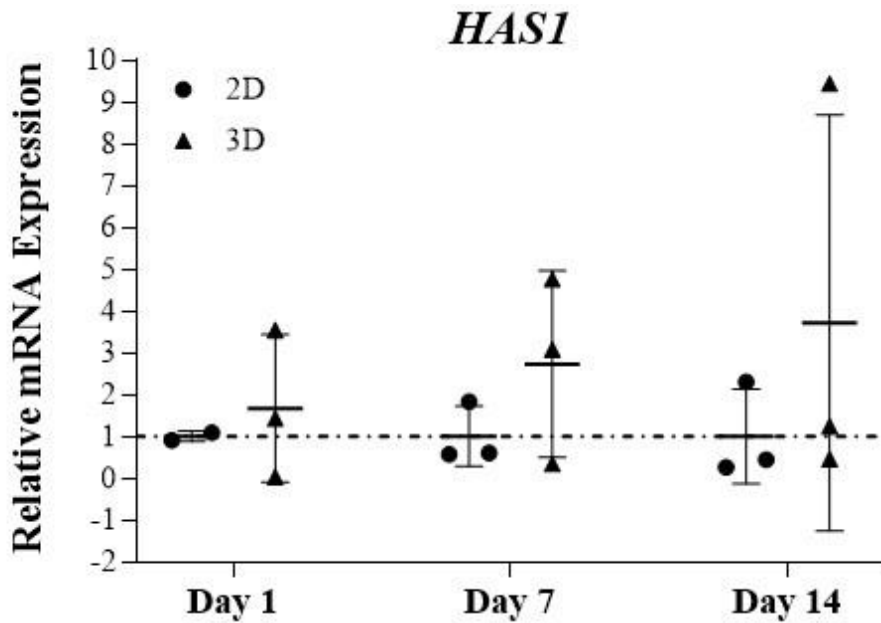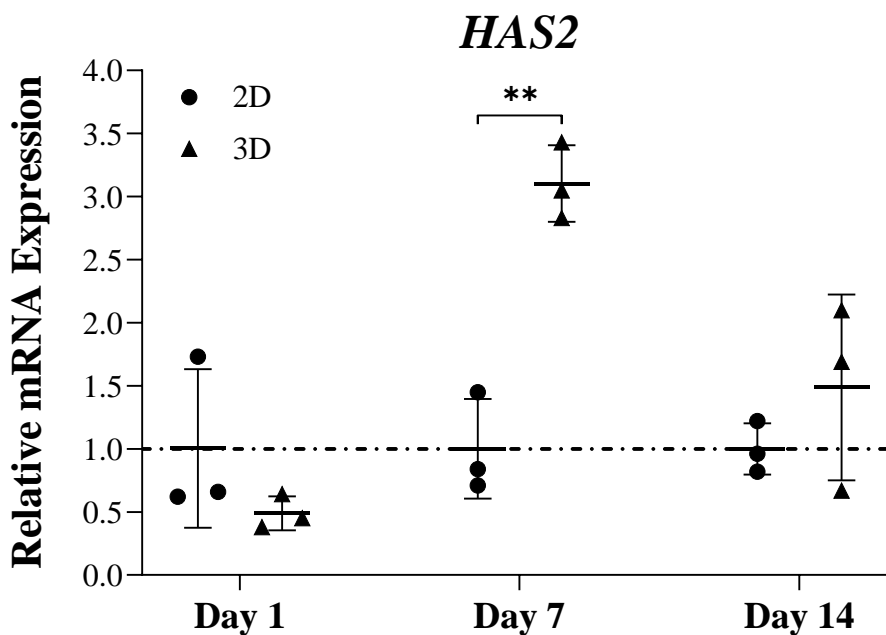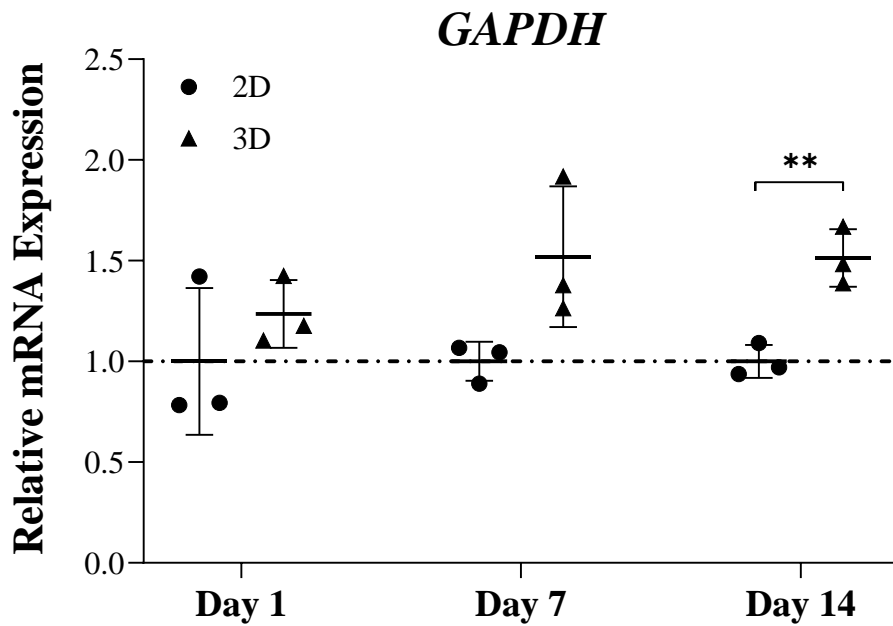
Figure 4.13: Relative mRNA expression of *GAPDH* in 2D vs. 3D. Relative expression of the target gene of interest was determined in comparison to the expression of the housekeeping reference genes. Variance was tested using unpaired t-test. Results shown are individual data points and the mean ± SD (n=3). p-value ≤0.05 = *, p-value ≤0.01 = **, p-value ≤0.001 = ***.
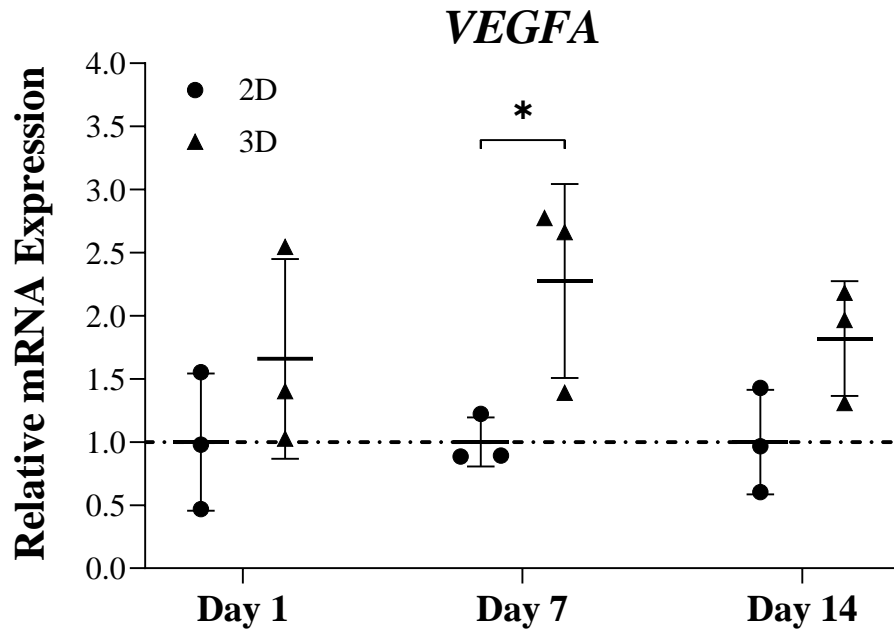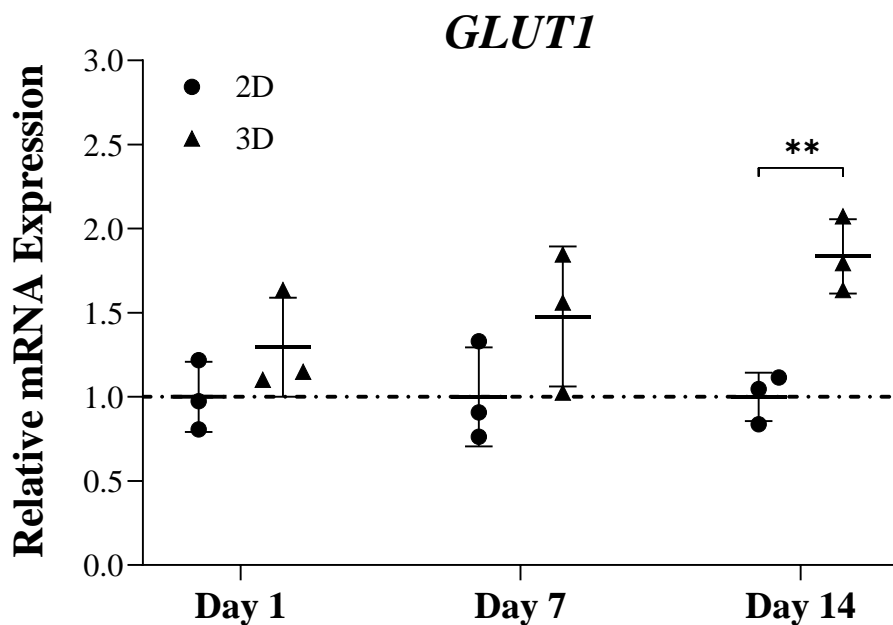

Figure 4.14: Relative mRNA expression of *GLUT1* in 2D vs. 3D. Relative expression of the target gene of interest was determined in comparison to the expression of the housekeeping reference genes. Variance was tested using unpaired t-test. Results shown are individual data points and the mean ± SD (n=3). p-value ≤0.05 = *, p-value ≤0.01 = **, p-value ≤0.001 = ***.
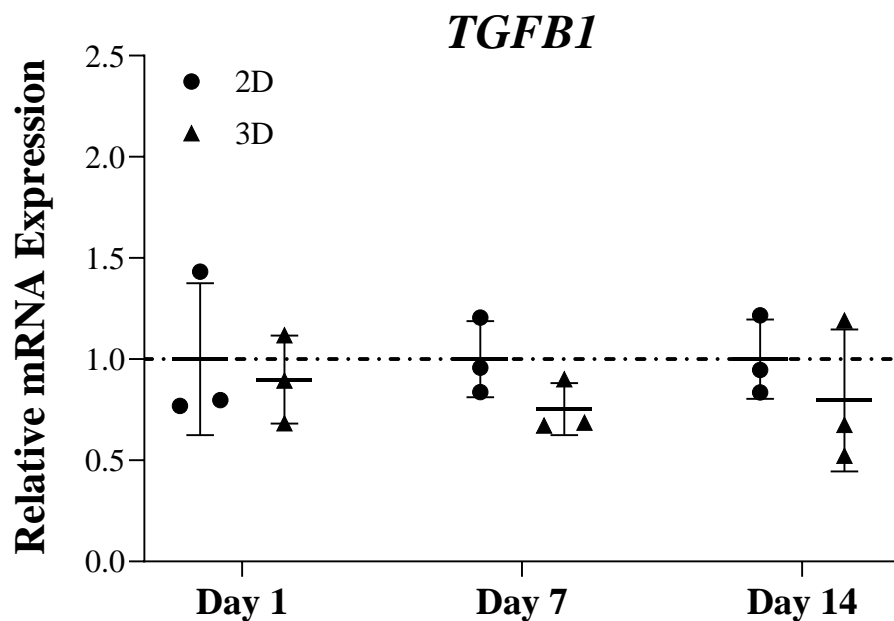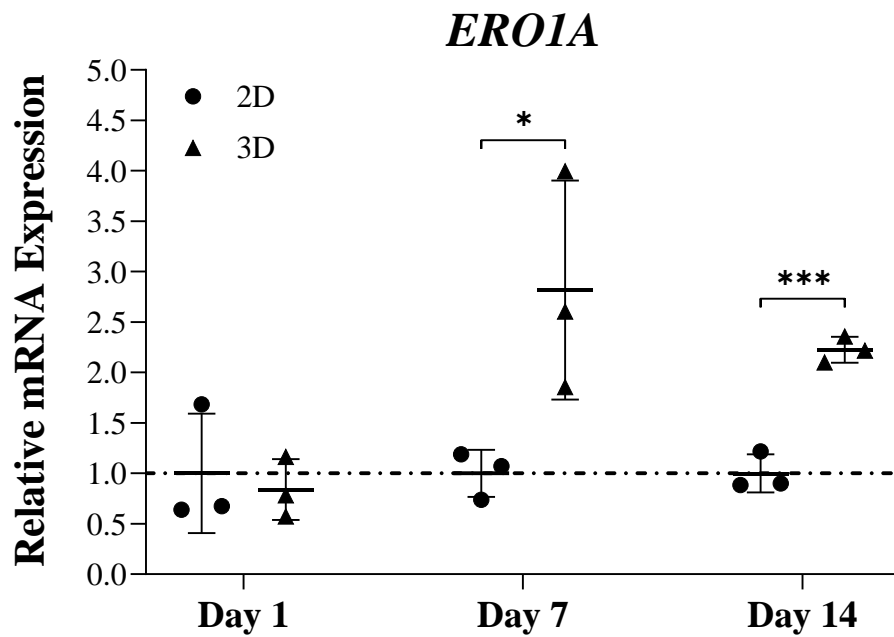
Figure 4.15: Relative mRNA expression of *ERO1A* in 2D vs. 3D. Relative expression of the target gene of interest was determined in comparison to the expression of the housekeeping reference genes. Variance was tested using unpaired t-test. Results shown are individual data points and the mean ± SD (n=3). p-value ≤0.05 = *, p-value ≤0.01 = **, p-value ≤0.001 = ***.
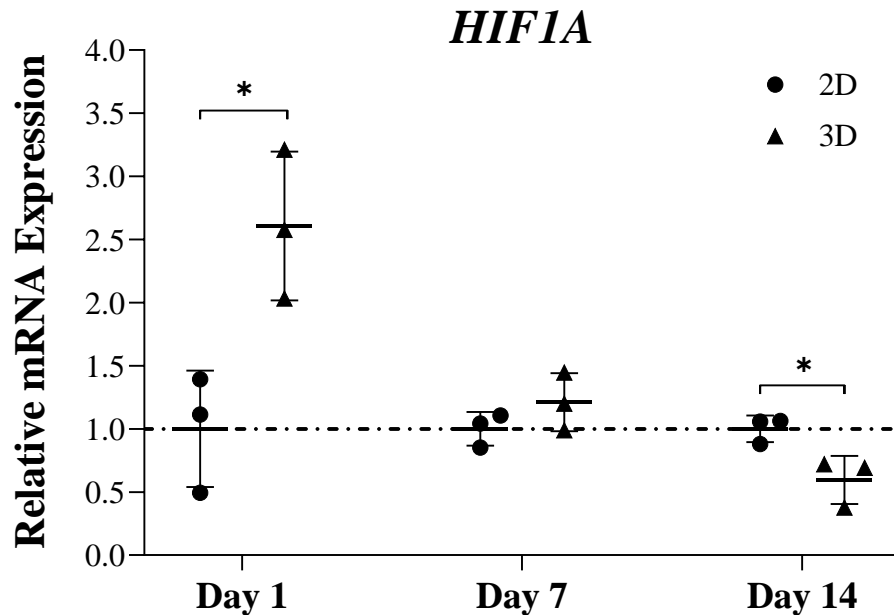
Figure 4.16: Relative mRNA expression of *HIF1A* in 2D vs. 3D. Relative expression of the target gene of interest was determined in comparison to the expression of the housekeeping reference genes. Variance was tested using unpaired t-test. Results shown are individual data points and the mean ± SD (n=3). p-value ≤0.05 = *, p-value ≤0.01 = **, p-value ≤0.001 = ***.

Gene expression in 3D cultures relative to 2D

Fold Change Colour Key (Log$_2$)
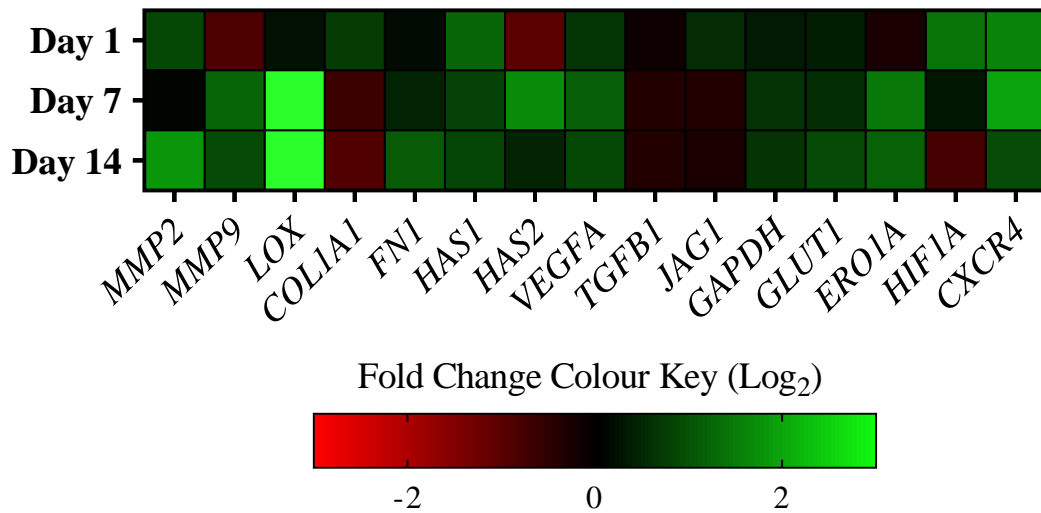
Figure 4.17: Summary heat map of all gene of interest expression in 2D vs. 3D. Log$_2$ fold change values for gene expression in 3D culture compared to 2D culture (set as calibrator/control). Relative expression values converted to Log$_2$ values and plotted as heat map. Log$_2$ values of greater than zero and green coloured implies increased expression in 3D compared to 2D while Log$_2$ values less than zero and red coloured imply reduced expression. Log$_2$ values closer to zero and black coloured (or dark green/red) imply minimal difference in expression between 3D and 2D culture.

4.4 Discussion

Beyond morphological impacts, there is great interest in the transcriptome of cells cultured in 3D culture models *in vitro*, and how significant changes in gene expression may be induced by the cell-matrix interactions and also the increased cell-cell interactions within these models compared to 2D cell culture. A limitation of 2D cell culture is the divergence of gene expression patterns from those observed for human cancers–and these changes tend to drive a more benign, less aggressive and generally homogenous morphology in 2D cultured cells [98,122]. This highlights one of the key potential advantages of 3D models, whereby gene expression patterns more closely resemble human cancers and offer a more complex phenotype than 2D cultured cells [382,383].

The culture of cells in a 3D scaffold environment drove significant alterations in the expression of a variety of genes involved in the modification of the ECM or synthesis of ECM components when compared to cells grown in standard 2D plastic dishes. Alterations within the ECM play a crucial role in both the development and spread of breast cancer [5,48]. The initial gene targets assessed were those that played a role in this alteration, either through modification/degradation of already present components or genes involved in the synthesis of ECM materials. *MMP2*, *MMP9* and *LOX* genes displayed increased expression at either or both Day 7 and Day 14. This observation conforms to works completed elsewhere comparing 2D and 3D culture, whereby MCF7 cells cultured within collagen-based scaffolds displayed significantly increased expression of *MMP2*, *MMP9* and *LOX* in comparison to 2D cultured MCF7s [186,194]. *LOX* displayed the largest fold change in expression upon 3D culture compared to all other gene of interests. The role of *LOX* in the crosslinking of collagen and thus the stiffening of the ECM is a key prognostic factor and plays a role in breast cancer progression and spread [4,80,81]. The natural induction of high *LOX*

expression in our 3D scaffold demonstrates an advantage of using such a model in potential research and exploratory routes–as *LOX* targeting is an area of interest in treating breast cancer [434,435]. Likewise, *MMP2* and *MMP9* are purported to play a role in metastasis due to their collagen degradation abilities [48,86,88], and both genes displayed increased expression in the 3D scaffolds. *MMP2* and *MMP9* are both subject to therapeutic investigation, with agents that inhibit their activity showing promise in disrupting metastatic potential in particular [436–438]. Thus, providing a 3D model that can be utilised in future explorations surrounding *MMP2* and *MMP9* is promising.

As referenced throughout this thesis, collagen plays a major role in makeup of the breast cancer ECM, and as such is a prominent factor in the disease–where increased collagen deposition, collagen fibre linearisation/remodelling and almost paradoxically collagen degradation (i.e., the basement membrane) influence breast cancer development, progression and ultimately its spread [6,48,57,91]. It was originally hypothesized that the 3D scaffolds may induce increased expression of the collagen type 1 synthesizing gene, *COL1A1*, mimicking the increased expression and resulting deposition of the collagen protein within the ECM seen in human breast cancers [54]. However, despite detecting the expression of *COL1A1*, no such increase in 3D was observed in comparison to 2D cultured cells. Though cancer cells themselves synthesise collagen [439], typically it is stromal cells, such as fibroblasts, that are powerhouses in the production of collagen and other major ECM components [440,441]. Thus, it may not be a surprise that the 3D environment did not stimulate the MCF7 cells to increase expression of *COL1A1* compared to 2D. In a previous study investigating the behaviour of both MCF7 and MDA-MB-231 cells in a collagen-based scaffold, picrosirius red staining (highly selective collagen stain) demonstrated that neither cell line induced an increase in collagen synthesis/deposition within the scaffolds [198]–thus

the above results are not in isolation. Deeper investigations into collagen synthesis and deposition within 3D scaffolds may seek to assess the expression of other collagen types or incorporate co-cultures with stromal cells such as fibroblasts to more accurately model collagen synthesis and deposition within an *in vitro* model. Fibronectin is a crucial glycoprotein that serves a variety of functions, controlling processes such as adhesion, migration and proliferation [48,387]. Its overexpression has a strong association with metastatic spread and progression of breast cancer [385,388]. *FN1* was significantly upregulated at both Day 7 and Day 14, though the difference between 2D and 3D was more pronounced at Day 14 (1.3 fold-change vs 2.3 fold-change), indicating a steady increase in FN1 expression as a function of time. Previously, culture of breast cancer cells (MDA-MB-231) within a 3D model (spheroid-based) compared to 2D saw an increase in *FN1* mRNA expression [442]. Within the tumour microenvironment, increases in hyaluronic acid are associated with breast cancer spread and metastasis [392].

Out of the two *HAS* genes assessed, only *HAS2* displayed a result of interest, with a significant increase in expression in 3D at Day 7. Thus, potential increases in the presence of hyaluronic acid within the scaffolds stemming from this increase in *HAS2* expression further corroborates that the MCF7 cells growing in 3D develop a more aggressive phenotype. Increased expression of *HAS2* in a 3D breast cancer *in vitro* model compared to 2D culture has not previously been reported, thus is a novel result. The increase in expression of ECM components observed, and potentially others not yet assessed within our lab, demonstrate the increasing complexity a 3D scaffold can offer. This is not only in terms of providing cells with an initial biologically relevant 3D scaffold structure composed of the primary ECM component collagen, but also in terms of driving the cells towards a genotype/phenotype that produces other ECM components that play key roles in disease

progression and spread, such as fibronectin and hyaluronic acid. The ever increasing complexity these *in vitro* scaffolds can achieve, the further we move away from reliance on 2D culture and the closer we get to bridging the gap to animal models and ultimately replicating processes in the human tumour microenvironment more accurately.

JAG1 and *TGFB1* are known to be overexpressed in breast cancer patients [394,395,416,417], no differences in expression levels in 3D compared to 2D was observed. *JAG1* and *TGFB1* have many functions but a key one in terms of cancer, and specifically cancer metastasis and disease progression, is their involvement in epithelial-to-mesenchymal transition (EMT) [422,443,444]. EMT is a mechanism by which epithelial cells lose their cell adhesion and accrue a more invasive phenotype with enhanced migratory ability, thus EMT is crucial in cancer spread and progression [445]. MCF7 cells are considered non-invasive and thus naturally do not show signs of EMT under 2D culture–typically it must be chemically induced to encourage the transition [446,447]. Our result is in contrast to another collagen-based scaffold whereby Chen *et al.* (2012) saw an upregulation in a variety of EMT and stem cell markers within MCF7 cells, including a significant upregulation of JAG1 [194]. Liverani *et al.* (2019) also saw an upregulation of *JAG1* and a moderate increase of *TGFB1* expression in MCF7 cells within a collagen scaffold [186]. Both of these works demonstrated that 3D scaffold culture models may induce EMT, thus paving the way for new *in vitro* models for research into a crucial aspect of breast cancer progression and metastasis. It is likely the case that the complex nature of 3D *in vitro* models, and differences in scaffolds including but not limited to scaffold architecture, mechanical properties and cell seeding densities can result in different expression profiles between different 3D models. While *JAG1* and *TGFB1* did not show increased expression, previously mentioned genes including *LOX* [80], *MMP2* and *MMP9* [448] and *FN1* [449,450] also are associated with

EMT induction and were highly expressed with our 3D collagen-based scaffolds. Thus, further work assessing additional targets associated with EMT, including at the protein level, could more conclusively investigate this aspect of cancer progression as the increased expression of relevant EMT-associated genes is of high interest. *CXCR4* plays a role in multiple functions including cell migration, metastasis and angiogenesis [418,451,452] and is frequently overexpressed in breast cancers and associated with a poor prognosis [418,419]. Within our scaffolds, at both Day 1 and Day 7, there was a significant upregulation of *CXCR4* in 3D cultured MCF7 cells compared to 2D. This expressional signature indicates the more aggressive and malignant phenotype the usually non-invasive and minimally aggressive MCF7 cell line accrues as a result of culture within our 3D model.

A crucial aspect of breast cancer that was of interest in this chapter was the potential development of hypoxia within the fabricated collagen-based scaffolds. Within Chapter 3, it was observed that upon culture within the scaffolds, even after just 24 h, cells were interacting with one another and forming spheroid-like aggregates. After two weeks of culture, larger aggregates were present, signalling that regions of hypoxia would likely be present throughout the scaffolds, similar to the hypoxic niches previously observed in a similar collagen scaffold culture study with breast cancer cells (both MCF7 and MDA-MB-231 cell lines) [186]. In addition, it is well documented that spheroids develop hypoxic cores [377,378]. Two key genes under investigation involved with hypoxia were *HIF1A* and *ERO1A*. *HIF1A* had a significantly higher expression level in 3D compared to 2D at the Day 1 timepoint. In a previous study, staining for low oxygen regions within a similar collagen scaffold seeded with MCF7 cells confirmed the presence of hypoxic niches within the scaffold after only 24 h [186]. Additionally, SEM analysis of cell seeded scaffolds in Chapter 3 identified the formation of small clusters of cells (known to have low oxygen

cores) at this early juncture, and much larger clusters were observed by Day 14 (Appendix 3.1). Furthermore, it has been shown that in response to hypoxia induction, increased expression of *HIF1A* is rapid and reaches a peak shortly after induction ($\leq$24 h) before returning to a lower baseline level of expression [453,454], which is similar to what was observed with a peak at Day 1 before a reduction in expression beyond 24 h. However, increased expression of *HIF1A* in isolation cannot definitively suggest development of hypoxia thus additional targets were necessary. *ERO1A*, a novel and emerging biomarker of hypoxia [407,408], has been observed to be overexpressed in breast cancer [409] and also in other cancers including colorectal, gastric and pancreatic [426,455,456]. *ERO1A* plays a role in disease progression through immune escape and modulating cancer cell proliferation/migration [426–428]. In contrast to *HIF1A*, alterations in *ERO1A* expression in 3D were prominent with significant expression increases at both Day 7 and Day 14 compared to 2D culture observed. To the best of our knowledge, this is the first evidence of increased *ERO1A* expression upon culture in a 3D breast cancer *in vitro* model. This result indicates the presence of hypoxia within the collagen-based scaffolds, highlighting the increased biological relevance to *in vivo* tumours that is achieved within 3D culture models in comparison to standard 2D cultures.

Induction of glycolysis and angiogenesis are two key cancer hallmarks and both processes are crucial in tumour survival and sustained growth [14]. *GAPDH*, while traditionally is a common housekeeping gene for qPCR normalisation, was found to have increased expression in 3D cultured MCF7 cells. *GAPDH* plays a key role in glycolysis and cell metabolism [398,399], and its elevation in expression as a function of time observed herein potentially indicates the switching towards anaerobic respiration (i.e., without oxygen) within the scaffolds. In addition, *GLUT1* displayed an extremely similar expression profile–

with slow increase in expression in 3D compared to 2D, reaching a significant difference by Day 14. *GLUT1* also plays a crucial role in cell glycolysis [402–404] and like *GAPDH*, is regulated by hypoxia [457]. *VEGFA* expression was significantly higher in 3D than 2D at Day 7 and trended higher at the other timepoints. VEGFA notably plays a crucial role in angiogenesis [393], and through the formation of new blood vessels in response to lowered levels of oxygen within tumours (hypoxia), it aids in tumour survival and progression [458,459]. As such, it was expected that *VEGFA* expression would increase within the collagen scaffolds developed. The temporal increase in expression of both glycolysis enzymes (*GAPDH* and *GLUT1*), *VEGFA*, and the previously discussed *ERO1A*, all point towards the development of hypoxic regions within the scaffolds, leading to a metabolic switch with increased glycolysis. These observations conform with studies into hypoxia development elsewhere, whereby Liverani *et al.* (2019) demonstrated 3D scaffold-based culture directly induced hypoxia, which lead to increased expression of *GAPDH*, increased immunohistochemical expression of GLUT1 and increased secretion of VEGF in both MCF7 and MDA-MB-231 breast cancer cells [186]. Hypoxic niches were further visualised using pimonidazole staining, which stains for poorly oxygenated cells, with large amounts of pimonidazole-positive cells observed as soon as 24 h after seeding within their collagen scaffolds [186]. While hypoxia plays a variety of roles in breast cancer pathology and general disease progression, it also plays a significant role in response to therapies, typically reducing the effectiveness of treatments and causing greater levels of chemoresistance [460,461]–representing a notable consequence of tumour hypoxia which will be discussed in greater detail within Chapter 5. As such, an *in vitro* model that can naturally induce hypoxia offers huge potential for investigation into the mechanisms behind hypoxia, the role of hypoxia in disease progression and spread, and additionally the interplay between low oxygen niches within tumours and therapeutic agents.

4.4.1 Concluding remarks

In conclusion, within our 3D collagen-based scaffolds, it was demonstrated that MCF7 cells acquire markers of matrix modulation, glycolysis and hypoxia–with significant increases in gene expression in 3D cultured cells (vs. 2D) of *LOX, MMP2, MMP9, FN1, HAS2, VEGFA, CXCR4, HIF1A, GLUT1, GAPDH* and *ERO1A*. A clear shift in the MCF7 cell populations growing within the scaffold towards a more aggressive and malignant genotype was observed. The ability of the fabricated scaffolds to drive changes in gene expression patterns highlight the potential such 3D models hold, allowing for investigations into a variety of pathways and genetic events that are involved in key processes that contribute to breast cancer development, progression and spread. The scaffolds offer a significant advantage over standard 2D cultures whereby these processes do not naturally develop as a function of time. 2D cultures are static, frozen in time and as our data shows, gene expression is relatively stable. Such results correlate well with what is understood about *in vivo* breast cancer (and other cancers) in terms of the expression of ECM modifying/synthesis genes and genes associated with hypoxia and metabolism, where these genes are frequently highly upregulated and overexpressed. In addition to further exploring phenomena and pathways involved in hypoxia or glycolysis, 3D culture also paves the way for novel biomarker discovery and finding new potential therapeutic targets to tackle breast cancer. The results within this chapter demonstrate how 3D culture within a scaffold significantly alters the genetic behaviour of cancer cells, shifting their expression profile away from what was observed in 2D culture and closer towards *in vivo* tumours.

05

Chapter 5: Assessment and validation of the collagen-based scaffolds for use as *in vitro* drug testing models

Table of Contents

5.1 Introduction

Over recent decades, there is no doubt about the advancements made in the treatment of cancers due to 2D culture and animal testing. However, as previously discussed in Chapter 1, a significant limitation to the use of 2D cultures is a greatly inflated response to drug compounds and therapeutic approaches. Similarly, the success of a drug compound in animal studies infrequently translates to success in human trials. Such inflated and altered responses results in only a ~5-10% concept to marketplace success rate, leading to significant loses in time, animal life and money [462,463]. Consequently, there is a need to develop new models that will enable better translation from bench to bedside, with 3D culture models emerging as a potential solution.

The use of 3D models has emerged in recent years, across a variety of cancers. In the most simplistic forms, these studies focused on the development of 3D spheroids and assessed the response levels towards therapeutic agents compared to traditional 2D culture [464–467]. Expanding on spheroid culture approach–research has progressed to adherence-based models including hydrogels, and of key interest to this thesis, 3D scaffold-based models [9,12,53,166,323,468]. Use of these 3D models offers an advancement on 2D cultures as they can more accurately reflect drug response *in vivo* and bridge the gap between 2D cultures and animal models/humans. From the literature, it has frequently been demonstrated across a range of cancers that there is an increase in resistance to drug-mediated cytotoxicity when cells are grown in 3D compared to 2D [9,12,166,468,469]–though this outcome can be cell line and drug dependent with the inverse outcome (i.e., increased susceptibility to drugs in 3D compared to 2D) a possibility [132,470]. Elsewhere, in the culture of both MCF7 and MDA-MB-231 breast cancer cells within a 3D collagen-based scaffold, it was found that

there was a significant increase in resistance to doxorubicin treatment in comparison to 2D culture. Notably the response profiles of cells within the 3D scaffolds as 3D culture models were analogous to responses within a mouse model, emphasising their potential to bridge the gap between 2D culture and animal models [355]. Key advantages for the use of 3D scaffolds in drug testing include: (1) identifying potential targets or candidate drugs, (2) determine response levels (for e.g., efficacy and effective/inhibitory concentrations), (3) high throughput screening of candidates, (4) toxicity studies and (5) modelling drug-cell pathway interactions [470–472]. In addition, use of 3D scaffolds may also pave the way for developing personalised medicine strategies through allowing for *ex vivo* culture of patient tumour fragments. This would allow for rapid screening of potential candidate drugs using a patient's own tumour cells to select for the best performing agent. While this is still a nascent area within 3D-based drug work, successful *ex vivo* culture of tumour fragments on 3D scaffolds has occurred for, including but not limited to, breast cancer [229,323,473], pancreatic cancer [474] and glioblastoma/renal cell carcinoma [475]. Two drugs were selected for investigation, tamoxifen and docetaxel, that are both routinely used in the treatment of breast cancer, thus are ideal candidates to assess within the 3D collagen-based scaffold culture model. Tamoxifen was an ideal candidate as it is a common treatment for estrogen receptor positive breast cancer patients–and the MCF7 cell line is a representation of estrogen receptive positive breast cancer and is known to respond to tamoxifen [476]. As a broad-spectrum chemotherapy, docetaxel was selected for its robust and well documented action against MCF7 cells [477–479], and it would provide a useful comparison to the hormone-based treatment of tamoxifen.

Tamoxifen is a hormone therapy that is used in the treatment of ER+ breast cancers, hence was a suitable compound to use due to the use of the MCF7 cell line, which is an ER+ cell

line. Tamoxifen is a selective estrogen receptor modulator, with both agonist and antagonist functions against the receptors depending on which tissue it is acting on. In regard to breast cancer, tamoxifen has antiestrogenic activity through inhibiting the binding of the estrogen hormone to the estrogen receptors [480,481]. Tamoxifen is largely cytostatic in the sense it halts cell division and maintains cells in non-dividing states rather than inducing cytotoxicity. However, in a dose-dependent manner, tamoxifen can also induce direct cell death primarily through caspase activation [482,483]. Upon administration of tamoxifen, it is metabolised by the cytochrome P450 superfamily in the liver to three metabolites, N-desmethyltamoxifen, 4-hydroxy-N-desmethyltamoxifen (endoxifen) and 4-Hydroxytamoxifen (4-OHT) [484]. For the purpose of this thesis, any tamoxifen work was carried out with the potent 4-OHT metabolite.

Docetaxel is a traditional chemotherapy belonging to the taxane family of anti-cancer drugs used in the treatment of a variety of cancers, including breast cancer. Docetaxel has been used against a variety of breast cancer subtypes as a single agent treatment, in combination with other chemotherapeutic agents, as an adjuvant therapy and also as a neoadjuvant treatment [485,486]. Docetaxel binds to microtubules, stabilising them and prevents their depolymerisation/disassembly. This results in a cancer cells progression through the cell cycle being arrested and future divisions not occurring, leading to eventual cell death [487,488]. Upon administration, docetaxel is transformed into four major metabolites by the cytochrome P450 superfamily [489]. Unlike with tamoxifen, the parent docetaxel drug is the most potent form of the drug rather than its metabolites [489].
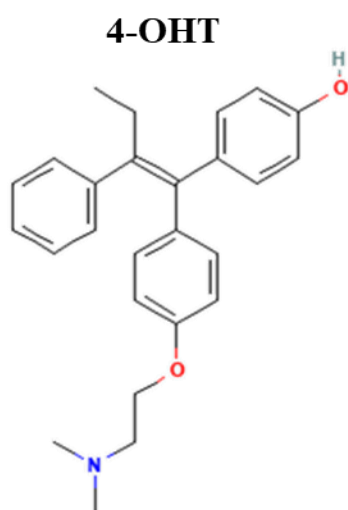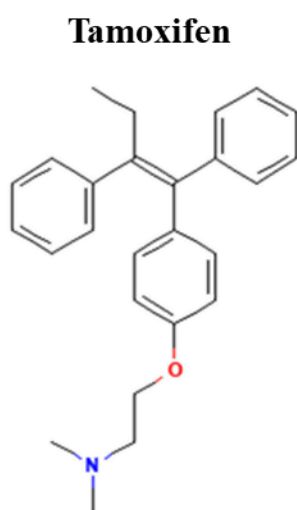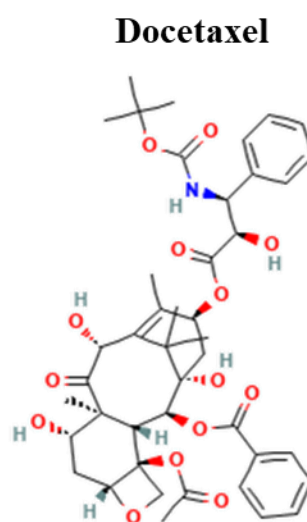
Figure 5.1: Structure of Tamoxifen and Docetaxel. **(A)** Tamoxifen and 4-OHT Structure. PubChem Identifier: CID 2733526 [490]. 4-OHT PubChem Identifier: CID 449459 [491]. **(B)** Docetaxel structure. PubChem Identifier: CID 148124 [492].

5.1.1 Chapter aims

Within this chapter, the primary objective was to assess and validate the use of fabricated collagen-based scaffolds as a suitable *in vitro* culture model for therapeutic assessment. Studies completed used the previously validated scaffold composition, w/Gel 0.15%.

Primary aims of this chapter were to:

- Determine response to tamoxifen and docetaxel in 2D culture of MCF7 cells
- Calculate the relative IC_{50} concentrations for both drugs for use in 3D cultures
- Assess the response of MCF7 cells cultured in 3D to drug treatment
- Investigate the effect of cell culture duration within the 3D scaffolds prior to drug exposure
- Investigate any potential effect of altered scaffold mechanical properties on cell proliferation rates and cellular response to drug treatment

5.2 Materials and methods

5.2.1 Solutions/reagents

Phosphate buffer saline solution 10X: 80 g sodium chloride (NaCl), 2 g potassium chloride (KCl), 14.4 g sodium phosphate dibasic dihydrate (Na$_2$HPO$_4$), 2.4 g potassium phosphate monobasic (KH$_2$PO$_4$) into 800 mL distilled water and adjusted to 1 L. Diluted to 1x when needed. All mentions of PBS in the following studies were a 1x /0.01 M concentration. All materials from Sigma-Aldrich Chemical Co, Wicklow, Ireland.

Tamoxifen: Tamoxifen was purchased as a 10 millimolar (mM) solution in absolute ethanol (Product Number - 5.08225; Sigma-Aldrich Chemical Co, Wicklow, Ireland). 10 mM tamoxifen stock was aliquoted into smaller volumes and stored at -20 °C until required.

Docetaxel: Docetaxel was purchased as a 1 mg powder (Product Number - 9886; Cell Signalling Technology, Massachusetts, United States) and was reconstituted to a 1 mM concentrated stock in DMSO. The concentrated stock was aliquoted into smaller volumes and stored at -20 °C until required.

5.2.2 Dose-Response curves in 2D for tamoxifen and docetaxel

Dose-Response curves were generated for MCF7 cells grown in 2D after exposure to both tamoxifen and docetaxel in 96 well plates. MCF7 cells were seeded at a density of 5 x 10^3 per well and maintained in 100 µL DMEM media at 37 °C for 24 h prior to drug exposure. Tamoxifen was prepared as detailed (§5.2.1) before cells were exposed to a serial dilution of a concentration range of 0 to 20 micromolar (µM). Serial dilutions (details in Table 5.1) were initially made to 2x (0 – 40 µM) and were diluted to 1x (0 – 20 µM) upon addition of

100 µL 2x drug/media to the 100 µL DMEM media already placed in the 96 well plates. For the initial 40 µM solution, per 1 mL, 4 µL of 10 mM tamoxifen stock was added to 996 µL DMEM media – volumes were scaled up to higher volumes as needed. For docetaxel (see §5.2.1 for preparation), cells were exposed to a serial dilution of a concentration range of 0 to 5 micromolar (µM). Serial dilutions (details in Table 5.2) were initially made to 2x (0 – 10 µM) and were diluted to 1x (0 – 5 µM) upon addition of 100 µL 2x drug/media to the 100 µL DMEM media already placed in the 96 well plates. For the initial 10 µM solution, per 1 mL, 10 µL of 1 mM docetaxel stock was added to 990 µL DMEM media – volumes were scaled up to higher volumes as needed. A vehicle control was setup alongside the serial dilutions, substituting the initial volume of tamoxifen or docetaxel stock in dilution 1 (Table 5.1 and Table 5.2) with an equal volume of the solvent used, in this case absolute ethanol or DMSO. In the serial dilutions shown, this was 10 µL of absolute ethanol diluted to a final volume of 2.5 mL with DMEM media (tamoxifen vehicle control) and 25 µL of DMSO diluted to a final volume of 2.5 mL with DMEM media (docetaxel vehicle control). This was to ensure the relevant drug solvent concentration was not toxic itself and also to correct the assay results for any potential background effect of DMSO or ethanol, leaving only the effect of tamoxifen or docetaxel being measured. Growth inhibition/cell viability was determined by the alamarBlue assay as per §3.2.7. The half maximal inhibitory concentration (IC_{50}) was calculated based on the dose-response curves as per §5.2.5. The IC_{50} value is the concentration of drug that produces the halfway response between the bottom and top of the dose response curve. Results were graphed as viability (percentage relative to the 100% viability representing vehicle control) vs. drug doses (Molar (M)). Doses within the serial dilution were converted to Mol by applying a log_{10} transformation.

Table 5.1: Serial dilution series for tamoxifen.

Dilution	Volume (µL)	Source	DMEM (µL)	Conc. 2x (µM)	Conc. 1x (µM)
1	10	10 mM stock	2490	40	20
2	500	Dilution 1	2000	8	4
3	500	Dilution 2	2000	1.6	0.8
4	500	Dilution 3	2000	0.32	0.16
5	500	Dilution 4	2000	0.064	0.032
6	500	Dilution 5	2000	0.0128	0.0064
7*	500	Dilution 6	2000	0.0026	0.0013

*Discard 500 µL from dilution 7 after mixing in order to obtain the correct volume and concentration.

Table 5.2: Serial dilution series for docetaxel.

Dilution	Volume (µL)	Source	DMEM (µL)	Conc. 2x (µM)	Conc. 1x (µM)
1	25	1 mM stock	2475	10	5
2	500	Dilution 1	2000	2	1
3	500	Dilution 2	2000	0.4	0.2
4	500	Dilution 3	2000	0.08	0.04
5	500	Dilution 4	2000	0.016	0.008
6	500	Dilution 5	2000	0.0032	0.0016
7*	500	Dilution 6	2000	0.00064	0.00032

*Discard 500 µL from dilution 7 after mixing in order to obtain the correct volume and concentration.

5.2.3 Docetaxel response in 3D cultures

5.2.3.1 Treatment of 3D scaffolds with docetaxel

w/Gel 0.15% scaffolds were prepared as per §3.2.3. Each scaffold was seeded with 1×10^5 MCF7 cells as per §3.2.5. Unless otherwise stated, each scaffold was then incubated in a humidified 5% CO_2 incubator at 37 °C for 7 days prior to drug exposure, to allow cells to grow to sufficient numbers and adapt to the 3D environment. Docetaxel was prepared as per §5.2.1. Three drug doses were used during studies including 3D culture; 0.00028 µM (IC_{50}), 0.1 µM and 1 µM (the specific doses used are listed under each study). To achieve these concentrations, the 1 mM docetaxel stock solution (§5.2.1) was aliquoted to lower concentrations by a series of direct dilutions, calculated by the $C_1V_1 = C_2V_2$ dilution formula, in order to achieve the listed final concentrations. Drug exposure was conducted over five days (120 h) in a humidified 5% CO_2 incubator at 37 °C, with replenishment of media at the midpoint. During 3D culture, scaffolds were submerged in 1.5 mL of DMEM media/docetaxel. Vehicle controls for each dose using the equivalent volume of DMSO-only were used in any works involving 3D scaffolds. Cell viability was calculated as a percentage relative to each vehicle control, with the vehicle control representing a theoretical max viability of 100%. Viability was determined using the previously described alamarBlue assay in §3.2.7.

5.2.3.2 Comparison of response to docetaxel in 2D vs. 3D

Response to docetaxel in both 2D and 3D was assessed to determine differential responses caused by the culture method rather than dosage concentration. 96-well plates for the 2D cultures were seeded with 5×10^3 MCF7 cells and maintained at 37 °C for just 24 h prior to drug exposure. Alongside, w/Gel 0.15% scaffolds were prepared as §5.2.3.1 and maintained

in humidified 5% CO_2 incubator at 37 °C for 7 days. After, the calculated IC_{50} concentration for docetaxel from §5.2.2 of 0.00028 µM (based on the 2D dose-response curves) was used, and additional doses of 0.1 µM and 1 µM were formulated. It was hypothesized that the low IC_{50} dose would produce a limited response in 3D thus two larger doses were also used to increase the cytotoxicity in 3D cultures and allow for better comparison between 2D and 3D setups. Viability was determined as previously described in §5.3.2.1.

5.2.3.3 Influence of 3D culture duration on response to docetaxel

As reported in Chapter 4, differential gene expression patterns were observed across the three timepoints investigated, Day 1, Day 7 and Day 14. As a result, it was decided to investigate if different culture periods prior to drug exposure have a meaningful impact on drug response, owing to cells undergoing changes in genotype/phenotype. Seeding and treatment of scaffolds was carried out as per §5.2.3.1. For this assessment, cells were cultured on the scaffolds for three periods rather than just one prior to treatment, 1, 7 or 14 days. Each scaffold was then exposed to a single docetaxel concentration of 1 µM, using the highest previously used concentration to maximise potential differences between the three pre-culture periods. Drug exposure was conducted over five days and viability was determined as previously described in §5.3.2.1.

5.2.4   Influence of scaffold mechanical properties on docetaxel response

The effect of varied scaffold mechanical properties on response to drug exposure was investigated. w/Gel 0.15% scaffolds were prepared using two different EDAC crosslinking regimes, as described previously in §2.2.6, to generate two groups of relatively low and high

elastic modulus. Elastic modulus was used as an indicator of stiffness to represent the increasing stiffness common of breast cancer tissue/ECM.

- Low Stiffness (4 mM EDAC per gram of scaffold)
- High Stiffness (80 mM EDAC per gram of scaffold)

4 mM was used rather than the previously used 6 mM (Chapter 2 §2.2.6) in an effort to increase the potential difference between the two scaffold groups. Scaffolds were characterised mechanically initially to ensure a sufficiently large difference in elastic modulus was achieved (§5.2.4.1). Each scaffold group was then assessed for cell proliferation rates to determine if the increase in elastic modulus had an effect on this (§5.2.4.2). Finally, each scaffold group was exposed to docetaxel to assess if the altered mechanical properties had any effect on response to treatment (§5.2.4.3).

5.2.4.1 Mechanical characterisation

Unconfined compression testing was completed as described in §2.2.10 to determine the elastic moduli for the two scaffold groups. Briefly, each w/Gel 0.15% scaffold of ~9 x 4.5 mm (diameter x height) was crosslinked and maintained in a hydrated state for the duration of testing. Testing was completed using a mechanical testing machine fitted with a 5 N load cell. Tests were performed at a rate of 10% strain/min to a maximum of 20%. The elastic modulus was calculated from the slope of the linear region (i.e., between 2-5% strain) of the stress vs. strain curves for each scaffold.

5.2.4.2 Impact of mechanical properties on cell proliferation

The potential effect of significantly increasing elastic modulus of the scaffold on the proliferation of cells was investigated. The two scaffold groups were prepared as above, §5.2.4 (and in full detail in §2.2.6). Each scaffold was then incubated overnight in DMEM supplemented with 50% FBS in a humidified 5% CO_2 incubator at 37 °C. Following this, each scaffold was seeded with 1 x 10^5 MCF7 cells as per §3.2.5. The duration of the study was 2-weeks, with analysis timepoints at Day 1, Day 4, Day 7 and Day 14. Cell proliferation was assessed through DNA quantification as per §3.2.8.

5.2.4.3 Effect of mechanical properties on docetaxel response

The 'low stiffness' (4 mM EDAC) and 'high stiffness' (80 mM EDAC) scaffolds were prepared as above for assessing if the increased elastic modulus affected response to docetaxel. Each scaffold tested was seeded with 1 x 10^5 MCF7 cells and then incubated in a humidified 5% CO_2 incubator at 37 °C for 7 days. Each scaffold was then treated with a docetaxel concentration of 1 µM with response levels determined as per previously described (§3.2.7).

5.2.5　Non-linear regression analysis of dose response curves

To determine the relative IC_{50} values, non-linear regression analysis was completed using the GraphPad Prism software, version 8.0.2 (GraphPad Software, Inc., San Diego, CA, www.graphpad.com), using the log(inhibitor) vs. response -- Variable slope (four parameters) equation. Where possible, GraphPad Prism was allowed to automatically fit the top and bottom plateaus. In the case of docetaxel, it was found that the top plateau could not be automatically defined to any degree of accuracy to due to steep hillslope of the curve.

Thus, as the vehicle control defined a lack of inhibition, a top plateau constraint value of 100 (i.e., 100% viability or 0% inhibition) was applied to the model. As data for 0% viability was not provided (i.e., 100% inhibition), no bottom plateau constraints were applied to either tamoxifen or docetaxel curves. The variable slope model automatically detects the curves hillslope. The above analysis produces a relative IC_{50} value, which represents the concentration of the drug that produces the halfway response between the bottom and top of the curve. This is in contrast to the absolute IC_{50}, which determines the concentration of drug required to cause a reduction in viability to 50% (i.e., the 50% mark of the Y-axis).

5.2.6 Statistical analysis

Statistical analysis was completed using the GraphPad Prism software (version 8.0.2). The minimum number of samples tested was n=3. One-way ANOVA (with Tukey post-hoc tests) or unpaired t-tests were performed to assess the difference between samples. For unpaired t-tests, statistical significance was determined without correction for multiple comparisons and each row was analysed individually, without assuming a consistent SD. Results calculated and shown in graphs were the mean $\pm$ the standard deviation (SD). p-value $\leq 0.05 = *$, p-value $\leq 0.01 = **$, p-value $\leq 0.001 = ***$.

5.3   Results

5.3.1   2D Dose-Response curves for tamoxifen and docetaxel

Dose response curves were initially generated in 2D using MCF7 cells to determine a baseline response by the cell line in use and to determine IC_{50} values that could be used moving forward in 3D applications. With tamoxifen, response to drug exposure was rather poorly defined (Fig. 5.2). After 24 h of treatment, there were no differences between the control and all concentrations of tamoxifen. At 48, 72 and 120 h, there was a large reduction in cell viability upon treatment with 20 µM tamoxifen (p-value $\leq$0.001, Appendix 5.1). For both 48 and 72 h exposure periods, barring the 20 µM concentration, mean viabilities remained high with values generally >90% and were not significantly different to the control. With 120 h exposure time, there was an increase in growth inhibition observed for all doses compared to the vehicle control, with mean viabilities for concentrations up to 4 µM ranging between 70-80% (p-value $\leq$0.001 vs. all other exposure times, Appendix 5.1). However, the trend remained that only by the maximum concentration was there a considerable effect. For all concentrations, exposure for 120 h resulted in a significantly higher level of growth inhibition (p-value $\leq$0.001, Appendix 5.2). Non-linear regression analysis failed to return a viable result in terms of IC_{50} for the 24 h exposure group. For the 48 h and 72 h exposures, analysis returned a consistent IC_{50} between the two groups of 17 µM (IC_{50} is labelled with a dotted line in Fig. 5.3). For the 120 h group, the IC_{50} was predicted to be off curve, a high dose of 114.8 µM.

To note, due to low efficacy and high concentrations required for measurable growth inhibition achieved using tamoxifen, its use was discontinued prior to commencing 3D culturing and assessment.
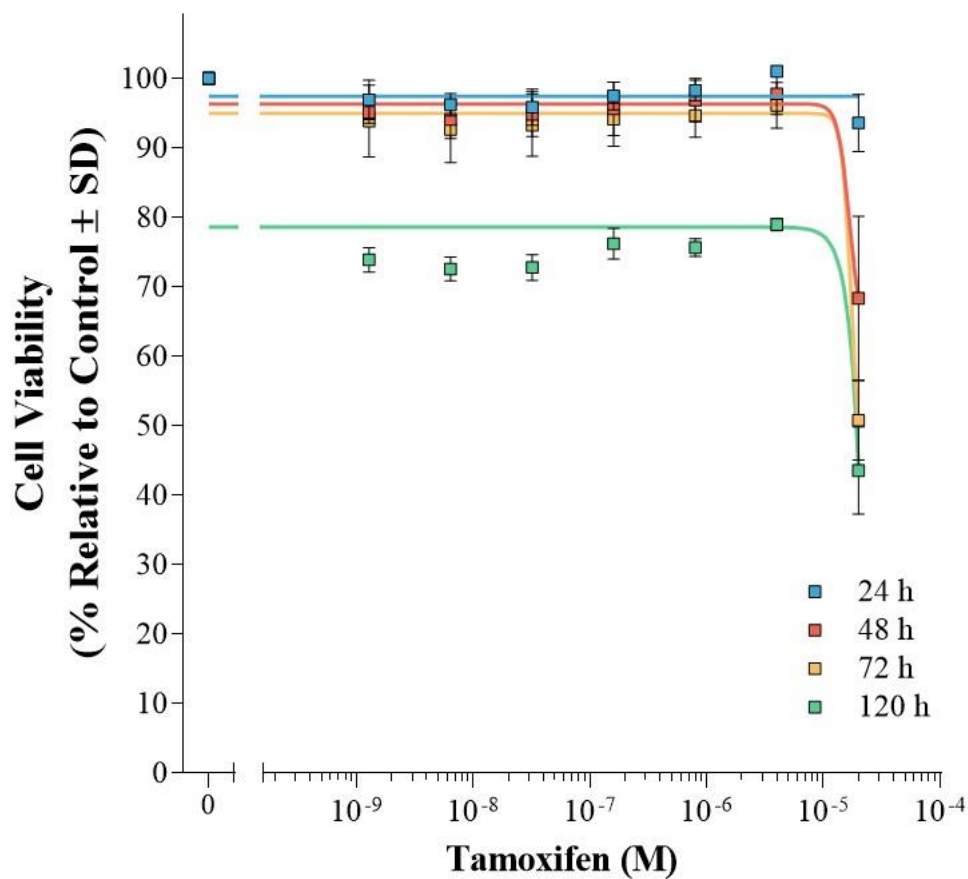
Figure 5.2: Dose response curve for tamoxifen. Dose response curves were constructed, consisting of a vehicle control (no tamoxifen) and a serially diluted 7-part concentration range. Cells were exposed to the range of tamoxifen concentrations for either 24, 48, 72 or 120 h. Cell viability was determined using the alamarBlue assay. Results show viability (percentage relative to the 100% viability representing vehicle control) vs. drug doses (M). Data points shown are the mean $\pm$ SD (n=3).
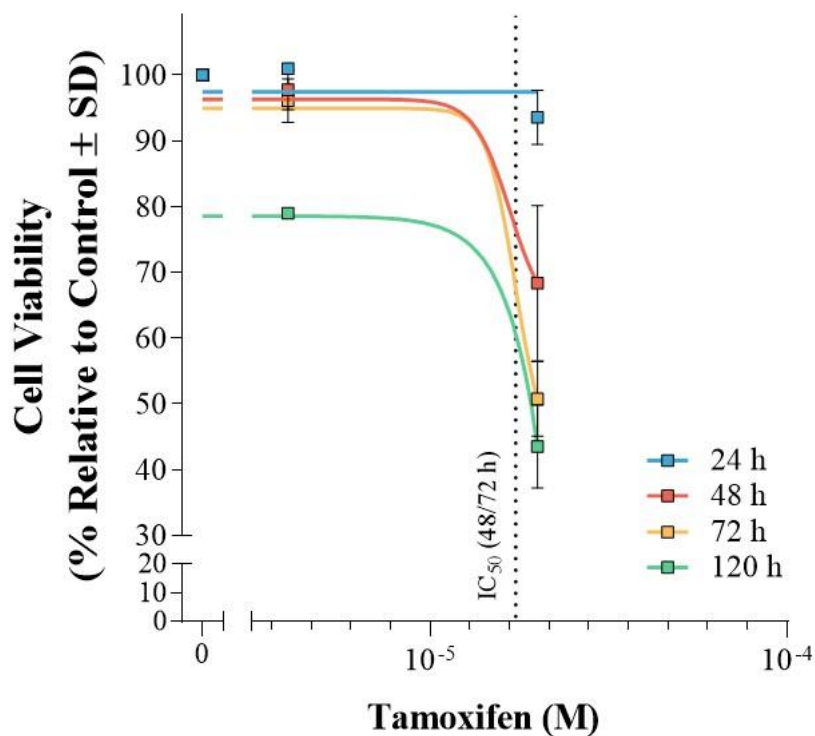
Figure 5.3: Dose response curve for tamoxifen – IC$_{50}$ focus. Dose response curves from Fig. 5.1 were magnified to focus on the region that non-linear regression calculated the IC$_{50}$ values within. The relative IC$_{50}$ values are represented by the dashed line. No IC$_{50}$ value could be accurately calculated for the 24 h exposure period and the relative IC$_{50}$ for 120 h exposure was off curve. Predicted IC$_{50}$ values after 48 and 72 h was 17 µM.

Docetaxel produced a better overall response in the MCF7 cell line, with more readily measured cytotoxicity and reduction in viability at all exposure periods, which was not seen in the tamoxifen dose curve whereby only the 120 h exposure period produced measurable growth inhibition at multiple concentrations of the drug. Across each exposure group, the maximal effect was reached rapidly, producing a steep hillslope in the dose response curve (Fig. 5.4). A large bottom plateau at this maximal effect was observed–despite further increases in docetaxel strength, no further increase in growth inhibition was observed. For the 24h, 72 h and 120 h exposure periods, there were no differences in cell viability/growth inhibition for the range of docetaxel concentrations investigated, while at 48 h there was a decrease in viability for all doses compared to the lowest 0.00032 µM concentration (p-value ≤0.05, Appendix 5.3). Across all concentrations, treatment for 72 h and 120 h resulted in a significant increase in growth inhibition compared to the 24 h treatment time (p-value ≤0.01, Appendix 5.4). Non-linear regression analysis resulted in largely consistent IC_{50} values across all four exposure times, with a relative IC_{50} of 0.00028 µM achieved. As it produced the largest total amount of growth inhibition/cytotoxicity, it was decided to utilise the 120 h exposure time for all remaining works in this thesis chapter. The relative IC_{50} for docetaxel and 120 h drug exposure was 0.00028 µM, which can be seen by the dotted line on the zoomed graph in Fig. 5.5.
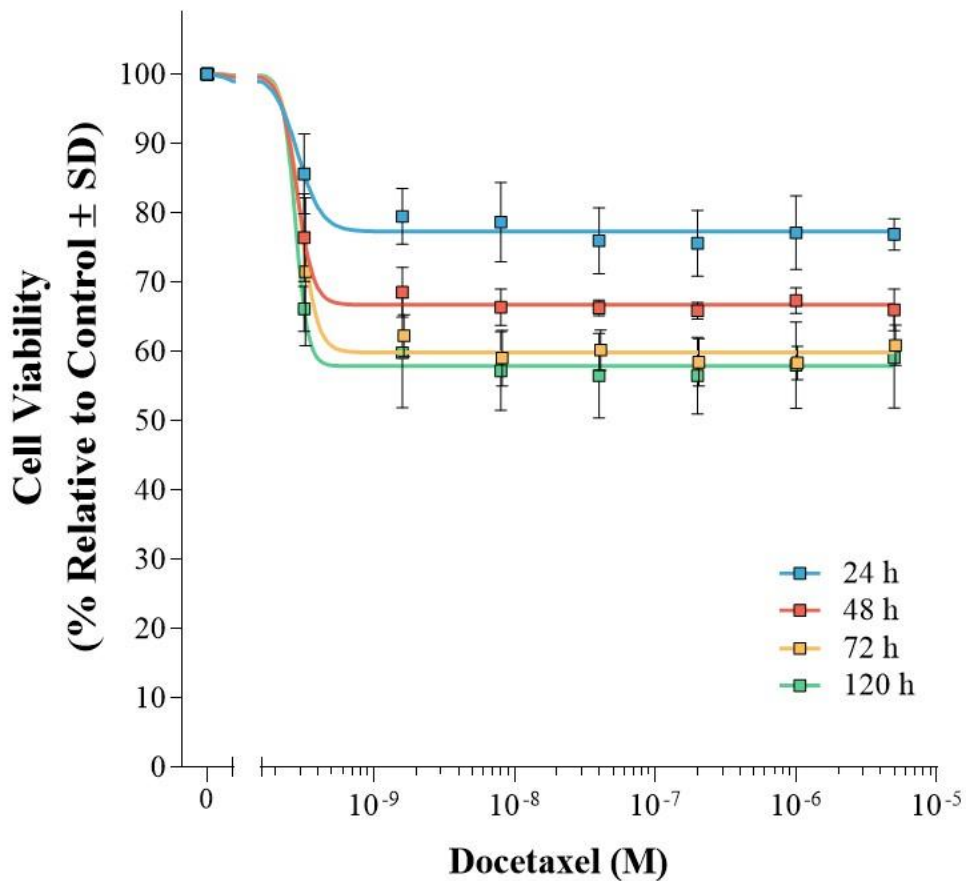
Figure 5.4: Dose response curve for docetaxel. Dose response curves were constructed, consisting of a vehicle control (no docetaxel) and a serially diluted 7-part concentration range. Cells were exposed to the range of docetaxel concentrations for either 24, 48, 72 or 120 h. Cell viability was determined using the alamarBlue assay. Results show viability (percentage relative to the 100% viability representing vehicle control) vs. drug doses (M). Data points shown are the mean $\pm$ SD (n=3).
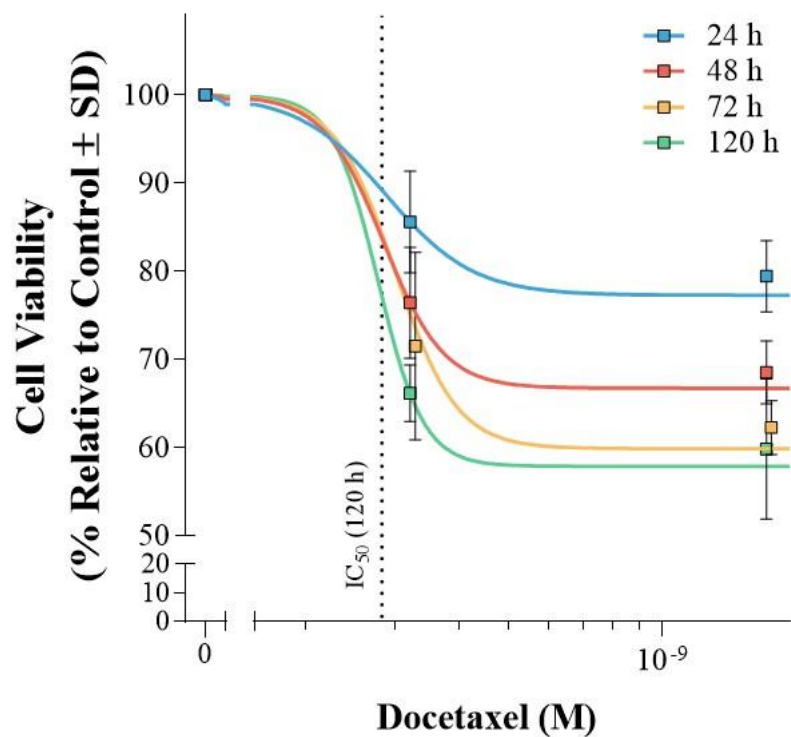
Figure 5.5: Dose response curve for docetaxel – IC$_{50}$ focus. Dose response curves from Fig. 5.4 were magnified to focus on the region that non-linear regression calculated the IC$_{50}$ value within. The relative IC$_{50}$ values are represented by the dashed line. IC$_{50}$ values were consistently across all four exposure periods at 0.00028 µM. As cytotoxicity levels were highest in cells exposed to docetaxel for 120 h, this exposure period was selected for future experiments.

5.3.2 Response to docetaxel in 2D vs. 3D

The response to three different concentrations of docetaxel (the previously calculated relative IC_{50} for docetaxel of 0.0028 µM, 0.1 µM and 1 µM) was assessed in both 2D and 3D (Fig. 5.6A-B), with a pre-culture duration of seven days and an exposure to docetaxel for five days. For all three doses, a significant difference in sensitivity to docetaxel was observed between the two culture conditions (p-value ≤0.001)–with cells grown in 3D displaying less growth inhibition than 2D counterparts (Fig. 5.6A). This demonstrated an increase in chemoresistance stemming from culturing the MCF7 cells in 3D compared to 2D. In 3D culture, there was limited response to the IC_{50} concentration, with a mean viability of >90%, with significantly less growth inhibition than seen in 2D at this dose (p-value ≤0.001). The two higher concentrations of 0.1 µM and 1 µM both produced a measurable cytotoxic effect and drop in MCF7 cell viability; however, this inhibition of growth was still significantly lower than achieved with the same doses in 2D cultures. In 2D cultures, 0.1 µM docetaxel reduced mean cell viability to 49.59 ± 0.10% while in 3D viability remained higher at 76.44 ± 4.85% (p-value ≤0.001). With the 1 µM docetaxel treatment, mean cell viability was reduced to 49.91 ± 1.11% in 2D cultures while in 3D mean viability was observed to be 77.55 ± 4.26% (p-value ≤0.001). Within 3D cultures (Fig. 5.6B), there was a significant increase in growth inhibition in both 0.1 µM and 1 µM treatments compared to the IC_{50} concentration (p-value ≤0.01).
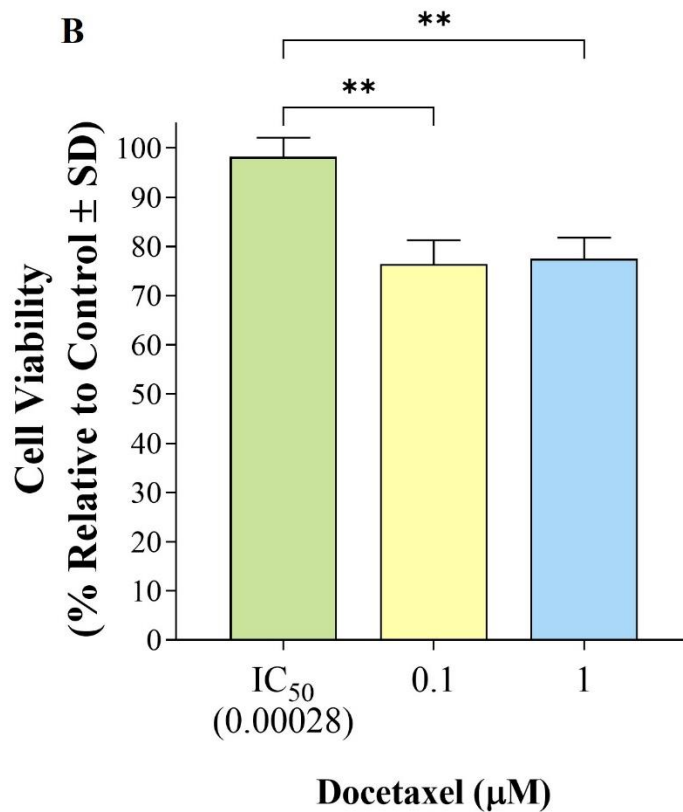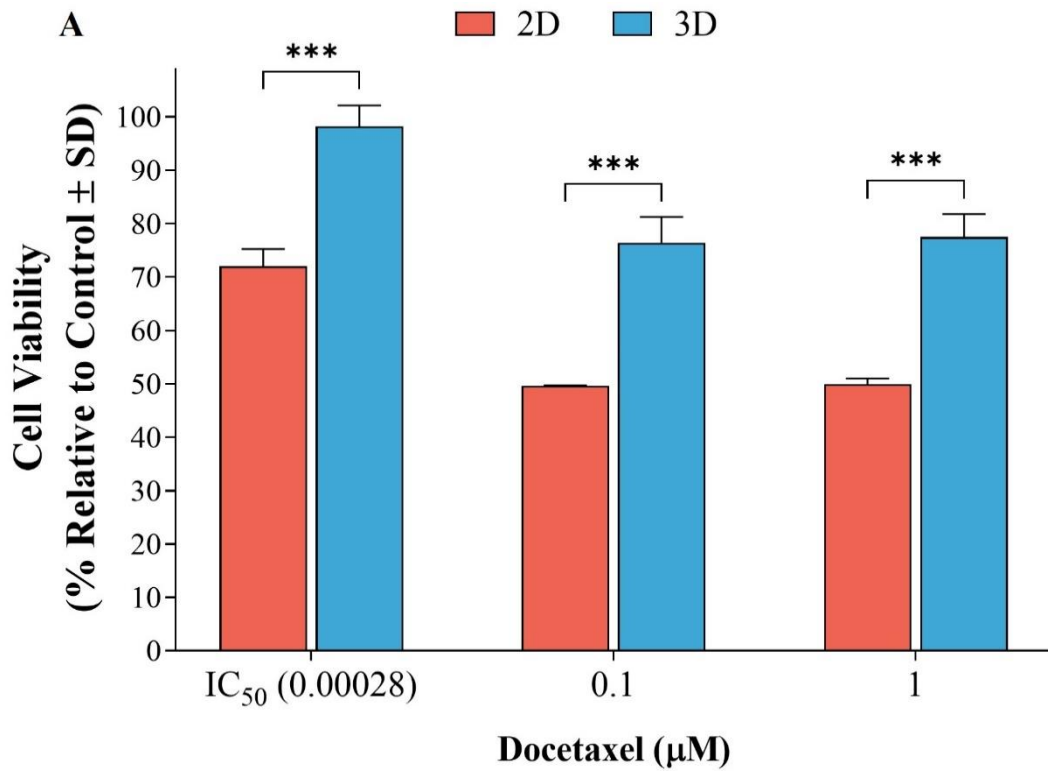
Figure 5.6: MCF7 response in 2D and 3D to varied docetaxel concentration. (A) Cells cultured in 2D or 3D scaffolds were exposed to the relative IC_{50} for docetaxel and an additional two doses of 0.1 and 1 µM. Variance was tested using two-way ANOVA with Bonferroni post-hoc test. **(B)** Highlights MCF7 viability data in 3D only. Variance was tested using one-way ANOVA with Tukey post-hoc test. Cell viability was determined using the alamarBlue assay. Results shown are the mean ± SD (n=3). p-value $\leq$0.05 = *, p-value $\leq$0.01 = **, p-value $\leq$0.001 = ***.

For further analysis, the values achieved from the vehicle controls and the three docetaxel doses in both 2D and 3D were graphed as dose response curves to calculate the respective IC_{50} values (Fig. 5.7). The 2D and 3D cultures displayed a large bottom plateau representing the maximal drug effect as seen in previous dose response curves (§5.3.1). Non-linear regression analysis produced a 2D relative IC_{50} of 0.00028 µM, consistent with the previously constructed dose response curves in §5.3.1. For the 3D culture however, the calculated IC_{50} was 0.00045 µM–greater than that seen in 2D culture. Dotted lines representing both relative IC_{50} values are shown, highlighting the large difference between the two culture conditions. This change represents a docetaxel concentration increase of 60.7% to achieve the halfway response between top and bottom plateaus (i.e., the IC_{50}) under 3D scaffold culture when compared to 2D.
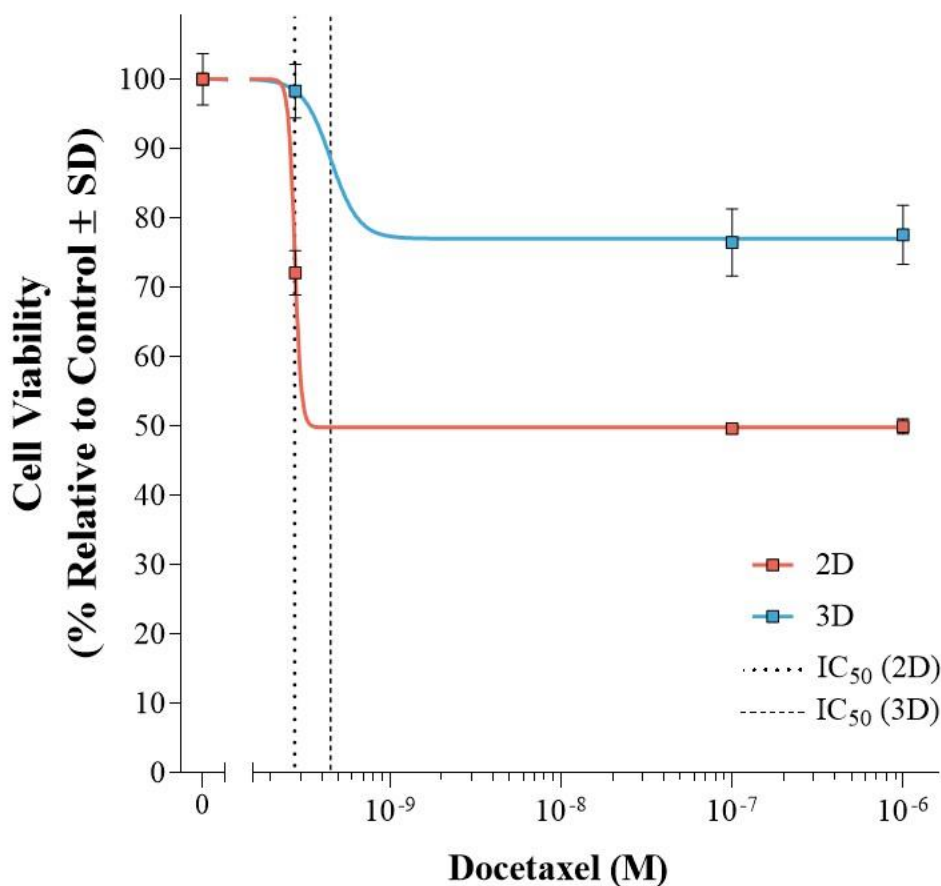
Figure 5.7: 2D vs. 3D dose response curve (docetaxel). 2D and 3D response data from Fig. 5.5 was converted to a four-point dose response curve (vehicle control and x3 docetaxel doses). Non-linear regression analysis was carried out to produce relative IC_{50} values for both 2D and 3D samples. Cell viability was determined using the alamarBlue assay. Results show viability (percentage relative to the 100% viability representing vehicle control) vs. drug doses (M). Data points shown are the mean $\pm$ SD (n=3).

5.3.3 Effect of culture duration prior to drug exposure

The duration of cell culture and acclimatisation to the 3D scaffold environment had a significant effect on the response to docetaxel exposure. Based on data from previous studies herein, it was decided to use a higher dose of docetaxel (1 µM) to maximise the level of cytotoxicity observed due to the lower response levels in 3D cultures. A large reduction in viability was observed in the 3D collagen-based scaffolds pre-cultured for only one day, with a mean viability of $56.2 \pm 1.1\%$ recorded (Fig. 5.8). There was an increase in resistance to cytotoxicity observed in both other groups, where cells were cultured for 7 days and 14 days prior to docetaxel exposure (p-value ≤ 0.001). Mean viabilities of $74.5 \pm 2.7\%$ and $69.9 \pm 5.1\%$ were recorded for the Day 7 and Day 14 exposures, respectively.
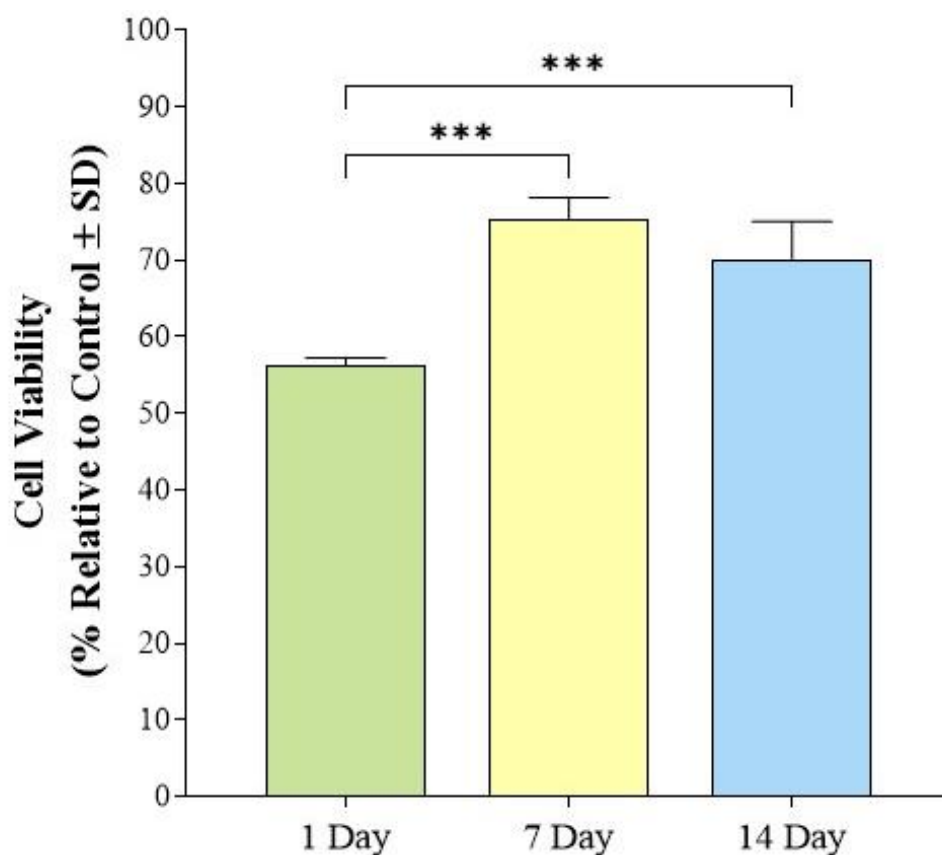
Figure 5.8: Effect of pre-culture duration on docetaxel response in 3D. MCF7 cells were pre-cultured prior to drug treatment for three different time periods, 1, 7 and 14 days, within the w/Gel 0.15% scaffolds. Then, the samples were treated with 1 µM of docetaxel for 120 h (5 days). Cell viability was determined using the alamarBlue assay. Variance was tested using one-way ANOVA with Tukey post-hoc test. Results shown are the mean ± SD (n=3). p-value ≤0.05 = *, p-value ≤0.01 = **, p-value ≤0.001 = ***.

5.3.4 Effect of scaffold mechanical properties on response to docetaxel

The potential impact of the mechanical properties of the scaffold was next assessed. Two scaffold groups of altered elastic modulus were utilised; a 'low stiffness' scaffold crosslinked with 4 mM EDAC and a 'high stiffness' scaffold crosslinked with 80 mM EDAC. For completeness, both scaffold groups were initially assessed against their mechanical properties (elastic modulus) and proliferation rates (DNA quantification). The high stiffness scaffold had an elastic modulus of 3.2 ± 0.28 kPa, and this was significantly larger than the low stiffness scaffolds which had an elastic modulus of 1.04 ± 0.14 kPa (Fig. 5.9, p-value ≤ 0.001).

The relative change of DNA quantity per scaffold was assessed over a 2-week period (Fig. 5.10). At both Day 4 and Day 7, there were no differences in the relative change values of DNA between the low and high stiffness scaffolds. However, by Day 14, there was a significant increase (p-value ≤ 0.001) in the DNA quantity (relative change to Day 1) of the high stiffness scaffolds. This indicates a large increase in cell proliferation within the scaffolds of increased elastic modulus.
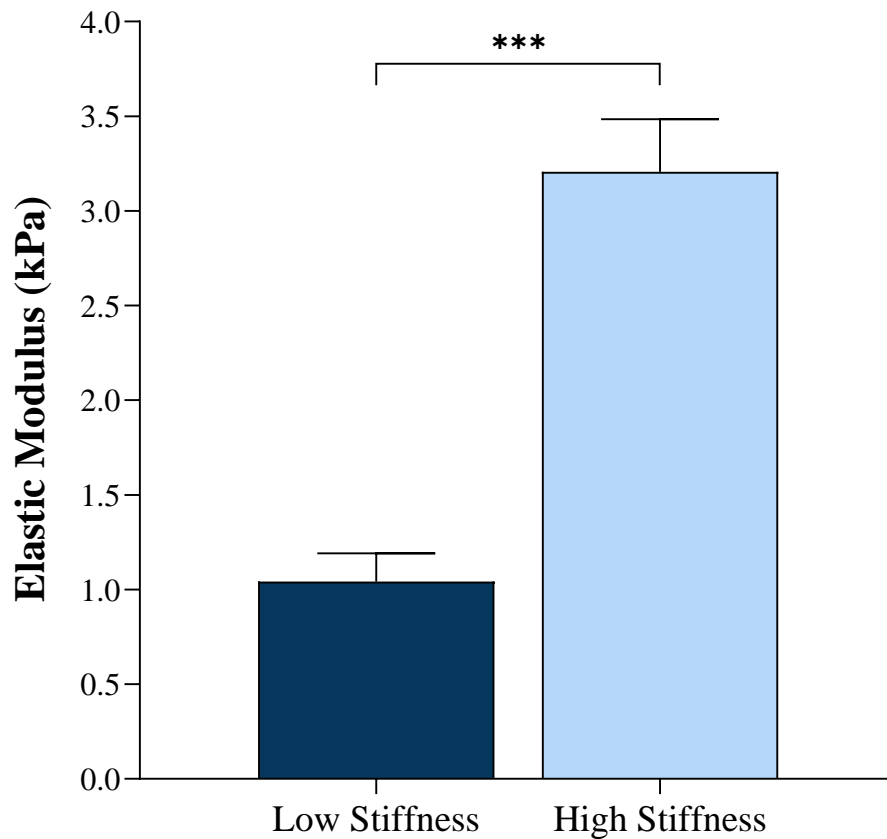
Figure 5.9: Mechanical characterisation of low/high stiffness scaffolds. The elastic modulus for each scaffold group, low stiffness (4 mM EDAC) and high stiffness (80 mM EDAC) was determined using unconfined compression testing in a hydrated environment. The modulus was determined through the slope of the line of the 2-5% linear region of the stress-strain curves. Variance was tested using an unpaired t-test. Results shown are the mean $\pm$ SD (n=5). p-value ≤ 0.05 = *, p-value ≤ 0.01 = **, p-value ≤ 0.001 = ***.
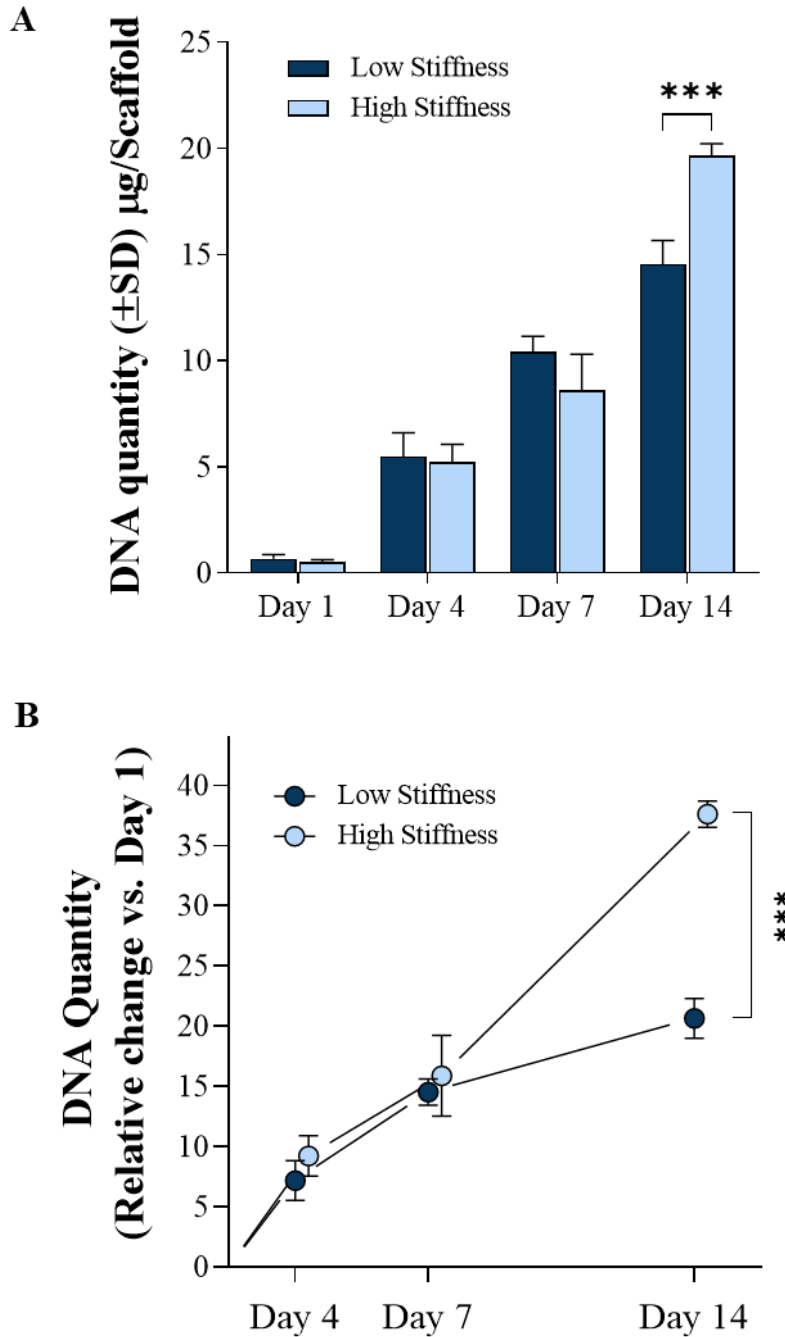
Figure 5.10: Quantification of DNA from MCF7 cells in low/high stiffness 3D scaffolds. (A) Raw quantification of DNA amounts per scaffold. Cells were seeded onto scaffolds for a two-week timeframe. Scaffold/Cell constructs were then digested via papain enzyme, with DNA quantified using the HOECHST-based fluorometric assay. **(B)** DNA quantity increases, relative to Day 1 (relative change). Variance was tested using two-way ANOVA with Bonferroni post-hoc test. Results shown are the mean ± SD (n=4). p-value ≤0.05 = *, p-value ≤0.01 = **, p-value ≤0.001 = ***.

Finally, response to drug treatment was investigated. MCF7 cells were cultured for 7 days prior to docetaxel exposure. There was a similar reduction in viability observed in both scaffold groups (Fig. 5.11). The low stiffness (4 mM) scaffold demonstrated a mean viability of 75.67 ± 6.88% while the high stiffness (80 mM) scaffold had a mean viability of 76.13 ± 1.34%. There was no impact of altering the scaffold elastic modulus in terms of chemosensitivity to docetaxel.
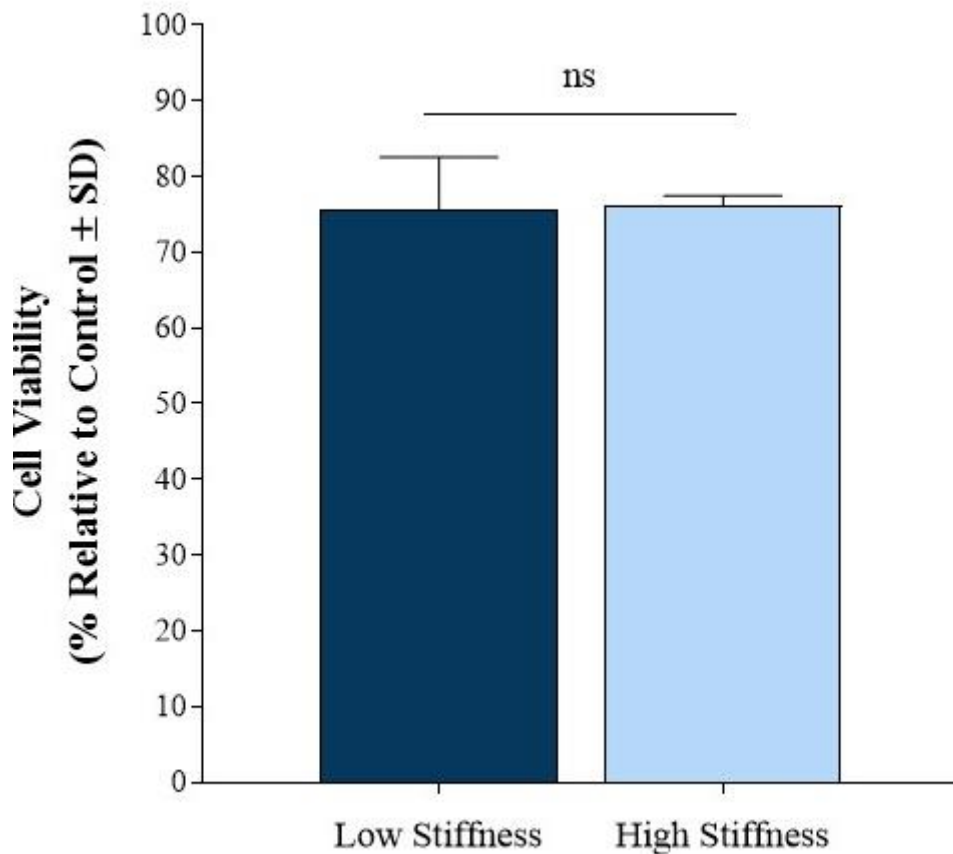
Figure 5.11: Effect of scaffold stiffness on docetaxel response. MCF7 cells were cultured on both low and high stiffness scaffolds for 7 days. Cells were then exposed to 1 µM of docetaxel for 120 h (5 days). Variance was tested using an unpaired t-test. Cell viability was determined using the alamarBlue assay. Results shown are the mean ± SD (n=3). p-value ≤0.05 = *, p-value ≤0.01 = **, p-value ≤0.001 = ***, ns = no significance.

5.4   Discussion

A crucial aspect of 3D *in vitro* models is the application in the field of drug testing and discovery. This chapter initially focused on the validation of the 3D collagen-based scaffolds as test beds for therapeutic agents. Stemming from this validation, it was then sought to assess certain aspects of the 3D scaffolds that may influence the response, such as the duration of culture of the cells prior to treatment and the mechanical properties of the scaffold.

Initial work was carried out in 2D, to determine a response by the MCF7 cells and to find out a starting point for 3D work by determining the relevant relative IC_{50} concentrations within our laboratory setup. In terms of the drugs assessed, tamoxifen was minimally effective in 2D and only at the max dosage was any measurable reduction in cell viability observed. As such, the non-linear regression analyses were poor fits across the different exposure periods (Fig. 5.2). As tamoxifen is typically cytostatic at low doses *in vitro* [482,483], this result was not unexpected. The curves produced were similar to previously reported findings, where tamoxifen (4-OHT) produced little to no growth inhibition in MCF7 cells (i.e., reduction in viability) at doses ≤10 µM (10^{-5} [M])–but at doses higher than 10 µM, there was a rapid and steep increase in growth inhibition [493,494]. In contrast, it has also been reported that greater growth inhibition occurred at lower doses using 4-OHT, whereby growth inhibition of ~40% was observed at doses including 2.5 µM [495] and 0.1 µM [496], again both in MCF7 cells. The calculated relative IC_{50} value of 17 µM is in line with many previously reported studies using tamoxifen (4-OHT) and MCF7 cells, where IC_{50} values in the range of 11.3-27 µM were documented [451,497–499]. Nonetheless, in terms of practicality, the use of the large doses/volumes of tamoxifen that were required for

measurable responses was not desirable. Docetaxel performed significantly better in 2D with a more pronounced, rapid and defined effect on cell viability observed (Fig. 5.4). Resulting non-linear regressions were excellent fits and allowed for the relative IC_{50} to reliably be calculated, with a consistent relative IC_{50} for 1, 2, 3 and 5 days of drug exposure. In previously reported studies, there are variations in reported IC_{50} values in similar studies using docetaxel and MCF7 cells. Elsewhere, IC_{50} values for docetaxel against MCF7 cells after 72 h exposure include 0.0038 µM [477], 0.007 µM [478] and 0.0074 µM [479]–and more closely matched to our data, an IC_{50} of 0.0004 µM was recorded after 96 h docetaxel treatment elsewhere [500]. Differences in IC_{50} are likely due to the nature of *in vitro* cytotoxicity testing and the inherent variation that arises due to many factors. It was decided to proceed with a five day exposure time for the remaining studies to maximise the total response as it was hypothesised that the response in 3D would be lower than in 2D, thus actual growth inhibition may not be detected at shorter exposure times. In addition, notwithstanding the calculation of an IC_{50} for tamoxifen that agreed with values observed in previously reported studies, it was decided to continue only with docetaxel for studies involving 3D culture. This was due to its more efficient performance at lower concentrations.

Following on from preliminary studies, validation of the scaffolds as a suitable test bed for therapies began with a three-dose study using the previously calculated relative IC_{50}, and two increased doses of 0.1 µM and 1 µM. MCF7 cells cultured on the scaffolds (i.e., 3D culture) and the same cells growing in standard 2D culture conditions were exposed to demonstrate that successful and measurable responses occurred in 3D and to assess potential differences to the comparator 2D cultures. Across the study, a significant alteration in response to docetaxel was demonstrated, with a persistent increase in chemoresistance in cells grown in 3D observed for all three dose levels when compared to 2D (Fig. 5.6). In 2D,

the IC_{50} dose had accounted for a growth inhibition of 20-25%, but there was a negligible response in 3D with this dose, with >95% cell viability reported. However, for the increased docetaxel doses, there was a clear cytotoxic effect–illustrating the successful use of the scaffolds in performing drug testing and analysis. Upon completing a non-linear regression analysis on the 2D vs. 3D data (Fig. 5.7), there was a 60.7% increase in the relative IC_{50} value in the 3D scaffolds compared to the 2D controls–demonstrating further the sizeable increase in chemoresistance observed. The alterations in response achieved above were an expected result, as it has been routinely observed in the literature that cells cultured in 3D (in a variety of models) displayed an increase in resistance to drug treatment compared to cells cultured in 2D, across a range of breast cancer [53,500,501]. Similar results have also been observed in other cancers including neuroblastoma, prostate, ovarian and brain [9,12,166,468].

Regarding breast cancer, MCF7 cells grown in a 3D collagen-based gel and treated with docetaxel for 96 h exhibited an increase in IC_{50} concentration of 100% compared to 2D cultured MCF7 cells (0.0004 µM to 0.0009 µM) [500]. MCF7 cells cultured in Matrigel[TM] and exposed to doxorubicin for 144 h had an estimated 44.4 times increase in IC_{50} concentration compared to 2D culture [53]. Looking at 3D culture models that more closely align with scaffolds used herein, Liverani *et al.* (2022) reported a significant decrease in sensitivity to doxorubicin treatment in collagen-based scaffolds (type 1 collagen, freeze-dried, 9x2 mm, porosity of 85%, pore size of 150-300 µM) using two breast cancer cell lines, MCF7 and MDA-MB-231 cells. Cells cultured in the 3D scaffolds were compared to both 2D cultures of the same cells and also a mouse model with tumours derived from both cell lines [355]. There was a significant increase in resistance in the MCF7 cells in 3D scaffolds, to the extent they were fully resistant across the full dose range in the study–and

222

this high resistance matched closely to the *in vivo* model. With MDA-MB-231 cells, once again there was a significant reduction in sensitivity to doxorubicin when cultured in the collagen scaffold (IC$_{50}$ 1.89 µM) compared to 2D (IC$_{50}$ 1.21 µM)–and the response in 3D mimicked closely the *in vivo* response (IC$_{50}$ 2.01) µM) [355]. Another interesting outcome from this study was the selection of resistant subpopulations within the collagen scaffolds from the originally seeded parental cells for both cell lines. Within the MDA-MB-231 cells, reduced drug uptake, increased lysosomal content of the drug and hypoxia mediated resistance were all observed within the 3D collagen scaffold model [355]. Results from this study demonstrate the huge potential of 3D scaffolds for *in vitro* drug research owing to the analogous performance compared to *in vivo* animal models. 3D scaffolds also enable the resistance to treatment to be modelled within a bench top culture model, which offers significant potential for increasing understanding of the mechanisms involved. Fitzgerald *et al.* (2015) saw a large increase in chemoresistance in 3D collagen-based scaffolds (freeze-dried, 0.5% (wt/v), 8 x 4 mm) upon exposure of LNCaP prostate cancer cells to docetaxel. Treatment with 1 nMol (0.001 µM) of docetaxel for 24 h saw a growth inhibition of 75% in 2D cultured cells while only a 10% inhibition in the 3D scaffolds, representing a significant decrease in drug effectiveness [9]. Finally, in another similar collagen-based scaffold (freeze-dried, 0.5% (wt/v), 6x4 mm), there was a 30-37% increase in chemoresistance in two neuroblastoma cell lines cultured in 3D compared to 2D following a 7 day treatment with cisplatin [12]. These studies, along with many others, reaffirm the significant increase in resistance to therapy induced by 3D culture observed within this thesis.

In 2D, cultures are monolayer and there is an even and direct exposure to the drug compounds in use. Within 3D scaffolds, there is a dense network of ECM materials, in this case collagen (and additionally non-ECM gelatin), impacting perfusion and transport of the

drug throughout the scaffold–as is seen *in vivo* with human ECM/tissue [502,503]. Furthermore, cells growing in dense clusters, as observed in Chapter 3, have an additional means of evading the effects of drug compounds, including hypoxia development in the spheroid/cluster core or physical means such as cells at the core of these dense spheroid-like clusters experiencing a lower concentration of drug compared to the more exposed outer layer of cells due to reduced drug perfusion [504–506]. Such response patterns have been demonstrated elsewhere, whereby spheroids displayed increased chemoresistance in comparison to 2D cultures [53,506,507]. Development of hypoxia within tumours and additionally within *in vitro* models has previously been linked to increased chemoresistance [460,461]. Li *et al.* (2022) observed that hypoxia induced increased resistance to docetaxel treatment in 2D cultures in the MDA-MB-231 breast cancer cell line [508]. In addition, hypoxia can induce expression of genes involved in drug resistance, including *HIF1A* [509] or multidrug resistance genes such as *MDR1* [510]–further demonstrating the impact of hypoxia in regard to drug resistance.

Within Chapter 4, key genes linked to hypoxia (both hypoxia related genes themselves and also genes involved in metabolism shift) including *ERO1A, GLUT1, GAPDH* and *HIF1A* were all expressed at significantly higher levels in 3D cultured MCF7 cells than their 2D counterparts. It's known from previously discussed studies in Chapter 4 that these expression signatures observed elsewhere were confirmed to be induced by hypoxic niches within a collagen-based scaffold also cultured with MCF7 (and MDA-MB-231) breast cancer cells [186]. This work, alongside our gene expression data further substantiates that hypoxic regions (likely the dense cell clusters within the scaffolds) are present in the developed scaffolds and may play an additional role in the increased chemoresistance observed within this chapter–an interplay that would be of key interest for future explorations.

From understanding the current state of the art, a gap in the knowledge surrounding the culture duration of cells within 3D scaffolds prior to drug exposure was identified. Drug exposure typically occurs at a set time, with no investigation into the impact the chosen exposure point had on response. There was a significant difference between 1 day of pre-culture to both other periods of 7 days and 14 days, whereby longer pre-culture significantly increased chemoresistance (Fig. 5.8). The response to treatment by the MCF7 cells cultured in 3D for just 1 day prior to exposure was similar in scale to 2D cultured MCF7 cells of the same treatment conditions. Treatment of cells within 3D scaffolds too soon after seeding may cause the same increased sensitivity seen in 2D cultures, negating any potential benefits of using 3D culture in the first place. Such a result suggests it is crucial to take into account the adaption of cells to their 3D environment, giving sufficient time for cell-cell and cell-matrix interactions to occur, and additionally for alterations in gene expression to take place.

Corroborating with the above findings, within Chapter 4, significant alterations in the MCF7 cells gene expression patterns in 3D compared to 2D after 7 days of culture were observed, while expression profiles were minimally different after only 1 day. These changes in expression pointed towards more aggressive cancer cells growing within the scaffolds, alongside an increase in expression of ECM modulating genes that would lend to an increase in the elastic modulus of the scaffold (such as *LOX* upregulation, a known ECM crosslinker [80]) and a further increase in previously mentioned genes associated with hypoxia and metabolism (*ERO1A, GLUT1, GAPDH* and *HIF1A*). This adaption as a function of time by cells to their 3D network also looks to play a role in response to drug exposure. To the best

225

of our knowledge, these results demonstrate for the first time how the duration of culture of cells within 3D scaffolds prior to drug exposure plays a significant role in response. As such, pre-culture duration proves to be a key parameter to be considered in experimental design for *in vitro* drug testing, as important data on drug efficacy and performance *in vitro* during drug discovery research may be lost due to not taking this aspect into account.

ECM/tissue stiffness plays a significant role in breast cancer and is associated with disease initiation, progression and ultimately spread [4,48,54,78,346]. As such, the impact of altering the elastic modulus of the w/Gel 0.15% scaffold elastic modulus was investigated–firstly in the sense of looking at proliferation rates of the cells on the scaffold and then assessing if there was a differential response to docetaxel treatment. From the proliferation data (Fig. 5.10), there was a large difference in rates of cell number increase between the low and high stiffness scaffold beyond 7 days, with the relative change value for the high stiffness scaffolds 90% higher compared to the low stiffness scaffolds. Cell number was increasing at a similar rate in both groups at the earlier timepoints. This finding is supported by previous studies that showed that 3D models with increased elastic modulus resulted in an increase in the proliferation rates and aggressiveness of cancer cells [213,313,511], and also based on the general theme within the literature on the interplay between tissue stiffness and cellular behaviour. MCF7 cells cultured for 7 days on the scaffolds were then exposed to docetaxel to examine the impact of mechanical properties on response. However, no differences in response were observed (Fig. 5.11). It may be worth noting that future investigation of such a comparison should assess longer pre-culture periods, beyond 7 days. Elsewhere, using MDA-MB-231 breast cancer cells, an increase in chemoresistance upon culture on a stiffer matrix towards doxorubicin [512] and cisplatin [513] has been observed. Of particular interest, Hunter Joyce *et al*. (2018) assessed the MCF7 cell line on

alginate-based hydrogels of varied elastic modulus and noted no stiffness-dependent response to doxorubicin [512]. It may be the case the less invasive epithelial MCF7 cell line does not interact with the 3D environment to the same degree as the more aggressive basal-type MDA-MB-231. This has been observed elsewhere, whereby MDA-MB-231 had greater interaction with collagen fibres/scaffolds than MCF7 cells, namely in terms of: increased migration along fibres [8,186,198], and also an ability of the MDA-MB-231 cells to significantly increase the stiffness of the collagen scaffolds used through *LOX* overexpression [198]. Potentially this means MCF7 cells do not respond to mechanical cues as readily as more aggressive breast cancer cell lines, thus stiffness-related drug resistance would not be a feature. As such, while varying the elastic modulus of the scaffold may be important when investigating other aspects of MCF7 behaviour, in regard to drug response, it may not be a crucial factor in model design. Expansion of the work completed could assess multiple other breast cancer cell lines to offer a more thorough analysis of the relationship between scaffold mechanical properties and response to therapy.

5.4.1 Concluding remarks

Within this chapter, the use of the collagen-based scaffolds for the assessment of therapeutic agents was successfully demonstrated. Measurable responses were achieved, in particular using docetaxel. Such repeatable observation of the desired effect of the drug compounds in use achieved the primary aim of this chapter, to validate the use of these scaffolds as a test bed for therapies. It was also demonstrated that there was a significant increase in chemoresistance in cells cultured in 3D compared to 2D–offering further system validation as this is a routinely observed response pattern within the literature. Validation of the scaffolds as an *in vitro* means to assess drug compounds paves the way for the expansion of scaffold use in the field. Not only can the scaffolds be applied in drug development research, but also in emerging areas such as using scaffolds as rapid drug screening tools in *ex vivo* research, allowing for personalised medicine strategies to be devised. To the best of our knowledge, it was demonstrated for the first time the significant alteration in response to therapeutic agents through changing the duration of cell pre-culture on the scaffolds. Cells displayed a significant increase in chemoresistance upon longer culture durations, highlighting that this aspect of experimental design is crucial in the *in vitro* analysis of drugs using 3D scaffolds. While it was demonstrated that the elastic modulus of the scaffold had a significant impact on cell proliferation rates, there was no observation of differential response to docetaxel. Overall, results confirm the use of collagen-based scaffolds in the assessment of therapeutic agents as a promising *in vitro* tool to improve the landscape of early-stage drug development.

06

Chapter 6: General Discussion and Concluding Remarks
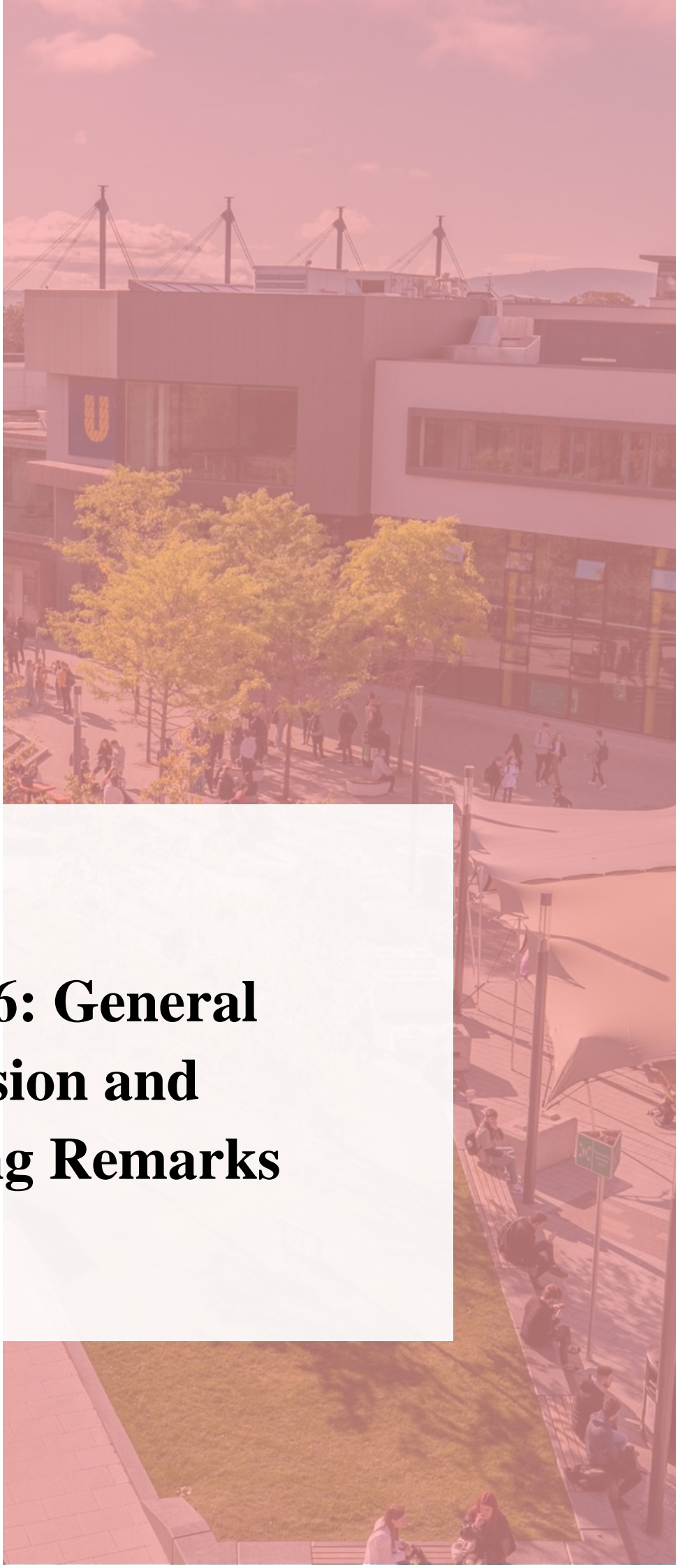
6.1 Overall discussion

In Ireland, breast cancer is the most commonly diagnosed cancer amongst women (excluding non-melanoma skin cancer) and accounts for 17% of female cancer-related deaths each year – thus representing a significant healthcare issue. The five-year survival is high (88%) in early-stage breast cancer [514]. However, once the cancer spreads from the breast, the five-year survival reduces to 26% [515], thus continued breast cancer research is paramount. This thesis aimed to develop a 3D collagen-based scaffold that can be used for breast cancer research. 3D *in vitro* culture models are an emerging tool in cancer research, overcoming limitations associated with 2D culture and bridging the gap to animal models. Within this chapter, the key findings of this thesis are presented.

Production of highly porous collagen-based scaffolds with an interconnected pore architecture, stable in vitro degradation kinetics and suitable mechanical properties

A range of collagen-based scaffolds were successfully and repeatably fabricated using a freeze-drying procedure. This controlled-rate fabrication technique allowed for the production of highly porous scaffolds with an interconnected pore network, with consistent architecture across all six compositions assessed. The addition of gelatin and hyaluronic acid led to a reduction in scaffold porosity, however the true scale of these differences was negligible and thus not considered detrimental to the scaffold architecture. Initial mechanical and degradative assessment of the collagen-based scaffolds showed that they had a low elastic modulus (and thus an indicator of low stiffness), and also an extremely rapid degradation profile. The use of chemical crosslinking (EDAC) was implemented to significantly bolster the scaffolds mechanical properties and degradation kinetics–and this was the outcome that was achieved. The mechanobiology of the breast cancer tumour

microenvironment plays a crucial role in the development and progression of the disease [4,48,54,78,346], thus it is paramount to fabricate a scaffold that replicates the mechanical properties of breast cancer tissue/ECM. From the literature review, a range of 0.5-3 kPa was determined to be a suitable range of elastic moduli to replicate values seen in breast cancer ECM/tissue [92,315]. All scaffolds fabricated had elastic moduli in the range of 1-2 kPa, thus satisfying our chosen criteria, demonstrating the replication of suitable and biologically relevant mechanical properties within our scaffolds. In addition, mechanical properties of our scaffolds closely matched reported elastic moduli of breast cancer ECM in a mouse model [93], highlighting how 3D scaffolds can be used to simulate the *in vivo* environment in animal models. A promising aspect of 3D scaffolds is their application in long-term cultures, without the need for passaging/sub-culturing cells–thus allowing for cells to adapt to their environment and grow undisturbed for long periods. This can pave the way for long term investigations into a variety of breast cancer features, such as hypoxia development or long-term monitoring of cancer metabolism and general cell behaviour. All scaffolds fabricated demonstrated long-term *in vitro* stability, degrading by less than 15% within a 2-week period. As such, our scaffolds confirmed their suitability for long-term *in vitro* research.

Confirmation of collagen-based scaffold biocompatibility and ability to support breast cancer cell attachment and proliferation

For suitability as an *in vitro* culture model, the fabricated scaffolds must demonstrate their ability to support the attachment of viable cells and the subsequent long-term proliferation of cell populations within the scaffold. The scaffolds developed were shown to be non-cytotoxic towards our selected breast cancer cell line. From the materials themselves

(collagen, gelatin and hyaluronic acid), to chemicals used in the fabrication process such as acetic acid (material solubilisation), EDAC/NHS (crosslinking agents) and ethanol (scaffold sterilisation)–there was no observed cytotoxicity to cells upon exposure to scaffold-based extracts in 2D culture. Furthermore, the scaffolds fabricated provided a suitable template for attachment and proliferation of viable breast cancer cells. Viability of MCF7 cells within scaffolds after 48 h was high, with all scaffold groups showing mean viabilities above 85%. Cell attachment of 40-70% was observed for all scaffold compositions investigated. The double-sided seeding technique used resulted in the successful infiltration of cells throughout the full depth of the scaffold, with the scaffold architectural properties (porosity and pore size) posing no constraints on this movement. Furthermore, the addition of gelatin and hyaluronic acid to the collagen scaffolds showed an improvement in cell infiltration at the early timepoint of 24 h, with an apparent greater number of cells observed in the central regions of the scaffold upon their addition. Long-term proliferation, spanning three weeks, was successfully demonstrated. Cell numbers continuously increased as a function of time, with rapid increases in cell number during the initial days before the proliferation rate began slowing. Alongside the degradation results, these studies demonstrate the application of the collagen-based scaffolds for long-term investigations spanning more than two weeks.

The majority of MCF7 cells growing within the scaffolds developed a rounded and spherical morphology. Within 24 h, the development of spheroid-like clusters was observed–demonstrating rapid occurrence of cell-cell interactions. The acquiring of a morphology that is more analogous to *in vivo* cancer cells, compared to the flat morphology of 2D cultured cells, further highlights the benefit of 3D scaffolds in improving the biological relevance of the *in vitro* model. Successful attachment and proliferation of cells within the scaffolds also reaffirms that the aforementioned scaffold physical properties, such as porosity and pore

size, are of an ideal range for cell attachment, infiltration, proliferation and cell-cell interactions.

Cells cultured in 3D collagen-based scaffolds develop altered gene expression patterns, with increased expression of genes associated with ECM modification, hypoxia and altered metabolism.

Upon culture in 3D, cells tend to acquire altered gene expression patterns compared to their counterparts in 2D. In Chapter 4, a range of targets were assessed that play key roles in ECM modification, ECM component synthesis, hypoxia and glycolysis. Interesting and significant results were observed across all processes investigated. Increased expression of hypoxia related targets, *HIF1A* and *ERO1A*, was observed in 3D cultured cells compared to 2D. Notably, *ERO1A*, a novel marker of hypoxia, was consistently overexpressed within the scaffolds–and this is the first demonstration of such an increase in contrast to 2D cultures in a breast cancer *in vitro* model. In addition, two markers associated with glycolysis/metabolism, *GLUT1* and *GAPDH*, were both overexpressed in 3D compared to 2D cultured cells. Both of these genes are regulated by hypoxia and are induced in order to promote anaerobic respiration in the absence of oxygen [399,404]. Thus, their overexpression further suggests that low oxygen regions develop within our scaffolds and owing to this induction of hypoxia, MCF7 cells underwent a metabolic switch in order to continue proliferation and growth within the scaffolds. These signatures of hypoxia and induction of glycolysis corroborate with previous studies reported in Chapter 3 whereby dense clusters of cells were observed. It is known that within spheroid-like clusters of cells such as those, that hypoxic cores are prevalent [377,378], highlighting the above expression patterns likely were induced by the formation of these dense cellular clusters. *VEGFA*, which

promotes angiogenesis in response to reduced oxygen and nutrient supply (hypoxia) [459], was also found to be increased in expression within 3D cultured cells. These gene expression patterns signal that hypoxia has developed within the collagen-based scaffolds, and in response an increase in glycolysis and associated angiogenesis genes was triggered. The ability to model naturally induced hypoxia within an *in vitro* model highlights a promising application of our collagen-based scaffold model.

Another major aspect of investigation was genes involved in the modification of breast cancer ECM and additionally, genes involved in synthesis of ECM components. *LOX*, *MMP2* and *MMP9* showed increased expression upon culture of cell within the scaffold compared to 2D cultured cells. These three genes play a key role in the modification of the ECM, through crosslinking and stiffening of collagen (*LOX*) and the breakdown/degradation of collagen type IV (*MMP2* and *MMP9*) [80,81,86,87]. These functions play an important role in the progression and spread of breast cancer, thus their overexpression within our model improves the mimicry of the *in vivo* tumour microenvironment–highlighting yet another beneficial feature of the culture model fabricated herein. Increased expression in 3D compared to 2D cultured cells was observed for both *FN1* and *HAS2,* which produce crucial components of the ECM (fibronectin and hyaluronic acid), and it is through their influence on cell migration, proliferation, adhesion and invasion that they play a role in breast cancer progression and metastasis [385,388,392]. Furthermore–*MMP2, MMP9, LOX* and *FN1* have additional roles in epithelial-to-mesenchymal transition (EMT), a crucial process which contributes to the spread and migration (i.e., metastasis) of cancer cells. While EMT was not a key research focus of this thesis, increased expression of EMT markers demonstrates further potential in applying the scaffolds as *in vitro* tools to investigate processes such as EMT, alongside the aforementioned hypoxia and glycolysis. Overall, the increase in

expression of ECM component synthesizing genes observed demonstrates the increasing complexity that can be achieved within the 3D collagen-based scaffolds, offering a more biologically relevant culture model compared to 2D culture.

Successful application of collagen-based scaffolds as an in vitro drug testing model

A key application of the scaffolds fabricated, was their use in *in vitro* drug testing. One of the noteworthy issues with 2D cultures as referenced throughout this thesis, is the altered or inflated response to therapies *in vitro* and the general poor translation of results seen in 2D culture compared to *in vivo* trials in animals and humans [112,470]. Within this thesis, it was sought to validate the use of the fabricated scaffolds in the assessment of therapeutic agents used to treat breast cancer. Culture of MCF7 cells in 3D resulted in a significant increase in resistance to docetaxel treatment, with a sizeable change in relative IC_{50} between 2D and 3D cultures. Confirmation that growth inhibition is lower in the 3D scaffolds achieves one of the key promises of 3D culture models, that they negate the often increased sensitivity to therapies seen in 2D and produce responses that are more analogous to *in vivo* animal models. While no animal study was carried out herein, elsewhere it was observed that response by MCF7/MDA-MB-231 breast cancer cells to doxorubicin in a 3D collagen scaffold was very similar to a mouse model, remarkably more so than the 2D culture control [355]. This highlights the promise of 3D scaffold-based drug research and how it can bridge the gap between 2D culture and animal models.

Within the literature, the effect of the cell culture duration within the scaffolds prior to drug exposure has not been investigated. Previously, cells were pre-cultured for seven days prior to treatment, to allow sufficient times for cells to adapt to the 3D environment. It was found

that when MCF7 cells were only cultured within the collagen-based scaffold for 24 h, there was a sizeable reduction in cell viability to ~55%, and this growth inhibition was of similar magnitude to the response levels in 2D using the same docetaxel concentration. This was in contrast to both other pre-culture durations of 7 and 14 days, whereby there was significantly less growth inhibition for both groups. This signals that cells must be provided with adequate time to adapt to the 3D environment, through cell-cell and cell-matrix interactions but also in terms of alterations in expression of a variety of genes. These adaptions appear to drive an increase in chemoresistance within the cells–while cells only cultured short-term within the scaffolds that have not adapted to the 3D scaffold still behave in a similar fashion to 2D cultures with inflated response to drug exposure. Hypoxia development has previously been demonstrated to impact chemosensitivity, causing increased resistance to treatment in cells growing under low oxygen conditions [460,461]–and significantly, this was observed to be the case with breast cancer cells exposed to docetaxel [508]. As hypoxia and related glycolysis genes did not show altered expression in 3D until the Day 7 mark within the collagen-based scaffolds, it illustrates that key cellular adaptions to the 3D scaffold that impact response to drug exposure takes time, and this must be accounted for when planning and conducting 3D *in vitro* drug testing.

Tissue/ECM stiffness plays a significant role in breast cancer development and progression [4,48,54,78,346], and also has a facilitative role in drug resistance [502,513,516]. Therefore, the effects of altering the elastic modulus of the collagen-based scaffolds were also investigated, simulating the increased stiffness that is a characteristic of the tumour microenvironment in breast cancer, to determine if this had any effect on response to docetaxel. Significantly increasing the elastic modulus (3-fold increase) of the scaffold resulted in a large increase in MCF7 proliferation rate within the scaffold. Thus, there was a

direct effect of the increasing the elastic modulus of the scaffold and cell proliferation. Previous proliferation studies (Chapter 3) have shown that there were no differences in proliferation rates amongst the different scaffold groups. However, the magnitude of difference between lowest and highest modulus using the standard crosslinking regime across the different scaffold compositions was not as large as described in the Chapter 5 study. This result demonstrates that the collagen-based scaffolds can be tailored in terms of their physical and mechanical properties in a more significant manner to drive a different behaviour within the same parental population of cells–which may have interest in future works investigating in more detail the relationship between the cell and the scaffold it is growing in. Upon exposure of both scaffold groups of altered elastic modulus to docetaxel, no difference in response between either the low or high modulus groups was observed. This was unexpected as it was hypothesised that an increase in chemoresistance would have been observed as a function of increasing modulus. The lack of difference may be a true result, or there may be limitations of the study design, perhaps in term of pre-culture duration or cell line related. Future work incorporating a range of different breast cancer cell lines and additionally different drugs may provide greater context on the interplay between scaffold modulus (as a representative comparison to tissue/ECM stiffness) and therapeutic agents.

6.2 Concluding remarks

This research thesis has fabricated and characterised in detail a range of 3D collagen-based breast cancer culture models. The scaffolds developed proved to be highly biocompatible with successful attachment and subsequent sustained long-term proliferation of MCF7 breast cancer cells achieved. Cells growing within the collagen-based scaffolds developed a rounded, globular morphology akin to cells growing *in vivo*. Cells growing in the 3D environment acquired markers of ECM modification and synthesis, low oxygen regions (hypoxia) and induction of glycolysis. These genetic alterations drove a shift in the MCF7 population to a more aggressive and malignant genotype. The use of these collagen-based scaffolds as an *in vitro* drug testing model was also successfully validated. Cells cultured in 3D displayed a sizeable increase in chemoresistance when compared to the same cells growing in 2D culture plates. Within our scaffolds, a novel impact of cell pre-culture duration prior to drug treatment was demonstrated. A significant increase in chemoresistance was observed in longer pre-culture times, in comparison to short-term periods (24 h) where cells within the scaffold displayed similar chemosensitivity to 2D cultured cells.

Overall, the overarching aim of this thesis was successfully achieved–the delivery of biomimetic, biocompatible 3D collagen-based scaffolds that support the attachment and proliferation of breast cancer cells. As a proven and validated culture model for undertaking breast cancer research, this thesis demonstrates the significant potential of the application of these scaffolds in research settings–paving the way for future discoveries and advancement in our knowledge of the disease, its progression and its treatment.

6.3 Future prospective

Further exploration into cell behaviour and phenotype within the scaffold.

The fabricated scaffolds all demonstrated relatively similar architectural and mechanical properties in terms of true magnitude, even though some significant differences in results were achieved. Fabricating scaffold compositions that achieved more extreme variations may allow for further optimisation of the scaffold and a greater understanding of the impact of scaffold properties on cell behaviour. Significant modification of scaffold elastic modulus in Chapter 5 demonstrated a large increase in cell proliferation rates, highlighting how greater alterations in scaffold physical properties can impact cell behaviour. The addition of other cell types would take place, as different breast cancer cell lines may have different behaviours within the scaffolds. The MDA-MB-231 (triple negative) cell line would be an ideal additional cell line, as it is much more aggressive in nature than the cells used in this thesis. Other aspects of cell behaviour of interest would include greater investigation of the movement of cells within the scaffold, and how this may correlate with their migratory or metastatic potential. This would involve profiling various markers and protein involved in the movement of cells (such as N- and E-cadherin), assessing how fast cells move throughout the scaffolds and if this migration can be altered using anti-metastatic drugs. The additional investigations into cell behaviour within the scaffold further improve the knowledge within the breast cancer field and may serve to provide breakthroughs in various mechanisms involved in breast cancers progression and spread.

Further exploration into cell behaviour and phenotype within the scaffold.

Within this thesis, qPCR was used to provide a detailed assessment of key cell markers and genes involved in a variety of processes such as ECM modification, ECM component

synthesis, glycolysis, hypoxia, metabolism and also into markers that are acquired upon increasing cell aggressiveness and invasive potential. Future work would significantly expand on the initial targets selected to get a better picture of gene expression within the scaffolds compared to 2D cultures. Technologies such as RNA-Seq would be used to assess the full transcriptome, removing any potential biases of selecting single targets at a time. While the transcriptome provides a useful insight into these properties and processes, further work to provide greater detail would be completed. This would involve, for some examples, protein analysis (western blots, protein microarrays and mass spectrometry) and secreted factor/protein analysis. More in depth assessment of cell aggressiveness and invasive potential using the above means would link into the further tumourigenicity animal study.

Assessment of tumourigenicity of 3D cultured cells in an animal model.

The culture of cells within a 3D scaffold can develop a profile of cell behaviour and give an indication into the 'aggressive' behaviour or potential of cell lines. A range of cell markers and gene of interests were profiled that suggested that MCF7 cells grown within the collagen-based scaffolds had evolved into a more aggressive phenotype. Ultimately an *in vivo* animal study would be required to study the tumourigenicity of the 3D cultured cells. This would involve the culture of selected breast cancer cells lines (e.g., MCF7 and MDA-MB-231) in both 2D and within our 3D collagen-based scaffolds for a defined period. After which, cells from either culture condition will be harvested and then injected into mammary tissue of a mouse model. Tumour growth and development would be monitored and assessed for tumour volume, mass and growth rate. This model would provide significant corroboration to previous works and postulations on the increase in cell aggressiveness upon culture within the scaffolds.

Application of collagen-based scaffolds as *ex vivo* culture models.

A further application of the scaffolds fabricated would be their potential use in *ex vivo* culture, which would represent an exciting application of the scaffolds with potential for real clinical impact. By culturing fragments of a patient's tumour, it allows us to gain a greater insight into a patient's own cancer and provides opportunities to develop personalised medicine strategies. Initially, work would consist of optimising the conditions for successful uptake of tumour fragments on the scaffolds to ensure an adequate fraction of tumour cells remain viable and begin proliferating within the scaffold. Validation that the cultured fragments can maintain the characteristics of the original tumour long-term (2-4 weeks) within the scaffolds would be carried out, ensuring any testing carried out on the *ex vivo* model would still be representative of the original patient tumour. Upon validation of the scaffolds as suitable *ex vivo* culture models, work would expand into therapeutic assessment, demonstrating the potential to use these scaffolds to improve patient outcome by devising personalised medicine strategies through rapidly *ex vivo* culture of patient tumours within a laboratory setting. *Ex vivo* of patient tumour fragments on 3D scaffolds has been carried out before, thus there would be no major concerns regarding ethical approval for these works. Optimising treatment options could greatly improve patient experience, through mitigating risks of non-response to treatments, which could result in significant patient suffering through side effects with no actual benefit in terms of tumour reduction.

Incorporation of immune cell function within the collagen-based scaffolds.

Xenograft tumours typically grown in immunocompromised mouse models, thus successful incorporation of immune function into the collagen-based scaffold would be a huge advantage of the culture model. Certain drugs work by inducing an immune response–so as a proof of principle study, tumours growing on the immunofunctionalised scaffolds would

be treated with a drug that provokes the immune system, such as Herceptin–which theoretically should perform better with provision of the immune component. Natural killer cells would be a suitable immune cell to incorporate, due to their prominent ability to induce antibody-dependent cell-mediated cytotoxicity and their reported interaction with Herceptin. Further cancer and immune cell interplay that could be investigated could be immune checkpoint inhibitors, such as PD-1 and PD-L1 inhibitors. Demonstration of immune function within a 3D *in vitro* tumour model would represent a huge advancement in model complexity and provide a significant advancement in the biological relevance of scaffolds. Scaffolds with immune function would genuinely represent bridging the gap to animal models in terms of lab-based research for cancer.

Bibliography

[1]   H. Sung, J. Ferlay, R.L. Siegel, M. Laversanne, I. Soerjomataram, A. Jemal, F. Bray, Global Cancer Statistics 2020: GLOBOCAN Estimates of Incidence and Mortality Worldwide for 36 Cancers in 185 Countries, CA. Cancer J. Clin. 71 (2021) 209–249.

[2]   F. Bray, J. Ferlay, I. Soerjomataram, R.L. Siegel, L.A. Torre, A. Jemal, Global cancer statistics 2018: GLOBOCAN estimates of incidence and mortality worldwide for 36 cancers in 185 countries, CA. Cancer J. Clin. 68 (2018) 394–424.

[3]   F. Cardoso, A. Costa, L. Norton, D. Cameron, T. Cufer, L. Fallowfield, P. Francis, J. Gligorov, S. Kyriakides, N. Lin, O. Pagani, E. Senkus, C. Thomssen, M. Aapro, J. Bergh, A. Di Leo, N. El Saghir, P.A. Ganz, K. Gelmon, A. Goldhirsch, N. Harbeck, N. Houssami, C. Hudis, B. Kaufman, M. Leadbeater, M. Mayer, A. Rodger, H. Rugo, V. Sacchini, G. Sledge, L. van't Veer, G. Viale, I. Krop, E. Winer, 1st International consensus guidelines for advanced breast cancer (ABC 1), The Breast. 21 (2012) 242–252.

[4]   K.R. Levental, H. Yu, L. Kass, J.N. Lakins, M. Egeblad, J.T. Erler, S.F.T. Fong, K. Csiszar, A. Giaccia, W. Weninger, M. Yamauchi, D.L. Gasser, V.M. Weaver, Matrix crosslinking forces tumor progression by enhancing integrin signaling., Cell. 139 (2009) 891–906.

[5]   P. Lu, V.M. Weaver, Z. Werb, The extracellular matrix: A dynamic niche in cancer progression, J. Cell Biol. 196 (2012) 395–406.

[6]   M. Fang, J. Yuan, C. Peng, Y. Li, Collagen as a double-edged sword in tumor progression., Tumour Biol. 35 (2014) 2871–82.

[7]   M.W. Pickup, J.K. Mouw, V.M. Weaver, The extracellular matrix modulates the hallmarks of cancer, (n.d.).

[8]   J.J. Campbell, A. Husmann, R.D. Hume, C.J. Watson, R.E. Cameron, Development of three-dimensional collagen scaffolds with controlled architecture for cell migration studies using breast cancer cell lines, Biomaterials. 114 (2017) 34–43.

[9]   K.A. Fitzgerald, J. Guo, E.G. Tierney, C.M. Curtin, M. Malhotra, R. Darcy, F.J.

O'Brien, C.M. O'Driscoll, The use of collagen-based scaffolds to simulate prostate cancer bone metastases with potential for evaluating delivery of nanoparticulate gene therapeutics, Biomaterials. 66 (2015) 53–66.

[10] C.S. Szot, C.F. Buchanan, J.W. Freeman, M.N. Rylander, 3D in vitro bioengineered tumors based on collagen I hydrogels., Biomaterials. 32 (2011) 7905–12.

[11] O. Hartman, C. Zhang, E.L. Adams, M.C. Farach-Carson, N.J. Petrelli, B.D. Chase, J.F. Rabolt, Microfabricated Electrospun Collagen Membranes for 3-D Cancer Models and Drug Screening Applications, Biomacromolecules. 10 (2009) 2019–2032.

[12] C. Curtin, J.C. Nolan, R. Conlon, L. Deneweth, C. Gallagher, Y.J. Tan, B.L. Cavanagh, A.Z. Asraf, H. Harvey, S. Miller-Delaney, J. Shohet, I. Bray, F.J. O'Brien, R.L. Stallings, O. Piskareva, A physiologically relevant 3D collagen-based scaffold–neuroblastoma cell system exhibits chemosensitivity similar to orthotopic xenograft models, Acta Biomater. 70 (2018) 84–97.

[13] D. Hanahan, R.A. Weinberg, The hallmarks of cancer., Cell. 100 (2000) 57–70.

[14] D. Hanahan, R.A. Weinberg, Hallmarks of Cancer: The Next Generation, Cell. 144 (2011) 646–674.

[15] Y. Feng, M. Spezia, S. Huang, C. Yuan, Z. Zeng, L. Zhang, X. Ji, W. Liu, B. Huang, W. Luo, B. Liu, Y. Lei, S. Du, A. Vuppalapati, H.H. Luu, R.C. Haydon, T.-C. He, G. Ren, Breast cancer development and progression: Risk factors, cancer stem cells, signaling pathways, genomics, and molecular pathogenesis., Genes Dis. 5 (2018) 77–106.

[16] U. Veronesi, P. Boyle, A. Goldhirsch, R. Orecchia, G. Viale, Breast cancer, Lancet. 365 (2005) 1727–1741.

[17] K. Polyak, Breast cancer: origins and evolution, J. Clin. Invest. 117 (2007) 3155.

[18] B. Weigelt, J.L. Peterse, L.J. Van't Veer, Breast cancer metastasis: markers and models, Nat. Rev. Cancer 2005 58. 5 (2005) 591–602.

[19] C.O. Madu, S. Wang, C.O. Madu, Y. Lu, Angiogenesis in Breast Cancer Progression, Diagnosis, and Treatment, J. Cancer. 11 (2020) 4474.

[20] M.B. Amin, ; Frederick, L. Greene, S.B. Edge, C.C. Compton, J.E. Gershenwald, R.K. Brookland, L. Meyer, D.M. Gress, ; David, R. Byrd, P. Winchester, The Eighth Edition AJCC Cancer Staging Manual: Continuing to build a bridge from a population-based to a more "personalized" approach to cancer staging, CA. Cancer J. Clin. 67 (2017) 93–99.

[21] Breast Cancer - Women's Health Issues - Merck Manuals Consumer Version, (n.d.).

[22] Y.-H. Hsiao, M.-C. Chou, C. Fowler, J.T. Mason, Y.-G. Man, Breast cancer heterogeneity: mechanisms, proofs, and implications., J. Cancer. 1 (2010) 6–13.

[23] W.L. McGuire, K.B. Horwitz, O.H. Pearson, A. Segaloff, Current status of estrogen and progesterone receptors in breast cancer., Cancer. 39 (1977) 2934–47.

[24] F. Meric-Bernstam, M.-C. Hung, Advances in Targeting Human Epidermal Growth Factor Receptor-2 Signaling for Cancer Therapy, Clin. Cancer Res. 12 (2006) 6326–6330.

[25] D. Slamon, G. Clark, S. Wong, W. Levin, A. Ullrich, W. McGuire, Human breast cancer: correlation of relapse and survival with amplification of the HER-2/neu oncogene, Science (80-.). 235 (1987) 177–182.

[26] C.A. Hudis, L. Gianni, Triple-negative breast cancer: an unmet medical need., Oncologist. 16 Suppl 1 (2011) 1–11.

[27] A.A. Onitilo, J.M. Engel, R.T. Greenlee, B.N. Mukesh, Breast cancer subtypes based on ER/PR and Her2 expression: comparison of clinicopathologic features and survival., Clin. Med. Res. 7 (2009) 4–13.

[28] E. De Azambuja, F. Cardoso, G. De Castro, M. Colozza, M.S. Mano, V. Durbecq, C. Sotiriou, D. Larsimont, M.J. Piccart-Gebhart, M. Paesmans, Ki-67 as prognostic marker in early breast cancer: A meta-analysis of published studies involving 12 155 patients, Br. J. Cancer. 96 (2007) 1504–1513.

[29] H. Trihia, S. Murray, K. Price, R.D. Gelber, R. Golouh, A. Goldhirsch, A.S. Coates, J. Collins, M. Castiglione-Gertsch, B.A. Gusterson, Ki-67 expression in breast carcinoma: Its association with grading systems, clinical parameters, and other prognostic factors - A surrogate marker?, Cancer. 97 (2003) 1321–1331.

[30] O. Yersal, S. Barutca, Biological subtypes of breast cancer: Prognostic and

therapeutic implications, World J. Clin. Oncol. 5 (2014) 412–424.

[31] M.C.U. Cheang, S.K. Chia, D. Voduc, D. Gao, S. Leung, J. Snider, M. Watson, S.
      Davies, P.S. Bernard, J.S. Parker, C.M. Perou, M.J. Ellis, T.O. Nielsen, Ki67 Index,
      HER2 Status, and Prognosis of Patients With Luminal B Breast Cancer, Artic. |
      JNCI. 101 (2009) 736.

[32] S. Bustreo, S. Osella-Abate, P. Cassoni, M. Donadio, M. Airoldi, F. Pedani, M.
      Papotti, A. Sapino, I. Castellano, Optimal Ki67 cut-off for luminal breast cancer
      prognostic evaluation: a large case series study with a long-term follow-up, Breast
      Cancer Res. Treat. 157 (2016) 363–371.

[33] N. Howlader, K.A. Cronin, A.W. Kurian, R. Andridge, Differences in breast cancer
      survival by molecular subtypes in the United States, Cancer Epidemiol. Biomarkers
      Prev. 27 (2018) 619–626.

[34] N. Arima, R. Nishimura, T. Osako, Y. Okumura, M. Nakano, M. Fujisue, Y.
      Nishiyama, Y. Toyozumi, Ki-67 index value and progesterone receptor status can
      predict prognosis and suitable treatment in node-negative breast cancer patients with
      estrogen receptor-positive and HER2-negative tumors, Oncol. Lett. 17 (2019) 616–
      622.

[35] F. Ades, D. Zardavas, I. Bozovic-Spasojevic, L. Pugliano, D. Fumagalli, E. De
      Azambuja, G. Viale, C. Sotiriou, M. Piccart, C.-T. Sotiriou, Luminal B Breast
      Cancer: Molecular Characterization, Clinical Management, and Future Perspectives,
      J Clin Oncol. 32 (2014).

[36] T. Sørlie, C.M. Perou, R. Tibshirani, T. Aas, S. Geisler, H. Johnsen, T. Hastie, M.B.
      Eisen, M. Van De Rijn, S.S. Jeffrey, T. Thorsen, H. Quist, J.C. Matese, P.O. Brown,
      D. Botstein, P.E. Lønning, A.L. Børresen-Dale, Gene expression patterns of breast
      carcinomas distinguish tumor subclasses with clinical implications, Proc. Natl.
      Acad. Sci. U. S. A. 98 (2001) 10869–10874.

[37] A. Borg, A.K. Tandon, H. Sigurdsson, G.M. Clark, M. Fernö, S.A. Fuqua, D.
      Killander, W.L. McGuire, HER-2/neu amplification predicts poor survival in node-
      positive breast cancer., Cancer Res. 50 (1990) 4332–7.

[38] M. National Cancer Institute. Bethesda, Breast SEER 5-Year Age-Adjusted

Incidence Rates, 2015-2019, (n.d.).

[39] A. Antoniou, P.D.P. Pharoah, S. Narod, H.A. Risch, J.E. Eyfjord, J.L. Hopper, N. Loman, H. Olsson, O. Johannsson, Å. Borg, B. Pasini, P. Radice, S. Manoukian, D.M. Eccles, N. Tang, E. Olah, H. Anton-Culver, E. Warner, J. Lubinski, J. Gronwald, B. Gorski, H. Tulinius, S. Thorlacius, H. Eerola, H. Nevanlinna, K. Syrjäkoski, O.-P. Kallioniemi, D. Thompson, C. Evans, J. Peto, F. Lalloo, D.G. Evans, D.F. Easton, Average Risks of Breast and Ovarian Cancer Associated with BRCA1 or BRCA2 Mutations Detected in Case Series Unselected for Family History: A Combined Analysis of 22 Studies, Am. J. Hum. Genet. 72 (2003) 1117–1130.

[40] V.C. Jordan, The role of tamoxifen in the treatment and prevention of breast cancer., Curr. Probl. Cancer. 16 (1992) 129–76.

[41] S. Chumsri, T. Howes, T. Bao, G. Sabnis, A. Brodie, Aromatase, aromatase inhibitors, and breast cancer, J. Steroid Biochem. Mol. Biol. 125 (2011) 13–22.

[42] P.E. Goss, J.N. Ingle, S. Martino, N.J. Robert, H.B. Muss, M.J. Piccart, M. Castiglione, D. Tu, L.E. Shepherd, K.I. Pritchard, R.B. Livingston, N.E. Davidson, L. Norton, E. a Perez, J.S. Abrams, D. a Cameron, M.J. Palmer, J.L. Pater, Randomized trial of letrozole following tamoxifen as extended adjuvant therapy in receptor-positive breast cancer: updated findings from NCIC CTG MA.17., J. Natl. Cancer Inst. 97 (2005) 1262–71.

[43] N.L. Spector, K.L. Blackwell, Understanding the Mechanisms Behind Trastuzumab Therapy for Human Epidermal Growth Factor Receptor 2–Positive Breast Cancer, J. Clin. Oncol. 27 (2009) 5838–5847.

[44] M. Xing, F. Yan, S. Yu, P. Shen, Efficacy and Cardiotoxicity of Liposomal Doxorubicin-Based Chemotherapy in Advanced Breast Cancer: A Meta-Analysis of Ten Randomized Controlled Trials, PLoS One. 10 (2015) e0133569.

[45] K.A. Lyseng-Williamson, C. Fenton, Docetaxel: a review of its use in metastatic breast cancer, Drugs. 65 (2005) 2513–2531.

[46] M. Khasraw, R. Bell, C. Dang, Epirubicin: Is it like doxorubicin in breast cancer? A clinical review, The Breast. 21 (2012) 142–149.

[47] L. Del Mastro, S. De Placido, P. Bruzzi, M. De Laurentiis, C. Boni, G. Cavazzini, A. Durando, A. Turletti, C. Nisticò, E. Valle, O. Garrone, F. Puglisi, F. Montemurro, S. Barni, A. Ardizzoni, T. Gamucci, G. Colantuoni, M. Giuliano, A. Gravina, P. Papaldo, C. Bighin, G. Bisagni, V. Forestieri, F. Cognetti, Fluorouracil and dose-dense chemotherapy in adjuvant treatment of patients with early-stage breast cancer: an open-label, 2×2 factorial, randomised phase 3 trial, Lancet (London, England). 385 (2015) 1863–1872.

[48] J. Insua-Rodríguez, T. Oskarsson, The extracellular matrix in breast cancer, Adv. Drug Deliv. Rev. 97 (2016) 41–55.

[49] J.K. Mouw, G. Ou, V.M. Weaver, Extracellular matrix assembly: a multiscale deconstruction, Nat. Rev. Mol. Cell Biol. 15 (2014) 771–785.

[50] J.D. Humphrey, E.R. Dufresne, M.A. Schwartz, Mechanotransduction and extracellular matrix homeostasis., Nat. Rev. Mol. Cell Biol. 15 (2014) 802–12.

[51] S. Schlie-Wolter, A. Ngezahayo, B.N. Chichkov, The selective role of ECM components on cell adhesion, morphology, proliferation and communication in vitro, Exp. Cell Res. 319 (2013) 1553–1561.

[52] T.N. Wight, M.G. Kinsella, E.E. Qwarnström, The role of proteoglycans in cell adhesion, migration and proliferation, Curr. Opin. Cell Biol. 4 (1992) 793–801.

[53] C.J. Lovitt, T.B. Shelper, V.M. Avery, Doxorubicin resistance in breast cancer cells is mediated by extracellular matrix proteins., BMC Cancer. 18 (2018) 41.

[54] C.E. Barcus, K.A. O'Leary, J.L. Brockman, D.E. Rugowski, Y. Liu, N. Garcia, M. Yu, P.J. Keely, K.W. Eliceiri, L.A. Schuler, Elevated collagen-I augments tumor progressive signals, intravasation and metastasis of prolactin-induced estrogen receptor alpha positive mammary tumor cells, Breast Cancer Res. 19 (2017) 9.

[55] P.P. Provenzano, D.R. Inman, K.W. Eliceiri, J.G. Knittel, L. Yan, C.T. Rueden, J.G. White, P.J. Keely, Collagen density promotes mammary tumor initiation and progression, BMC Med. 6 (2008) 11.

[56] M.W. Conklin, J.C. Eickhoff, K.M. Riching, C.A. Pehlke, K.W. Eliceiri, P.P. Provenzano, A. Friedl, P.J. Keely, Aligned collagen is a prognostic signature for survival in human breast carcinoma., Am. J. Pathol. 178 (2011) 1221–32.

[57] M.W. Conklin, P.J. Keely, Why the stroma matters in breast cancer, Cell Adh. Migr. 6 (2012) 249–260.

[58] I. Acerbi, L. Cassereau, I. Dean, Q. Shi, A. Au, C. Park, Y.Y. Chen, J. Liphardt, E.S. Hwang, V.M. Weaver, Human breast cancer invasion and aggression correlates with ECM stiffening and immune cell infiltration., Integr. Biol. (Camb). 7 (2015) 1120–34.

[59] S. Ricard-Blum, The collagen family., Cold Spring Harb. Perspect. Biol. 3 (2011) a004978.

[60] K. Gelse, E. Pöschl, T. Aigner, Collagens—structure, function, and biosynthesis, Adv. Drug Deliv. Rev. 55 (2003) 1531–1546.

[61] M.K. Gordon, R.A. Hahn, Collagens., Cell Tissue Res. 339 (2010) 247–57.

[62] M.A. Weis, D.M. Hudson, L. Kim, M. Scott, J.-J. Wu, D.R. Eyre, Location of 3-Hydroxyproline Residues in Collagen Types I, II, III, and V/XI Implies a Role in Fibril Supramolecular Assembly, J. Biol. Chem. 285 (2010) 2580–2590.

[63] R.A. Berg, D.J. Prockop, The thermal transition of a non-hydroxylated form of collagen. Evidence for a role for hydroxyproline in stabilizing the triple-helix of collagen, Biochem. Biophys. Res. Commun. 52 (1973) 115–120.

[64] S.M. Krane, S.R. Pinnell, R.W. Erbe, Lysyl-protocollagen hydroxylase deficiency in fibroblasts from siblings with hydroxylysine-deficient collagen., Proc. Natl. Acad. Sci. U. S. A. 69 (1972) 2899–903.

[65] M. Yamauchi, C. Noyes, Y. Kuboki, G.L. Mechanic, Collagen structural microheterogeneity and a possible role for glycosylated hydroxylysine in type I collagen., Proc. Natl. Acad. Sci. U. S. A. 79 (1982) 7684–8.

[66] K.E. Kadler, D.F. Holmes, J.A. Trotter, J.A. Chapman, Collagen fibril formation, 1996.

[67] E.G. Canty, K.E. Kadler, Procollagen trafficking, processing and fibrillogenesis., J. Cell Sci. 118 (2005) 1341–53.

[68] M.D. Shoulders, R.T. Raines, Collagen structure and stability., Annu. Rev. Biochem. 78 (2009) 929–58.

[69] L. Bozec, M. Odlyha, Thermal denaturation studies of collagen by microthermal analysis and atomic force microscopy, Biophys. J. 101 (2011) 228–236.

[70] P. Bornstein, E.H. Sage, Matricellular proteins: extracellular modulators of cell function, Curr. Opin. Cell Biol. 14 (2002) 608–616.

[71] D.E. White, W.J. Muller, Multifaceted Roles of Integrins in Breast Cancer Metastasis, J. Mammary Gland Biol. Neoplasia. 12 (2007) 135–142.

[72] W. Guo, F.G. Giancotti, Integrin signalling during tumour progression, Nat. Rev. Mol. Cell Biol. 5 (2004) 816–826.

[73] J.S. Desgrosellier, D.A. Cheresh, Integrins in cancer: biological implications and therapeutic opportunities, Nat. Rev. Cancer. 10 (2010) 9–22.

[74] J.A. Conti, T.J. Kendall, A. Bateman, T.A. Armstrong, A. Papa-Adams, Q. Xu, G. Packham, J.N. Primrose, R.C. Benyon, J.P. Iredale, The desmoplastic reaction surrounding hepatic colorectal adenocarcinoma metastases aids tumor growth and survival via alphav integrin ligation., Clin. Cancer Res. 14 (2008) 6405–13.

[75] A.J. Engler, S. Sen, H.L. Sweeney, D.E. Discher, Matrix Elasticity Directs Stem Cell Lineage Specification, Cell. 126 (2006) 677–689.

[76] F.M. Watt, W.T.S.S. Huck, Role of the extracellular matrix in regulating stem cell fate, Nat. Rev. Mol. Cell Biol. 14 (2013) 467–473.

[77] H. Lv, L. Li, M. Sun, Y. Zhang, L. Chen, Y. Rong, Y. Li, Mechanism of regulation of stem cell differentiation by matrix stiffness, Stem Cell Res. Ther. 6 (2015) 103.

[78] R.G. Wells, The role of matrix stiffness in regulating cell behavior, Hepatology. 47 (2008) 1394–1400.

[79] S. Kauppila, F. Stenbäck, J. Risteli, A. Jukkola, L. Risteli, Aberrant type I and type III collagen gene expression in human breast cancerin vivo, J. Pathol. 186 (1998) 262–268.

[80] Q. Xiao, G. Ge, Lysyl oxidase, extracellular matrix remodeling and cancer metastasis., Cancer Microenviron. 5 (2012) 261–73.

[81] J.T. Erler, K.L. Bennewith, M. Nicolau, N. Dornhöfer, C. Kong, Q.-T. Le, J.-T.A. Chi, S.S. Jeffrey, A.J. Giaccia, Lysyl oxidase is essential for hypoxia-induced

metastasis, Nature. 440 (2006) 1222–1226.

[82]   J. Helleman, M.P.H.M. Jansen, K. Ruigrok-Ritstier, I.L. van Staveren, M.P. Look, M.E. Meijer-van Gelder, A.M. Sieuwerts, J.G.M. Klijn, S. Sleijfer, J.A. Foekens, E.M.J.J. Berns, Association of an Extracellular Matrix Gene Cluster with Breast Cancer Prognosis and Endocrine Therapy Response, Clin. Cancer Res. 14 (2008) 5555–5564.

[83]   C. Leo, C. Cotic, V. Pomp, D. Fink, Z. Varga, Overexpression of Lox in triple-negative breast cancer, Ann. Diagn. Pathol. 34 (2018) 98–102.

[84]   R.G. Rowe, S.J. Weiss, Breaching the basement membrane: who, when and how?, Trends Cell Biol. 18 (2008) 560–574.

[85]   V.S. LeBleu, B. MacDonald, R. Kalluri, Structure and Function of Basement Membranes, Exp. Biol. Med. 232 (2007) 1121–1129.

[86]   Z.-S. Zeng, A.M. Cohen, J.G. Guillem, Loss of basement membrane type IV collagen is associated with increased expression of metalloproteinases 2 and 9 (MMP-2 and MMP-9) during human colorectal tumorigenesis, Carcinogenesis. 20 (1999) 749–755.

[87]   D.. Roach, R.. Fitridge, P.. Laws, S.. Millard, A. Varelias, P.. Cowled, Up-regulation of MMP-2 and MMP-9 Leads to Degradation of Type IV Collagen During Skeletal Muscle Reperfusion Injury; Protection by the MMP Inhibitor, Doxycycline, Eur. J. Vasc. Endovasc. Surg. 23 (2002) 260–269.

[88]   M.J. Duffy, T.M. Maguire, A. Hill, E. McDermott, N. O'Higgins, Metalloproteinases: role in breast carcinogenesis, invasion and metastasis., Breast Cancer Res. 2 (2000) 252–7.

[89]   A. Talvensaari-Mattila, P. Pääkkö, M. Höyhtyä, G. Blanco-Sequeiros, T. Turpeenniemi-Hujanen, Matrix metalloproteinase-2 immunoreactive protein: a marker of aggressiveness in breast carcinoma., Cancer. 83 (1998) 1153–62.

[90]   P.P. Provenzano, K.W. Eliceiri, J.M. Campbell, D.R. Inman, J.G. White, P.J. Keely, Collagen reorganization at the tumor-stromal interface facilitates local invasion, BMC Med. 4 (2006) 38.

[91]   A. Brabrand, I.I. Kariuki, M.J. Engstrøm, O.A. Haugen, L.A. Dyrnes, B.O. Asvold,

M.B. Lilledahl, A.M. Bofin, Alterations in collagen fibre patterns in breast cancer. A premise for tumour invasiveness?, (2014).

[92] M. Plodinec, M. Loparic, C.A. Monnier, E.C. Obermann, R. Zanetti-Dallenbach, P. Oertle, J.T. Hyotyla, U. Aebi, M. Bentires-Alj, R.Y.H. Lim, C.-A. Schoenenberger, The nanomechanical signature of breast cancer, Nat. Nanotechnol. 7 (2012) 757–765.

[93] J.I. Lopez, I. Kang, W.-K. You, D.M. McDonald, V.M. Weaver, In situ force mapping of mammary gland transformation., Integr. Biol. (Camb). 3 (2011) 910–21.

[94] M.J. Paszek, N. Zahir, K.R. Johnson, J.N. Lakins, G.I. Rozenberg, A. Gefen, C.A. Reinhart-King, S.S. Margulies, M. Dembo, D. Boettiger, D.A. Hammer, V.M. Weaver, Tensional homeostasis and the malignant phenotype, Cancer Cell. 8 (2005) 241–254.

[95] E.J. Song, Y.M. Sohn, M. Seo, Tumor stiffness measured by quantitative and qualitative shear wave elastography of breast cancer, Br. J. Radiol. 91 (2018).

[96] J.M. Chang, I.A. Park, S.H. Lee, W.H. Kim, M.S. Bae, H.R. Koo, A. Yi, S.J. Kim, N. Cho, W.K. Moon, Stiffness of tumours measured by shear-wave elastography correlated with subtypes of breast cancer, Eur. Radiol. 23 (2013) 2450–2458.

[97] M. Denis, A. Gregory, M. Bayat, R.T. Fazzio, D.H. Whaley, K. Ghosh, S. Shah, M. Fatemi, A. Alizad, Correlating tumor stiffness with immunohistochemical subtypes of breast cancers: Prognostic value of comb-push ultrasound shear elastography for differentiating luminal subtypes, PLoS One. 11 (2016).

[98] J. Hoarau-Véchot, A. Rafii, C. Touboul, J. Pasquier, Halfway between 2D and animal models: Are 3D cultures the ideal tool to study cancer-microenvironment interactions?, Int. J. Mol. Sci. 19 (2018).

[99] M. Kapałczyńska, T. Kolenda, W. Przybyła, M. Zajączkowska, A. Teresiak, V. Filas, M. Ibbs, R. Bliźniak, Ł. Łuczewski, K. Lamperska, 2D and 3D cell cultures – a comparison of different types of cancer cell cultures, Arch. Med. Sci. 14 (2018) 910–919.

[100] R. Eglen, T. Reisine, Primary Cells and Stem Cells in Drug Discovery: Emerging Tools for High-Throughput Screening, Assay Drug Dev. Technol. 9 (2011) 108–

124.

[101] J. Zieba, M. Ksiazkiewcz, K. Janik, M. Banaszczyk, J. Peciak, S. Piaskowski, M. Lipinski, M. Olczak, E. Stoczynska-Fidelus, P. Rieske, Sensitivity of neoplastic cells to senescence unveiled under standard cell culture conditions., Anticancer Res. 35 (2015) 2759–68.

[102] E. Stoczynska-Fidelus, S. Piaskowski, M. Bienkowski, M. Banaszczyk, K. Hulas-Bigoszewska, M. Winiecka-Klimek, A. Radomiak-Zaluska, W. Och, M. Borowiec, J. Zieba, C. Treda, P. Rieske, The Failure in the Stabilization of Glioblastoma-Derived Cell Lines: Spontaneous In Vitro Senescence as the Main Culprit, PLoS One. 9 (2014) e87136.

[103] J.-P. Gillet, S. Varma, M.M. Gottesman, The Clinical Relevance of Cancer Cell Lines, JNCI J. Natl. Cancer Inst. 105 (2013) 452–458.

[104] S. V. Sharma, D.A. Haber, J. Settleman, Cell line-based platforms to evaluate the therapeutic efficacy of candidate anticancer agents, Nat. Rev. Cancer. 10 (2010) 241–253.

[105] A. Marusyk, K. Polyak, Tumor heterogeneity: Causes and consequences, Biochim. Biophys. Acta - Rev. Cancer. 1805 (2010) 105–117.

[106] S. Domcke, R. Sinha, D.A. Levine, C. Sander, N. Schultz, Evaluating cell lines as tumour models by comparison of genomic profiles, Nat. Commun. 4 (2013) 2126.

[107] A. Li, J. Walling, Y. Kotliarov, A. Center, M.E. Steed, S.J. Ahn, M. Rosenblum, T. Mikkelsen, J.C. Zenklusen, H.A. Fine, Genomic Changes and Gene Expression Profiles Reveal That Established Glioma Cell Lines Are Poorly Representative of Primary Human Gliomas, Mol. Cancer Res. 6 (2008) 21–30.

[108] C.R. Thoma, M. Zimmermann, I. Agarkova, J.M. Kelm, W. Krek, 3D cell culture systems modeling tumor growth determinants in cancer target discovery, Adv. Drug Deliv. Rev. 69–70 (2014) 29–41.

[109] Y.-J. Kim, H.-I. Bae, O. Kyoung Kwon, M.-S. Choi, Three-dimensional gastric cancer cell culture using nanofiber scaffold for chemosensitivity test, Int. J. Biol. Macromol. 45 (2009) 65–71.

[110] A. Riedl, M. Schlederer, K. Pudelko, M. Stadler, S. Walter, D. Unterleuthner, C.

Unger, N. Kramer, M. Hengstschläger, L. Kenner, D. Pfeiffer, G. Krupitza, H. Dolznig, Comparison of cancer cells in 2D vs 3D culture reveals differences in AKT–mTOR–S6K signaling and drug responses, J. Cell Sci. 130 (2017) 203–218.

[111] S. Melissaridou, E. Wiechec, M. Magan, M.V. Jain, M.K. Chung, L. Farnebo, K. Roberg, The effect of 2D and 3D cell cultures on treatment response, EMT profile and stem cell features in head and neck cancer, Cancer Cell Int. 19 (2019) 16.

[112] L. Hutchinson, R. Kirk, High drug attrition rates—where are we going wrong?, Nat. Rev. Clin. Oncol. 8 (2011) 189–190.

[113] M. De Jong, T. Maina, Of mice and humans: Are they the same? - Implications in cancer translational research, J. Nucl. Med. 51 (2010) 501–504.

[114] I.W. Mak, N. Evaniew, M. Ghert, Lost in translation: animal models and clinical trials in cancer treatment., Am. J. Transl. Res. 6 (2014) 114–8.

[115] M.S. O'Reilly, T. Boehm, Y. Shing, N. Fukai, G. Vasios, W.S. Lane, E. Flynn, J.R. Birkhead, B.R. Olsen, J. Folkman, Endostatin: an endogenous inhibitor of angiogenesis and tumor growth., Cell. 88 (1997) 277–85.

[116] T. Boehm, J. Folkman, T. Browder, M.S. O'Reilly, Antiangiogenic therapy of experimental cancer does not induce acquired drug resistance, Nature. 390 (1997) 404–407.

[117] J.P. Eder, J.G. Supko, J.W. Clark, T.A. Puchalski, R. Garcia-Carbonero, D.P. Ryan, L.N. Shulman, J. Proper, M. Kirvan, B. Rattner, S. Connors, M.T. Keogan, M.J. Janicek, W.E. Fogler, L. Schnipper, N. Kinchla, C. Sidor, E. Phillips, J. Folkman, D.W. Kufe, Phase I Clinical Trial of Recombinant Human Endostatin Administered as a Short Intravenous Infusion Repeated Daily, J. Clin. Oncol. 20 (2002) 3772–3784.

[118] J.P. Thomas, R.Z. Arzoomanian, D. Alberti, R. Marnocha, F. Lee, A. Friedl, K. Tutsch, A. Dresen, P. Geiger, J. Pluda, W. Fogler, J.H. Schiller, G. Wilding, Phase I Pharmacokinetic and Pharmacodynamic Study of Recombinant Human Endostatin in Patients With Advanced Solid Tumors, J. Clin. Oncol. 21 (2003) 223–231.

[119] M.H. Kulke, E.K. Bergsland, D.P. Ryan, P.C. Enzinger, T.J. Lynch, A.X. Zhu, J.A. Meyerhardt, J. V Heymach, W.E. Fogler, C. Sidor, A. Michelini, K. Kinsella, A.P.

Venook, C.S. Fuchs, Phase II study of recombinant human endostatin in patients with advanced neuroendocrine tumors., J. Clin. Oncol. 24 (2006) 3555–61.

[120] J. Tannenbaum, B.T. Bennett, Russell and Burch's 3Rs then and now: the need for clarity in definition and purpose., J. Am. Assoc. Lab. Anim. Sci. 54 (2015) 120–32.

[121] J. Bin Kim, Three-dimensional tissue culture models in cancer biology, Semin. Cancer Biol. 15 (2005) 365–377.

[122] A. Nyga, U. Cheema, M. Loizidou, 3D tumour models: novel in vitro approaches to cancer studies, J. Cell Commun. Signal. 5 (2011) 239–248.

[123] C. Criscitiello, A. Esposito, L. Gelao, L. Fumagalli, M. Locatelli, I. Minchella, L. Adamoli, A. Goldhirsch, G. Curigliano, Immune approaches to the treatment of breast cancer, around the corner?, Breast Cancer Res. 16 (2014) 204.

[124] H. Gonzalez, C. Hagerling, Z. Werb, Roles of the immune system in cancer: From tumor initiation to metastatic progression, Genes Dev. 32 (2018) 1267–1284.

[125] D.P. Saraiva, A.T. Matias, S. Braga, A. Jacinto, M.G. Cabral, Establishment of a 3D Co-culture With MDA-MB-231 Breast Cancer Cell Line and Patient-Derived Immune Cells for Application in the Development of Immunotherapies, Front. Oncol. 10 (2020) 1543.

[126] T.N. Augustine, T. Dix-Peek, R. Duarte, G.P. Candy, Establishment of a heterotypic 3D culture system to evaluate the interaction of TREG lymphocytes and NK cells with breast cancer, J. Immunol. Methods. 426 (2015) 1–13.

[127] N.A. Zumwalde, J.D. Haag, D. Sharma, J.A. Mirrielees, L.G. Wilke, M.N. Gould, J.E. Gumperz, Analysis of immune cells from human mammary ductal epithelial organoids reveals Vδ2+ T cells that efficiently target breast carcinoma cells in the presence of bisphosphonate, Cancer Prev. Res. 9 (2016) 305–316.

[128] H. Sha, Z. Zou, K. Xin, X. Bian, X. Cai, W. Lu, J. Chen, G. Chen, A.M. Blair, P. Cao, B. Liu, Tumor-penetrating peptide fused EGFR single-domain antibody enhances cancer drug penetration into 3D multicellular spheroids and facilitates effective gastric cancer therapy, J. Control. Release. 200 (2015) 188–200.

[129] M. Zietarska, C.M. Maugard, A. Filali-Mouhim, M. Alam-Fahmy, P.N. Tonin, D.M. Provencher, A. Mes-Masson, Molecular description of a 3D in vitro model for the

study of epithelial ovarian cancer (EOC), Mol. Carcinog. 46 (2007) 872–885.

[130] S.F. Boj, C.-I. Hwang, L.A. Baker, I.I.C. Chio, D.D. Engle, V. Corbo, M. Jager, M. Ponz-Sarvise, H. Tiriac, M.S. Spector, A. Gracanin, T. Oni, K.H. Yu, R. van Boxtel, M. Huch, K.D. Rivera, J.P. Wilson, M.E. Feigin, D. Öhlund, A. Handly-Santana, C.M. Ardito-Abraham, M. Ludwig, E. Elyada, B. Alagesan, G. Biffi, G.N. Yordanov, B. Delcuze, B. Creighton, K. Wright, Y. Park, F.H.M. Morsink, I.Q. Molenaar, I.H. Borel Rinkes, E. Cuppen, Y. Hao, Y. Jin, I.J. Nijman, C. Iacobuzio-Donahue, S.D. Leach, D.J. Pappin, M. Hammell, D.S. Klimstra, O. Basturk, R.H. Hruban, G.J. Offerhaus, R.G.J. Vries, H. Clevers, D.A. Tuveson, Organoid models of human and mouse ductal pancreatic cancer., Cell. 160 (2015) 324–38.

[131] L. Zhao, L. Huang, S. Yu, J. Zheng, H. Wang, Y. Zhang, Decellularized tongue tissue as an in vitro model for studying tongue cancer and tongue regeneration, Acta Biomater. 58 (2017) 122–135.

[132] L.W. Dunne, Z. Huang, W. Meng, X. Fan, N. Zhang, Q. Zhang, Z. An, Human decellularized adipose tissue scaffold as a model for breast cancer cell growth and drug treatments, Biomaterials. 35 (2014) 4940–4949.

[133] L.A. Gurski, A.K. Jha, C. Zhang, X. Jia, M.C. Farach-Carson, Hyaluronic acid-based hydrogels as 3D matrices for in vitro evaluation of chemotherapeutic drugs using poorly adherent prostate cancer cells, Biomaterials. 30 (2009) 6076–6085.

[134] Y. Fang, R.M. Eglen, Three-Dimensional Cell Cultures in Drug Discovery and Development, SLAS Discov. 22 (2017) 456–472.

[135] O. Habanjar, M. Diab-Assaf, F. Caldefie-Chezet, L. Delort, 3D Cell Culture Systems: Tumor Application, Advantages, and Disadvantages, Int. J. Mol. Sci. 22 (2021).

[136] D. Liu, S. Chen, M.W. Naing, A review of manufacturing capabilities of cell spheroid generation technologies and future development, Biotechnol. Bioeng. 118 (2021) 542–554.

[137] S. Sant, P.A. Johnston, The production of 3D tumor spheroids for cancer drug discovery, Drug Discov. Today Technol. 23 (2017) 27–36.

[138] B. MA, B. M, H. A, C. A, H. H, I. D, D. A, Influence of Matrigel on Single- and

Multiple-Spheroid Cultures in Breast Cancer Research, SLAS Discov. Adv. Life Sci. R D. 24 (2019) 563–578.

[139] Å.M. Ballangrud, W.H. Yang, S. Palm, R. Enmon, P.E. Borchardt, V.A. Pellegrini, M.R. McDevitt, D.A. Scheinberg, G. Sgouros, Alpha-particle emitting atomic generator (actinium-225)-labeled trastuzumab (Herceptin) targeting of breast cancer spheroids: Efficacy versus HER2/neu expression, Clin. Cancer Res. 10 (2004) 4489–4497.

[140] T. Jiang, J.G. Munguia-Lopez, S. Flores-Torres, J. Grant, S. Vijayakumar, A. De Leon-Rodriguez, J.M. Kinsella, Directing the Self-Assembly of Tumour Spheroids by Bioprinting Cellular Heterogeneous Models within Alginate/Gelatin Hydrogels, Sci. Rep. 7 (2017) 1–9.

[141] W. Zhang, C. Li, B.C. Baguley, F. Zhou, W. Zhou, J.P. Shaw, Z. Wang, Z. Wu, J. Liu, Optimization of the formation of embedded multicellular spheroids of MCF-7 cells: How to reliably produce a biomimetic 3D model, Anal. Biochem. 515 (2016) 47–54.

[142] H. WY, Y. SK, H. CL, R. RA, A. NB, Development of multicellular tumor spheroid (MCTS) culture from breast cancer cell and a high throughput screening method using the MTT assay, PLoS One. 7 (2012).

[143] J. Kim, B.K. Koo, J.A. Knoblich, Human organoids: model systems for human biology and medicine, Nat. Rev. Mol. Cell Biol. 21 (2020) 571–584.

[144] J. Drost, H. Clevers, Organoids in cancer research, Nat. Rev. Cancer. 18 (2018) 407–418.

[145] G. Rossi, A. Manfrin, M.P. Lutolf, Progress and potential in organoid research, Nat. Rev. Genet. 19 (2018) 671–687.

[146] S.I. Djomehri, B. Burman, M.E. Gonzalez, S. Takayama, C.G. Kleer, A reproducible scaffold-free 3D organoid model to study neoplastic progression in breast cancer, J. Cell Commun. Signal. 13 (2019) 129–143.

[147] Y. Baert, J. De Kock, J.P. Alves-Lopes, O. Söder, J.B. Stukenborg, E. Goossens, Primary Human Testicular Cells Self-Organize into Organoids with Testicular Properties, Stem Cell Reports. 8 (2017) 30–38.

[148] C. Roelofs, F. Hollande, R. Redvers, R.L. Anderson, D. Merino, Breast tumour organoids: Promising models for the genomic and functional characterisation of breast cancer, Biochem. Soc. Trans. 47 (2019) 109–117.

[149] N. Sachs, H. Clevers, Organoid cultures for the analysis of cancer phenotypes, Curr. Opin. Genet. Dev. 24 (2014) 68–73.

[150] P.W. Nagle, J.T.M. Plukker, C.T. Muijs, P. van Luijk, R.P. Coppes, Patient-derived tumor organoids for prediction of cancer treatment response, Semin. Cancer Biol. 53 (2018) 258–264.

[151] N. Sachs, J. de Ligt, O. Kopper, E. Gogola, G. Bounova, F. Weeber, A.V. Balgobind, K. Wind, A. Gracanin, H. Begthel, J. Korving, R. van Boxtel, A.A. Duarte, D. Lelieveld, A. van Hoeck, R.F. Ernst, F. Blokzijl, I.J. Nijman, M. Hoogstraat, M. van de Ven, D.A. Egan, V. Zinzalla, J. Moll, S.F. Boj, E.E. Voest, L. Wessels, P.J. van Diest, S. Rottenberg, R.G.J. Vries, E. Cuppen, H. Clevers, A Living Biobank of Breast Cancer Organoids Captures Disease Heterogeneity, Cell. 172 (2018) 373-386.e10.

[152] A.J. Walsh, R.S. Cook, M.E. Sanders, L. Aurisicchio, G. Ciliberto, C.L. Arteaga, M.C. Skala, Quantitative optical imaging of primary tumor organoid metabolism predicts drug response in breast cancer, Cancer Res. 74 (2014) 5184–5194.

[153] E. McLachlan, Q. Shao, H.L. Wang, S. Langlois, D.W. Laird, Connexins act as tumor suppressors in three-dimensional mammary cell organoids by regulating differentiation and angiogenesis, Cancer Res. 66 (2006) 9886–9894.

[154] S.D. Diermeier, K.C. Chang, S.M. Freier, J. Song, O. El Demerdash, A. Krasnitz, F. Rigo, C.F. Bennett, D.L. Spector, Mammary Tumor-Associated RNAs Impact Tumor Cell Proliferation, Invasion, and Migration, Cell Rep. 17 (2016) 261–274.

[155] E. Campaner, A. Zannini, M. Santorsola, D. Bonazza, C. Bottin, V. Cancila, C. Tripodo, M. Bortul, F. Zanconati, S. Schoeftner, G. Del Sal, Breast cancer organoids model patient-specific response to drug treatment, Cancers (Basel). 12 (2020) 1–19.

[156] B. Nayak, G.M. Balachander, S. Manjunath, A. Rangarajan, K. Chatterjee, Tissue mimetic 3D scaffold for breast tumor-derived organoid culture toward personalized chemotherapy, Colloids Surfaces B Biointerfaces. 180 (2019) 334–343.

[157] T.K. Rajab, T.J. O'Malley, V. Tchantchaleishvili, Decellularized scaffolds for tissue engineering: Current status and future perspective, Artif. Organs. 44 (2020) 1031–1043.

[158] J. Liao, B. Xu, R. Zhang, Y. Fan, H. Xie, X. Li, Applications of decellularized materials in tissue engineering: advantages, drawbacks and current improvements, and future perspectives, J. Mater. Chem. B. 8 (2020) 10023–10049.

[159] S.R. Meyer, B. Chiu, T.A. Churchill, L. Zhu, J.R.T. Lakey, D.B. Ross, Comparison of aortic valve allograft decellularization techniques in the rat, J. Biomed. Mater. Res. Part A. 79A (2006) 254–262.

[160] S.B. Lumpkins, N. Pierre, P.S. McFetridge, A mechanical evaluation of three decellularization methods in the design of a xenogeneic scaffold for tissue engineering the temporomandibular joint disc, Acta Biomater. 4 (2008) 808–816.

[161] B. Yang, Y. Zhang, L. Zhou, Z. Sun, J. Zheng, Y. Chen, Y. Dai, Development of a Porcine Bladder Acellular Matrix with Well-Preserved Extracellular Bioactive Factors for Tissue Engineering, Https://Home.Liebertpub.Com/Tec. 16 (2010) 1201–1211.

[162] E. García-Gareta, Y. Abduldaiem, P. Sawadkar, C. Kyriakidis, F. Lali, K.V. Greco, Decellularised scaffolds: just a framework? Current knowledge and future directions, J. Tissue Eng. 11 (2020).

[163] G. Liu, B. Wang, S. Li, Q. Jin, Y. Dai, Human breast cancer decellularized scaffolds promote epithelial-to-mesenchymal transitions and stemness of breast cancer cells in vitro, J. Cell. Physiol. 234 (2019) 9447–9456.

[164] Q. Jin, G. Liu, S. Li, H. Yuan, Z. Yun, W. Zhang, S. Zhang, Y. Dai, Y. Ma, Decellularized breast matrix as bioactive microenvironment for in vitro three-dimensional cancer culture, J. Cell. Physiol. 234 (2019) 3425–3435.

[165] A.L. Wishart, S.J. Conner, J.R. Guarin, J.P. Fatherree, Y. Peng, R.A. McGinn, R. Crews, S.P. Naber, M. Hunter, A.S. Greenberg, M.J. Oudin, Decellularized extracellular matrix scaffolds identify full-length collagen VI as a driver of breast cancer cell invasion in obesity and metastasis, Sci. Adv. 6 (2020).

[166] D. Lv, S.-C. Yu, Y.-F. Ping, H. Wu, X. Zhao, H. Zhang, Y. Cui, B. Chen, X. Zhang,

J. Dai, X.-W. Bian, X.-H. Yao, A three-dimensional collagen scaffold cell culture system for screening anti-glioma therapeutics., Oncotarget. 7 (2016) 56904–56914.

[167] B.S. Sack, J.R. Mauney, C.R. Estrada, Jr., Silk fibroin scaffolds for urologic tissue engineering, Curr. Urol. Rep. 17 (2016) 16.

[168] Y.-H. Zhao, C.-M. Niu, J.-Q. Shi, Y.-Y. Wang, Y.-M. Yang, H.-B. Wang, Novel conductive polypyrrole/silk fibroin scaffold for neural tissue repair, Neural Regen. Res. 13 (2018) 1455.

[169] K. Wang, F.M. Kievit, S.J. Florczyk, Z.R. Stephen, M. Zhang, 3D Porous Chitosan–Alginate Scaffolds as an In Vitro Model for Evaluating Nanoparticle-Mediated Tumor Targeting and Gene Delivery to Prostate Cancer, Biomacromolecules. 16 (2015) 3362–3372.

[170] S.J. Florczyk, F.M. Kievit, K. Wang, A.E. Erickson, R.G. Ellenbogen, M. Zhang, 3D porous chitosan–alginate scaffolds promote proliferation and enrichment of cancer stem-like cells, J. Mater. Chem. B. 4 (2016) 6326–6334.

[171] F.M. Kievit, S.J. Florczyk, M.C. Leung, K. Wang, J.D. Wu, J.R. Silber, R.G. Ellenbogen, J.S.H. Lee, M. Zhang, Proliferation and enrichment of CD133+ glioblastoma cancer stem cells on 3D chitosan-alginate scaffolds, Biomaterials. 35 (2014) 9137–9143.

[172] T.J. Levingstone, A. Matsiko, G.R. Dickson, F.J. O'Brien, J.P. Gleeson, A biomimetic multi-layered collagen-based scaffold for osteochondral repair, Acta Biomater. 10 (2014) 1996–2004.

[173] S.S. Rao, J. Dejesus, A.R. Short, J.J. Otero, A. Sarkar, J.O. Winter, Glioblastoma behaviors in three-dimensional collagen-hyaluronan composite hydrogels., ACS Appl. Mater. Interfaces. 5 (2013) 9276–84.

[174] J.Y. Lai, Biocompatibility of chemically cross-linked gelatin hydrogels for ophthalmic use, J. Mater. Sci. Mater. Med. 21 (2010) 1899–1911.

[175] C. Wang, R. Wang, X. Liang, al -, C. Yu, Q. Liu, C. Chen, G. Janani, M.M. Pillai, R. Selvakumar, A. Bhattacharyya, C. Sabarinath, An in vitro 3D model using collagen coated gelatin nanofibers for studying breast cancer metastasis, Biofabrication. 9 (2017) 015016.

[176] X. Wu, Y. Liu, X. Li, P. Wen, Y. Zhang, Y. Long, X. Wang, Y. Guo, F. Xing, J. Gao, Preparation of aligned porous gelatin scaffolds by unidirectional freeze-drying method, Acta Biomater. 6 (2010) 1167–1177.

[177] S. Pradhan, I. Hassani, W.J. Seeto, E.A. Lipke, PEG-fibrinogen hydrogels for three-dimensional breast cancer cell culture, J. Biomed. Mater. Res. Part A. 105 (2017) 236–252.

[178] F. Del Bufalo, T. Manzo, V. Hoyos, S. Yagyu, I. Caruana, J. Jacot, O. Benavides, D. Rosen, M.K. Brenner, 3D modeling of human cancer: A PEG-fibrin hydrogel system to study the role of tumor microenvironment and recapitulate the in vivo effect of oncolytic adenovirus, Biomaterials. 84 (2016) 76–85.

[179] C. Fischbach, R. Chen, T. Matsumoto, T. Schmelzle, J.S. Brugge, P.J. Polverini, D.J. Mooney, Engineering tumors with 3D scaffolds, Nat. Methods. 4 (2007) 855–860.

[180] S.P. Pathi, C. Kowalczewski, R. Tadipatri, C. Fischbach, A novel 3-D mineralized tumor model to study breast cancer bone metastasis., PLoS One. 5 (2010) e8849.

[181] O. Hartman, C. Zhang, E.L. Adams, M.C. Farach-Carson, N.J. Petrelli, B.D. Chase, J.F. Rabolt, Biofunctionalization of electrospun PCL-based scaffolds with perlecan domain IV peptide to create a 3-D pharmacokinetic cancer model., Biomaterials. 31 (2010) 5700–18.

[182] S. Feng, X. Duan, P.-K. Lo, S. Liu, X. Liu, H. Chen, Q. Wang, Expansion of breast cancer stem cells with fibrous scaffolds, Integr. Biol. 5 (2013) 768.

[183] E.L.S. Fong, S.-E. Lamhamedi-Cherradi, E. Burdett, V. Ramamoorthy, A.J. Lazar, F.K. Kasper, M.C. Farach-Carson, D. Vishwamitra, E.G. Demicco, B.A. Menegaz, H.M. Amin, A.G. Mikos, J.A. Ludwig, Modeling Ewing sarcoma tumors in vitro with 3D scaffolds, Proc. Natl. Acad. Sci. 110 (2013) 6500–6505.

[184] K.Y. Lee, D.J. Mooney, Hydrogels for Tissue Engineering, (2001).

[185] A.S. Hoffman, Hydrogels for biomedical applications, Adv. Drug Deliv. Rev. 64 (2012) 18–23.

[186] C. Liverani, A. De Vita, S. Minardi, Y. Kang, L. Mercatali, D. Amadori, A. Bongiovanni, F. La Manna, T. Ibrahim, E. Tasciotti, F. La Manna, T. Ibrahim, E.

Tasciotti, A biomimetic 3D model of hypoxia-driven cancer progression, Sci. Rep. 9 (2019).

[187] A. Lode, M. Meyer, S. Brüggemeier, B. Paul, H. Baltzer, M. Schröpfer, C. Winkelmann, F. Sonntag, M. Gelinsky, Additive manufacturing of collagen scaffolds by three-dimensional plotting of highly viscous dispersions, Biofabrication. 8 (2016) 015015.

[188] M. James-Bhasin, P.M. Siegel, S.N. Nazhat, A three-dimensional dense collagen hydrogel to model cancer cell/osteoblast interactions, J. Funct. Biomater. 9 (2018).

[189] E.E. Antoine, P.P. Vlachos, M.N. Rylander, Review of collagen I hydrogels for bioengineered tissue microenvironments: characterization of mechanics, structure, and transport., Tissue Eng. Part B. Rev. 20 (2014) 683–96.

[190] N. Abbasi, S. Hamlet, R.M. Love, N.T. Nguyen, Porous scaffolds for bone regeneration, J. Sci. Adv. Mater. Devices. 5 (2020) 1–9.

[191] S. Nath, G.R. Devi, Three-dimensional culture systems in cancer research: Focus on tumor spheroid model, Pharmacol. Ther. 163 (2016) 94–108.

[192] M. Ravi, V. Paramesh, S.R. Kaviya, E. Anuradha, F.D. Paul Solomon, 3D Cell Culture Systems: Advantages and Applications, J. Cell. Physiol. 230 (2015) 16–26.

[193] J. Redmond, H. McCarthy, P. Buchanan, T.J. Levingstone, N.J. Dunne, Advances in biofabrication techniques for collagen-based 3D in vitro culture models for breast cancer research, Mater. Sci. Eng. C. 122 (2021) 111944.

[194] L. Chen, Z. Xiao, Y. Meng, Y. Zhao, J. Han, G. Su, B. Chen, J. Dai, The enhancement of cancer stem cell properties of MCF-7 cells in 3D collagen scaffolds for modeling of cancer and anti-cancer drugs, Biomaterials. 33 (2012) 1437–1444.

[195] R.F. Cox, A. Jenkinson, K. Pohl, F.J. O'Brien, M.P. Morgan, Osteomimicry of Mammary Adenocarcinoma Cells In Vitro; Increased Expression of Bone Matrix Proteins and Proliferation within a 3D Collagen Environment, PLoS One. 7 (2012).

[196] R. Marlow, G. Honeth, S. Lombardi, M. Cariati, S. Hessey, A. Pipili, V. Mariotti, B. Buchupalli, K. Foster, D. Bonnet, A. Grigoriadis, P. Rameshwar, A. Purushotham, A. Tutt, G. Dontu, A novel model of dormancy for bone metastatic breast cancer cells, Cancer Res. 73 (2013) 6886–6899.

[197] K.M. Riching, B.L. Cox, M.R. Salick, C. Pehlke, A.S. Riching, S.M. Ponik, B.R. Bass, W.C. Crone, Y. Jiang, A.M. Weaver, K.W. Eliceiri, P.J. Keely, 3D collagen alignment limits protrusions to enhance breast cancer cell persistence, Biophys. J. 107 (2015) 2546–2558.

[198] C. Liverani, L. Mercatali, L. Cristofolini, E. Giordano, S. Minardi, G. Della Porta, A. De Vita, G. Miserocchi, C. Spadazzi, E. Tasciotti, D. Amadori, T. Ibrahim, Investigating the Mechanobiology of Cancer Cell–ECM Interaction Through Collagen-Based 3D Scaffolds, Cell. Mol. Bioeng. 10 (2017) 223–234.

[199] J. Yang, J. Richards, P. Bowman, R. Guzman, J. Enami, K. McCormick, S. Hamamoto, D. Pitelka, S. Nandi, Sustained growth and three-dimensional organization of primary mammary tumor epithelial cells embedded in collagen gels., Proc. Natl. Acad. Sci. U. S. A. 76 (1979) 3401–5.

[200] F.R. Miller, D. McEachern, B.E. Miller, Growth regulation of mouse mammary tumor cells in collagen gel cultures by diffusible factors produced by normal mammary gland epithelium and stromal fibroblasts., Cancer Res. 49 (1989) 6091–7.

[201] W. Jones, A.E. Lee, P. Riddle, R.R. Dils, R.C. Hallowes, Phenotypic responses of mouse mammary tumours and normal mammary epithelium cultured in collagen gels: correlation with tumour type and progression., Tissue Cell. 24 (1992) 879–94.

[202] C.W. Daniel, J.J. Berger, P. Strickland, R. Garcia, Similar growth pattern of mouse mammary epithelium cultivated in collagen matrix in vivo and in vitro., Dev. Biol. 104 (1984) 57–64.

[203] E.M. Ahmed, Hydrogel: Preparation, characterization, and applications: A review, J. Adv. Res. 6 (2015) 105–121.

[204] C.B. Raub, J. Unruh, V. Suresh, T. Krasieva, T. Lindmo, E. Gratton, B.J. Tromberg, S.C. George, Image correlation spectroscopy of multiphoton images correlates with collagen mechanical properties., Biophys. J. 94 (2008) 2361–73.

[205] M. Achilli, D. Mantovani, Tailoring mechanical properties of collagen-based scaffolds for vascular tissue engineering: The effects of pH, temperature and ionic strength on gelation, Polymers (Basel). 2 (2010) 664–680.

[206] J. Lee, B. Song, R. Subbiah, J.J. Chung, U.H. Choi, K. Park, S.H. Kim, S.J. Oh,

Effect of chain flexibility on cell adhesion: Semi-flexible model-based analysis of cell adhesion to hydrogels, Sci. Rep. 9 (2019) 1–8.

[207] I. Rault, V. Frei, D. Herbage, N. Abdul-Malak, A. Huc, Evaluation of different chemical methods for cros-linking collagen gel, films and sponges, J. Mater. Sci. Mater. Med. 7 (1996) 215–221.

[208] C.A. Mullen, T.J. Vaughan, K.L. Billiar, L.M. McNamara, The effect of substrate stiffness, thickness, and cross-linking density on osteogenic cell behavior., Biophys. J. 108 (2015) 1604–1612.

[209] C.A. Mullen, M.G. Haugh, M.B. Schaffler, R.J. Majeska, L.M. McNamara, Osteocyte differentiation is regulated by extracellular matrix stiffness and intercellular separation., J. Mech. Behav. Biomed. Mater. 28 (2013) 183–94.

[210] S. Gao, Z. Yuan, W. Guo, M. Chen, S. Liu, T. Xi, Q. Guo, Comparison of glutaraldehyde and carbodiimides to crosslink tissue engineering scaffolds fabricated by decellularized porcine menisci, Mater. Sci. Eng. C. 71 (2017) 891–900.

[211] H.M. Powell, S.T. Boyce, EDC cross-linking improves skin substitute strength and stability, Biomaterials. 27 (2006) 5821–5827.

[212] S.N. Park, J.C. Park, H.O. Kim, M.J. Song, H. Suh, Characterization of porous collagen/hyaluronic acid scaffold modified by 1-ethyl-3-(3-dimethylaminopropyl)carbodiimide cross-linking, Biomaterials. 23 (2002) 1205–1212.

[213] M.G. Haugh, C.M. Murphy, R.C. McKiernan, C. Altenbuchner, F.J. O'Brien, F.J. O'brien, Crosslinking and Mechanical Properties Significantly Influence Cell Attachment, Proliferation, and Migration Within Collagen Glycosaminoglycan Scaffolds., Tissue Eng. - Part A. 17 (2011) 1201–1208.

[214] Q. Jiang, N. Reddy, S. Zhang, N. Roscioli, Y. Yang, Water-stable electrospun collagen fibers from a non-toxic solvent and crosslinking system, J. Biomed. Mater. Res. Part A. 101A (2013) 1237–1247.

[215] H.K. Kleinman, G.R. Martin, Matrigel: Basement membrane matrix with biological activity, Semin. Cancer Biol. 15 (2005) 378–386.

[216] G. Benton, H.K. Kleinman, J. George, I. Arnaoutova, Multiple uses of basement membrane-like matrix (BME/Matrigel) in vitro and in vivo with cancer cells, Int. J. Cancer. 128 (2011) 1751–1757.

[217] R. Fridman, G. Giaccone, T. Kanemoto, G.R. Martin, A.F. Gazdar, J.L. Mulshine, Reconstituted basement membrane (matrigel) and laminin can enhance the tumorigenicity and the drug resistance of small cell lung cancer cell lines., Proc. Natl. Acad. Sci. 87 (1990) 6698–6702.

[218] S. Xu, Z.-F. Jia, C. Kang, Q. Huang, G. Wang, X. Liu, X. Zhou, P. Xu, P. Pu, Upregulation of SEPT7 Gene Inhibits Invasion of Human Glioma Cells, Cancer Invest. 28 (2010) 248–258.

[219] C.E. Barcus, P.J. Keely, K.W. Eliceiri, L.A. Schuler, Stiff Collagen Matrices Increase Tumorigenic Prolactin Signaling in Breast Cancer Cells, J. Biol. Chem. 288 (2013) 12722–12732.

[220] M.G. Haugh, C.M. Murphy, F.J. O'Brien, Novel freeze-drying methods to produce a range of collagen-glycosaminoglycan scaffolds with tailored mean pore sizes., Tissue Eng. Part C. Methods. 16 (2010) 887–94.

[221] F.J. O'Brien, B.A. Harley, I. V. Yannas, L. Gibson, Influence of freezing rate on pore structure in freeze-dried collagen-GAG scaffolds, Biomaterials. 25 (2004) 1077–1086.

[222] G.M. Cunniffe, G.R. Dickson, S. Partap, K.T. Stanton, Development and characterisation of a collagen nano-hydroxyapatite composite scaffold for bone tissue engineering., J. Mater. Sci. Mater. Med. 21 (2010) 2293–2301.

[223] C.M. Tierney, M.G. Haugh, J. Liedl, F. Mulcahy, B. Hayes, F.J. O'Brien, The effects of collagen concentration and crosslink density on the biological, structural and mechanical properties of collagen-GAG scaffolds for bone tissue engineering, J. Mech. Behav. Biomed. Mater. 2 (2009) 202–209.

[224] N. Davidenko, T. Gibb, C. Schuster, S.M. Best, J.J. Campbell, C.J. Watson, R.E. Cameron, Biomimetic collagen scaffolds with anisotropic pore architecture, Acta Biomater. 8 (2012) 667–676.

[225] C.. Lee, A.. Grodzinsky, M. Spector, The effects of cross-linking of collagen-

glycosaminoglycan scaffolds on compressive stiffness, chondrocyte-mediated contraction, proliferation and biosynthesis, Biomaterials. 22 (2001) 3145–3154.

[226] N. Davidenko, C.F. Schuster, D. V Bax, N. Raynal, R.W. Farndale, S.M. Best, R.E. Cameron, Control of crosslinking for tailoring collagen-based scaffolds stability and mechanics., Acta Biomater. 25 (2015) 131–42.

[227] M.G. Haugh, M.J. Jaasma, F.J. O'Brien, The effect of dehydrothermal treatment on the mechanical and structural properties of collagen-GAG scaffolds, J. Biomed. Mater. Res. Part A. 89A (2009) 363–369.

[228] K.S. Weadock, E.J. Miller, L.D. Bellincampi, J.P. Zawadsky, M.G. Dunn, Physical crosslinking of collagen fibers: Comparison of ultraviolet irradiation and dehydrothermal treatment, J. Biomed. Mater. Res. 29 (1995) 1373–1379.

[229] R.D. Hume, S. Pensa, E.J. Brown, P.A. Kreuzaler, J. Hitchcock, A. Husmann, J.J. Campbell, A.O. Lloyd-Thomas, R.E. Cameron, C.J. Watson, Tumour cell invasiveness and response to chemotherapeutics in adipocyte invested 3D engineered anisotropic collagen scaffolds, Sci. Rep. 8 (2018) 1–15.

[230] G.S. Offeddu, J.C. Ashworth, R.E. Cameron, M.L. Oyen, Multi-scale mechanical response of freeze-dried collagen scaffolds for tissue engineering applications, J. Mech. Behav. Biomed. Mater. 42 (2015) 19–25.

[231] D.G. Simpson, B.S. Jha, C.E. Ayres, J.R. Bowman, T.A. Telemeco, S.A. Sell, G.L. Bowlin, Electrospun collagen: A tissue engineering scaffold with unique functional properties in a wide variety of applications, J. Nanomater. 2011 (2011).

[232] J. Doshi, D.H. Reneker, Electrospinning process and applications of electrospun fibers, J. Electrostat. 35 (1995) 151–160.

[233] W.E. Teo, S. Ramakrishna, A review on electrospinning design and nanofibre assemblies, Nanotechnology. 17 (2006) R89–R106.

[234] A. Greiner, J.H. Wendorff, Electrospinning: A Fascinating Method for the Preparation of Ultrathin Fibers, Angew. Chemie Int. Ed. 46 (2007) 5670–5703.

[235] Z.-M. Huang, Y.-Z. Zhang, M. Kotaki, S. Ramakrishna, A review on polymer nanofibers by electrospinning and their applications in nanocomposites, Compos. Sci. Technol. 63 (2003) 2223–2253.

[236] J. Zeng, X. Xu, X. Chen, Q. Liang, X. Bian, L. Yang, X. Jing, Biodegradable electrospun fibers for drug delivery, J. Control. Release. 92 (2003) 227–231.

[237] V. Chaurey, P.-C. Chiang, C. Polanco, Y.-H. Su, C.-F. Chou, N.S. Swami, Interplay of Electrical Forces for Alignment of Sub-100 nm Electrospun Nanofibers on Insulator Gap Collectors, Langmuir. 26 (2010) 19022–19026.

[238] V. Beachley, X. Wen, Effect of electrospinning parameters on the nanofiber diameter and length., Mater. Sci. Eng. C. Mater. Biol. Appl. 29 (2009) 663–668.

[239] X. Zong, K. Kim, D. Fang, S. Ran, B.S. Hsiao, B. Chu, Structure and process relationship of electrospun bioabsorbable nanofiber membranes, Polymer (Guildf). 43 (2002) 4403–4412.

[240] J.. Deitzel, J. Kleinmeyer, D. Harris, N.. Beck Tan, The effect of processing variables on the morphology of electrospun nanofibers and textiles, Polymer (Guildf). 42 (2001) 261–272.

[241] R.M. Nezarati, M.B. Eifert, E. Cosgriff-Hernandez, Effects of humidity and solution viscosity on electrospun fiber morphology., Tissue Eng. Part C. Methods. 19 (2013) 810–9.

[242] L. Huang, K. Nagapudi, R.P. Apkarian, E.L. Chaikof, Engineered collagen-PEO nanofibers and fabrics., J. Biomater. Sci. Polym. Ed. 12 (2001) 979–93.

[243] B. Tarus, N. Fadel, A. Al-Oufy, M. El-Messiry, Effect of polymer concentration on the morphology and mechanical characteristics of electrospun cellulose acetate and poly (vinyl chloride) nanofiber mats, Alexandria Eng. J. 55 (2016) 2975–2984.

[244] H. Fong, I. Chun, D.. Reneker, Beaded nanofibers formed during electrospinning, Polymer (Guildf). 40 (1999) 4585–4592.

[245] X. Yuan, Y. Zhang, C. Dong, J. Sheng, Morphology of ultrafine polysulfone fibers prepared by electrospinning, Polym. Int. 53 (2004) 1704–1710.

[246] W. Zuo, M. Zhu, W. Yang, H. Yu, Y. Chen, Y. Zhang, Experimental study on relationship between jet instability and formation of beaded fibers during electrospinning, Polym. Eng. Sci. 45 (2005) 704–709.

[247] J. Rnjak-Kovacina, A.S. Weiss, Increasing the pore size of electrospun scaffolds,

Tissue Eng. - Part B Rev. 17 (2011) 365–372.

[248] M.C. Phipps, W.C. Clem, J.M. Grunda, G.A. Clines, S.L. Bellis, Increasing the pore sizes of bone-mimetic electrospun scaffolds comprised of polycaprolactone, collagen I and hydroxyapatite to enhance cell infiltration, Biomaterials. 33 (2012) 524–534.

[249] A. Guimarães, A. Martins, E.D. Pinho, S. Faria, R.L. Reis, N.M. Neves, Solving cell infiltration limitations of electrospun nanofiber meshes for tissue engineering applications, Nanomedicine. 5 (2010) 539–554.

[250] C.S. Szot, C.F. Buchanan, P. Gatenholm, M.N. Rylander, J.W. Freeman, Investigation of cancer cell behavior on nanofibrous scaffolds, Mater. Sci. Eng. C. 31 (2011) 37–42.

[251] B.A. Blakeney, A. Tambralli, J.M. Anderson, A. Andukuri, D.J. Lim, D.R. Dean, H.W. Jun, Cell infiltration and growth in a low density, uncompressed three-dimensional electrospun nanofibrous scaffold, Biomaterials. 32 (2011) 1583–1590.

[252] Y.Z. Zhang, Y. Feng, Z.M. Huang, S. Ramakrishna, C.T. Lim, Fabrication of porous electrospun nanofibres, Nanotechnology. 17 (2006) 901–908.

[253] C. Tran, V. Kalra, Fabrication of porous carbon nanofibers with adjustable pore sizes as electrodes for supercapacitors, J. Power Sources. 235 (2013) 289–296.

[254] P. Katta, M. Alessandro, R.D. Ramsier, G.G. Chase, Continuous Electrospinning of Aligned Polymer Nanofibers onto a Wire Drum Collector, (2004).

[255] B. Sundaray, V. Subramanian, T.S. Natarajan, R.-Z. Xiang, C.-C. Chang, W.-S. Fann, Electrospinning of continuous aligned polymer fibers, Appl. Phys. Lett. 84 (2004) 1222–1224.

[256] A. Theron, E. Zussman, A.L. Yarin, Electrostatic field-assisted alignment of electrospun nanofibres, Nanotechnology. 12 (2001) 384–390.

[257] Q.P. Pham, U. Sharma, A.G. Mikos, Electrospinning of Polymeric Nanofibers for Tissue Engineering Applications: A Review, Tissue Eng. 12 (2006) 1197–1211.

[258] E.J. Mulholland, A. Ali, T. Robson, N.J. Dunne, H.O. McCarthy, Delivery of RALA/siFKBPL nanoparticles via electrospun bilayer nanofibres: An innovative

angiogenic therapy for wound repair, J. Control. Release. 316 (2019) 53–65.

[259] H.M. Pauly, B.N. Sathy, D. Olvera, H.O. McCarthy, D.J. Kelly, K.C. Popat, N.J. Dunne, T.L. Haut Donahue, Hierarchically Structured Electrospun Scaffolds with Chemically Conjugated Growth Factor for Ligament Tissue Engineering, Tissue Eng. Part A. 23 (2017) 823–836.

[260] S. Srouji, A.T. Kizhner, A.E. Suss-Tobi, A.E. Livne, A.E. Zussman, 3-D Nanofibrous electrospun multilayered construct is an alternative ECM mimicking scaffold, (n.d.).

[261] W. Liu, Y. Wang, J. Yao, Z. Shao, X. Chen, Tamoxifen-loaded silk fibroin electrospun fibers, Mater. Lett. 178 (2016) 31–34.

[262] O. Aras, M. Kazanci, Production of collagen micro- and nanofibers for potential drug-carrier systems, J. Enzyme Inhib. Med. Chem. 30 (2015) 1013–1016.

[263] A. Fiorani, C. Gualandi, S. Panseri, M. Montesi, M. Marcacci, M.L. Focarete, A. Bigi, Comparative performance of collagen nanofibers electrospun from different solvents and stabilized by different crosslinkers, J. Mater. Sci. Mater. Med. 25 (2014) 2313–2321.

[264] Z.G. Chen, P.W. Wang, B. Wei, X.M. Mo, F.Z. Cui, Electrospun collagen–chitosan nanofiber: A biomimetic extracellular matrix for endothelial cell and smooth muscle cell, Acta Biomater. 6 (2010) 372–382.

[265] S. Zhong, W.E. Teo, X. Zhu, R.W. Beuerman, S. Ramakrishna, L.Y.L. Yung, An aligned nanofibrous collagen scaffold by electrospinning and its effects onin vitro fibroblast culture, J. Biomed. Mater. Res. Part A. 79A (2006) 456–463.

[266] B. Dong, O. Arnoult, M.E. Smith, G.E. Wnek, Electrospinning of Collagen Nanofiber Scaffolds from Benign Solvents, Macromol. Rapid Commun. 30 (2009) 539–542.

[267] J.A. Matthews, G.E. Wnek, D.G. Simpson, G.L. Bowlin, Electrospinning of collagen nanofibers., Biomacromolecules. 3 (2002) 232–8.

[268] A.D. Juncos Bombin, N.J. Dunne, H.O. McCarthy, Electrospinning of natural polymers for the production of nanofibres for wound healing applications, Mater. Sci. Eng. C. 114 (2020) 110994.

[269] K.J. Shields, M.J. Beckman, G.L. Bowlin, J.S. Wayne, Mechanical Properties and Cellular Proliferation of Electrospun Collagen Type II, Tissue Eng. 10 (2004) 1510–1517.

[270] D.H. Margarit, N.S. González, L.M. Romanelli, X. Dai, L. Yu, X. Zhao, al -, S. Kumar, R. Kulkarni, S. Sen -, E.I. Prieto, E.B. A Mojares, J.J. M Cortez, M.R. Vasquez Jr, Electrospun nanofiber scaffolds for the propagation and analysis of breast cancer stem cells in vitro, Biomed. Mater. 16 (2021) 035004.

[271] M. Rabionet, M. Yeste, T. Puig, J. Ciurana, Electrospinning PCL Scaffolds Manufacture for Three-Dimensional Breast Cancer Cell Culture, Polymers (Basel). 9 (2017) 328.

[272] C. Achille, S. Sundaresh, B. Chu, M. Hadjiargyrou, Cdk2 Silencing via a DNA/PCL Electrospun Scaffold Suppresses Proliferation and Increases Death of Breast Cancer Cells, PLoS One. 7 (2012) e52356.

[273] J. Sims-Mourtada, R.A. Niamat, S. Samuel, C. Eskridge, E.B. Kmiec, Enrichment of breast cancer stem-like cells by growth on electrospun polycaprolactone-chitosan nanofiber scaffolds, Int. J. Nanomedicine. 9 (2014) 995–1003.

[274] S. Saha, X. Duan, L. Wu, P.K. Lo, H. Chen, Q. Wang, Electrospun fibrous scaffolds promote breast cancer cell alignment and epithelial-mesenchymal transition, Langmuir. 28 (2012) 2028–2034.

[275] S. Knowlton, S. Onal, C.H. Yu, J.J. Zhao, S. Tasoglu, Bioprinting for cancer research, Trends Biotechnol. 33 (2015) 504–513.

[276] J. An, J.E.M. Teoh, R. Suntornnond, C.K. Chua, Design and 3D Printing of Scaffolds and Tissues, Engineering. 1 (2015) 261–268.

[277] S. V Murphy, A. Atala, 3D bioprinting of tissues and organs, Nat. Biotechnol. 32 (2014) 773–785.

[278] I. Donderwinkel, J.C.M. Van Hest, N.R. Cameron, Bio-inks for 3D bioprinting: recent advances and future prospects, Polym. Chem. 8 (2017) 4451.

[279] C.C. DuFort, M.J. Paszek, V.M. Weaver, Balancing forces: architectural control of mechanotransduction., Nat. Rev. Mol. Cell Biol. 12 (2011) 308–19.

[280] Y.B. Kim, H. Lee, G.H. Kim, Strategy to Achieve Highly Porous/Biocompatible Macroscale Cell Blocks, Using a Collagen/Genipin-bioink and an Optimal 3D Printing Process, ACS Appl. Mater. Interfaces. 8 (2016) 32230–32240.

[281] D. Petta, A.R. Armiento, D. Grijpma, M. Alini, D. Eglin, M. D'Este, 3D bioprinting of a hyaluronan bioink through enzymatic-and visible light-crosslinking, Biofabrication. 10 (2018) 044104.

[282] S. Ibusuki, G.J. Halbesma, M.A. Randolph, R.W. Redmond, I.E. Kochevar, T.J. Gill, Photochemically Cross-Linked Collagen Gels as Three-Dimensional Scaffolds for Tissue Engineering, Tissue Eng. 13 (2007) 1995–2001.

[283] G. Kim, S. Ahn, H. Yoon, Y. Kim, W. Chun, A cryogenic direct-plotting system for fabrication of 3D collagen scaffolds for tissue engineering, J. Mater. Chem. 19 (2009) 8817.

[284] A.D. Nocera, R. Comín, N.A. Salvatierra, M.P. Cid, Development of 3D printed fibrillar collagen scaffold for tissue engineering, Biomed. Microdevices. 20 (2018) 26.

[285] B.A. Nerger, P.T. Brun, C.M. Nelson, Microextrusion printing cell-laden networks of type i collagen with patterned fiber alignment and geometry, Soft Matter. 15 (2019) 5728–5738.

[286] A. Shahin-Shamsabadi, P.R. Selvaganapathy, A rapid biofabrication technique for self-assembled collagen-based multicellular and heterogeneous 3D tissue constructs, Acta Biomater. 92 (2019) 172–183.

[287] J.A. Reid, X.L. Palmer, P.A. Mollica, N. Northam, P.C. Sachs, R.D. Bruno, A 3D bioprinter platform for mechanistic analysis of tumoroids and chimeric mammary organoids, Sci. Reports 2019 91. 9 (2019) 1–10.

[288] L. Koch, A. Deiwick, S. Schlie, S. Michael, M. Gruene, V. Coger, D. Zychlinski, A. Schambach, K. Reimers, P.M. Vogt, B. Chichkov, Skin tissue generation by laser cell printing, Biotechnol. Bioeng. 109 (2012) 1855–1863.

[289] J.W. Lee, Y.-J. Choi, W.-J. Yong, F. Pati, J.-H. Shim, K.S. Kang, I.-H. Kang, J. Park, D.-W. Cho, Development of a 3D cell printed construct considering angiogenesis for liver tissue engineering, Biofabrication. 8 (2016) 015007.

[290] A. Skardal, D. Mack, E. Kapetanovic, A. Atala, J.D. Jackson, J. Yoo, S. Soker, Bioprinted Amniotic Fluid-Derived Stem Cells Accelerate Healing of Large Skin Wounds, Stem Cells Transl. Med. 1 (2012) 792–802.

[291] J.Y. Park, J.-C. Choi, J.-H. Shim, J.-S. Lee, H. Park, S.W. Kim, J. Doh, D.-W. Cho, A comparative study on collagen type I and hyaluronic acid dependent cell behavior for osteochondral tissue bioprinting, Biofabrication. 6 (2014) 035004.

[292] J.U. Lee, M. Yeo, W.J. Kim, Y.W. Koo, G.H. Kim, Development of a tannic acid cross-linking process for obtaining 3D porous cell-laden collagen structure, Int. J. Biol. Macromol. 110 (2018) 497–503.

[293] W.J. Kim, G.H. Kim, An innovative cell-printed microscale collagen model for mimicking intestinal villus epithelium, Chem. Eng. J. 334 (2018) 2308–2318.

[294] D. Yip, C.H. Cho, A multicellular 3D heterospheroid model of liver tumor and stromal cells in collagen gel for anti-cancer drug testing, Biochem. Biophys. Res. Commun. 433 (2013) 327–332.

[295] P. Friedl, K. Maaser, C.E. Klein, B. Niggemann, G. Krohne, K.S. Zänker, Migration of highly aggressive MV3 melanoma cells in 3-dimensional collagen lattices results in local matrix reorganization and shedding of alpha2 and beta1 integrins and CD44., Cancer Res. 57 (1997) 2061–70.

[296] A. Nyga, M. Loizidou, M. Emberton, U. Cheema, A novel tissue engineered three-dimensional in vitro colorectal cancer model., Acta Biomater. 9 (2013) 7917–26.

[297] F.J. O'Brien, B.A. Harley, I.V. Yannas, L.J. Gibson, The effect of pore size on cell adhesion in collagen-GAG scaffolds, Biomaterials. 26 (2005) 433–441.

[298] R.E. Coleman, R.D. Rubens, The clinical course of bone metastases from breast cancer, Br. J. Cancer. 55 (1987) 61–66.

[299] Q. Wu, J. Li, S. Zhu, J. Wu, C. Chen, Q. Liu, W. Wei, Y. Zhang, S. Sun, Breast cancer subtypes predict the preferential site of distant metastases: A SEER based study, Oncotarget. 8 (2017) 27990–27996.

[300] K.N. Weilbaecher, T.A. Guise, L.K. McCauley, Cancer to bone: A fatal attraction, Nat. Rev. Cancer. 11 (2011) 411–425.

[301] J. Tan, E. Buache, M.-P. Chenard, N. Dali-Youcef, M.-C. Rio, Adipocyte is a non-trivial, dynamic partner of breast cancer cells, Int. J. Dev. Biol. 55 (2011) 851–859.

[302] Y.Y. Wang, C. Attané, D. Milhas, B. Dirat, S. Dauvillier, A. Guerard, J. Gilhodes, I. Lazar, N. Alet, V. Laurent, S. Le Gonidec, D. Biard, C. Hervé, F. Bost, G.S. Ren, F. Bono, G. Escourrou, M. Prentki, L. Nieto, P. Valet, C. Muller, Mammary adipocytes stimulate breast cancer invasion through metabolic remodeling of tumor cells, JCI Insight. 2 (2017).

[303] M. Wang, X. Wu, F. Chai, Y. Zhang, J. Jiang, Plasma prolactin and breast cancer risk: A meta-analysis, Sci. Rep. 6 (2016).

[304] S.S. Tworoger, S.E. Hankinson, Prolactin and breast cancer etiology: An epidemiologic perspective, J. Mammary Gland Biol. Neoplasia. 13 (2008) 41–53.

[305] C. V. Clevenger, P.A. Furth, S.E. Hankinson, L.A. Schuler, The role of prolactin in mammary carcinoma, Endocr. Rev. 24 (2003) 1–27.

[306] D.M. Gilkes, G.L. Semenza, Role of hypoxia-inducible factors in breast cancer metastasis, Futur. Oncol. 9 (2013) 1623–1636.

[307] G.L. Semenza, The hypoxic tumor microenvironment: A driving force for breast cancer progression, Biochim. Biophys. Acta - Mol. Cell Res. 1863 (2016) 382–391.

[308] A.D. Leeper, J. Farrell, L.J. Williams, J.S. Thomas, J. Michael Dixon, S.E. Wedden, D.J. Harrison, E. Katz, Determining tamoxifen sensitivity using primary breast cancer tissue in collagen-based three-dimensional culture, Biomaterials. 33 (2012) 907–915.

[309] C.M. Murphy, M.G. Haugh, F.J. O'Brien, The effect of mean pore size on cell attachment, proliferation and migration in collagen–glycosaminoglycan scaffolds for bone tissue engineering, Biomaterials. 31 (2010) 461–466.

[310] J. An, J. Lee, S.H. Lee, J. Park, B. Kim, Separation of malignant human breast cancer epithelial cells from healthy epithelial cells using an advanced dielectrophoresis-activated cell sorter (DACS), Anal. Bioanal. Chem. 394 (2009) 801–809.

[311] Z. Liu, Y. Lee, J.H. Jang, Y. Li, X. Han, K. Yokoi, M. Ferrari, L. Zhou, L. Qin, Microfluidic cytometric analysis of cancer cell transportability and invasiveness,

Sci. Rep. 5 (2015).

[312] M. Cavo, M. Fato, L. Peñuela, F. Beltrame, R. Raiteri, S. Scaglione, Microenvironment complexity and matrix stiffness regulate breast cancer cell activity in a 3D in vitro model, 6 (2016) 1–13.

[313] A.J. Berger, C.M. Renner, I. Hale, X. Yang, S.M. Ponik, P.S. Weisman, K.S. Masters, P.K. Kreeger, Scaffold stiffness influences breast cancer cell invasion via EGFR-linked Mena upregulation and matrix remodeling, Matrix Biol. 85–86 (2020) 80–93.

[314] K. Chatterjee, S. Lin-Gibson, W.E. Wallace, S.H. Parekh, Y.J. Lee, M.T. Cicerone, M.F. Young, C.G. Simon, The effect of 3D hydrogel scaffold modulus on osteoblast differentiation and mineralization revealed by combinatorial screening, Biomaterials. 31 (2010) 5051–5062.

[315] A. Ansardamavandi, M. Tafazzoli-Shadpour, R. Omidvar, I. Jahanzad, Quantification of effects of cancer on elastic properties of breast tissue by Atomic Force Microscopy, J. Mech. Behav. Biomed. Mater. 60 (2016) 234–242.

[316] J.M. Tse, G. Cheng, J.A. Tyrrell, S.A. Wilcox-Adelman, Y. Boucher, R.K. Jain, L.L. Munn, Mechanical compression drives cancer cells toward invasive phenotype, Proc. Natl. Acad. Sci. U. S. A. 109 (2012) 911–916.

[317] B.A. Harley, J.H. Leung, E.C.C.M. Silva, L.J. Gibson, Mechanical characterization of collagen-glycosaminoglycan scaffolds, Acta Biomater. 3 (2007) 463–474.

[318] M.E. Bregenzer, E.N. Horst, P. Mehta, C.M. Novak, S. Raghavan, C.S. Snyder, G. Mehta, Integrated cancer tissue engineering models for precision medicine, PLoS One. 14 (2019) e0216564.

[319] J.M. Northcott, I.S. Dean, J.K. Mouw, V.M. Weaver, Feeling stress: The mechanics of cancer progression and aggression, Front. Cell Dev. Biol. 6 (2018) 17.

[320] Y. Li, M. Chen, J. Hu, R. Sheng, Q. Lin, X. He, M. Guo, Volumetric Compression Induces Intracellular Crowding to Control Intestinal Organoid Growth via Wnt/β-Catenin Signaling, Cell Stem Cell. 28 (2021) 63-78.e7.

[321] B.T. MacDonald, K. Tamai, X. He, Wnt/β-Catenin Signaling: Components, Mechanisms, and Diseases, Dev. Cell. 17 (2009) 9–26.

[322] J. Heino, The collagen family members as cell adhesion proteins, BioEssays. 29 (2007) 1001–1010.

[323] S. Charmsaz, É. Hughes, F.T. Bane, P. Tibbitts, M. McIlroy, C. Byrne, S. Cocchiglia, J. McBryan, B.T. Hennessy, R.M. Dwyer, M.J. Kerin, A.D. Hill, L.S. Young, S100β as a serum marker in endocrine resistant breast cancer, BMC Med. 15 (2017) 79.

[324] S.M. Lien, L.Y. Ko, T.J. Huang, Effect of pore size on ECM secretion and cell growth in gelatin scaffold for articular cartilage tissue engineering, Acta Biomater. 5 (2009) 670–679.

[325] X. Liu, L.A. Smith, J. Hu, P.X. Ma, Biomimetic nanofibrous gelatin/apatite composite scaffolds for bone tissue engineering, Biomaterials. 30 (2009) 2252–2258.

[326] B.P. Toole, Hyaluronan: from extracellular glue to pericellular cue, Nat. Rev. Cancer 2004 47. 4 (2004) 528–539.

[327] S. Misra, V.C. Hascall, R.R. Markwald, S. Ghatak, Interactions between Hyaluronan and Its Receptors (CD44, RHAMM) Regulate the Activities of Inflammation and Cancer, Front. Immunol. 6 (2015).

[328] K.L. Schwertfeger, M.K. Cowman, P.G. Telmer, E.A. Turley, J.B. McCarthy, Hyaluronan, inflammation, and breast cancer progression, Front. Immunol. 6 (2015) 236.

[329] R.S. Yahya, A.A. El-Bindary, H.A. El-Mezayen, H.M. Abdelmasseh, M.A. Eissa, Biochemical evaluation of hyaluronic acid in breast cancer, Clin. Lab. 60 (2014) 1115–1121.

[330] I. V Yannas, A. V Tobolsky, Cross-linking of gelatine by dehydration., Nature. 215 (1967) 509–10.

[331] C.M. Ofner, W.A. Bubnis, Chemical and swelling evaluations of amino group crosslinking in gelatin and modified gelatin matrices, Pharm. Res. 13 (1996) 1821–1827.

[332] J. Zhang, H. Mao, X. Zou, G. Deng, Use of medical sodium hyaluronate gel in surgical removal of a glassintraocular foreign body, J. Int. Med. Res. 48 (2020).

[333] C.T. Rueden, J. Schindelin, M.C. Hiner, B.E. DeZonia, A.E. Walter, E.T. Arena, K.W. Eliceiri, ImageJ2: ImageJ for the next generation of scientific image data, BMC Bioinforma. 2017 181. 18 (2017) 1–26.

[334] J. Krishnamoorthi, P. Ramasamy, V. Shanmugam, A. Shanmugam, Isolation and partial characterization of collagen from outer skin of Sepia pharaonis (Ehrenberg, 1831) from Puducherry coast, Biochem. Biophys. Reports. 10 (2017) 39–45.

[335] T. Riaz, R. Zeeshan, F. Zarif, K. Ilyas, N. Muhammad, S.Z. Safi, A. Rahim, S.A.A. Rizvi, I.U. Rehman, FTIR analysis of natural and synthetic collagen, Appl. Spectrosc. Rev. 53 (2018) 703–746.

[336] Y. Zhang, Q.-S. Wang, K. Yan, Y. Qi, G.-F. Wang, Y.-L. Cui, Preparation, characterization, and evaluation of genipin crosslinked chitosan/gelatin three-dimensional scaffolds for liver tissue engineering applications, J. Biomed. Mater. Res. Part A. 104 (2016) 1863–1870.

[337] Y. Deng, D. Liu, G. Du, X. Li, J. Chen, Preparation and characterization of hyaluronan/chitosan scaffold cross- linked by 1-ethyl-3-(3-dimethylaminopropyl) carbodiimide, Polym. Int. 56 (2007) 738–745.

[338] J.C. Antunes, J.M. Oliveira, R.L. Reis, J.M. Soria, J.L. Gómez-Ribelles, J.F. Mano, Novel poly(L-lactic acid)/hyaluronic acid macroporous hybrid scaffolds: Characterization and assessment of cytotoxicity, J. Biomed. Mater. Res. Part A. 94A (2010) 856–869.

[339] Y. Wang, C. Yang, X. Chen, N. Zhao, Development and characterization of novel biomimetic composite scaffolds based on bioglass-collagen-hyaluronic acid-phosphatidylserine for tissue engineering applications, Macromol. Mater. Eng. 291 (2006) 254–262.

[340] A.J. Ryan, J.P. Gleeson, A. Matsiko, E.M. Thompson, F.J. O'Brien, Effect of different hydroxyapatite incorporation methods on the structural and biological properties of porous collagen scaffolds for bone repair, J. Anat. 227 (2015) 732–745.

[341] Q.L. Loh, C. Choong, Three-dimensional scaffolds for tissue engineering applications: Role of porosity and pore size, Tissue Eng. - Part B Rev. 19 (2013)

485–502.

[342] E. Tsuruga, H. Takita, H. Itoh, Y. Wakisaka, Y. Kuboki, Pore size of porous hydroxyapatite as the cell-substratum controls BMP-induced osteogenesis, J. Biochem. 121 (1997) 317–324.

[343] M.J. Gupte, W.B. Swanson, J. Hu, X. Jin, H. Ma, Z. Zhang, Z. Liu, K. Feng, G. Feng, G. Xiao, N. Hatch, Y. Mishina, P.X. Ma, Pore size directs bone marrow stromal cell fate and tissue regeneration in nanofibrous macroporous scaffolds by mediating vascularization, Acta Biomater. 82 (2018) 1–11.

[344] E. Song, S. Yeon Kim, T. Chun, H.J. Byun, Y.M. Lee, Collagen scaffolds derived from a marine source and their biocompatibility, Biomaterials. 27 (2006) 2951–2961.

[345] G.S. Offeddu, J.C. Ashworth, R.E. Cameron, M.L. Oyen, Structural determinants of hydration, mechanics and fluid flow in freeze-dried collagen scaffolds, Acta Biomater. 41 (2016) 193–203.

[346] N.F. Boyd, Q. Li, O. Melnichouk, E. Huszti, L.J. Martin, A. Gunasekara, G. Mawdsley, M.J. Yaffe, S. Minkin, Evidence that breast tissue stiffness is associated with risk of breast cancer, PLoS One. 9 (2014).

[347] C.N. Grover, R.E. Cameron, S.M. Best, Investigating the morphological, mechanical and degradation properties of scaffolds comprising collagen, gelatin and elastin for use in soft tissue engineering, J. Mech. Behav. Biomed. Mater. 10 (2012) 62–74.

[348] J. Necas, L. Bartosikova, P. Brauner, J. Kolar, Hyaluronic acid (hyaluronan): a review, Vet. Med. (Praha). 53 (2008) 397–411.

[349] M. Dovedytis, Z.J. Liu, S. Bartlett, Hyaluronic acid and its biomedical applications: A review, Eng. Regen. 1 (2020) 102–113.

[350] N. Davidenko, J.J. Campbell, E.S. Thian, C.J. Watson, R.E. Cameron, Collagen-hyaluronic acid scaffolds for adipose tissue engineering, Acta Biomater. 6 (2010) 3957–3968.

[351] P. Taheri, R. Jahanmardi, M. Koosha, S. Abdi, Physical, mechanical and wound healing properties of chitosan/gelatin blend films containing tannic acid and/or

bacterial nanocellulose, Int. J. Biol. Macromol. 154 (2020) 421–432.

[352] R. Parenteau-Bareil, R. Gauvin, F. Berthod, R. Parenteau-Bareil, R. Gauvin, F. Berthod, Collagen-Based Biomaterials for Tissue Engineering Applications, Materials (Basel). 3 (2010) 1863–1887.

[353] K. Unnikrishnan, L.V. Thomas, R.M. Ram Kumar, Advancement of Scaffold-Based 3D Cellular Models in Cancer Tissue Engineering: An Update, Front. Oncol. 11 (2021) 4468.

[354] G. Rijal, W. Li, 3D scaffolds in breast cancer research, Biomaterials. 81 (2016) 135–156.

[355] C. Liverani, A. De Vita, C. Spadazzi, G. Miserocchi, C. Cocchi, A. Bongiovanni, A. De Lucia, F. La Manna, F. Fabbri, M. Tebaldi, D. Amadori, E. Tasciotti, G. Martinelli, L. Mercatali, T. Ibrahim, Lineage-specific mechanisms and drivers of breast cancer chemoresistance revealed by 3D biomimetic culture, Mol. Oncol. 16 (2022) 921–939.

[356] B. Sarker, R. Singh, R. Silva, J.A. Roether, J. Kaschta, R. Detsch, D.W. Schubert, I. Cicha, A.R. Boccaccini, Evaluation of fibroblasts adhesion and proliferation on alginate-gelatin crosslinked hydrogel, PLoS One. 9 (2014).

[357] H.A. Awad, M.Q. Wickham, H.A. Leddy, J.M. Gimble, F. Guilak, Chondrogenic differentiation of adipose-derived adult stem cells in agarose, alginate, and gelatin scaffolds, Biomaterials. 25 (2004) 3211–3222.

[358] S. Khan, M. Ul-Islam, M. Ikram, M.W. Ullah, M. Israr, F. Subhan, Y. Kim, J.H. Jang, S. Yoon, J.K. Park, Three-dimensionally microporous and highly biocompatible bacterial cellulose-gelatin composite scaffolds for tissue engineering applications †, (2016).

[359] W.W. Thein-Han, J. Saikhun, C. Pholpramoo, R.D.K. Misra, Y. Kitiyanant, Chitosan-gelatin scaffolds for tissue engineering: Physico-chemical properties and biological response of buffalo embryonic stem cells and transfectant of GFP-buffalo embryonic stem cells, Acta Biomater. 5 (2009) 3453–3466.

[360] G.E. Davis, Affinity of integrins for damaged extracellular matrix: αvβ3 binds to denatured collagen type I through RGD sites, Biochem. Biophys. Res. Commun.

182 (1992) 1025–1031.

[361] A. V. Taubenberger, M.A. Woodruff, H. Bai, D.J. Muller, D.W. Hutmacher, The effect of unlocking RGD-motifs in collagen I on pre-osteoblast adhesion and differentiation, Biomaterials. 31 (2010) 2827–2835.

[362] A. Matsiko, T.J. Levingstone, F.J. O'Brien, J.P. Gleeson, Addition of hyaluronic acid improves cellular infiltration and promotes early-stage chondrogenesis in a collagen-based scaffold for cartilage tissue engineering, J. Mech. Behav. Biomed. Mater. 11 (2012) 41–52.

[363] ISO - ISO 10993-5:2009 - Biological evaluation of medical devices — Part 5: Tests for in vitro cytotoxicity, (n.d.).

[364] L.L. Fernandes, C.X. Resende, D.S. Tavares, G.A. Soares, L.O. Castro, J.M. Granjeiro, Cytocompatibility of chitosan and collagen-chitosan scaffolds for tissue engineering, Polimeros. 21 (2011) 1–6.

[365] S.K. Swain, D. Sarkar, Fabrication, bioactivity, in vitro cytotoxicity and cell viability of cryo-treated nanohydroxyapatite-gelatin-polyvinyl alcohol macroporous scaffold, J. Asian Ceram. Soc. 2 (2014) 241–247.

[366] M.O. Wang, J.M. Etheridge, J.A. Thompson, C.E. Vorwald, D. Dean, J.P. Fisher, Evaluation of the in vitro cytotoxicity of cross-linked biomaterials, Biomacromolecules. 14 (2013) 1321–1329.

[367] S.N. Rampersad, Multiple applications of alamar blue as an indicator of metabolic function and cellular health in cell viability bioassays, Sensors (Switzerland). 12 (2012) 12347–12360.

[368] V.M.C. Quent, D. Loessner, T. Friis, J.C. Reichert, D.W. Hutmacher, Discrepancies between metabolic activity and DNA content as tool to assess cell proliferation in cancer research., J. Cell. Mol. Med. 14 (2010) 1003–13.

[369] J. Natas Bussador Do Amaral, M.S. Urabayashi, G. Ucia, M. Machado-Santelli, Cell death and lumen formation in spheroids of MCF-7 cells, Cell Biol. Int. 34 (2010) 267–274.

[370] I. Yakavets, A. Francois, A. Benoit, J.L. Merlin, L. Bezdetnaya, G. Vogin, Advanced co-culture 3D breast cancer model for investigation of fibrosis induced by

external stimuli: optimization study, Sci. Rep. 10 (2020).

[371] D.S. Masson-Meyers, L. Tayebi, Vascularization strategies in tissue engineering approaches for soft tissue repair, J. Tissue Eng. Regen. Med. 15 (2021) 747.

[372] S.J. Singh, W. Turner, D.E. Glaser, K.E. McCloskey, F. V. Filipp, Metabolic shift in density-dependent stem cell differentiation, Cell Commun. Signal. 2017 151. 15 (2017) 1–12.

[373] H. BC, B. PP, P. PR, L. SK, X. Y, B. F, V. SS, Effect of cell-seeding density on the proliferation and gene expression profile of human umbilical vein endothelial cells within ex vivo culture, Cytotherapy. 13 (2011) 606–617.

[374] N. Kulkarni, S.D. Shinde, G.S. Jadhav, D.R. Adsare, K. Rao, M. Kachhia, M. Maingle, S.P. Patil, N. Arya, B. Sahu, Peptide-Chitosan Engineered Scaffolds for Biomedical Applications., Bioconjug. Chem. 32 (2021) 448–465.

[375] B. Sarker, J. Rompf, R. Silva, N. Lang, R. Detsch, J. Kaschta, B. Fabry, A.R. Boccaccini, Alginate-based hydrogels with improved adhesive properties for cell encapsulation, Int. J. Biol. Macromol. 78 (2015) 72–78.

[376] B. Fallica, J.S. Maffei, S. Villa, G. Makin, M. Zaman, Alteration of Cellular Behavior and Response to PI3K Pathway Inhibition by Culture in 3D Collagen Gels, PLoS One. 7 (2012) e48024.

[377] S. Däster, N. Amatruda, D. Calabrese, R. Ivanek, E. Turrini, R.A. Droeser, P. Zajac, C. Fimognari, G.C. Spagnoli, G. Iezzi, V. Mele, M.G. Muraro, S. Däster, N. Amatruda, D. Calabrese, R. Ivanek, E. Turrini, R.A. Droeser, P. Zajac, C. Fimognari, G.C. Spagnoli, G. Iezzi, V. Mele, M.G. Muraro, Induction of hypoxia and necrosis in multicellular tumor spheroids is associated with resistance to chemotherapy treatment, Oncotarget. 8 (2016) 1725–1736.

[378] C. Schmitz, E. Potekhina, V. V. Belousov, A. Lavrentieva, Hypoxia Onset in Mesenchymal Stem Cell Spheroids: Monitoring With Hypoxia Reporter Cells, Front. Bioeng. Biotechnol. 0 (2021) 23.

[379] A. Emami Nejad, S. Najafgholian, A. Rostami, A. Sistani, S. Shojaeifar, M. Esparvarinha, R. Nedaeinia, S. Haghjooy Javanmard, M. Taherian, M. Ahmadlou, R. Salehi, B. Sadeghi, M. Manian, The role of hypoxia in the tumor

microenvironment and development of cancer stem cell: a novel approach to developing treatment, Cancer Cell Int. 2021 211. 21 (2021) 1–26.

[380] J.P. Gleeson, N.A. Plunkett, F.J. O'Brien, Addition of hydroxyapatite improves stiffness, interconnectivity and osteogenic potential of a highly porous collagen-based scaffold for bone tissue regeneration, Eur. Cells Mater. (2010).

[381] P. Thevenot, A. Nair, J. Dey, J. Yang, L. Tang, Method to Analyze Three-Dimensional Cell Distribution and Infiltration in Degradable Scaffolds, Tissue Eng. Part C. Methods. 14 (2008) 319.

[382] A. Birgersdotter, R. Sandberg, I. Ernberg, Gene expression perturbation in vitro—A growing case for three-dimensional (3D) culture systems, Semin. Cancer Biol. 15 (2005) 405–412.

[383] C. Jensen, Y. Teng, Is It Time to Start Transitioning From 2D to 3D Cell Culture?, Front. Mol. Biosci. 7 (2020) 33.

[384] J.C. Fontoura, C. Viezzer, F.G. dos Santos, R.A. Ligabue, R. Weinlich, R.D. Puga, D. Antonow, P. Severino, C. Bonorino, Comparison of 2D and 3D cell culture models for cell growth, gene expression and drug resistance, Mater. Sci. Eng. C. 107 (2020) 110264.

[385] Y. Wang, H. Xu, B. Zhu, Z. Qiu, Z. Lin, Systematic identification of the key candidate genes in breast cancer stroma, Cell. Mol. Biol. Lett. 23 (2018) 1–15.

[386] J. Liu, J.-X. Shen, H.-T. Wu, X.-L. Li, X.-F. Wen, C.-W. Du, G.-J. Zhang, Collagen 1A1 (COL1A1) Promotes Metastasis of Breast Cancer and Is a Potential Therapeutic Target, Discov. Med. 25 (2018) 211–223.

[387] S. Spada, A. Tocci, F. Di Modugno, P. Nisticò, Fibronectin as a multiregulatory molecule crucial in tumor matrisome: from structural and functional features to clinical practice in oncology, J. Exp. Clin. Cancer Res. 2021 401. 40 (2021) 1–14.

[388] E. Ioachim, A. Charchanti, E. Briasoulis, V. Karavasilis, H. Tsanou, D.L. Arvanitis, N.J. Agnantis, N. Pavlidis, Immunohistochemical expression of extracellular matrix components tenascin, fibronectin, collagen type IV and laminin in breast cancer: their prognostic value and role in tumour invasion and progression, Eur. J. Cancer. 38 (2002) 2362–2370.

[389] R.H. Tammi, A.G. Passi, K. Rilla, E. Karousou, D. Vigetti, K. Makkonen, M.I. Tammi, Transcriptional and post-translational regulation of hyaluronan synthesis, FEBS J. 278 (2011) 1419–1428.

[390] W. Wu, L. Chen, Y. Wang, J. Jin, X. Xie, J. Zhang, Hyaluronic acid predicts poor prognosis in breast cancer patients: A protocol for systematic review and meta analysis, Medicine (Baltimore). 99 (2020) e20438.

[391] N. Nguyen, A. Kumar, S. Chacko, R.J. Ouellette, A. Ghosh, Human hyaluronic acid synthase-1 promotes malignant transformation via epithelial-to-mesenchymal transition, micronucleation and centrosome abnormalities., Cell Commun. Signal. 15 (2017) 48.

[392] P. Li, T. Xiang, H. Li, Q. Li, B. Yang, J. Huang, X. Zhang, Y. Shi, J. Tan, G. Ren, Hyaluronan synthase 2 overexpression is correlated with the tumorigenesis and metastasis of human breast cancer., Int. J. Clin. Exp. Pathol. 8 (2015) 12101–14.

[393] P. Taneja, D. Maglic, F. Kai, S. Zhu, R.D. Kendig, E.A. Fry, K. Inoue, Classical and Novel Prognostic Markers for Breast Cancer and their Clinical Significance., Clin. Med. Insights. Oncol. 4 (2010) 15–34.

[394] P. Manders, L.V.A.M. Beex, V.C.G. Tjan-Heijnen, P.N. Span, C.G.J. Sweep, Vascular Endothelial Growth Factor is Associated with the Efficacy of Endocrine Therapy in Patients with Advanced Breast Carcinoma, Cancer. 98 (2003) 2125–2132.

[395] X. Cao, J. Geradts, M.W. Dewhirst, H.W. Lo, Upregulation of VEGF-A and CD24 gene expression by the tGLI1 transcription factor contributes to the aggressive behavior of breast cancer cells, Oncogene 2012 311. 31 (2011) 104–115.

[396] L. Kubiczkova, L. Sedlarikova, R. Hajek, S. Sevcikova, TGF-β – an excellent servant but a bad master, J. Transl. Med. 10 (2012) 183.

[397] J.M. Zarzynska, Two Faces of TGF-Beta1 in Breast Cancer, Mediators Inflamm. 2014 (2014).

[398] J.Y. Zhang, F. Zhang, C.Q. Hong, A.E. Giuliano, X.J. Cui, G.J. Zhou, G.J. Zhang, Y.K. Cui, Critical protein GAPDH and its regulatory mechanisms in cancer cells, Cancer Biol. Med. 12 (2015) 10.

[399] A. Colell, D.R. Green, J.E. Ricci, Novel roles for GAPDH in cell death and carcinogenesis, Cell Death Differ. 2009 1612. 16 (2009) 1573–1581.

[400] K. Liu, Z. Tang, A. Huang, P. Chen, P. Liu, J. Yang, W. Lu, J. Liao, Y. Sun, S. Wen, Y. Hu, P. Huang, Glyceraldehyde-3-phosphate dehydrogenase promotes cancer growth and metastasis through upregulation of SNAIL expression, Int. J. Oncol. 50 (2017) 252–262.

[401] F. Révillion, V. Pawlowski, L. Hornez, J.P. Peyrat, Glyceraldehyde-3-phosphate dehydrogenase gene expression in human breast cancer, Eur. J. Cancer. 36 (2000) 1038–1042.

[402] G.D. Holman, Structure, function and regulation of mammalian glucose transporters of the SLC2 family, Pflügers Arch. - Eur. J. Physiol. 2020 4729. 472 (2020) 1155–1175.

[403] J. Wang, C. Ye, C. Chen, H. Xiong, B. Xie, J. Zhou, Y. Chen, S. Zheng, L. Wang, J. Wang, C. Ye, C. Chen, H. Xiong, B. Xie, J. Zhou, Y. Chen, S. Zheng, L. Wang, Glucose transporter GLUT1 expression and clinical outcome in solid tumors: a systematic review and meta-analysis, Oncotarget. 8 (2017) 16875–16886.

[404] K. Adekola, S.T. Rosen, M. Shanmugam, Glucose transporters in cancer metabolism, Curr. Opin. Oncol. 24 (2012) 650.

[405] S.S. Kang, Y.K. Chun, M.H. Hur, H.K. Lee, Y.J. Kim, S.R. Hong, J.H. Lee, S.G. Lee, Y.K. Park, Clinical Significance of Glucose Transporter 1 (GLUT1) Expression in Human Breast Carcinoma, Japanese J. Cancer Res. 93 (2002) 1123–1128.

[406] C.H.F. Peiró, M.M. Perez, G.S.A. de Aquino, J.F.A. Encinas, L.V. de A. Sousa, G.L. da Veiga, A. del Giglio, F.L.A. Fonseca, B. da Costa Aguiar Alves, Diagnostic potential of hypoxia-induced genes in liquid biopsies of breast cancer patients, Sci. Reports 2021 111. 11 (2021) 1–7.

[407] B. Gess, K.H. Hofbauer, R.H. Wenger, C. Lohaus, H.E. Meyer, A. Kurtz, The cellular oxygen tension regulates expression of the endoplasmic oxidoreductase ERO1-Lalpha, Eur. J. Biochem. 270 (2003) 2228–2235.

[408] N. Takei, A. Yoneda, M. Kosaka, K. Sakai-Sawada, Y. Tamura, ERO1α is a novel

endogenous marker of hypoxia in human cancer cell lines, BMC Cancer. 19 (2019) 1–10.

[409] G. Kutomi, Y. Tamura, T. Tanaka, T. Kajiwara, K. Kukita, T. Ohmura, H. Shima, T. Takamaru, F. Satomi, Y. Suzuki, T. Torigoe, N. Sato, K. Hirata, Human endoplasmic reticulum oxidoreductin 1-α is a novel predictor for poor prognosis of breast cancer, Cancer Sci. 104 (2013) 1091–1096.

[410] Y.H. Shi, W.G. Fang, Hypoxia-inducible factor-1 in tumour angiogenesis, World J. Gastroenterol. 10 (2004) 1082.

[411] J.E. Ziello, I.S. Jovin, Y. Huang, Hypoxia-Inducible Factor (HIF)-1 regulatory pathway and its potential for therapeutic intervention in malignancy and ischemia., Yale J. Biol. Med. 80 (2007) 51–60.

[412] C. Nie, H. Lv, L. Bie, H. Hou, X. Chen, Hypoxia-inducible factor 1-alpha expression correlates with response to neoadjuvant chemotherapy in women with breast cancer, Medicine (Baltimore). 97 (2018).

[413] A. Jögi, A. Ehinger, L. Hartman, S. Alkner, Expression of HIF-1α is related to a poor prognosis and tamoxifen resistance in contralateral breast cancer, PLoS One. 14 (2019) e0226150.

[414] Z. ji Liu, G.L. Semenza, H. feng Zhang, Hypoxia-inducible factor 1 and breast cancer metastasis, J. Zhejiang Univ. Sci. B. 16 (2015) 32.

[415] M. xi Xiu, Y. meng Liu, B. hai Kuang, The oncogenic role of Jagged1/Notch signaling in cancer, Biomed. Pharmacother. 129 (2020).

[416] B.C. Dickson, A.M. Mulligan, H. Zhang, G. Lockwood, F.P. O'Malley, S.E. Egan, M. Reedijk, High-level JAG1 mRNA and protein predict poor outcome in breast cancer, Mod. Pathol. 2007 206. 20 (2007) 685–693.

[417] S.F. Zohny, M.A. Zamzami, A.L. Al-Malki, N.H. Trabulsi, Highly Expressed DLL4 and JAG1: Their Role in Incidence of Breast Cancer Metastasis, Arch. Med. Res. 51 (2020) 145–152.

[418] Z. Zhang, C. Ni, W. Chen, P. Wu, Z. Wang, J. Yin, J. Huang, F. Qiu, Expression of CXCR4 and breast cancer prognosis: A systematic review and meta-analysis, BMC Cancer. 14 (2014) 1–8.

[419] H. Kang, G. Watkins, A. Douglas-Jones, R.E. Mansel, W.G. Jiang, The elevated level of CXCR4 is correlated with nodal metastasis of human breast cancer, The Breast. 14 (2005) 360–367.

[420] N. Kawaguchi, T.T. Zhang, T. Nakanishi, Involvement of CXCR4 in Normal and Abnormal Development, Cells 2019, Vol. 8, Page 185. 8 (2019) 185.

[421] E.A. Bruford, B. Braschi, P. Denny, T.E.M. Jones, R.L. Seal, S. Tweedie, Guidelines for Human Gene Nomenclature, Nat. Genet. 52 (2020) 754.

[422] J. Xu, S. Lamouille, R. Derynck, TGF-β-induced epithelial to mesenchymal transition, Cell Res. 2009 192. 19 (2009) 156–172.

[423] N. Sethi, X. Dai, C.G. Winter, Y. Kang, Tumor-Derived Jagged1 Promotes Osteolytic Bone Metastasis of Breast Cancer by Engaging Notch Signaling in Bone Cells, Cancer Cell. 19 (2011) 192–205.

[424] D. Wu, P. Yotnda, Induction and Testing of Hypoxia in Cell Culture, J. Vis. Exp. (2011) 2899.

[425] G.L. Semenza, HIF-1 mediates metabolic responses to intratumoral hypoxia and oncogenic mutations, J. Clin. Invest. 123 (2013) 3664.

[426] T. Tanaka, G. Kutomi, T. Kajiwara, K. Kukita, V. Kochin, T. Kanaseki, T. Tsukahara, Y. Hirohashi, T. Torigoe, Y. Okamoto, K. Hirata, N. Sato, Y. Tamura, Cancer-associated oxidoreductase ERO1-α promotes immune escape through up-regulation of PD-L1 in human breast cancer, Oncotarget. 8 (2017) 24706–24718.

[427] N. Takei, A. Yoneda, K. Sakai-Sawada, M. Kosaka, K. Minomi, Y. Tamura, Hypoxia-inducible ERO1α promotes cancer progression through modulation of integrin-β1 modification and signalling in HCT116 colorectal cancer cells, Sci. Reports 2017 71. 7 (2017) 1–11.

[428] B.D. Johnson, W.J. Geldenhuys, L.A. Hazlehurst, The Role of ERO1α in Modulating Cancer Progression and Immune Escape., J. Cancer Immunol. 2 (2020) 103–115.

[429] J. Ye, G. Coulouris, I. Zaretskaya, I. Cutcutache, S. Rozen, T.L. Madden, Primer-BLAST: a tool to design target-specific primers for polymerase chain reaction, BMC Bioinformatics. 13 (2012) 134.

[430] W.A. Kibbe, OligoCalc: an online oligonucleotide properties calculator, Nucleic Acids Res. 35 (2007) W43–W46.

[431] J. Vandesompele, K. De Preter, F. Pattyn, B. Poppe, N. Van Roy, A. De Paepe, F. Speleman, Accurate normalization of real-time quantitative RT-PCR data by geometric averaging of multiple internal control genes, Genome Biol. 3 (2002) research0034.1.

[432] J. Hellemans, G. Mortier, A. De Paepe, F. Speleman, J. Vandesompele, qBase relative quantification framework and software for management and automated analysis of real-time quantitative PCR data, Genome Biol. 8 (2007) R19.

[433] K.J. Livak, T.D. Schmittgen, Analysis of Relative Gene Expression Data Using Real-Time Quantitative PCR and the 2−ΔΔCT Method, Methods. 25 (2001) 402–408.

[434] A. Bondavera, C.M. Downey, F. Ayres, W. Liu, S.K. Boyd, B. Hallgrimsson, F.R. Jirik, The Lysyl Oxidase Inhibitor, β-Aminopropionitrile, Diminishes the Metastatic Colonization Potential of Circulating Breast Cancer Cells, PLoS One. 4 (2009) e5620.

[435] O. Saatci, A. Kaymak, U. Raza, P.G. Ersan, O. Akbulut, C.E. Banister, V. Sikirzhytski, U.M. Tokat, G. Aykut, S.A. Ansari, H.T. Dogan, M. Dogan, P. Jandaghi, A. Isik, F. Gundogdu, K. Kosemehmetoglu, O. Dizdar, S. Aksoy, A. Akyol, A. Uner, P.J. Buckhaults, Y. Riazalhosseini, O. Sahin, Targeting lysyl oxidase (LOX) overcomes chemotherapy resistance in triple negative breast cancer, Nat. Commun. 11 (2020).

[436] R. Zhou, L. Xu, M. Ye, M. Liao, H. Du, H. Chen, Formononetin inhibits migration and invasion of MDA-MB-231 and 4T1 breast cancer cells by suppressing MMP-2 and MMP-9 through PI3K/AKT signaling pathways, Horm. Metab. Res. 46 (2014) 753–760.

[437] D. Stellas, A. El Hamidieh, E. Patsavoudi, Monoclonal antibody 4C5 prevents activation of MMP2 and MMP9 by disrupting their interaction with extracellular HSP90 and inhibits formation of metastatic breast cancer cell deposits., BMC Cell Biol. 11 (2010) 51.

[438] S. Pei, X. Yang, H. Wang, H. Zhang, B. Zhou, D. Zhang, D. Lin, Plantamajoside, a potential anti-tumor herbal medicine inhibits breast cancer growth and pulmonary metastasis by decreasing the activity of matrix metalloproteinase-9 and -2., BMC Cancer. 15 (2015) 965.

[439] S. Xu, H. Xu, W. Wang, S. Li, H. Li, T. Li, W. Zhang, X. Yu, L. Liu, The role of collagen in cancer: from bench to bedside, J. Transl. Med. 17 (2019) 309.

[440] T. Liu, L. Zhou, D. Li, T. Andl, Y. Zhang, Cancer-Associated Fibroblasts Build and Secure the Tumor Microenvironment, Front. Cell Dev. Biol. 7 (2019).

[441] C. García-Pravia, J.A. Galván, N. Gutiérrez-Corral, L. Solar-García, E. García-Pérez, M. García-Ocaña, J. Del Amo-Iribarren, P. Menéndez-Rodríguez, J. García-García, J.R. de los Toyos, L. Simón-Buela, L. Barneo, Overexpression of COL11A1 by Cancer-Associated Fibroblasts: Clinical Relevance of a Stromal Marker in Pancreatic Cancer, PLoS One. 8 (2013) e78327.

[442] H.J. Park, D.M. Helfman, Up-regulated fibronectin in 3D culture facilitates spreading of triple negative breast cancer cells on 2D through integrin β-5 and Src, Sci. Reports 2019 91. 9 (2019) 1–14.

[443] J. Zavadil, L. Cermak, N. Soto-Nieves, E.P. Böttinger, Integration of TGF-beta/Smad and Jagged1/Notch signalling in epithelial-to-mesenchymal transition, EMBO J. 23 (2004) 1155–1165.

[444] K.G. Leong, K. Niessen, I. Kulic, A. Raouf, C. Eaves, I. Pollet, A. Karsan, Jagged1-mediated Notch activation induces epithelial-to-mesenchymal transition through Slug-induced repression of E-cadherin, J. Exp. Med. 204 (2007) 2935–2948.

[445] D. Ribatti, R. Tamma, T. Annese, Epithelial-Mesenchymal Transition in Cancer: A Historical Overview, Transl. Oncol. 13 (2020).

[446] E. Ziegler, M.-T. Hansen, M. Haase, G. Emons, C. Gründker, Generation of MCF-7 cells with aggressive metastatic potential in vitro and in vivo, Breast Cancer Res. Treat. 148 (2014) 269–277.

[447] M. Ricciardi, M. Zanotto, G. Malpeli, G. Bassi, O. Perbellini, M. Chilosi, F. Bifari, M. Krampera, Epithelial-to-mesenchymal transition (EMT) induced by inflammatory priming elicits mesenchymal stromal cell-like immune-modulatory

properties in cancer cells, Br. J. Cancer 2015 1126. 112 (2015) 1067–1075.

[448] C. Gialeli, A.D. Theocharis, N.K. Karamanos, Roles of matrix metalloproteinases in cancer progression and their pharmacological targeting, FEBS J. 278 (2011) 16–27.

[449] C.L. Li, D. Yang, X. Cao, F. Wang, D.Y. Hong, J. Wang, X.C. Shen, Y. Chen, Fibronectin induces epithelial-mesenchymal transition in human breast cancer MCF-7 cells via activation of calpain, Oncol. Lett. 13 (2017) 3889–3895.

[450] J. Park, J.E. Schwarzbauer, Mammary epithelial cell interactions with fibronectin stimulate epithelial-mesenchymal transition, Oncogene 2014 3313. 33 (2013) 1649–1657.

[451] B.K. Aravindan, J. Prabhakar, T. Somanathan, L. Subhadra, The role of chemokine receptor 4 and its ligand stromal cell derived factor 1 in breast cancer, Ann. Transl. Med. 3 (2015).

[452] S. Chatterjee, B. Behnam Azad, S. Nimmagadda, The Intricate Role of CXCR4 in Cancer, Adv. Cancer Res. 124 (2014) 31.

[453] R.S. BelAiba, S. Bonello, C. Zähringer, S. Schmidt, J. Hess, T. Kietzmann, A. Görlach, Hypoxia Up-Regulates Hypoxia-Inducible Factor-1α Transcription by Involving Phosphatidylinositol 3-Kinase and Nuclear Factor κB in Pulmonary Artery Smooth Muscle Cells, Mol. Biol. Cell. 18 (2007) 4691.

[454] Y. Zhang, J. Yan, L. Wang, H. Dai, N. Li, W. Hu, H. Cai, HIF-1α Promotes Breast Cancer Cell MCF-7 Proliferation and Invasion Through Regulating miR-210, Cancer Biother. Radiopharm. 32 (2017) 297–301.

[455] S.Y. Seol, C. Kim, J.Y. Lim, S.O. Yoon, S.W. Hong, J.W. Kim, S.H. Choi, J.Y. Cho, Overexpression of Endoplasmic Reticulum Oxidoreductin 1-α (ERO1L) Is Associated with Poor Prognosis of Gastric Cancer, Cancer Res. Treat. 48 (2016) 1196.

[456] J. Zhang, J. Yang, C. Lin, W. Liu, Y. Huo, M. Yang, S.H. Jiang, Y. Sun, R. Hua, Endoplasmic Reticulum stress-dependent expression of ERO1L promotes aerobic glycolysis in Pancreatic Cancer, Theranostics. 10 (2020) 8400.

[457] M. Hayashi, M. Sakata, T. Takeda, T. Yamamoto, Y. Okamoto, K. Sawada, A. Kimura, R. Minekawa, M. Tahara, K. Tasaka, Y. Murata, Induction of glucose

transporter 1 expression through hypoxia-inducible factor 1α under hypoxic conditions in trophoblast-derived cells, J. Endocrinol. 183 (2004) 145–154.

[458] J.H. Harmey, D. Bouchier-Hayes, Vascular endothelial growth factor (VEGF), a survival factor for tumour cells: Implications for anti-angiogenic therapy, BioEssays. 24 (2002) 280–283.

[459] E.M. Hendriksen, P.N. Span, J. Schuuring, J.P.W. Peters, F.C.G.J. Sweep, A.J. van der Kogel, J. Bussink, Angiogenesis, hypoxia and VEGF expression during tumour growth in a human xenograft tumour model, Microvasc. Res. 77 (2009) 96–103.

[460] D.C. Belisario, J. Kopecka, M. Pasino, M. Akman, E. De Smaele, M. Donadelli, C. Riganti, Hypoxia Dictates Metabolic Rewiring of Tumors: Implications for Chemoresistance, Cells 2020, Vol. 9, Page 2598. 9 (2020) 2598.

[461] X. Jing, F. Yang, C. Shao, K. Wei, M. Xie, H. Shen, Y. Shu, Role of hypoxia in cancer therapy by regulating the tumor microenvironment, Mol. Cancer 2019 181. 18 (2019) 1–15.

[462] Y. Bhattacharjee, Biomedicine. Pharma firms push for sharing of cancer trial data., Science. 338 (2012) 29.

[463] G.A. Van Norman, Limitations of Animal Studies for Predicting Toxicity in Clinical Trials: Is it Time to Rethink Our Current Approach?, JACC Basic to Transl. Sci. 4 (2019) 845.

[464] G. Chen, W. Liu, B. Yan, Breast Cancer MCF-7 Cell Spheroid Culture for Drug Discovery and Development, J. Cancer Ther. 13 (2022) 117.

[465] Y. Imamura, T. Mukohara, Y. Shimono, Y. Funakoshi, N. Chayahara, M. Toyoda, N. Kiyota, S. Takao, S. Kono, T. Nakatsura, H. Minami, Comparison of 2D- and 3D-culture models as drug-testing platforms in breast cancer, Oncol. Rep. 33 (2015) 1837–1843.

[466] M.A. Theodoraki, C.O. Rezende, O. Chantarasriwong, A.D. Corben, E.A. Theodorakis, M.L. Alpaugh, Spontaneously-forming spheroids as an in vitro cancer cell model for anticancer drug screening, Oncotarget. 6 (2015) 21255.

[467] J. Friedrich, C. Seidel, R. Ebner, L.A. Kunz-Schughart, Spheroid-based drug screen: considerations and practical approach, Nat. Protoc. 2009 43. 4 (2009) 309–324.

[468] H. Song, G.-H. Cai, J. Liang, D.-S. Ao, H. Wang, Z.-H. Yang, Three-dimensional culture and clinical drug responses of a highly metastatic human ovarian cancer HO-8910PM cells in nanofibrous microenvironments of three hydrogel biomaterials., J. Nanobiotechnology. 18 (2020) 90.

[469] M. Muguruma, S. Teraoka, K. Miyahara, A. Ueda, M. Asaoka, M. Okazaki, T. Kawate, M. Kuroda, Y. Miyagi, T. Ishikawa, Differences in drug sensitivity between two-dimensional and three-dimensional culture systems in triple-negative breast cancer cell lines, Biochem. Biophys. Res. Commun. 533 (2020) 268–274.

[470] K.A. Fitzgerald, M. Malhotra, C.M. Curtin, F.J. O' Brien, C.M. O' Driscoll, Life in 3D is never flat: 3D models to optimise drug delivery, J. Control. Release. 215 (2015) 39–54.

[471] S.A. Langhans, Three-Dimensional in Vitro Cell Culture Models in Drug Discovery and Drug Repositioning, Front. Pharmacol. 9 (2018) 6.

[472] T.H. Booij, L.S. Price, E.H.J. Danen, 3D Cell-Based Assays for Drug Screens: Challenges in Imaging, Image Analysis, and High-Content Analysis, Slas Discov. 24 (2019) 615.

[473] T. De, S. Goyal, G. Balachander, K. Chatterjee, P. Kumar, K. Govind Babu, A. Rangarajan, A Novel Ex Vivo System Using 3D Polymer Scaffold to Culture Circulating Tumor Cells from Breast Cancer Patients Exhibits Dynamic E-M Phenotypes, J. Clin. Med. 8 (2019) 1473.

[474] J. Kokkinos, G. Sharbeen, K.S. Haghighi, R.M.C. Ignacio, C. Kopecky, E. Gonzales-Aloy, J. Youkhana, P. Timpson, B.A. Pereira, S. Ritchie, E. Pandzic, C. Boyer, T.P. Davis, L.M. Butler, D. Goldstein, J.A. McCarroll, P.A. Phillips, Ex vivo culture of intact human patient derived pancreatic tumour tissue, Sci. Reports 2021 111. 11 (2021) 1–15.

[475] K.C. Hribar, C.J. Wheeler, A. Bazarov, K. Varshneya, R. Yamada, P. Buckley, C.G. Patil, A Simple Three-dimensional Hydrogel Platform Enables Ex Vivo Cell Culture of Patient and PDX Tumors for Assaying Their Response to Clinically Relevant Therapies., Mol. Cancer Ther. 18 (2019) 718–725.

[476] A.S. Levenson, V. Jordan, Craig, MCF-7: The First Hormone-responsive Breast

Cancer Cell Line, Cancer Res. 57 (1997) 3071–3078.

[477] F. Odeh, R. Naffa, H. Azzam, I.S. Mahmoud, W. Alshaer, A. Al Bawab, S. Ismail, Co-encapsulation of thymoquinone with docetaxel enhances the encapsulation efficiency into PEGylated liposomes and the chemosensitivity of MCF7 breast cancer cells to docetaxel, Heliyon. 5 (2019) e02919.

[478] L. Vesci, V. Carollo, G. Roscilli, L. Aurisicchio, F.F. Ferrara, L. Spagnoli, R. De Santis, Trastuzumab and docetaxel in a preclinical organotypic breast cancer model using tissue slices from mammary fat pad: Translational relevance, Oncol. Rep. 35 (2016) 602.

[479] Y.I. Poltavets, A.S. Zhirnik, V. V. Zavarzina, Y.P. Semochkina, V.G. Shuvatova, A.A. Krasheninnikova, S. V. Aleshin, D.O. Dronov, E.A. Vorontsov, V.Y. Balabanyan, G.A. Posypanova, In vitro anticancer activity of folate-modified docetaxel-loaded PLGA nanoparticles against drug-sensitive and multidrug-resistant cancer cells, Cancer Nanotechnol. 10 (2019) 1–17.

[480] Shagufta, I. Ahmad, Tamoxifen a pioneering drug: An update on the therapeutic potential of tamoxifen derivatives, Eur. J. Med. Chem. 143 (2018) 515–531.

[481] C.K. Osborne, Tamoxifen in the Treatment of Breast Cancer, N. Engl. J. Med. 339 (1998) 1609–1618.

[482] S. Mandlekar, A.N.T. Kong, Mechanisms of tamoxifen-induced apoptosis, Apoptosis 2001 66. 6 (2001) 469–477.

[483] A. Bollig, L. Xu, A. Thakur, J. Wu, T.H. Kuo, J.D. Liao, Regulation of intracellular calcium release and PP1α in a mechanism for 4-hydroxytamoxifen-induced cytotoxicity, Mol. Cell. Biochem. 305 (2007) 45–54.

[484] V.C. Jordan, New insights into the metabolism of tamoxifen and its role in the treatment and prevention of breast cancer, Steroids. 72 (2007) 829–842.

[485] S. Alken, C.M. Kelly, Benefit risk assessment and update on the use of docetaxel in the management of breast cancer, Cancer Manag. Res. 5 (2013) 357.

[486] E. Saloustros, D. Mavroudis, V. Georgoulias, Paclitaxel and docetaxel in the treatment of breast cancer, Expert Opin. Pharmacother. 9 (2008) 2603–2616.

[487] M. Imran, S. Saleem, A. Chaudhuri, J. Ali, S. Baboota, Docetaxel: An update on its molecular mechanisms, therapeutic trajectory and nanotechnology in the treatment of breast, lung and prostate cancer, J. Drug Deliv. Sci. Technol. 60 (2020) 101959.

[488] A. Montero, F. Fossella, G. Hortobagyi, V. Valero, Docetaxel for treatment of solid tumours: a systematic review of clinical data, Lancet Oncol. 6 (2005) 229–239.

[489] J.J.M.A. Hendrikx, A.C. Dubbelman, H. Rosing, A.H. Schinkel, J.H.M. Schellens, J.H. Beijnen, Quantification of docetaxel and its metabolites in human plasma by liquid chromatography/tandem mass spectrometry, Rapid Commun. Mass Spectrom. 27 (2013) 1925–1934.

[490] National Center for Biotechnology Information, PubChem Compound Summary for CID 2733526, Tamoxifen, (2022).

[491] National Center for Biotechnology Information, PubChem Compound Summary for CID 449459, 4-Hydroxytamoxifen, (2022).

[492] National Center for Biotechnology Information, PubChem Compound Summary for CID 148124, Docetaxel, (2022).

[493] Q. Fang, S. Yao, G. Luo, X. Zhang, Identification of differentially expressed genes in human breast cancer cells induced by 4-hydroxyltamoxifen and elucidation of their pathophysiological relevance and mechanisms, Oncotarget. 9 (2018) 2475.

[494] C.G. Roberts, E. Gurisik, T.J. Biden, R.L. Sutherland, A.J. Butt, Synergistic cytotoxicity between tamoxifen and the plant toxin persin in human breast cancer cells is dependent on Bim expression and mediated by modulation of ceramide metabolism, Mol. Cancer Ther. 6 (2007) 2777–2785.

[495] Y. Wang, Q. Wang, X. Li, G. Luo, M. Shen, J. Shi, X. Wang, L. Tang, Paeoniflorin Sensitizes Breast Cancer Cells to Tamoxifen by Downregulating microRNA-15b via the FOXO1/CCND1/β-Catenin Axis, Drug Des. Devel. Ther. 15 (2021) 245–257.

[496] C. Zhou, Q. Zhong, L. V. Rhodes, I. Townley, M.R. Bratton, Q. Zhang, E.C. Martin, S. Elliott, B.M. Collins-Burow, M.E. Burow, G. Wang, Proteomic analysis of acquired tamoxifen resistance in MCF-7 cells reveals expression signatures associated with enhanced migration., Breast Cancer Res. 14 (2012) R45.

[497] N. Abu, M.N. Akhtar, S.K. Yeap, K.L. Lim, W.Y. Ho, A.J. Zulfadli, A.R. Omar, M.R. Sulaiman, M.P. Abdullah, N.B. Alitheen, Flavokawain A induces apoptosis in MCF-7 and MDA-MB231 and inhibits the metastatic process in vitro, PLoS One. 9 (2014).

[498] H. Seeger, J. Huober, D. Wallwiener, A.O. Mueck, Inhibition of human breast cancer cell proliferation with estradiol metabolites is as effective as with tamoxifen, Horm. Metab. Res. 36 (2004) 277–280.

[499] B.Y. Chang, S.A. Kim, B. Malla, S.Y. Kim, The Effect of Selective Estrogen Receptor Modulators (SERMs) on the Tamoxifen Resistant Breast Cancer Cells, Toxicol. Res. 27 (2011) 85–93.

[500] K. Stock, M.F. Estrada, S. Vidic, K. Gjerde, A. Rudisch, V.E. Santo, M. Barbier, S. Blom, S.C. Arundkar, I. Selvam, A. Osswald, Y. Stein, S. Gruenewald, C. Brito, W. Van Weerden, V. Rotter, E. Boghaert, M. Oren, W. Sommergruber, Y. Chong, R. De Hoogt, R. Graeser, Capturing tumor complexity in vitro: Comparative analysis of 2D and 3D tumor models for drug discovery, Sci. Reports 2016 61. 6 (2016) 1–15.

[501] S. Breslin, L. O'Driscoll, The relevance of using 3D cell cultures, in addition to 2D monolayer cultures, when evaluating breast cancer drug sensitivity and resistance, Oncotarget. 7 (2016) 45745–45756.

[502] E. Henke, R. Nandigama, S. Ergün, Extracellular Matrix in the Tumor Microenvironment and Its Impact on Cancer Therapy, Front. Mol. Biosci. 6 (2020) 160.

[503] O. Trédan, C.M. Galmarini, K. Patel, I.F. Tannock, Drug Resistance and the Solid Tumor Microenvironment, JNCI J. Natl. Cancer Inst. 99 (2007) 1441–1454.

[504] R.M. Sutherland, Cell and Environment Interactions in Tumor Microregions: The Multicell Spheroid Model, Science (80-.). 240 (1988) 177–184.

[505] G. Hamilton, B. Rath, Role of circulating tumor cell spheroids in drug resistance, Cancer Drug Resist. 2 (2019) 762.

[506] D.S. Reynolds, K.M. Tevis, W.A. Blessing, Y.L. Colson, M.H. Zaman, M.W. Grinstaff, Breast Cancer Spheroids Reveal a Differential Cancer Stem Cell

Response to Chemotherapeutic Treatment, Sci. Reports 2017 71. 7 (2017) 1–12.

[507] Z. Huang, P. Yu, J. Tang, Characterization of Triple-Negative Breast Cancer MDA-MB-231 Cell Spheroid Model, Onco. Targets. Ther. 13 (2020) 5395.

[508] H. Li, X. Su, J. Li, W. Liu, G. Pan, A. Mao, J. Liu, Q. Zhang, L. Rao, X. Xie, X. Sheng, Hypoxia induces docetaxel resistance in triple-negative breast cancer via the HIF-1α/miR-494/Survivin signaling pathway, Neoplasia. 32 (2022) 100821.

[509] L. Yong, S. Tang, H. Yu, H. Zhang, Y. Zhang, Y. Wan, F. Cai, The role of hypoxia-inducible factor-1 alpha in multidrug-resistant breast cancer, Front. Oncol. 12 (2022) 3787.

[510] K.. Comerford, T.. Wallace, J. Karhausen, N.. Louis, M.. Montalto, S.. Colgan, Hypoxia-inducible Factor-1-dependent Regulation of the Multidrug Resistance (MDR1) Gene, Cancer Res. 62 (2002) 3387–3394.

[511] M.B. Keogh, F.J. O'Brien, J.S. Daly, Substrate stiffness and contractile behaviour modulate the functional maturation of osteoblasts on a collagen–GAG scaffold, Acta Biomater. 6 (2010) 4305–4313.

[512] M. Hunter Joyce, C. Lu, E.R. James, R. Hegab, S.C. Allen, L.J. Suggs, A. Brock, Phenotypic basis for matrix stiffness-dependent chemoresistance of breast cancer cells to doxorubicin, Front. Oncol. 8 (2018) 337.

[513] Y. Lv, H. Wang, G. Li, B. Zhao, Three-dimensional decellularized tumor extracellular matrices with different stiffness as bioengineered tumor scaffolds, Bioact. Mater. 6 (2021) 2767–2782.

[514] National Cancer Registry Ireland, Cancer in Ireland 1994-2020: Annual Statistical Report of the National Cancer Registry, (2022).

[515] National Cancer Registry Ireland, Cancer in Ireland 1994-2015 with estimates for 2015-2017: Annual Report of the National Cancer Registry, (2017).

[516] Y. Jiang, H. Zhang, J. Wang, Y. Liu, T. Luo, H. Hua, Targeting extracellular matrix stiffness and mechanotransducers to improve cancer therapy, J. Hematol. Oncol. 15 (2022) 34.
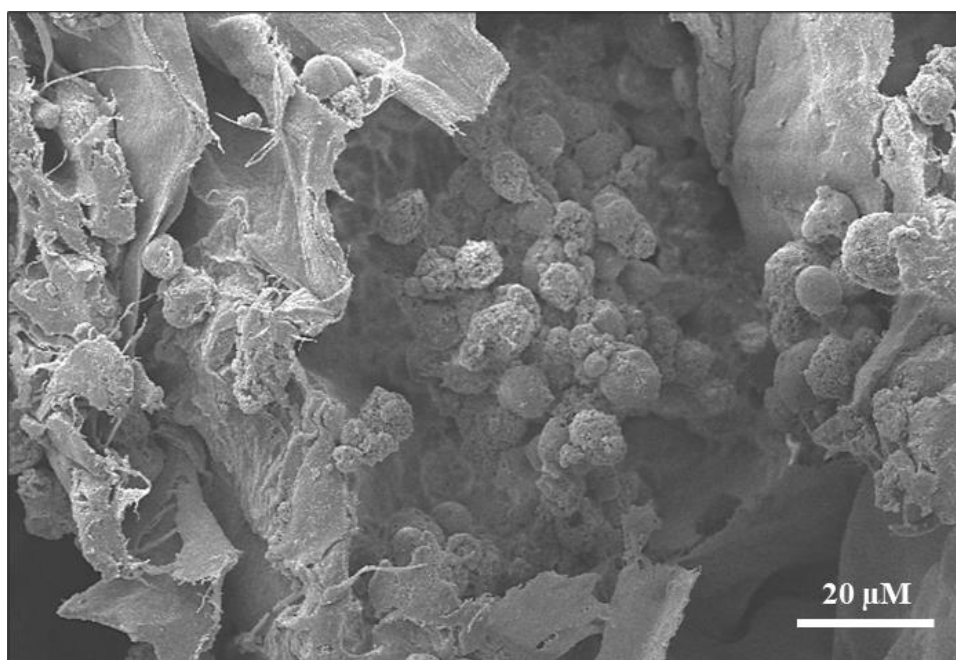
Appendix

Appendix Chapter 1

Appendix 1.1 – Thermocouple probe report for freeze drying cycle.
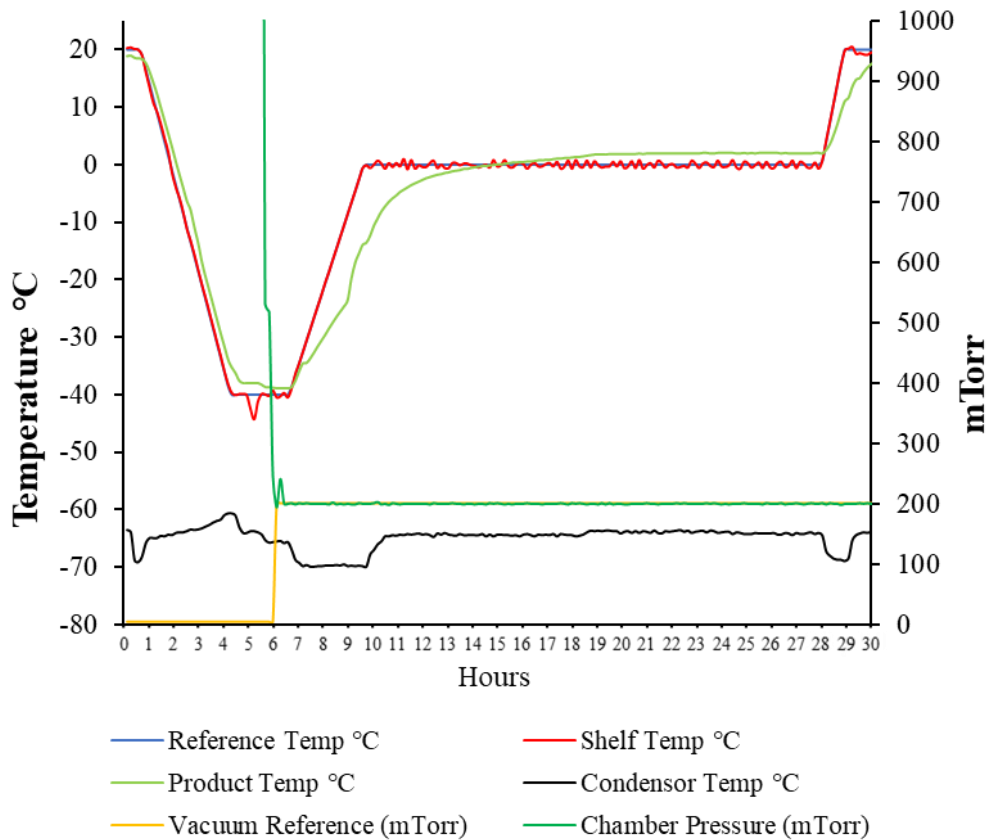
Appendix 1.1: Thermocouple probe report for freeze drying cycle. Thermocouples were used to ensure collagen-based solutions were progressing through the freeze drying cycles, both thermal and drying phases, in the correct manner. In the above report example, it can be seen that the collagen (product temp line) demonstrates a slight hysteresis when the reference/shelf temperatures are increasing. However, solution cooling/heating remains satisfactory. Vacuum reference (Vac ref) and chamber pressure sensors demonstrate the rapid and successful reaching of the vacuum required for the freeze drying cycle. The condenser rapidly reached the desired low temperature range of -60 to -70 °C and maintained between this range for the full cycle.
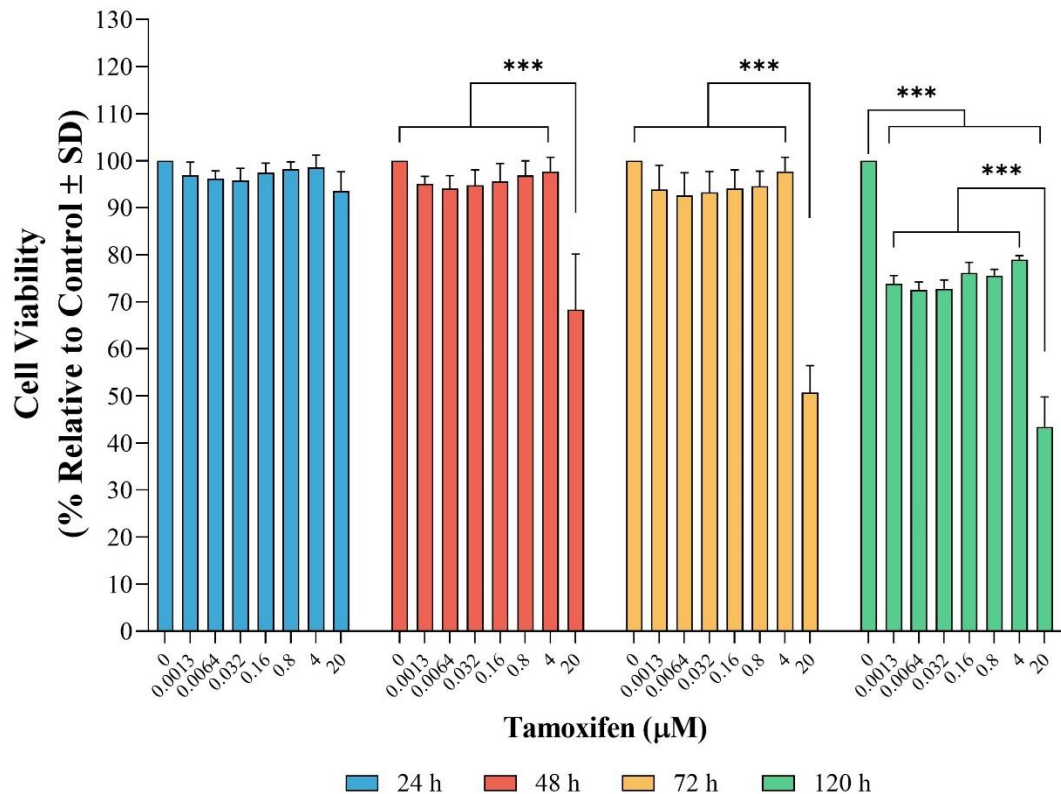
Appendix Chapter 3

Appendix 3.1: Large cluster of MCF7 cells within w/Gel 0.15% scaffold.

Appendix 3.1: Large cluster of MCF7 cells within w/Gel 0.15% scaffold. MCF7 cells within the w/Gel 0.15% at Day 14 forming a large spheroid-like cluster of cells within the porous architecture.

Appendix Chapter 5

Appendix 5.1 – Tamoxifen - dose effect at each timepoint

Appendix 5.1: Tamoxifen - dose effect at each timepoint. Dose response curves were converted to standard bar charts, to assess the dose concentration effect within each timepoint. At 48, 72 and 120 h, there was a large reduction in cell viability upon treatment with 20 μM docetaxel. After 120 h, there was an increase in growth inhibition observed for all doses compared to the vehicle control. Cell viability was determined using the alamarBlue assay. Results shown are the mean ± SD (n=3). p-value ≤0.05 = *, p-value ≤0.01 = **, p-value ≤0.001 = ***.
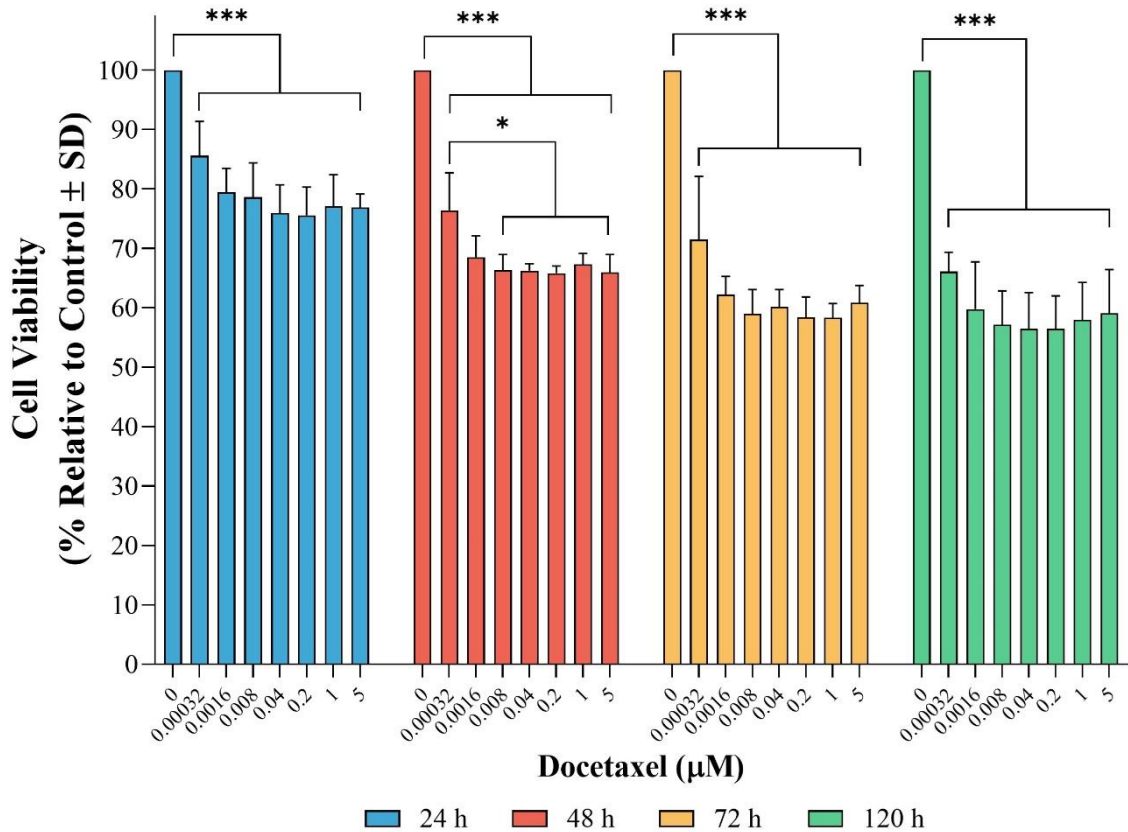
Appendix 5.2 – Tamoxifen - timepoint effect at each dose
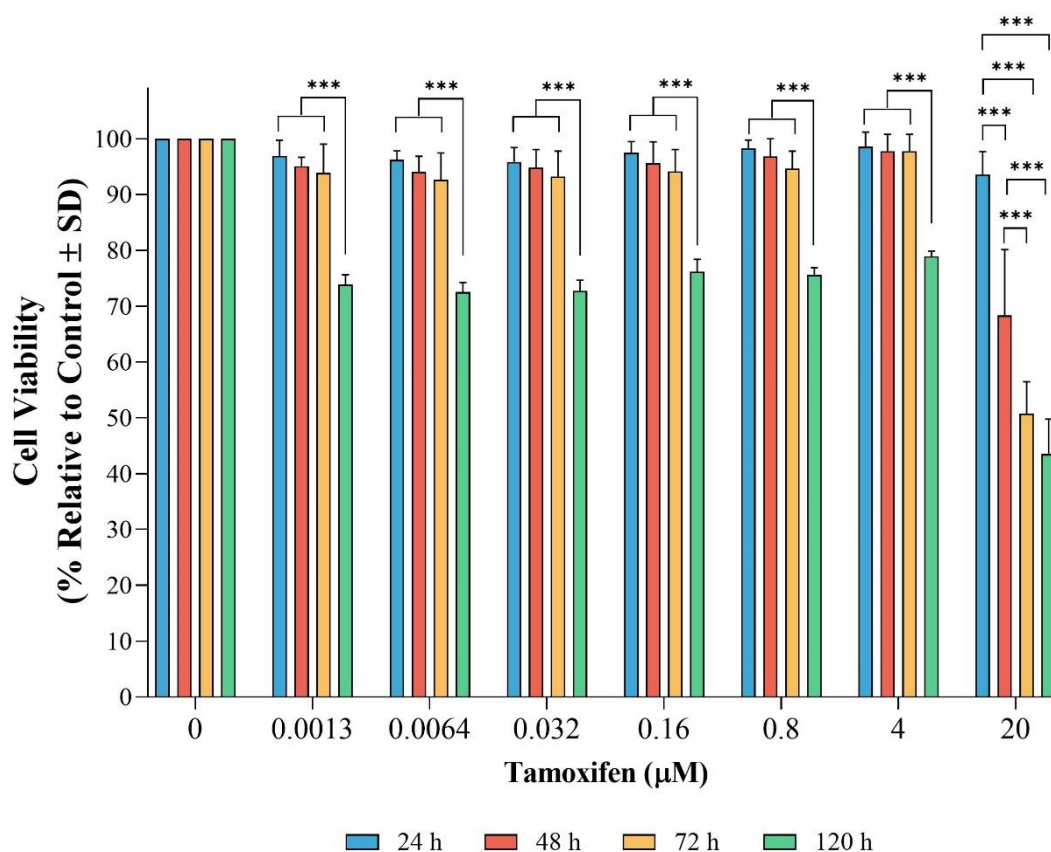
Appendix 5.2: Tamoxifen - timepoint effect at each dose. Dose response curves were converted to standard bar charts, to assess the effect of the exposure period within each concentration. Exposure for 120 h resulted in increased growth inhibition compared to all other exposure periods for all concentrations of tamoxifen assessed. In addition, at a concentration of 20 μM, both 48 and 72 h displayed increase inhibition to 24 h. Finally, both 72 and 120 h of exposure resulted in increased growth inhibition at 20 μM compared to 48 h exposure. Cell viability was determined using the alamarBlue assay. Results shown are the mean ± SD (n=3). p-value ≤0.05 = *, p-value ≤0.01 = **, p-value ≤0.001 = ***.
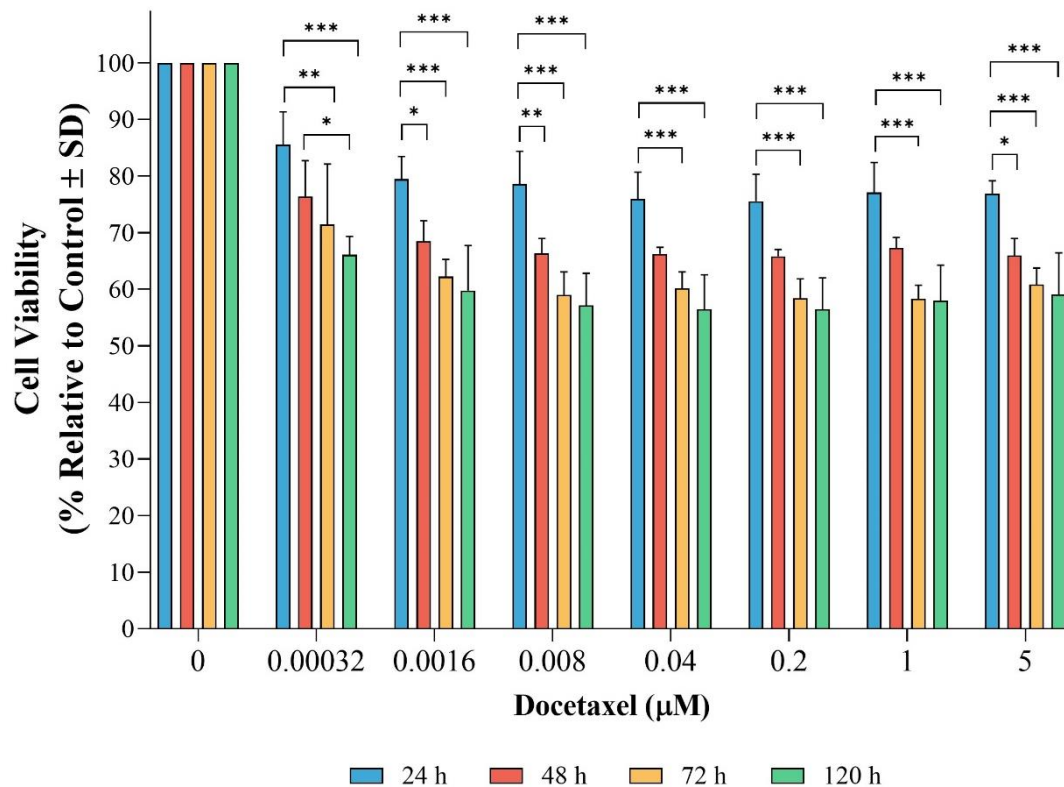
Appendix 5.3 – Docetaxel - dose effect at each timepoint

Appendix 5.3: Docetaxel - dose effect at each timepoint. Dose response curves were converted to standard bar charts, to assess the dose concentration effect within each timepoint. All concentrations of docetaxel used resulted in increased growth inhibition compared to the vehicle control. In addition, within the 48 h exposure group, all other concentrations had increased growth inhibition compared to the 0.00032 µM dose. Cell viability was determined using the alamarBlue assay. Results shown are the mean ± SD (n=3). p-value ≤0.05 = *, p-value ≤0.01 = **, p-value ≤0.001 = ***.

Appendix 5.4 – Docetaxel - timepoint effect at each dose

Appendix 5.4: Docetaxel - timepoint effect at each dose. Dose response curves were converted to standard bar charts, to assess the effect of the exposure period within each concentration. Treatment for 72 h and 120 h resulted in a significant increase in growth inhibition compared to the 24 h treatment time at all concentrations. Cell viability was determined using the alamarBlue assay. Results shown are the mean ± SD (n=3). p-value ≤0.05 = *, p-value ≤0.01 = **, p-value ≤0.001 = ***.